Production and Evaporation of Higher Dimensional Black Holes

Marco Oliveira Pena Sampaio

Churchill College

A dissertation submitted to the University of Cambridge
for the degree of Doctor of Philosophy
March 2010

Production and Evaporation of Higher Dimensional Black Holes

Marco Oliveira Pena Sampaio

Abstract

This thesis is a study of the theory and phenomenology of trans-Planckian black holes, in TeV gravity extra-dimensional theories. The introduction starts with the motivation for this beyond the Standard Model scenario (chapter 1), a summary of the theoretical tools to formulate the theory, and a summary of the best bounds from experiment (chapter 2).

In chapter 3, after setting up some notation and describing well known solutions in $4 + n$-dimensional general relativity, we construct an approximate effective background for a brane charged rotating higher-dimensional black hole. This is achieved by solving Maxwell's equations perturbatively on the brane to obtain the electromagnetic field. A brief study of the effect of rotation on the absorption of classical particles is also provided.

Chapter 4 is a review of methods to model black hole production focusing on the trapped surface method. A model for the mass and angular momentum loss into gravitational radiation is described.

A detailed study of the effects of particle mass and charge, for fermions and scalars on the effective brane charged background, is presented in chapters 5 and 6. After coupling the fields to the background, the separated radial wave equations for both perturbations are obtained (chapter 5) and they are integrated using a detailed numerical method as well as analytic approximations (chapter 6). Similarly, a method is described to obtain high accuracy angular functions based on series expansions. We conclude the theoretical study by evaluating the Hawking spectra for various combinations of spin, mass, charge and rotation parameters, and discuss them comparatively.

The last part of the thesis is on the implementation of the theoretical results in the new `CHARYBDIS2` Monte Carlo simulation of black hole production and decay (chapter 7), and on the analysis of the phenomenological consequences (chapter 8). The main new features implemented in `CHARYBDIS2` are: a full treatment of the spin-down phase using the angular and energy distributions of the associated Hawking radiation; an improved model for energy and angular momentum loss in the production process, and a wider range of options for the Planck-scale termination of the decay. The main conclusions of this thesis and an outlook on future directions are summarised in the final chapter.

Declaration

This dissertation is the result of my own work, except where explicit reference is made to the work of others, and has not been submitted for another qualification to this or any other university.

The approximate charged rotating background constructed in chapter 3 was published in [1]. The original study of charge and mass effects developed in chapters 5 and 6 was published in [1, 2]. The event generator described in chapter 7 was released in [3] and published in [4] with part of the phenomenological study of chapter 8.

This thesis does not exceed the 60,000 word limit prescribed by the Degree Committee for Physics and Chemistry.

Marco Oliveira Pena Sampaio

Acknowledgements

I start by thanking my supervisor Prof. Bryan Webber for all his support, guidance, patience and positive thinking throughout my PhD. I have learnt a lot about doing research, and the process of building independent ideas. I must thank him in particular for the incredible continuous feedback provided during the preparation of this document.

I am very grateful for the pleasure of having collaborated with: Marc Casals, Sam Dolan, Jonathan Gaunt, and especially Prof. M. Andrew Parker and James Frost. I must single out James for his dedication and support to the `CHARYBDIS2` project, especially for his good-humoured and friendly character, positiveness and loyalty.

I have been lucky to be surrounded by many other stimulating researchers in the Cambridge high energy physics group and the Cambridge Supersymmetry working group. I have learned from them through discussions about many interesting areas of particle physics. In particular, I thank my near office mates Deirdre Black, Steve Kom, Are Raklev and the lineage of PhD students Jenni Smillie, Seyi Latunde-Dada, Andreas Papaefstathiou, Jo Gaunt, Lucian Harland-Lang and Eleni Vryonidou. With them I had the most satisfying discussions, and shared problems, hopes and successes.

A special note must go to a collaborator from a different project, and friend, Carlos Herdeiro for his wise advice and positiveness during some important periods of my PhD.

This project was funded by Fundação para a Ciência e Tecnologia (FCT) - Portugal, grant SFRH/BD/23052/2005 co-financed by POPH/FSE. I am grateful to Churchill College for providing not only academic resources, but most importantly, a home.

I thank Bryan, James and Jo for proof-reading the document.

There are so many people outside physics who made these years the best. I especially want to single out Martin Huarte-Espinosa, Johann von Kirchbach, Kasia Gilewicz, Frida Weierud, Carlos Guedes, Chris Edge and Raquel Ribeiro for being my Cambridge family. I was also lucky to spend many hours with the Cambridge Volleyball friends, who kept me physically healthy and cheerful. In Portugal, I thank my friends from Neiva, Viana do Castelo and Porto for always receiving me as if I had never left.

I am most grateful of all to my two siblings and my parents. They believe and support everything I do, and they are the constants in my life.

Contents

Chapter 1

Introduction

In this chapter we summarize the current formulation of the Standard Model of particle physics (SM) by describing its particle content and interactions, as well as Einstein's theory of gravity. We then analyse the main puzzles arising when the two theories are compared, and discuss ways of extending them. Finally we present some alternatives and emphasize extra-dimensional models which are discussed in detail in the next chapter.

1.1 Particle physics and the Standard Model

Particle physics is dedicated to the search of ever more fundamental indivisible units which constitute the building blocks of all known matter. The best picture available so far is one where fundamental point particles are modelled by quantum fields. Experimental data up to the present date provides extremely detailed and accurate verification of most of the predictions of the so called Standard Model (SM) [5]. The first step in constructing the Standard Model is to realize what are the fundamental degrees of freedom observed in experiments. These can be organised in two classes:

1. The force carriers, bosonic spin-1 fields which are responsible for the electromagnetic and strong forces through the massless fields A_α and G^i_α ($i = 1 \dots 8$) respectively, and the weak forces through the massive fields $W^\pm_\alpha$ and Z_α.

2. The matter fermionic spin-1/2 fields which can be of two sub-types (all fields are Dirac spinors):

   - Quarks – They are of up-type u^i_a or down-type d^i_a with electric charges $+2/3$ and $-1/3$ respectively. There are three families, $a = 1 \dots 3$ with increasing

masses (up, charm, top, for up-type; and down, strange, bottom, for down-type). The index $i = 1 \ldots 3$ is a label for the strong force colour charge.

- Leptons – Here the equivalent of the up-type particles are the neutrinos[1] ν_a which are electrically neutral and the down-type particles are electron-like, e_a with electric charge -1. The family index runs through $a = 1 \ldots 3$ (electron, muon and tau families respectively).

With this particle content, we can construct free Lagrangians plus interactions. The main leading principles in the construction of the SM Lagrangian are: Lorentz invariance, renormalisability, unitarity and gauge invariance. In particular to obtain charged current or coloured current interactions (for the $W^{\pm}_{\alpha}$ and the gluons respectively) the gauge group must be non-abelian. Since the $W^{\pm}_{\alpha}$ is a massive particle and there are no non-abelian massive gauge theories which are unitary and renormalisable, a mechanism must be invoked to give mass to the gauge bosons. One of the simplest ways to achieve this is the Higgs mechanism, where an extra scalar field H is used.

The model is constructed by postulating a gauge group, at the fundamental level, which is $SU(3)_C \times SU(2)_L \times U(1)_Y$. The gauge fields are the gluon G^i_{α}, the weak isospin boson A^i_{α} and the weak hypercharge boson B_{α}. The coupling constants are denoted g_i with $i = 1, 2, 3$ respectively, and the coupling to matter is achieved through covariantisation using the gauge covariant derivative

$$\partial_{\alpha} \rightarrow D_{\alpha} = \partial_{\alpha} + ig_1 \mathbf{G}_{\alpha} \cdot \mathbf{T}_1 + ig_2 \mathbf{A}_{\alpha} \cdot \mathbf{T}_2 + ig_3 Y B_{\alpha} \, , \tag{1.1}$$

where the dot $\cdot$ denotes summation over the gauge group generators, and bold face fields denote column vectors composed of the gauge field components. $\mathbf{T}_1$ and $\mathbf{T}_2$ are the generators of the corresponding gauge groups in the fundamental representation and Y is the hypercharge.

The Yang-Mills Lagrangian for the theory is (given a convenient choice of generators in the adjoint representation)

$$\mathcal{L}_{\text{pure gauge}} = -\frac{1}{4} \mathbf{G}_{\alpha\beta} \cdot \mathbf{G}^{\alpha\beta} - \frac{1}{4} \mathbf{A}_{\alpha\beta} \cdot \mathbf{A}^{\alpha\beta} - \frac{1}{4} B_{\alpha\beta} B^{\alpha\beta} \, , \tag{1.2}$$

[1]Note however that right-handed neutrinos have not been observed experimentally, although the non-zero neutrino masses indicate their existence.

where we denote the field strengths by the same letter as the corresponding gauge field. For a generic gauge field F^i_α with coupling g the field strength is

$$\mathbf{F}_{\alpha\beta} = \partial_\alpha \mathbf{F}_\beta - \partial_\beta \mathbf{F}_\alpha + g\left[\mathbf{F}_\alpha, \mathbf{F}_\beta\right] \ . \tag{1.3}$$

To generate masses for the weak bosons, the Higgs field is introduced. This is chosen to be a singlet under $SU(3)_C$ and in the fundamental representations of $SU(2)_L \times U(1)_Y$, i.e. $(\mathbf{1}, \mathbf{2}, 1/2)$, with Lagrangian

$$\mathcal{L}_{\text{Higgs}} = \left(D^\alpha H\right)^\dagger D_\alpha H - \frac{1}{2}\lambda\left(H^\dagger H - \frac{1}{2}v^2\right)^2 \ . \tag{1.4}$$

The real parameters $\lambda > 0$ and v are constants. At the ground state of the potential, the Higgs develops a non-zero expectation value (VEV) which breaks the $SU(2)_L \times U(1)_Y$ symmetry to $U(1)_Q$. The three Nambu-Goldstone bosons, associated with the flat directions of the potential around the vacuum, are absorbed by three of the weak field degrees of freedom giving them longitudinal components and therefore mass. The remaining $U(1)_Q$ symmetry corresponds to the electromagnetic field. With an appropriate choice of gauge it is possible to express the low energy physical degrees of freedom as

$$H = \frac{1}{\sqrt{2}}(v+h)\begin{pmatrix} 0 \\ 1 \end{pmatrix} \tag{1.5}$$

$$W_\alpha = \frac{1}{\sqrt{2}}\left(A^1_\alpha - iA^2_\alpha\right) \tag{1.6}$$

$$Z_\alpha = \cos\theta_W A^3_\alpha - \sin\theta_W B_\alpha \tag{1.7}$$

$$A_\alpha = \sin\theta_W A^3_\alpha + \cos\theta_W B_\alpha \tag{1.8}$$

where $h(x)$ is the remaining real Higgs scalar field. We can switch from the set $\{g_2, g_3, \lambda\}$ to $\{e, \cos\theta_W, m_h\}$ where e is the QED coupling, m_h is the Higgs mass and $\theta_W \in [0, \pi/2]$ is the Weinberg angle. These are defined by

$$\begin{aligned} g_2 \sin\theta_W &= e \\ g_3 \cos\theta_W &= e \\ m_h^2 &= \lambda v^2 \end{aligned} \quad . \tag{1.9}$$

The gauge/Higgs sector of the SM after symmetry breaking is then

$$\begin{aligned}\mathcal{L}_{s=\{0,1\}} &= \frac{1}{2}\partial^\alpha h\partial_\alpha h - \frac{m_h^2}{2}h^2 - \frac{\lambda}{8}h^3\left(h+4v\right) - \frac{1}{4}\,\mathbf{G}_{\alpha\beta}\cdot\mathbf{G}^{\alpha\beta} + \\ &\quad -\frac{1}{2}W^\dagger_{\alpha\beta}W^{\alpha\beta} + m_W^2 W^\dagger_\alpha W^\alpha - \frac{1}{4}Z_{\alpha\beta}Z^{\alpha\beta} + \frac{m_Z^2}{2}Z_\alpha Z^\alpha - \frac{1}{4}A_{\alpha\beta}A^{\alpha\beta} + \\ &\quad \frac{1}{4}h\left(h+4v\right)\left(\frac{2e^2}{\sin^2(2\theta_W)}Z_\alpha Z^\alpha + \frac{e^2}{\sin^2\theta_W}W^\dagger_\alpha W^\alpha\right) + \\ &\quad +iW_\alpha W^\dagger_\beta\left(eA^{\alpha\beta} + \frac{e}{\tan\theta_W}Z^{\alpha\beta}\right) + \frac{e^2}{2\sin^2\theta_W}\left(\left|W_\alpha W^\alpha\right|^2 - \left(W^\dagger_\alpha W^\alpha\right)^2\right)\end{aligned} \tag{1.10}$$

where we can identify the Higgs free Lagrangian and self interactions, the electroweak vector bosons free Lagrangians and self interactions, the Higgs/vector interactions and the vector/vector interactions respectively[2]. In this effective Lagrangian, the Nambu-Goldstones are no longer identified as physical degrees of freedom at low energies, because they are part of the W and Z fields. However it is known that at high energies, a longitudinal state of a W or a Z in an external leg of a matrix element can be replaced by a Nambu-Goldstone boson state. This is the so called Goldstone boson equivalence theorem (for a discussion see section 21.2 of [6]).

The fermionic matter sector is constructed similarly by considering all possible renormalisable terms before symmetry breaking. The field content and gauge representations are chosen as to reproduce the chiral structure of the interactions and the electric and colour charges observed in experiments. The up-type and down-type left-handed components of the Dirac fields are placed in $SU(2)_L$ doublets transforming in the fundamental representation, and the right-handed parts on $SU(2)_L$ singlets. The leptons are placed in singlets under $SU(3)_C$, whereas the quarks transform in the fundamental representation. Finally the hypercharges are chosen as to produce the correct $U(1)_Q$ electric charges after symmetry breaking. The fermion content is then (leptons and quarks respectively)

$$\begin{aligned} L^a = \begin{pmatrix}\hat{\nu}_L^a \\ \hat{e}_L^a\end{pmatrix} \to \left(\mathbf{1},\mathbf{2},-\tfrac{1}{2}\right), \qquad & R^a = \hat{e}_R^a \to \left(\mathbf{1},\mathbf{1},-1\right) \\ Q^a = \begin{pmatrix}\hat{u}_L^a \\ \hat{d}_L^a\end{pmatrix} \to \left(\mathbf{3},\mathbf{2},\tfrac{1}{6}\right), & \begin{aligned} U^a = \hat{u}_R^a &\to \left(\mathbf{3},\mathbf{1},\tfrac{2}{3}\right) \\ D^a = \hat{d}_R^a &\to \left(\mathbf{3},\mathbf{1},-\tfrac{1}{3}\right)\end{aligned}\end{aligned} \tag{1.11}$$

[2]Here the field strengths $W_{\alpha\beta}, Z_{\alpha\beta}, A_{\alpha\beta}$ are defined as before for the abelian field B_α.

where the representations are denoted in parenthesis and the hats are a reminder that these are fields before electroweak symmetry breaking. Note that for simplicity we have not included right-handed neutrinos, which must be singlets under the full SM gauge group. This would allow a Majorana mass term which can explain the small left-handed neutrino masses and the decoupling of the right-handed neutrino through the seesaw mechanism. Nevertheless, for the processes we will consider, left-handed neutrino masses are negligible, so we can safely ignore the mechanism of mass generation for neutrinos and exclude right-handed neutrinos. Then the Lagrangian is[3]

$$\begin{aligned}\mathcal{L}_{\frac{1}{2}} &= \bar{L}^a i\not{\partial} L^a + \bar{R}^a i\not{\partial} R^a + \bar{Q}^a i\not{\partial} Q^a + \bar{U}^a i\not{\partial} U^a + \bar{D}^a i\not{\partial} D^a \\ &\quad -\sqrt{2}\left(\bar{L}^a \lambda^R_{ab} H R^b + \bar{Q}^a \lambda^U_{ab} H^c U^b + \bar{Q}^a \lambda^D_{ab} H D^b + c.c.\right) , \end{aligned} \tag{1.12}$$

where λ^i_{ab} are complex Yukawa matrices in general. After the Higgs boson acquires a VEV and electroweak symmetry is broken:

$$\begin{aligned}\mathcal{L}_{s=\frac{1}{2}} &= \bar{e}^a \left(i\not{\partial} - m_{e_a}\right) e^a + \bar{\nu}^a i\not{\partial} \nu^a + \bar{u}^a \left(i\not{\partial} - m_{u_a}\right) u^a + \bar{d}^a \left(i\not{\partial} - m_{d_a}\right) d^a + \\ &\quad -\frac{h}{v}\left(m_{e_a}\bar{e}^a e^a + m_{u_a}\bar{u}^a u^a + m_{d_a}\bar{d}^a d^a\right) + \\ &\quad -\frac{e}{2\sqrt{2}\sin\theta_W}\left(J^\alpha_W W_\alpha + c.c.\right) - e J^\alpha_A A_\alpha - \frac{e}{\sin(2\theta_W)} J^\alpha_Z Z_\alpha - g_1 J^\alpha_{G,i}\, G^i_\alpha \end{aligned} \tag{1.13}$$

with the free kinetic terms, the Higgs/fermion interactions and the vector/fermion interactions.[4] The various currents are

$$J^\alpha_A = -\bar{e}^a \gamma^\alpha e^a + \frac{2}{3}\bar{u}^a \gamma^\alpha u^a - \frac{1}{3}\bar{d}^a \gamma^\alpha d^a \tag{1.14}$$

$$J^\alpha_{G,i} = \bar{u}^a \gamma^\alpha T_i u^a + \bar{d}^a \gamma^\alpha T_i d^a \tag{1.15}$$

$$J^\alpha_W = \bar{\nu}^a \gamma^\alpha \left(1-\gamma_5\right) e^a + \bar{u}^a \gamma^\alpha \left(1-\gamma_5\right) V_{ab} d^b \tag{1.16}$$

$$\begin{aligned} J^\alpha_Z &= \frac{1}{2}\left[\bar{\nu}^a \gamma^\alpha \left(1-\gamma_5\right)\nu^a - \bar{e}^a \gamma^\alpha \left(1-\gamma_5-4\sin^2\theta_W\right) e^a\right] + \\ &\quad +\frac{1}{2}\left[\bar{u}^a \gamma^\alpha \left(1-\gamma_5-\frac{8}{3}\sin^2\theta_W\right) u^a - \bar{d}^a \gamma^\alpha \left(1-\gamma_5-\frac{4}{3}\sin^2\theta_W\right) d^a\right] \end{aligned} \tag{1.17}$$

and now the Yukawa couplings λ^i_{ab} are replaced by the masses of the physical particles and the CKM matrix V_{ab} (after diagonalising the original mass matrices by rotating the

[3] We use the usual slash notation for contraction with the Dirac gamma matrices $\gamma^\alpha V_\alpha \equiv \not{V}$.

[4] Note that we have removed the hats from the fermion fields after symmetry breaking and used the e symbol both for the charged leptons and the electric coupling constant.

original weak states to the physical states).

1.2 Gravity

The remaining fundamental force which is known up to the present is gravity, and it is described by Einstein's theory of General Relativity (GR). It is also a gauge field theory but with a spin-2 field g_{ab}[5]. It has been probed only classically at very large scales compared to the fundamental scale in the theory: the 4-dimensional Planck length L_4. Its dynamics and interaction with matter are governed by the Einstein-Hilbert action together with the action for the matter fields. The latter is covariantised with respect to g_{ab} by replacing all partial derivatives with curved spacetime covariant derivatives and the Minkowski metric by g_{ab}. The full action is

$$\begin{aligned} \mathcal{S} &= \mathcal{S}_{EH} + \mathcal{S}_{matter} \\ &= \int d^4x \sqrt{|g|} \left[\frac{M_4^2}{2} R + \mathcal{L}_{matter} \right] \end{aligned} \tag{1.18}$$

where R is the Ricci scalar and $M_4 \equiv 1/L_4$ the Planck mass. This prescription ensures that gravity couples universally to all fields. Since all known particles are described by the SM, the matter Lagrangian is simply the curved spacetime covariantised version of the Lagrangian in section 1.1. When varied with respect to g_{ab}, (1.18) provides the Einstein equations of motion

$$\mathcal{G}_{ab} = M_4^{-2} T_{ab} \equiv \frac{2}{M_4^2 \sqrt{|g|}} \frac{\delta S_{matter}}{\delta g^{ab}} \, . \tag{1.19}$$

Except for the need to invoke dark matter at cosmological scales or to explain galaxy rotation curves, all the gravitational observations performed so far are consistent with GR. Some of the most precise measurements include [7]:

- The weak equivalence principle, Lorentz invariance and local position invariance have been confirmed with precisions of $10^{-13}, 10^{-22}$ and 10^{-4} respectively,
- Weak field effects in solar system experiments with accuracies up to 10^{-3},
- Some tests of the strong field regime in binary pulsar systems with precision 10^{-4},
- and torsion-balance measurements which test the inverse square dependence of the gravitational force between test masses (confirmed, down to $56\,\mu$m [8, 9]).

[5] We denote curved spacetime indices by lower case letters from the Latin alphabet.

These experiments support the validity of GR for classical gravitational phenomena and more importantly the strong field regime, where for example black hole physics is included. However, gravity has only been probed well above M_4, so for example it is not known how it behaves at the quantum level. In particular, straightforward quantisation of the GR perturbations on a background is not renormalisable so it cannot provide a full theory of quantum gravity. Some examples of theories of quantum gravity are string theory [10] or canonical quantisation [11, 12]. We will restrict our study to phenomena which are typically away from this regime.

1.3 Comparing couplings

To better understand the scales in the SM and GR and how they compare to each other it is instructive to rewrite the previous Lagrangians using a common probe length scale L. We rescale all lengths by this amount as well as all the SM fields and the Ricci scalar according to their mass dimensions. In addition, we assume that any interaction occurs at proper length scales which are small with respect to the typical curvature scale of spacetime, so that we can work in a locally inertial frame where, to a first approximation, the metric is expanded around Minkowski spacetime plus linear perturbations:

$$g_{ab} = \eta_{ab} + \frac{L_4}{L} h_{ab} \, . \tag{1.20}$$

We have normalised h_{ab} such that the kinetic term from the Einstein-Hilbert action takes a canonical form. It follows from straightforward dimensional analysis and linearisation that no new factors of L_4/L appear in the SM Lagrangian, except for new terms which are related to the coupling to gravity through products with h_{ab}. Furthermore any dimensionful quantity comes divided by an appropriate number of powers of L. The action, up to linear order, is then given by the zeroth order SM action in Minkowski space plus the Fierz-Pauli Lagrangian which describes linearized gravity (see for example [11])

$$\mathcal{S}_{FP} = \int d^4x \left[\frac{1}{8} \left(h^{ab,c} h_{ab,c} - 2h^{ab,c} h_{ac,b} + 2h^{ac}{}_{,a} h_{,c} - h_{,b} h^{,b} \right) + \frac{L_4}{2L} T_{ab} h^{ab} \right] \, , \tag{1.21}$$

where the comma denotes partial differentiation. Another way to estimate the magnitude of the gravitational interaction is by using a Newtonian approximation. In the limit of non-relativistic collisions we can use the classical expressions for the electrical (F_e)

Interaction	Types of Operators	Couplings	at $E \sim 1$ TeV
Matter/Gravity	$T_{ab}h^{ab}$	$\frac{E}{M_4}$	10^{-16}
Fermions/Vectors	$\bar{f}f'\{A, Z, W, G\}$	$e, \frac{e}{\sin(2\theta_W)}, \frac{\sqrt{2}e}{4\sin\theta_W}, g_1$	0.3, 0.4, 0.2, 1.2
W/Vectors	$W^\dagger W\{A, Z\}$	$e, \frac{e}{\tan\theta_W}$	0.3, 0.6
W/W	$\frac{1}{2!}W^\dagger W W^\dagger W$	$\frac{e^2}{\sin^2\theta_W}$	0.4
Gluon/Gluon	$\{G^4, G^2\partial_\alpha G\}$	g_1^2, g_1	1.4, 1.2
Higgs/Higgs	$\left\{\frac{h^4}{4!}, \frac{h^3}{3!}\right\}$	$3\left(\frac{m_h}{v}\right)^2, \frac{v}{E}$	0.8, 0.25
Higgs/Fermions	$h\bar{f}f$	$\frac{m_f}{v}$	$2.10^{-6} - 0.7$
Higgs/Vectors	$\frac{h^2}{2!}\left\{\frac{1}{2!}ZZ, W^\dagger W\right\}$	$\frac{2e^2}{\sin^2(2\theta_W)}, \frac{e^2}{2\sin^2\theta_W}$	0.2, 0.2
	$h\left\{\frac{1}{2!}ZZ, W^\dagger W\right\}$	$\frac{4e^2}{\sin^2(2\theta_W)}\frac{v}{E}, \frac{e^2}{\sin^2\theta_W}\frac{v}{E}$	0.1, 0.1

Table 1.1: *Interaction couplings for all known fields*: The various types of interactions among SM particles and gravity are shown schematically. The couplings in the third column and their approximate values at 1 TeV in the fourth column are in one-to-one correspondence with the operators in the second column.

and gravitational (F_g) forces. For estimate purposes take a particle at rest and compute the forces on another charged test particle of the same type. Using the Newtonian approximation and the Coulomb force, and writing all the lengths and masses in natural units

$$\frac{F_g}{F_e} = \frac{\left(\frac{m}{M_4}\right)^2 . \left(\frac{L_4}{r}\right)^2}{\alpha . \left(\frac{L_4}{r}\right)^2} = \frac{1}{\alpha}\left(\frac{m}{M_4}\right)^2 = \frac{1}{\alpha}\left(\frac{L_4}{L}\right)^2 , \tag{1.22}$$

where m, M_4, L_4 are the mass of the particle, Planck mass and Planck length respectively, $\alpha = e^2/(4\pi)$ is the fine structure constant and we have identified $L \sim 1/m$ as the typical length scale for the process. From these estimates we see that the gravitational coupling constant for a process at a scale L is controlled by L_4/L or equivalently E/M_4 ($E \sim 1/L$

is the typical energy for the process). Table 1.1 summarizes the SM and gravitational couplings. In the first line, we observe that for the typical energies achieved in laboratory experiments today, gravity is truly negligible. This is due to the extreme smallness of the Planck length or equivalently the extremely large Planck mass which sets the energy scale for strong gravity. This large scale justifies why no quantum gravitational effects have been observed so far. In particular, there seems to be no hope for near future observations of quantum gravity effects. However, this statement should be taken with care, because of the enormous extrapolation involved along sixteen orders of magnitude. There could be some modification at smaller length scales, such that the conventional 4-dimensional Planck length is an effective scale derived from a more fundamental high energy theory. In fact the modern view of quantum field theories is that the low energy theories we observe are effective theories, from which the cutoff scale is not obvious (for a discussion on gravity see [13]).

1.4 Hierarchies and other unexplained properties

In section 1.3 we have seen how gravity is many orders of magnitude weaker than all known forces in the microscopic domain of particle physics. This is a manifestation of the hierarchy problem which is observed in Standard Model loop corrections as follows. If we take the SM as an effective field theory, we have to decide on a cutoff energy scale. In this interpretation, the predictions of the theory are made at energies below the cutoff, which sets the limit where new physics starts to arise. For the theory to be natural, its low energy limit couplings should be stable under small variations of the couplings at the cutoff [14]. The largest energy scale we know in nature is the Planck mass which would be the most natural first guess for a cutoff. In the SM, the low energy Higgs mass is expected to be of order[6] $\sim 10^2$ GeV, but the bare mass (at the Planck scale) receives corrections which are quadratic in the cutoff when renormalised to lower energies. This can be seen by looking at the Higgs Lagrangian (1.4) with v solved for m_h

$$\mathcal{L}_{\text{Higgs}} = \left(D^\alpha H\right)^\dagger D_\alpha H - \frac{1}{2}\lambda\left(H^\dagger H\right)^2 + \frac{1}{2}m_h^2 H^\dagger H + \text{constant} \ , \tag{1.23}$$

and by considering the self coupling and the Yukawa coupling to fermions $\lambda_f H\bar{f}f$ which give one loop corrections to the Higgs mass as in figure 1.1:

[6] Perturbative unitarity bounds imply $m_H \lesssim 870$ GeV (see for example [15]).

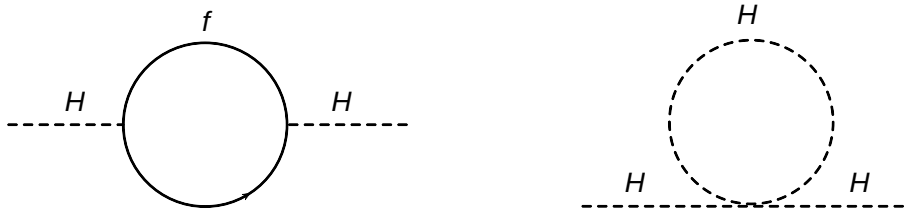

Figure 1.1: *Lowest order loop contributions to the Higgs mass quadratic divergence:* Fermion contributions (left) and scalar contributions (right).

$$\delta m_h^2 = \left(|\lambda_f|^2 - \frac{1}{2}\lambda \right) \frac{\Lambda_{\text{cutoff}}^2}{8\pi^2} + \dots \tag{1.24}$$

The largest contribution from fermion loops in the SM comes from the top Yukawa coupling. So, if Λ_{cutoff} is the Planck mass (which is ~ 17 orders of magnitude larger than the Higgs mass) the bare mass will be at the Planck mass scale and a small relative variation induces a very large variation of the low energy mass parameter. Therefore, the bare Higgs mass squared has to be unnaturally fine tuned with a precision of one part in 10^{34}. All the other couplings of the SM have a better ultraviolet behaviour either due to gauge symmetry or chiral symmetry [6]. However, since all the masses in the SM are generated either through the Higgs mechanism (for vector bosons) or the Yukawa interactions (for fermions) all masses are fine tuned indirectly through the Higgs VEV [16].

Some solutions of the hierarchy problem involve including new fields to improve the ultra-violet (UV) behaviour of the loop correction so as to cancel the quadratic divergences in the Higgs boson mass corrections. For example in Supersymmetry, each fermion has two scalar partners, such that $|\lambda_f|^2 = \lambda$ and the relative minus sign in equation (1.24) takes care of the cancellation [16]. In little Higgs models a similar cancellation occurs between bosons or between fermions [17]. Alternatively, in strong dynamics theories, instead of invoking a symmetry, the Higgs is replaced by a pion-like field of a new strong sector and the small mass is explained by a (natural) exponential running [14]. It is important to note that these solutions still do not explain why gravity is so much weaker than all other forces, so though the fine tuning problem is resolved, strictly speaking the hierarchy problem remains.

Finally, there are other properties of the SM which are not well understood such as: family replication; the large number of free parameters; the flavour structure in the Yukawa couplings (which induces large mass splittings among the fermions, and mixings in the quark sector); the (apparent) insufficient CP violation in the SM to generate the

baryon/anti-baryon asymmetry in the early Universe; and the generation of small neutrino masses (which appear to be at the eV scale) as well as the pattern of their mixings.

1.5 Extra dimensions

A very different, but still natural, way of solving the hierarchy problem is possible if we introduce extra dimensions. These constructions will be the focus of the remainder of this work. The simple idea behind such models is to take the TeV scale as the cutoff in the effective theory. This is assumed to be the only short distance fundamental scale, controlling in particular the strength of the gravitational force. This scenario was first proposed by Antoniadis, Arkani-Hamed, Dimopoulos and Dvali [18–21] in models with large compact extra dimensions (ADD scenario). The motivation arises from observing that the only scale which is well established experimentally in the microscopic domain is $M_{EW} \sim 1$ TeV. This solves the hierarchy problem trivially, because the fine tuning of the Higgs mass was due to the large cutoff scale. By setting such a cutoff close to the scale of the expected Higgs mass, the problem disappears.

Since in the ADD scenario the only fundamental scale is ~ 1 TeV, in particular the Planck mass must be of that order. This means that the true fundamental Planck mass is much smaller than the conventional Planck mass measured in gravitational experiments at large length scales. This difference in magnitude is explained by postulating the existence of compact extra dimensions, with sizes below the lengths probed in gravitational experiments. At short distances (well below the size of the extra dimensions) gravity is higher dimensional and controlled by the fundamental Planck mass, whereas at long distances, an effective theory for gravity arises from integrating out the extra dimensions. It is this procedure of integrating out the extra dimensions that raises the Planck mass by a large extra dimensional volume making gravity weak at large scales. Heuristically gravity gets diluted by the extra dimensional volume.

Another class of extra-dimensional models which solves the hierarchy problem by assuming TeV scale gravity and one curved extra dimension has been suggested by Randall and Sundrum (RS scenarios [22, 23]). In the original proposal two types of models were possible. In the first one the large effective Planck mass is due to the large curvature along a compactified extra dimension with a small radius, whereas the second contains a semi-infinite extra dimension with a small curvature (or equivalently large curvature radius). The latter is in some sense more similar to ADD. Both options (ADD and RS)

are presented in more detail in the next chapter.

A crucial feature of these models is that gravity becomes strong at energy scales ~ 1 TeV (note for example that the suppressing factors in (1.22) become of order 1 at the Planck scale). Therefore new phenomena arises above the TeV scale, in particular we would expect quantum gravitational effects. Since we do not known in advance what the new physics of quantum gravity above 1 TeV is, the only predictions we can trust are in particular limits where we hope that a combination of classical GR and quantum field theory holds. This is the semi-classical limit. It includes for example strong gravity at length scales large compared to the Planck length. This does not mean however that the process is bound to be at low energies because of the IR/UV correspondence in gravitational theories where large length scales are actually related to large concentrations of energy [24]. In particular black holes are examples of such systems where their size grows with the energy scale, so they can be formed in high energy processes where the collapsing matter interacts gravitationally at large separations. Thus the gravitational interaction can be effectively described by the classical theory at length scales large compared to the Planck length even though the amount of energy involved in the process is above the Planck mass. This is exactly what happens in astrophysical systems such as stars and black holes so we would not expect quantum gravity to be necessary. This limit is the strong semi-classical trans-Planckian regime which is the focus of this work. Other calculable regimes exist in the weak trans-Planckian limit at large distances [25] and sub-Planckian limit [26, 27] which we will not explore in detail.

Chapter 2

Theories with extra dimensions

Theories with extra dimensions were first introduced in 1912 by Nordström and in the 1920s by Kaluza and Klein as an attempt to provide a unified description of gravity and electromagnetism (see for example [28] where the original papers have been re-printed). Recently, they have been motivated and explored intensively in the context of String Theory which attempts to unify gravity and quantum mechanics. Regardless of the fundamental theory, extra dimensions may exist, and in fact the consequences of their existence can be explored without making many assumptions about a possible high energy (or UV) completion. In the remainder of this thesis, we will consider the existence of extra dimensions at low energies and adopt an effective theory approach where the model is built with a minimal set of assumptions consistent with current experimental bounds. In addition some extra assumptions are made which motivate the theory as a solution to known problems. This minimal approach is very useful because it provides a way to test different UV completions which reduce to the same type of low energy effective theory.

The purpose of this chapter is to present details on how to formulate extra dimensional effective field theories in general, then introduce the main extra dimensional scenarios that have been proposed as solutions to the hierarchy problem as well as an overview of more elaborate constructions, and finally present the main experimental bounds on extra dimensions.

2.1 General formulation

Extra-dimensional theories are formulated similarly to 4-dimensional theories. In general we assume an action of the form

$$\mathcal{S} = \int d^D X \sqrt{|G|}\,(\mathcal{L}_{grav} + \mathcal{L}_{matter}) \tag{2.1}$$

$$= \int d^D X \sqrt{G}\left(-\Lambda_D + \frac{1}{2}\hat{M}_D^{D-2}\mathcal{R}_D + \ldots + \mathcal{L}_{matter}\right) \tag{2.2}$$

where $D = 4 + n$ is the number of spacetime dimensions and $\hat{M}_D$ is the reduced Planck mass (see A.2). The dots denote higher curvature gravitational terms which we assume are suppressed compared to the leading Einstein-Hilbert action with a cosmological constant Λ_D. The minimal matter Lagrangian must contain the SM fields properly imbedded into the higher-dimensional spacetime consistently with current experimental data. The details of the imbedding are model dependent.

Most of the models studied at present can be formulated as effective theories on a particular background gravitational field. In many realisations the SM fields are confined to a lower dimensional space called the brane. The general formalism for writing down an effective theory on a background Minkowski spacetime, with a brane containing SM fields, was presented in [29]. In principle, most of the results can be applied to a curved background with a brane, so we summarize them and point out when specialisation to Minkowski spacetime simplifies the framework. The basic assumption is that the small amplitude and low energy perturbations, can be expanded perturbatively around the following background[1]:

$$\begin{aligned} &E_M^A(X) = E^{(0)}{}_M^A(X) \overset{Mink.}{\longrightarrow} \delta_M^A \qquad G_{MN}(X) = G_{MN}^{(0)}(X) \overset{Mink.}{\longrightarrow} \delta_M^A \eta_{MN} \\ &Y^M(X) = Y_{(0)}{}^M(X) \overset{Mink.}{\longrightarrow} \delta_a^M x^a \qquad\qquad\qquad \phi(x) = v \end{aligned} \tag{2.3}$$

where X are the bulk coordinates, $G_{MN}(X)$ is the bulk metric, η_{MN} is the D-dimensional

[1] Uppercase Latin indices from the middle of the alphabet $(M, N \ldots)$ denote full bulk spacetime components and uppercase Latin indices from the beginning of the alphabet $(A, B \ldots)$ denote bulk local Lorentz frame indices. Lower case Latin indices from the beginning of the alphabet $(a, b, \ldots)$ denote brane components and indices from the middle of the alphabet $(m, n, \ldots)$ denote extra dimensional components. Greek indices are reserved for local Lorentz frame components from the beginning of the alphabet $(\alpha, \beta, \ldots)$ for the first four dimensional components and the middle $(\mu, \nu, \ldots)$ for extra-dimensional components.

Minkowski metric, $E^A_M(X)$ is the D-bein defined by

$$\begin{aligned} E^A_M \eta_{AB} E^B_N &= G_{MN} \\ E^A_M G^{MN}(X) E^B_N &= \eta^{AB} \,, \end{aligned} \tag{2.4}$$

$Y^M(x)$ are the bulk coordinates of the brane, x^a are coordinates on the brane and ϕ is a scalar field which serves as Higgs (so it has a constant value on the brane but not necessarily in the bulk). On the brane we can construct the induced metric

$$g_{ab}(x) = G_{MN}(Y)\partial_a Y^M \partial_b Y^N \tag{2.5}$$

and the induced vierbein

$$e^\alpha_a(x) = R^\alpha_A(Y) E^A_M(Y) \partial_a Y^M \,, \tag{2.6}$$

where $R(Y)$ is the solution of

$$R^\mu_B(Y) E^B_M(Y) \partial_a Y^M = 0, \quad \forall\ \mu, a \tag{2.7}$$

and can be obtained through a perturbative series in terms of the fluctuation in Y. For example in Minkowski spacetime, if we set Y to its background value in equation (2.3), the solution is trivially $R^A_B = \delta^A_B$ and the induced vierbein is simply a projection of the bulk D-bein. The same lowest order solution holds for a curved spacetime where $E^{(0)}{}^\mu_a(Y) = 0$ (see appendix A.3). With these ingredients it is straightforward to write down the effective theory for the bulk and brane perturbations. For the pure gravity sector, this is just the Lagrangian provided in Eq. (2.1). For brane degrees of freedom we write down a 4-dimensional effective action

$$\mathcal{S}_{brane} = \int d^4x \sqrt{g} \left(-f^4 + \mathcal{L}_0 + \mathcal{L}_{\frac{1}{2}} + \mathcal{L}_1 \right) \tag{2.8}$$

where f is a brane tension and we have scalar, fermion and vector boson Lagrangians respectively. The Lagrangians are obtained by covariantising the SM Lagrangian with respect to g_{ab} by replacing all partial derivatives by space-time covariant derivatives ∇_a, i.e. for bosons using the metric connection (or Christoffel symbols)

$$\Gamma^a_{bc} = \frac{1}{2} g^{ad} \left(g_{bd,c} + g_{cd,b} - g_{bc,d} \right) \tag{2.9}$$

and for fermions the spin-connection

$$\omega_a^{\alpha\beta} = \frac{1}{2} g^{bc} e_b^{[\alpha} e^{\beta]}_{[c,a]} + \frac{1}{4} g^{bc} g^{de} e_b^{[\alpha} e_d^{\beta]} e^{\gamma}_{[c,e]} e^{\delta}_a \eta_{\gamma\delta} \,, \tag{2.10}$$

where the brackets denote commutation over the indices involved. Furthermore gamma matrices (γ^α) or Pauli matrices (σ^α) are lifted from the local Lorentz frame using the inverse of the induced vierbein. Then for a fermion ψ and a vector V^a

$$\begin{aligned} \gamma^a \partial_a \psi &\rightarrow \gamma^a \nabla_a \psi = e^a_\alpha \gamma^\alpha \left(\partial_a + \frac{1}{8} \omega_a^{\alpha\beta} \gamma_{[\alpha} \gamma_{\beta]} \right) \psi \equiv \not{\nabla} \psi \\ \partial_a V^b &\rightarrow \nabla_a V^b = \partial_a V^b + \Gamma^b_{ac} V^c \,. \end{aligned} \tag{2.11}$$

Note the generalised "slash" notation with the curved spacetime gamma matrices $\gamma^a = e^a_\alpha \gamma^\alpha$. With this formalism, after the background has been fixed, we can study perturbations (in particular quantum mechanically) by expanding all fields around their background values. This provides an effective Lagrangian with all the free parts for each degree of freedom, plus interactions. In this construction the degrees of freedom available are:

- All the SM fields on the brane,
- The higher dimensional graviton H_{AB} given by expanding [13]

$$G_{AB} = {G^{(0)}}_{AB} + \frac{1}{M_D^{D/2-1}} H_{AB} + \dots \,, \tag{2.12}$$

  which (due to gauge freedom) contains $(n+4)(n+1)/2$ degrees of freedom,
- The fields $\mathcal{Z}^M$ describing fluctuations of the brane around its background position

$$Y^M(x) = Y^M_{(0)}(x) + \frac{1}{f^2} \mathcal{Z}^M \tag{2.13}$$

  where only n degrees of freedom are dynamical since there is a residual gauge freedom on the brane due to general coordinate invariance (only fluctuations transverse to the brane are physical). From the brane point of view they are n scalar fields.

In this study we assume a fixed background and study perturbations for each field around the background. Thus we neglect interactions between different perturbations or higher order self-interactions. Nevertheless, when appropriate, we will assess the magnitudes of the neglected terms to justify the approximations.

2.2 The ADD scenario

The main scenario we will consider is the large extra dimensions class of models of Antoniadis, Arkani-Hamed, Dimopoulos and Dvali [19–21] (ADD). As mentioned in the introduction, this was proposed as a solution to the hierarchy problem by assuming the fundamental scale of electroweak physics to be the same as for gravitational physics. The fundamental theory is assumed to be extra-dimensional and the fundamental Planck mass M_D is set to 1 TeV. Furthermore, the background spacetime manifold is chosen in the form $\mathcal{M}^4 \times \mathcal{N}^n$ where $\mathcal{M}^4$ corresponds to a 4-dimensional Minkowski manifold on which the SM brane is placed, and $\mathcal{N}^n$ corresponds to n extra-dimensional directions which are typically chosen with some compactification. The compactification radii may or may not be equal, and the curvature vanishes or is small (so that the extra-dimensional space is close to being flat). The canonical example is $\mathcal{N}^n = \mathbb{T}^n$ a flat n-torus with common radii R. In what follows, for simplicity, we consider this case, though some of the considerations do not depend on this choice. Nevertheless this model is a good benchmark scenario to obtain bounds from experiments. This choice of background metric corresponds to the Minkowski limit of (2.3) with X^m compactified with radii R and X^a infinite in size. We also assumed that the brane thickness is much smaller than R, typically at the Electroweak scale $1/M_D$. We will see in section 2.5 how current experimental constraints impose this condition.

In this scenario, at short distances (much smaller than R), gravity is higher dimensional with the generalised Newton force law

$$F(r) = G_D \frac{m_1 m_2}{r^{2+n}} \tag{2.14}$$

where the fundamental Newton constant is

$$G_D = \frac{1}{\hat{M}_D^{2+n} S_{(2+n)}} \,, \tag{2.15}$$

$S_{(2+n)}$ is the area of the $(2+n)$-sphere and m_1, m_2 are test masses. Equation (2.14) is obtained using Gauss' law or by working with the gravitational part of the Lagrangian (2.1) coupled to test masses in the Newtonian limit [21]. On the other hand, for macroscopic objects on the brane (with sizes much larger than R), gravity will be effectively 4-dimensional. This can be seen by taking for example a macroscopic body on the brane. With respect to variations on the brane, its gravitational field must be fairly constant

along the extra dimensions. Then, the gravitational action (2.1) can be integrated along the extra dimensions to get an effective 4-dimensional action. The effective 4-dimensional reduced Planck mass $\hat{M}_4$ obtained is just a rescaling of $\hat{M}_D$ by an extra-dimensional volume factor $V_{(n)} = \int d^n X$:

$$\hat{M}_4^2 = \hat{M}_D^{2+n} V_{(n)} \ . \tag{2.16}$$

Similarly the Newton force at macroscopic distances is obtained either using Gauss' law, a Newtonian approximation, or the leading term in a Kaluza-Klein expansion of the potential [21]

$$F(r) = G_4 \frac{m_1 m_2}{r^2} \ , \tag{2.17}$$

which agrees with the usual 4-dimensional result.

Finally, let us define a characteristic length scale for the extra dimensions through $V_{(n)} = (2\pi L)^n$. The 2π factor is included, because the Kaluza-Klein (KK) mass splitting for the toroidal compactification is L^{-1} so, for example, it describes better the deviations from the Newtonian potential at short distances (see (2.27) below)[2]. The Planck mass and length are

$$M_D^{2+n} \equiv (2\pi)^n \hat{M}_D^{2+n} \ , \qquad L_D \equiv M_D^{-1} \ , \tag{2.18}$$

so the following relation arises from (2.16)

$$\frac{M_4}{M_D} = \left(\frac{L}{L_D} \right)^{\frac{n}{2}} \ . \tag{2.19}$$

Now it becomes clear how the hierarchy problem is solved. The question of why the 4-dimensional Planck mass and the electroweak scale are separated by several orders of magnitude is replaced by the dynamical problem of generating an extra dimensional space with a large size/volume (large compared to the electroweak length L_D).

2.3 The Randall-Sundrum scenario

In more general constructions, the extra dimensions do not have to be flat. An example of such are the Randall-Sundrum models RS1 [22] and RS2 [23] which explain the Planck/electroweak hierarchy by introducing a curved extra dimension. The question of

[2]The Kaluza-Klein expansion is obtained from a dimensional reduction of the theory by Fourier expanding the fields in the Lagrangian along the extra-dimensions and integrate the the extra-dimensions to get a four-dimensional theory with an infinite tower of fields (see for example equation (2.30).

how spacetime evolved to that state is again dynamical and remains open. The geometry of the model is defined by the non-factorisable $(4+1)$-dimensional ground state metric

$$ds^2 = e^{-2ky}\eta_{\mu\nu}dx^\mu dx^\nu - dy^2, \tag{2.20}$$

so

$$E_M^A = \begin{cases} e^{ky} & A = M = 0, \ldots, 3 \\ 1 & A = M = 4 \\ 0 & \text{otherwise} \end{cases} \tag{2.21}$$

In these coordinates space-time looks like 4-dimensional Minkowski with the lengths rescaled by e^{-ky} as we vary y. It can be seen more explicitly that the geometry is actually that of the AdS_5 space-time through a coordinate transformation $\rho = e^{ky}/k$. This gives the usual form of the AdS_5 metric $ds^2 = (k\rho)^{-1}\eta_{AB}dX^A dX^B$ which emphasizes its conformal flatness.

In RS1, spacetime is compactified on an $S^1/\mathbb{Z}_2$ orbifold by letting $y \in [-\pi R, \pi R]$ and identifying $y \leftrightarrow -y$. Two branes are present, one at each of the fixed points $y = 0$ and $y = \pi R$ with (constant) positive and negative tensions respectively given by $V_{hidden} = -V_{visible} = 6\hat{M}_D^3 k$. The bulk cosmological constant is $\Lambda_5 = 6\hat{M}_5^3 k^2$. Using the formalism in section 2.1 it is possible to show [22] that the Einstein field equations obtained from the effective gravitational action (with brane matter perturbations set to zero)

$$\mathcal{S} = \int d^4x \int_{-\pi R}^{\pi R} dy \sqrt{|G|} \left[-\Lambda_5 + \frac{1}{2}M_5^3 \mathcal{R} - V_{visible}\delta(y - \pi R) - V_{hidden}\delta(y) \right] \tag{2.22}$$

are solved by the metric (2.20). Furthermore, the effective Planck scale at large distances is again obtained from integration over the extra dimension and keeping the zero mode massless graviton. Then

$$M_4^2 = \frac{M_5^3}{k}\left(1 - e^{-2\pi kR}\right) , \tag{2.23}$$

so for this large curvature case (i.e. kR large), the effective Planck mass depends little on R. The way the hierarchy problem is solved in this case is through the exponential scaling of the metric $e^{-2\pi kR}$ between the hidden brane, at $y = 0$, and the visible brane, at $y = \pi R$, which rescales all masses on the hidden brane to the physical masses on the visible brane. So in RS1, the fundamental mass scale is still at the usual four-dimensional Planck scale[3] and the hierarchy on the visible brane is generated through the exponential

[3]Similarly all fundamental scales in the model such as R and k can be chosen using such a scale.

scaling created by the mild hierarchy $kR \sim 10$.

The RS2 scenario, on the other hand, can be seen as the limit $R \to +\infty$ of the RS1 scenario but with the visible brane placed at $y = 0$. So the extra dimension is semi-infinite, $y \in [0, +\infty[$ and the Standard Model fields are confined to the 3-brane at $y = 0$ with $Y^A = \delta^A_\mu x^\mu$. The effective four dimensional gravitational action in this case is the special limit of (2.23)

$$M_4^2 = \frac{M_5^3}{k} \Rightarrow \left(\frac{M_5}{M_4}\right)^2 = \frac{k}{M_4} \,. \tag{2.24}$$

$L \equiv 1/k$ takes the role of an effective size for the infinite extra dimension which localises the zero mode graviton on the brane, so (2.24) becomes

$$\left(\frac{M_4}{M_5}\right)^2 = \frac{L}{L_5} \,. \tag{2.25}$$

This shows that the hierarchy is again due to the large typical (effective) size of the infinite extra dimension, or equivalently the small curvature. In some sense RS2 is similar to ADD in how it solves the hierarchy problem, since the fundamental Planck scale is set to $M_5 = M_{EW}$, in contrast with RS1 where all scales are at M_4. All the masses on the brane are naturally of the order of M_{EW}. At very short distances, as long as the curvature k is small enough, we can use a flat metric for RS2.

2.4 Further brane constructions and other scenarios

In general the situation could be more complicated, with a combination of curvature and compactification. Furthermore, in a realistic situation we would not expect the SM fields to be confined to an infinitely thin brane, but instead to propagate in a subspace with a typical thickness along the extra dimensions.

So in a complicated scenario we could have several extra dimensions compactified with a large radius and/or large curvature, combined with thin sub-spaces, with or without large curvature, where the SM fields can propagate along some or several extra dimensions. Such thin branes can be effectively described by the Universal Extra Dimensions (UED) scenario of [30]. The upper bound on the extra dimensional width for a thin brane is [31, 32] $R \simeq (700\,\mathrm{GeV})^{-1}$. These bounds come mainly from considering electroweak loop corrections to vector boson self energies, which receive contributions from virtual Kaluza-Klein states, and comparing them to electron-positron collider data from the LEP

experiments, and also rare decays such as $\bar{B} \to X_s\gamma$.

This bound on R is many orders of magnitude below the scale needed in a large extra dimensions scenario (for $n \lesssim 15$) to explain the size of the Planck mass in the spirit of [19, 20]. So for example, if the thin brane is imbedded in a thicker compactified space, gravitational effects at distances larger than R can still be described by a large extra dimensions (or small curvature) effective theory.

More elaborate setups have been proposed where different SM fields are placed on different branes imbedded in a thicker brane of size $R \lesssim 1\,(\mathrm{TeV})^{-1}$ [33, 34]. Such constructions aim to suppress the effects of dangerous operators which, for example, might allow fast proton decay. The solution is to confine the fermions to different branes, such that for example the overlap of the wavefunction between quarks and leptons is small, preventing fast proton decay. Furthermore such models are interesting on their own as an explanation for the hierarchy of the fermion masses in the SM by adjusting the positions of the sub-branes.

We should note that if we look at gravitational processes occurring at length scales sufficiently above the maximum thickness of the thick brane where all the SM sub-branes live, we can treat all SM fields as being effectively on a single brane. Furthermore, if at the same time the process is well below the size of the large extra dimensions, then gravity is stronger and higher dimensional. These considerations justify the use of a single brane first approximation to study higher-dimensional strong trans-Planckian gravitational effects.

2.5 Experimental bounds on extra dimensions

In this section we provide a summary of the most important experimental results which provide bounds on extra-dimensional models.

2.5.1 Laboratory bounds

Gravity at mesoscopic scales

At large lengths r just above L, the usual gravitational force law starts to get modified. Bounds on the size of L can be found by looking at deviations from the Newtonian force law at the threshold $r \gtrsim L$, or by looking at dense systems where the inter-particle distance is much smaller than L. The various limits for the classical gravitational effective potential of the theories we consider are as follows [21, 23, 35]. At very short distances

there is a limit where the gravitational potential is higher dimensional for all the models.

$$\frac{V(r)}{G_4 L^{-1} m_1 m_2} = \left(\frac{L}{r}\right)^{n+1} S_n \Gamma(n) + \dots \ , \quad r \ll L \ . \tag{2.26}$$

This is true at distances which are much smaller than the compactification radius or the curvature radius. At large distances, we obtain the Newtonian potentials with corrections:

$$\frac{V(r)_{ADD}}{G_4 L^{-1} m_1 m_2} = \sum_{k_1,\dots,k_n} \frac{L}{r} e^{-\frac{|\mathbf{k}|r}{L}} \sim \frac{L}{r} + 2n\frac{L}{r} e^{-\frac{r}{L}} + \dots \ , \quad r \gg L \tag{2.27}$$

$$\frac{V(r)_{RS1}}{G_4 L^{-1} m_1 m_2} = \frac{L}{r} + \frac{L}{r}\Phi_1^2(0) e^{-\mu_1 r} + \dots \ , \quad r \gg R \tag{2.28}$$

$$\frac{V(r)_{RS2}}{G_4 L^{-1} m_1 m_2} = \frac{L}{r} + \frac{2}{3}\left(\frac{L}{r}\right)^3 + \dots \ , \quad r \gg L \tag{2.29}$$

where $\mathbf{k} = (k_1, \dots, k_n)$ is a vector of integers, $\mu_1 \sim 1/R$ is the first Kaluza-Klein (KK) mass for the RS1 scenario and $\Phi_1(0)$ is the corresponding first KK wavefunction evaluated at zero. The strongest experimental bounds for deviations from the Newton law come from torsion-balance experiments [8, 9] and are summarised in table 2.1. Note that for RS2, the first correction in the $r \gg L$ limit is less suppressed than the corresponding correction for $n = 1$ ADD, so whenever ADD is excluded by these experiments, so will the RS2 model with the same L. Note that at short distances RS2 behaves exactly the same as $n = 1$ ADD. For RS1, since the compactification radius is of the same order as the four dimensional Planck length the scenario is not excluded by these experiments.

Collider bounds

At sub-Planckian energies, the quantum fluctuations of the gravitational field can be treated as linearised perturbations in Minkowski spacetime, to obtain a higher dimensional graviton (see equation (2.12) for example). Since we are looking at linearised perturbations, the interaction with matter is given by the higher dimensional generalisation of the Fierz-Pauli Lagrangian (1.21). Therefore, matter interacts linearly with the higher dimensional graviton through its energy-momentum tensor. From the 4-dimensional point of view on the brane, this can be expanded in a tower of Kaluza-Klein states with increasingly larger masses controlled by the inverse compactification radius. We have already seen a manifestation of the KK tower for example in the expression for the gravitational

potential (2.27). In general (see [26, 36]), from the 4-dimensional perspective, it can be shown that we have: a tower of massive spin-2 gravitons $G^{(i)}_{kk\alpha\beta}$ that couple directly to the energy momentum tensor of matter on the brane; a tower of spin-1 particles which do not couple at linear order, and a tower of spin-0 particles which couple only to the trace of the energy-momentum tensor (however this vanishes under the equations of motion at tree level for a massless gauge theory). The effective Lagrangian for the relevant degrees of freedom is

$$\mathcal{L}^{(i)} = -\frac{1}{2}G^{(i)\,\alpha\beta}_{kk}\left(\Box + m^2_{(i)}\right)G^{(i)}_{kk\alpha\beta} + \frac{1}{2}G^{(i)\,\alpha}_{kk\alpha}\left(\Box + m^2_{(i)}\right)G^{(i)\,\beta}_{kk\beta} + \\ - G^{(i)\,\alpha\beta}_{kk}\partial_\alpha\partial_\beta G^{(i)\,\gamma}_{kk\gamma} + G^{(i)\,\alpha\beta}_{kk}\partial_\alpha\partial_\gamma G^{(i)\,\gamma}_{kk\beta} - \frac{1}{\hat{M}_4}G^{(i)\,\alpha\beta}_{kk}T_{\alpha\beta}\,. \quad (2.30)$$

The energy momentum tensor for a matter Lagrangian with a fermion field f coupled to a gauge field F_α with strength $F_{\alpha\beta}$ contains operators of the form (schematically) $\gamma_\alpha\partial_\beta\bar{f}f$, $\gamma_\alpha\bar{f}\partial_\beta f$, $\gamma_\alpha F_\beta\bar{f}f$ and $F^2_{\alpha\beta}$. Note that even though the coupling to each KK graviton is controlled by the four dimensional Planck mass, the spacing between KK modes is very small ($\sim 1/R$) so for processes at high energies there will be a large number of KK modes. It can be shown that this enhances the cross-section to produce an overall coupling of $1/\hat{M}_D^2$ instead of $1/\hat{M}_4^2$.

With these interaction vertices, the main processes for collider searches are tree level graviton production with a photon or a jet [37, 38] $f\bar{f} \to \gamma G^{(i)}_{kk}$ or $f\bar{f} \to G G^{(i)}_{kk}$, and tree level dilepton or diphoton production through KK graviton [39,40] $f\bar{f} \to G^{(i)}_{kk} \to f'\bar{f}'$ and $f\bar{f} \to G^{(i)}_{kk} \to \gamma\gamma$, which were searched for at LEP and the Tevatron.

Similar considerations apply to the RS1 model, but however, the KK mass spacing is now large due to the small extra dimension. Thus instead of a contribution from a continuum of modes we have well separated resonances with TeV scale masses and a coupling controlled by the TeV scale. The main effect is then resonant production of KK gravitons which appear as peaks in the dilepton or diphoton invariant mass spectra [41].

The most restrictive bounds are summarised in table 2.1.

2.5.2 Astrophysics and cosmology

Another source of constraints, comes from astrophysical systems, where very high energies are reached. In that case, KK gravitons provide a new competing channel in high energy collisions of SM particles, so they may be produced and decay, changing the dynamics.

Note however, that bounds from these systems do not apply to RS1, since the first KK resonance mass is supposed to be at the TeV scale.

Supernovae

The most restrictive bounds come from Supernovae [42]. In these systems, a large number of KK gravitons can be produced in the new channel $nn \to nnG_{kk}^{(i)}$ (n denotes a neutron). The KK gravitons are either gravitationally trapped in a halo around the neutron star formed after the supernova explosion or emitted as invisible energy. This new competing channel reduces the neutrino signal emitted in the explosion. Furthermore, the cooling of the neutron star is slower, because the KK gravitons trapped in the halo are an extra heat source through their decay, $G_{kk}^{(i)} \to \gamma\gamma$, into two photons which can fall into the star. On the other hand if the photons are emitted outwards, they contribute to an enhanced gamma ray flux from the neutron star which would be visible.

Finally, the diffuse γ-ray background would be enhanced by the photons emitted in the decay of KK gravitons produced in all the Supernovae formed throughout the cosmological evolution [42].

Early Universe KK gravitons

Similarly, in the early Universe, KK gravitons can be produced. The dominant channels are $2\gamma \to G_{kk}^{(i)}$, $\nu\bar{\nu} \to G_{kk}^{(i)}$, $e^+e^- \to G_{kk}^{(i)}$. This would lead to unacceptably large amounts of KK gravitons surviving the cosmological evolution, which would overclose the Universe [43]. Note that even though the coupling of each KK graviton to brane particles is suppressed by $1/\hat{M}_4$, it can be shown that the lifetimes involved are of the order of the Hubble time [43].

A further restriction [43] comes from the possible decay of the KK gravitons into photons which would distort the diffuse γ-rays background observed at present.

2.5.3 Summary of the bounds

Table 2.1 provides a summary of the bounds on M_D from various sources. The general conclusion is that a Planck mass at the TeV scale for extra-dimensional models with $n = 1$ is definitely excluded. However, the laboratory bounds still allow $n \geq 2$, whereas cosmology and astrophysics prefer $n > 3$. Note however that the modelling of astrophysical and cosmological systems often contains model dependent assumptions so the values should be

$n = D - 4$	1	2	3	4	5	6	7
Newton law deviations [8, 9]	$> 10^5$	8.0	$< 10^{-3}$	$< 10^{-3}$	$< 10^{-3}$	$< 10^{-3}$	$< 10^{-3}$
KK gravitons at colliders [37–40]	—	1.4	1.1	1.0	0.98	0.94	—
KK gravitons in Supernovae [42]	$> 10^5$	1.7×10^3	77	9.4	2.1	0.67	0.28
KK gravitons in the early Universe [43]	—	$68 - 155$	$5 - 28$	$0.8 - 7.7$	$0.2 - 3.2$	—	—

Table 2.1: This table summarises the most restrictive lower bounds for M_D (in TeV) for various number of extra dimensions. In the last row an interval of values is given for various choices of reheating maximum temperature.

taken as indicative (for example, for the early Universe production of KK gravitons, the bounds vary strongly with the assumed maximum temperature reached during reheating). Note also that the RS1 scenario is not excluded but instead there is a lower bound for the first KK resonance to have a mass above 250 GeV [41].

Chapter 3

Strong gravity I: Charged rotating black holes

We have seen in the previous chapters how physics can change at short distances and how gravity can become stronger and higher dimensional. In particular, if we look at the higher dimensional Newton force between test masses, now the coupling is controlled by the higher dimensional Planck mass, i.e. $E/M_4 \to E/M_D$. This means that gravity not only becomes strong, but for energies above M_D it is dominant compared to all other SM interactions. In the remainder of this work we are mainly interested in such strong trans-Planckian processes in D-dimensional general relativity.

A crucial question is to understand what occurs in such high energy processes. We are interested in processes where a collision occurs between two SM particles with a centre of mass energy $\sqrt{s} \gg M_D$. Well established results in classical general relativity say that when a certain amount of mass/energy is trapped in a small compact volume a region is formed from which nothing can escape. This is usually referred to as the hoop conjecture [44] and it is based on intuition from the simplest black hole solution – the static spherically symmetric Schwarzschild black hole. The latter has a typical size given by the Schwarzschild radius which grows with the trapped mass. The hoop conjecture says that if a certain amount of mass/energy is trapped within a hoop defined by its Schwarzschild radius, a black hole is formed. This argument was first invoked in [24, 45, 46] to suggest that a black hole is produced in trans-Planckian collisions with a small impact parameter in extra dimensional models. An interesting feature of the Schwarzschild radius is that it grows with $\sqrt{s}$. This implies that the gravitational interaction can be treated classically since it occurs at large distances. This is an example of the ultraviolet/infrared connection

in theories of gravity [24] (i.e. high energies are associated with large lengths).

In the next chapters we consider collisions occurring on the background models presented in chapter 2, at scales of the order $\gtrsim 1$ TeV. So even though the extra dimensions may be compactified, the black hole so formed can effectively be treated as a $(4+n)$-dimensional object because the compactification radius is very large. In general the black hole is characterized by a mass M, angular momentum J and some Standard Model charges inherited from the colliding particles. In particular, for proton-proton collisions, the black hole can have an electric charge Q and colour charges from the colliding quarks and/or gluons.

Before examining in detail the process of black hole production in chapter 4, in this chapter we present an overview of black hole solutions. This is useful for several reasons. Black hole solutions are good to model the gravitational field of realistic concentrations of matter. An example of such is again the Schwarzschild metric which gives the exact behaviour of the external gravitational field for a spherically symmetric star (Birkhoff's theorem). Even for rotating bodies, we would expect black hole metrics with rotation to give a good approximation for the gravitational field away from the massive body. Furthermore, since we have two particles in the collision interacting predominantly gravitationally, exact black hole solutions will be useful to model their interaction. Finally, our final state after the collision contains a black hole, so a black hole solution with the correct properties is necessary.

The outline of the chapter is the following. First we provide an overview of some useful well known black hole solutions in $(4+n)$-dimensions. In section 3.2 the approximate brane metric for a brane charged rotating black hole (constructed in [1]) is described, and finally in section 3.3 some geometrical properties of the solutions are presented through the study of their geodesics.

3.1 Black holes in general relativity

Black holes are solutions of the Einstein field equations (coupled or not to matter) containing a region which is invisible to an outside observer. The boundary of such a region is called the event horizon. They are associated with a high concentration of matter/energy in a small volume which creates a gravitational field configuration such that no signal can escape. The first suggestion of such dense objects goes back to Michell and Laplace who suggested dark stars within Newtonian theory. The first solutions in Einstein's theory

of gravity appeared shortly after it was proposed. In this section we present some basic definitions regarding the causal structure of spacetimes and some specific black hole metrics.

3.1.1 Definitions and properties

A rigorous definition of a black hole relies on the global causal structure of the spacetime. For all cases of interest, we take the spacetime to be asymptotically flat. This is because we are considering black hole production occurring on a flat Minkowski background.

The causal structure of a given spacetime can be understood schematically by constructing its Penrose-Carter conformal diagram. Intuitively, for example in Minkowski spacetime, this is obtained by changing variables such that the radial and time coordinates are squeezed down to a finite range and the metric is rescaled by a conformal factor. Then, by omitting the angular part, a metric with the same causal structure is obtained. This is true because null rays are invariant under conformal transformations. So if we consider Minkowski spacetime in D-dimensions expressed in spherical coordinates[1]

$$ds^2 = dt^2 - dr^2 - r^2 d\Omega_{D-2}^2 \tag{3.1}$$

and perform the transformation

$$ds^2 \to d\bar{s}^2 = 4\cos^2\left(\tfrac{\mathcal{U}}{2}\right)\cos^2\left(\tfrac{\mathcal{V}}{2}\right) ds^2 = d\mathcal{U}d\mathcal{V} - \sin^2\left(\tfrac{\mathcal{U}-\mathcal{V}}{2}\right) d\Omega_{D-2}^2 \tag{3.2}$$

where

$$t \mp r = \tan\left(\tfrac{1}{2}\{\mathcal{U},\mathcal{V}\}\right) \qquad -\pi \leq \mathcal{U} \leq \mathcal{V} \leq \pi\ , \tag{3.3}$$

the diagram in figure 3.1 is obtained (by suppressing the angular part). Null rays are represented by straight lines at $\pm\pi/4$, so at each point we get two perpendicular null rays which define the light cone. The horizontal curves of constant t (regularly spaced in t) map to spacelike geodesics and they all converge to spacelike infinity which is represented by the point I^0. On the other hand, all timelike curves (regularly spaced in r) originate from timelike past infinity I^- and terminate at future timelike infinity I^+. Similarly, all null curves originate at $\mathcal{J}^-$ and terminate at $\mathcal{J}^+$. In this diagram the left-hand side corresponds to extending r to negative values, so if for physical reasons we decide to allow

[1] $d\Omega_{D-2}^2$ is the line element on a $(D-2)$-sphere.

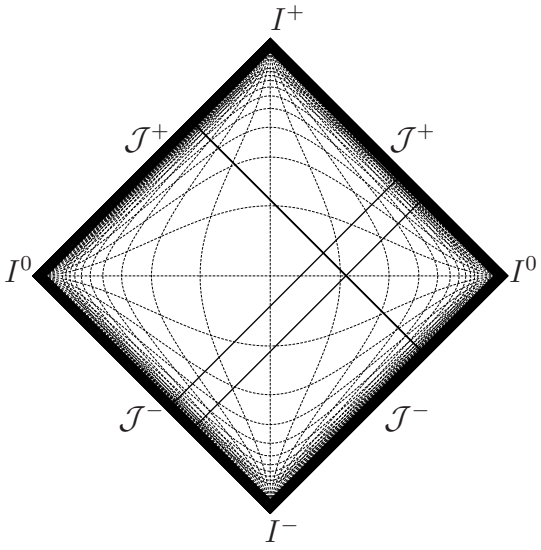

Figure 3.1: *Penrose-Carter diagram for Minkowski spacetime.*

only r positive, the corresponding diagram is obtain by reflecting the left-hand side onto the right-hand part of the diagram (or equivalently identifying the points which are mirror symmetric with respect to the vertical axis).

We are interested in spacetimes which are asymptotically flat in the past before the black hole is formed, and at large spacelike distances after formation. So when considering Penrose diagrams for black hole spacetimes, we will always have a part which maps onto a section of Minkowski with I^0, $I^\pm$ and $\mathcal{J}^\pm$. Then a natural definition of black hole is a region of spacetime from which no timelike or null rays can escape to reach I^+ and $\mathcal{J}^+$ respectively. The event horizon is the boundary of such a region which must be a null surface. This definition is global in nature and it requires a knowledge of the full history of the spacetime (or at least up to very late times after formation).

3.1.2 Some solutions in four dimensions

The Kerr-Newman family

Various 4-dimensional analytic solutions of the Einstein field equations coupled to matter have been constructed throughout the years to model systems with different matter content. These exact solutions are useful to understand fundamental properties of the theory and, more pragmatically, to model realistic systems. Typically they must have a high degree of (at least approximate) symmetry so that the analytic system is completely integrable. Various solutions have been constructed which are physically relevant in cos-

mological and astrophysical contexts (see for example chapter 5 of [47]). In this study, we are interested in solutions describing localized concentrations of matter, in particular black holes.

In four dimensions, the most general stationary axisymmetric solutions of the Einstein-Maxwell equations are the Kerr-Newman family of metrics and Maxwell potentials (see for example chapter 3.6 of [48]). This can be expressed in Boyer-Lindquist $\{t, r, \theta, \phi\}$ coordinates

$$ds^2 = \left(1 - \frac{r^2 + a^2 - \Delta}{\Sigma}\right) dt^2 + \frac{(r^2 + a^2 - \Delta)\, 2a \sin^2\theta}{\Sigma} dt d\phi - \frac{\Sigma}{\Delta} dr^2 - \\ - \Sigma d\theta^2 - \left(r^2 + a^2 + \frac{a^2 (r^2 + a^2 - \Delta) \sin^2\theta}{\Sigma}\right) \sin^2\theta d\phi^2 \ , \quad (3.4)$$

where

$$\Delta = r^2 + a^2 + Q^2 - 2Mr \, , \qquad \Sigma = r^2 + a^2 \cos^2\theta \ , \quad (3.5)$$

and

$$A_a dx^a = -Q \frac{r}{\Sigma} \left(dt - a \sin^2\theta d\phi\right) \ . \quad (3.6)$$

This spacetime is asymptotically flat, which can be seen more explicitly by separating the metric into two contributions and making a change of variables

$$\begin{cases} x &= \sqrt{r^2 + a^2} \sin\theta \cos\phi \\ y &= \sqrt{r^2 + a^2} \sin\theta \sin\phi \\ z &= r \cos\theta \end{cases} \ , \quad (3.7)$$

which define a spheroid (through their relation to r) according to

$$\frac{x^2 + y^2}{r^2 + a^2} + \frac{z^2}{r^2} = 1 \ . \quad (3.8)$$

Then (3.4) takes the form

$$ds^2 = dt^2 - dx^2 - dy^2 - dz^2 \\ - \frac{2Mr^3 - Q^2 r^2}{r^4 + a^2 z^2} \left[\left(dt + \frac{aydx - axdy}{r^2 + a^2}\right)^2 + \frac{1}{\Delta} \left(xdx + ydy + \frac{\sqrt{r^2 + a^2}}{r} zdz\right)^2\right] \ , \quad (3.9)$$

where the last term vanishes in the limit $r \to +\infty$. This spacetime contains two horizons

defined by the roots of $\Delta = 0$. In the form (3.4) or (3.9), the metric has coordinate singularities at the horizons which are removable through a change of coordinates.

This solution describes a black hole with a mass M, angular momentum $J = Ma$ and electric charge Q. The physical interpretation of these parameters can be made more transparent by comparing the first few asymptotic terms of the metric and the Maxwell strength when $r \to +\infty$, with those for an isolated non-relativistic weakly gravitating system [49]. The general results are expressed in a coordinate independent way through the Komar surface integrals on a sphere at $r \to +\infty$ and constant t

$$\begin{aligned} M &= \frac{1}{4\pi} \oint \nabla^a \mathbf{k}_t^b dS_{ab} \\ J &= \frac{1}{8\pi} \oint \nabla^a \mathbf{k}_\phi^b dS_{ab} \\ Q &= \frac{1}{4\pi} \oint \mathbf{F}^{ab} dS_{ab} \ , \end{aligned} \tag{3.10}$$

where $\mathbf{k}_t = \partial_t$ and $\mathbf{k}_\phi = \partial_\phi$ are the asymptotic killing vectors associated with time translations and rotation symmetry respectively, and $\mathbf{F}$ is the electromagnetic field strength. $dS_{ab} = dS\, n^t_{[a}\, n^r_{b]}$ is the surface element where n^t and n^r are the time-like and radial normals suitably anti-symmetrised. Furthermore, it is clear from (3.8) that the surfaces of constant r are spheroids with oblateness a^2/r^2, so the black hole horizon is squashed.

A maximal extension of the spacetime can be obtained using several coverings. We will not present the technical details, but instead summarize the main properties by analysing the Penrose-Carter diagrams of figure 3.2 (based on the discussion in [47]).

The simplest case is the Schwarzschild black hole ($a = Q = 0$) represented in the bottom left diagram. This is the unique static, spherically symmetric solution which represents the exterior field of a mass M. Its maximal extension contains a white hole (region-II', inside $r < r_H$) with a singularity, at $r = 0$, to the past of the (disconnected) asymptotically flat regions I and I'. For a realistic black hole, formed from collapsing matter, the white hole and the second asymptotically flat region-I' are not present. Note that the singularity at $r = 0$ cannot be removed through a change of coordinates. This can be seen by evaluating the curvature scalar invariant $R^{abcd}R_{abcd} \sim 1/r^6$. The black hole (region-II inside $r < r_H$) contains a singularity at $r = 0$, in the future of regions I and I'. It can be reached by any causal observer, who once inside it will necessarily hit the singularity. This property is related to the fact that any point inside region-II represents a closed trapped surface, i.e. any future directed light ray propagates to a region of smaller

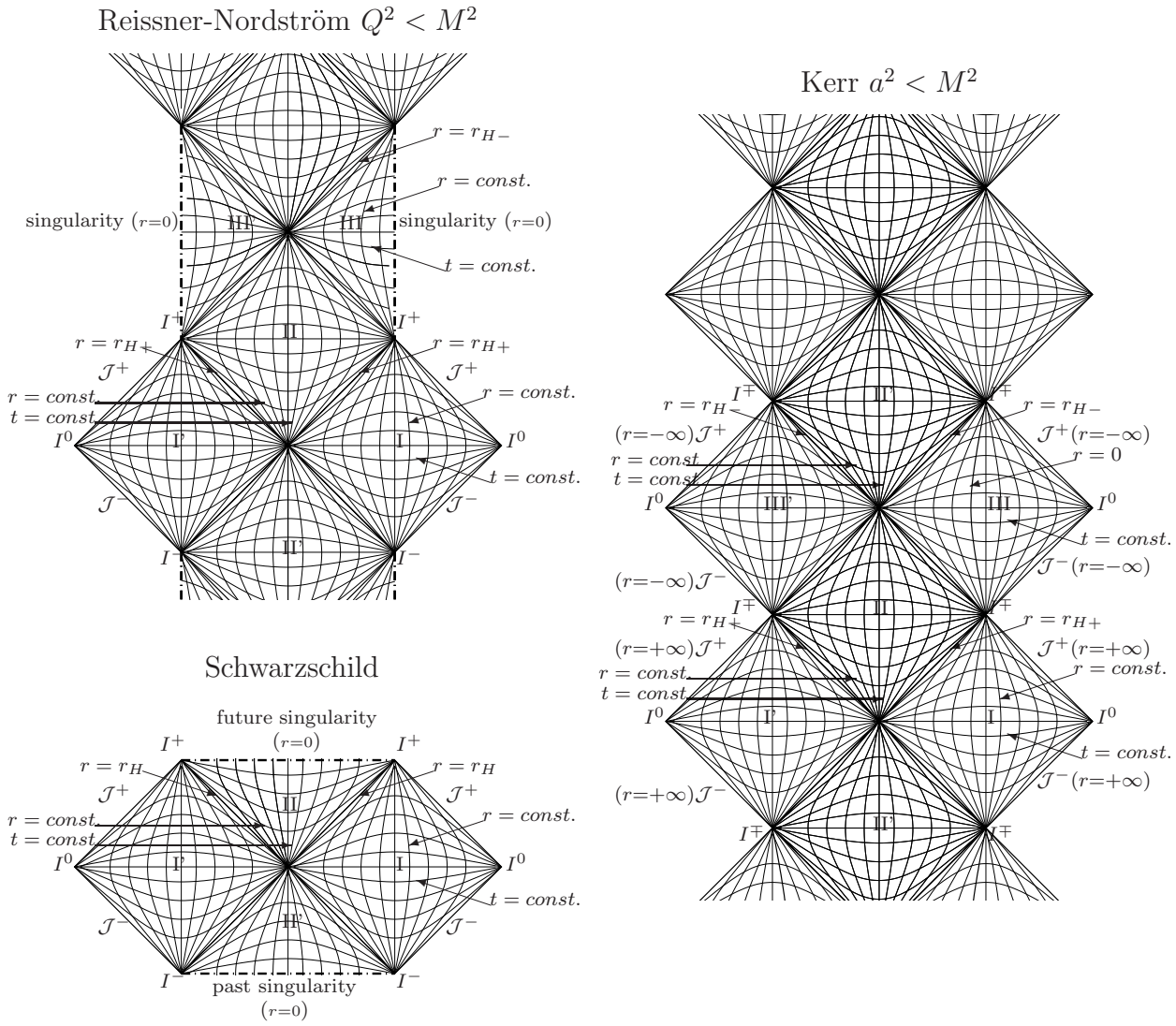

Figure 3.2: *Penrose-Carter diagrams for some cases of the Kerr-Newman family.* We show three qualitatively different cases of the maximal analytic extensions with some causal regions and their boundaries (such as horizons and singularities) indicated. In all diagrams region-I corresponds to the exterior region where an asymptotic observer propagates. The right diagram is for a direction along the axis of rotation of the black hole.

r (note that the horizontal curves in region-II are of constant r – decreasing upwards).

Turning on the charge parameter Q, we obtain the Reissner-Nordström black hole. There are three qualitatively different cases. If $Q^2 > M^2$ there are no horizons and the singularity at $r = 0$ is naked. So the Penrose-Carter diagram is similar to Minkowksi (see figure 3.1) except that a singularity is placed at $r = 0$. The diagram for $Q^2 < M^2$ is the top left of figure 3.2. Again, it contains a white hole in the past (region-II') which is absent in a realistic collapse. Regions I and I' are similar to the Schwarzschild case. Regarding horizons, now there is an outer horizon r_+ (causally similar to the horizon of the Schwarzschild black hole) which separates the black hole region-II from the outside observers in the asymptotically flat region. The main difference is the second horizon at a smaller radius $r = r_-$, which introduces two new causal regions-III and III'. In those regions, the points no longer represent closed trapped surfaces, so a causal observer can travel back to a larger r and emerge in a new white hole region. The latter communicates with another asymptotically flat region (repeating the bottom part of the diagram). Thus a timelike observer can avoid hitting the (timelike) singularity. For the special case $Q^2 = M^2$ the horizons are degenerate and regions II and II' do not exist.

Finally, if we set $Q = 0$ and turn on a, we obtain the Kerr metric[2]. Since the metric is no longer spherically symmetric, now the singularity is a ring. This is particularly intuitive in spheroidal coordinates where the ring is defined by $x^2 + y^2 = a^2$. An observer travelling along the axis passes through the disk at $x^2 + y^2 < a^2$ without hitting the singularity. The direction along the axis was used to draw the conformal diagram in figure 3.2 (representing the maximal analytic extension). Regions I, I', II and II' are similar to those of the Reissner-Nordström black hole (again we have an outer horizon and an inner horizon). Once the observer crosses the inner horizon, he/she can proceed to another white hole region-II' as before, or go through $r = 0$ to negative r into a new asymptotically flat region (III or III') without hitting the singularity. More relevant for an asymptotic physical observer in region-I is the so called ergoregion. This is the region outside the black hole where the Killing vector $\mathbf{k}_t$ (which defines the asymptotic static observers) becomes spacelike. From the point of view of an outside observer, no causal observer in the ergoregion can travel along an orbit of $\mathbf{k}_t$ and remain at rest with respect to infinity. Locally, it is still possible to find a timelike Killing vector by forming a linear combination of $\mathbf{k}_t$ and $\mathbf{k}_\phi$, so the solution is stationary, though not with respect to infinity.

[2]Note that the causal structure of the full Kerr-Newman metric is very similar.

3.1.3 Exact solutions in higher dimensions

The Myers-Perry family

Since we are interested in theories with extra dimensions, we need some generalisations of the 4-dimensional metrics in the previous section. The most general metric describing a higher dimensional rotating black hole was found by Myers and Perry [50]. While in four dimensions the angular momentum is described by a spatial pseudo-vector which defines the axis of rotation, in $(4+n)$ dimensions there are more angular momentum generators than spatial directions so in general we will have several axes of rotation. More rigorously, if we consider massive representations of the Lorentz group in $(4+n)$ dimensions, $SO(3+n,1)$, they can be labelled by the mass associated with the eigenvalue of the Casimir operator constructed from the generators of translations $P^a P_a = m^2$ and the eigenvalues of the $[(3+n)/2]$ Casimirs[3] of the little group $SO(3+n)$ [50]. The latter are the angular momentum invariants. In our study, we are mostly interested in the special case of a single rotation axis, because we will study particles colliding on the brane so their angular momentum is constrained. In Boyer-Lindquist coordinates the metric is

$$ds^2 = \left(1 - \frac{r^2+a^2-\Delta}{\Sigma}\right) dt^2 + \frac{(r^2+a^2-\Delta)\, 2a\sin^2\theta}{\Sigma} dt d\phi - \frac{\Sigma}{\Delta} dr^2 - \\ - \Sigma d\theta^2 - \left(r^2 + a^2 + \frac{a^2\,(r^2+a^2-\Delta)\sin^2\theta}{\Sigma}\right) \sin^2\theta d\phi^2 - r^2\cos^2\theta d\Omega_n^2 \ , \quad (3.11)$$

where

$$\Delta = r^2 + a^2 - \frac{\bar{\mu}}{r^{n-1}} \, , \qquad \Sigma = r^2 + a^2\cos^2\theta \ . \quad (3.12)$$

Note that $\{t, r, \theta, \phi\}$ have the same properties as in (3.4). The only two independent parameters in (3.11) are $\{\bar{\mu}, a\}$ which are related to the physical mass M and angular momentum J of the black hole obtained using the higher dimensional generalisations of the Komar integrals (3.10)

$$\frac{M}{M_D} = \frac{(n+2)}{2} S_{2+n} (2\pi)^{-\frac{n(n+1)}{n+2}} M_D^{n+1} \bar{\mu} \ , \quad (3.13)$$

$$J = S_{2+n} (2\pi)^{-\frac{n(n+1)}{n+2}} M_D^{n+2}\, a\, \bar{\mu} = \frac{2}{n+2} Ma \ . \quad (3.14)$$

[3] The brackets denote the integer part.

Furthermore, we can switch to a third pair of parameters, closely related to the geometrical properties of the black hole: $\{r_H, a_*\}$. The first parameter is defined by the location of the horizon of the black hole at the largest positive root of $\Delta(r_H) = 0$. r_H is directly related to the surface curvature of the horizon and thus (in some sense) has a frame independent meaning. The second is $a_* = a/r_H$ which is the oblateness of the (spheroidal) horizon (see equation (3.8)).

Brane tension and split branes

In section 2.1 we saw that in general we can place the SM fields on different branes (split brane scenario) which may have a non-zero tension. When considering a black hole formed in a SM brane these effects could in principle be important. The simplest case would be a black hole formed on a single tense brane. For the case of various split branes which are separated by small distances compared to the black hole size, from the gravitational point of view, this should be similar to a single effective brane. As pointed out in section 2.4, this is the case for the scenario we are considering where the black holes formed have masses well above 1 TeV. Thus the typical Schwarzschild radius is above $1 \sim 2\,(\mathrm{TeV})^{-1}$ and the minimum diameter should be $3 \sim 4\,(\mathrm{TeV})^{-1}$, which is already well above the upper bound on the width of the thick brane discussed in section 2.4.

However, even for the case of a single tense brane, the relevant black hole solutions known in the literature tend to be limited to the case of codimension-2 branes in six dimensions [51–55]. An example is the singly rotating black hole background with tension, where the main conclusion is that the brane projected metric remains unchanged up to a rescaling of the Planck mass [51, 53, 54]. Thus processes occurring on the brane remain qualitatively the same (with an effective brane Planck mass) and only processes in the bulk are qualitatively different. These observations, together with the fact that there are a large number of brane degrees of freedom, justify neglecting the effect of brane tension in 6-dimensions, for study of the Hawking evaporation in chapter 5 (note that $D = 6$ is anyway disfavoured from the bounds in [42, 56, 57]). For the phenomenologically favoured cases of codimension larger than 2, there are virtually no detailed studies of brane tension effects. We may hope that a similar effect of rescaling of the Planck mass will occur for brane fields, in which case our model does not need to be adapted, but further work is required to understand if such an assumption holds.

Boosted solutions

So far we have been looking at solutions that describe the gravitational field of a massive object in its rest frame. In the next chapter we will consider the gravitational interaction between two colliding particles. The gravitational field of a massive particle with no spin and no charge can be obtained from boosting the Schwarzschild metric in isotropic coordinates, which describes exactly the exterior gravitational field. This was first done in four dimensions by Aichelburg and Sexl [58]. In general D-dimensions the result is

$$ds^2 = (1+A)^{4/(D-3)}\left(dt^2 - dx^2 - dx_T^2\right) - \left[(1+A)^{4/(D-3)} - \left(\frac{1-A}{1+A}\right)^2\right]\frac{(dt-vdx)^2}{(1-v^2)} \tag{3.15}$$

with

$$A \equiv \frac{G_D E\sqrt{1-v^2}}{2\left[\left(\frac{x-vt}{\sqrt{1-v^2}}\right)^2 + \rho^2\right]^{(D-3)/2}}\,, \quad \rho^2 \equiv \sum_{i=2}^{D} x_i^2\,, \quad dx_T^2 \equiv \sum_{i=2}^{D} dx_i^2 \tag{3.16}$$

where the boost was along the ∂_x direction with velocity v to give the particle an energy E. It is easy to check that off the plane $x = vt$, for distances

$$\frac{\rho}{G_D^{1/(D-2)}} \gg \left(G_D^{1/(D-2)}E/2\right)^{1/(D-3)}\left(1-v^2\right)^{2/(D-3)}\,, \tag{3.17}$$

or

$$\frac{x-vt}{G_D^{1/(D-2)}} \gg \left(G_D^{1/(D-2)}E/2\right)^{1/(D-3)}\left(1-v^2\right)^{1+2/(D-3)} \equiv \epsilon\,, \tag{3.18}$$

$A \ll 1$ so the metric becomes flat. Thus close to the speed of light the region of high curvature is squeezed on the transverse plane $x = vt$ with a width ϵ. This can be made more explicit by taking the special limit of an infinite boost $v \to 1$ and $M \to 0$ while keeping the energy of the particle fixed. The result describes the gravitational field of a massless particle (or the approximate gravitational field of an ultra-relativistic particle) [59]

$$ds^2 = d\bar{u}d\bar{v} - d\bar{\rho}^2 - \bar{\rho}^2 d\bar{\Omega}_{D-3}^2 - \Phi(\bar{\rho})\delta(\bar{u})d\bar{u}^2 \tag{3.19}$$

$$\Phi(\bar{\rho}) = \begin{cases} -8G_D E\log\bar{\rho} & , D=4 \\ \dfrac{16\pi G_D E}{S_{D-3}(D-4)\bar{\rho}^{D-4}} & , D>4 \end{cases}\,, \tag{3.20}$$

where we have used a radial coordinate $\bar{\rho} = \rho$, the angular coordinates $\bar{\Omega}_{D-3}$ on the transverse hyper-plane and the null coordinates $\bar{u}$ and $\bar{v}$. Now it is clear that the spacetime before and after the gravitational shock is flat. On the plane $\bar{u} = 0$, we have a singularity which introduces a discontinuity on the geodesics and their tangent vectors. This can be fixed by changing coordinates [59]

$$\begin{aligned} \bar{u} &= u \\ \bar{v} &= v + \theta(u)\Phi + \frac{u\theta(u)(\partial_r \Phi)^2}{4} \\ \bar{\rho} &= r\left(1 - \frac{u\theta(u)}{2}\partial_r \Phi\right) \\ d\bar{\Omega}^2_{D-3} &= d\Omega^2_{D-3} \end{aligned} \tag{3.21}$$

where $\theta(u)$ is the Heaviside step function, to obtain

$$ds^2 = dudv - \left[1 + (D-3)\frac{u}{r^{D-2}}\theta(u)\right]^2 dr^2 - r^2\left[1 - \frac{u}{r^{D-2}}\theta(u)\right]^2 d\Omega^2_{D-3}\,. \tag{3.22}$$

3.2 Construction of a brane charged background

In the previous section we have described some solutions which can be used to model realistic higher-dimensional brane black holes. However, we have focused mostly on vacuum solutions in $(4+n)$ dimensions or solutions with a Maxwell field in four dimensions. In a more general scenario we want to study objects which are higher dimensional but also contain several types of charges and intrinsic spin. Furthermore, given that we are working with a brane world scenario, we may need to confine some of the matter fields to the brane. For full consistency this would require finding exact solutions where the gravitational field of the brane is also taken into account (an example of such a self-consistent solution is the Randall-Sundrum model where the brane tensions are included). This is generically difficult.

In what follows we adopt a simpler approach by assuming that the gravitational field of the matter on the brane is a small perturbation. Then, the leading contribution to the gravitational field is sourced by the mass trapped inside the black hole, and the other contributions from matter fields propagating outside the black hole are treated as small perturbations. This can be shown to be consistent by performing some estimates using the formalism in section 2.1. Consider the higher-dimensional black hole background (3.11)

and assume a brane is placed at a constant value of the higher dimensional coordinates of the n-sphere. Clearly the line element takes the form

$$G_{MN}dX^M dX^N = G_{ab}dX^a dX^b + G_{mn}dX^m dX^n \tag{3.23}$$

with no cross terms between the first four coordinates and the extra dimensional coordinates. Thus we can consider each line element independently and construct respectively a vierbein e^α_b and an n-bein e^μ_m. It then follows that a D-bein for the full spacetime is given by the combination of the two, i.e. $E^\alpha_b = e^\alpha_b$ and $E^\mu_m = e^\mu_m$ with the extra constraints $E^\mu_a = E^\alpha_m = 0$. The induced metric and induced vierbein on the brane is a simple projection of the corresponding higher-dimensional quantity. Thus the combination of the Einstein-Hilbert action with the brane action for a matter perturbation is

$$\mathcal{S} = \int d^D X \sqrt{|G|} \left(\frac{1}{2}\hat{M}_D^{D-2}\mathcal{R}_D + \mathcal{L}_{brane}\frac{\delta^{(n)}(X^m)}{\sqrt{|h|}} \right) \tag{3.24}$$

where $h_{mn} = G_{mn}$. The Einstein equations become

$$\mathcal{G}_{MN} = \frac{1}{M_D^{2+n}} T_{ab}\delta^a_M \delta^b_N \frac{\delta^{(n)}(X^m)}{\sqrt{|h|}} \tag{3.25}$$

where we have assumed that $\delta g^{ab} \sim \delta G^{ab}$, $\delta \mathcal{S}_{matter}/\delta g^{mn} \sim \delta \mathcal{S}_{matter}/\delta g^{an} \sim 0$. In a realistic situation, the δ function would be replaced by a smeared function with support on the brane. From the constraints in section 2.4 we can estimate such a factor by replacing it with a typical inverse volume for the thin brane $\sim 1/R^n$, with $R \lesssim 1$ TeV^{-1}. Then

$$\mathcal{G}_{MN} \sim \frac{1}{M_D^2} T_{ab}\delta^a_M \delta^b_N \left(\frac{L_D}{R}\right)^n . \tag{3.26}$$

In the absence of matter, the Einstein tensor for the background we are considering vanishes. However, we know that the cancellation occurs from a linear combination of components of the Riemann tensor which are non-zero, so we can compare them with the perturbation. Furthermore the components of the Riemann tensor only give a meaningful magnitude of the tidal forces felt by a local observer in an orthonormal frame. This was done in [50]. For simplicity we set the rotation to zero and obtain

$$\mathcal{R}_{MNOP} \sim \frac{\mu}{r^{3+n}} \sim \frac{M}{M_D^{2+n} r^{3+n}} . \tag{3.27}$$

This dependence agrees for example with the $\sqrt{R_{abcd}R^{abcd}}$ curvature invariant for the Schwarzschild black hole. Finally for the energy momentum tensor, taking the example of the Reissner-Nordström black hole we get (we will see this again in section 3.2.2)

$$T_{ab} \sim \frac{Q^2}{r^4} \, . \tag{3.28}$$

Inserting this estimate on the right hand side of equation (3.26) and requiring it is small compared to the Riemann tensor component (3.26) gives the condition

$$\frac{M}{M_D} \gg Q^2 \left(\frac{r}{L_D}\right)^{n-1} \left(\frac{L_D}{R}\right)^n \, . \tag{3.29}$$

So provided Q is small and the black hole mass is large (as long as R is not too small compared to L_D and we are looking at distances not too large compared to L_D) the electromagnetic field can be treated as a perturbation. Similarly we can include the brane tension term in the brane action and estimate

$$T_{ab} \sim f^4 \, , \tag{3.30}$$

so the corresponding condition is

$$\frac{M}{M_D} \gg \left(\frac{f}{M_D}\right)^4 \left(\frac{r}{L_D}\right)^{3+n} \left(\frac{L_D}{R}\right)^n \, , \tag{3.31}$$

which holds similarly for trans-Planckian black holes as long as the tension is small compared to M_D.

In the remainder of this section, we will focus on a Maxwell field confined to the 4-dimensional brane rather than a higher dimensional Maxwell field propagating in the full bulk. The background brane metric used in the construction is the projection of (3.11). For brane degrees of freedom, this suffices as an effective metric to describe how the gravitational field affects them. In the remainder of this section we use Planck units $M_D = 1$ unless stated otherwise.

3.2.1 The brane Maxwell field as a perturbation

The simplest perturbation of the background field, which is relevant for the phenomenological scenario we are considering, is a classical abelian gauge field. This describes elec-

tromagnetism and it is relevant because several Standard Model fields are electrically charged.

We want to solve Maxwell's equations for the vector potential A_a using the metric (3.11) as the gravitational background. The combined gravitational plus electromagnetic background can then be coupled to other fields to study the quantum propagation of the corresponding perturbations on the background. In chapter 5 we will be interested in the Hawking effect.

We want the solution to retain the symmetries of the effective four dimensional background. This has exactly the same symmetries as the Kerr-Newman solution so we use the type of ansatz in equation (3.6)

$$A_a dx^a = -Q\frac{r}{\Sigma}\left(dt - a\sin^2\theta d\phi\right) \ , \tag{3.32}$$

where A_a is the vector potential. It can be checked that (3.32) solves the sourceless Maxwell equations on the brane

$$D_a A^{ab} = \frac{1}{\sqrt{|g|}}\partial_a\left(\sqrt{|g|}A^{ab}\right) = 0 \ . \tag{3.33}$$

This result follows because $\sqrt{|g|} = \Sigma\sin\theta$ is exactly the same as for the Kerr-Newman metric. In addition the identities

$$D_{[a}A_{bc]} = 0 \tag{3.34}$$

where the brackets denote cyclic permutation of indices, are also satisfied. Note how the modified r^{1-n} term in Δ, which gives a $1/r^{2+n}$ gravitational force law away from the black hole, does not affect the stationary brane Maxwell field. Thus a brane charged particle propagating outside the black hole feels an electric force that scales like $1/r^2$ and a gravitational force that scales like $1/r^{2+n}$.

Gauss' theorem applied to equation (3.33) allows the matching of Q to the physical charge of the black hole[4]

$$\int D_a A^{ab} d\Sigma_b = 4\pi\int d\Sigma_c\sqrt{|g|}J^c \Rightarrow Q = \int d^3x\sqrt{|g|}J^0 \ . \tag{3.35}$$

Here we have integrated over spatial hypersurfaces of constant t with normal hypervolume $d\Sigma_b = d^3x\delta^0_b$, applyed Gauss' theorem and integrated the left side on a sphere at $r \to +\infty$.

[4] Q coincides with the Komar charge defined in (3.10).

3.2.2 Comments on backreaction

From the equivalence principle, we know that any SM field should source the right hand side of Einstein's equations through its energy-momentum tensor. In other words all fields gravitate and generate a correction to the metric.

In section 3.2.1 we have found a consistent solution of the brane Maxwell field equations on the background of a Myers-Perry projected black hole. Now we try to find self-consistent corrections to the gravitational field. Ideally we would have to solve the coupled Einstein/brane-Maxwell equations in the full $(4+n)$-dimensional space with the Maxwell field confined to the brane, so it would involve finding a specific mechanism to confine the field. This is too difficult in general and we are mostly interested in justifying the smallness of the backreaction. Thus, we analyse the Einstein equations and introduce a self-consistent ansatz to approximate corrections on the brane.

It can be checked, by direct computation, that the brane Einstein tensor for the background projected metric is not vacuum like. This is not surprising since the actual vacuum black hole solution lives in $(4+n)$-dimensions. The non-zero components are

$$\begin{aligned}
\mathcal{G}^{(0)}{}^{r}_{r} &= \frac{n\bar{\mu}r^{1-n}}{\Sigma^2} \\
\mathcal{G}^{(0)}{}^{\theta}_{\theta} &= -\frac{\mathcal{G}^{(0)}{}^{r}_{r}}{2r^2}\left[(n+1)r^2+(n-1)a^2\cos^2\theta\right] \\
\mathcal{G}^{(0)}{}^{\phi}_{\phi} &= -\frac{\mathcal{G}^{(0)}{}^{r}_{r}}{2r^2\Sigma}\left[(n+1)r^4+(n+3)r^2a^2+(n-3)r^2a^2\cos^2\theta+(n-1)a^4\cos^2\theta\right] \\
\mathcal{G}^{(0)}{}^{t}_{t} &= \frac{\mathcal{G}^{(0)}{}^{r}_{r}}{2r^2\Sigma}\left[2r^4+(n+3)r^2a^2-(n+1)r^2a^2\cos^2\theta+(n-1)a^4\cos^2\theta\sin^2\theta\right] \\
\mathcal{G}^{(0)}{}^{\phi}_{t} &= \frac{a\mathcal{G}^{(0)}{}^{r}_{r}}{2r^2\Sigma}\left[(n+1)r^2+(n-1)a^2\cos^2\theta\right] \\
\mathcal{G}^{(0)}{}^{t}_{\phi} &= -\mathcal{G}^{(0)}{}^{\phi}_{t}\Sigma_0\sin^2\theta\,,
\end{aligned} \tag{3.36}$$

where $\Sigma_0 = r^2+a^2$. So from the brane point of view, an observer performing gravitational measurements sees a black hole space-time together with an effective fluid due to the embedding into the extra dimensions.

Before suggesting corrections to the metric it is useful to note some properties. We expect such a corrected metric to reduce to the projected metric (3.11) in the $Q=0$ limit and to the Kerr-Newman solution when $n=0$. Furthermore, it should exhibit the same symmetries as the Kerr-Newman metric if we want the Maxwell field to be of the same form as in equation (3.32). Compared to the Kerr ($Q=0$) limit, the Kerr-Newman

metric is modified by a shift of the mass term $\bar{\mu}r$ in Δ to $\bar{\mu}r - Q^2$. The term $\bar{\mu}r$ is related to the gravitational potential which in the chargeless $(4+n)$-dimensional case is simply replaced by $\bar{\mu}r^{1-n}$. Similarly, we adopt an ansatz where $\bar{\mu}r^{1-n}$ is shifted to $\bar{\mu}r^{1-n} - Q^2$ (or equivalently $\Delta \to \Delta + Q^2$)[5]. Then the effective brane metric ansatz takes the same form as the projected metric (3.11) but with

$$\Delta = r^2 + a^2 + Q^2 - \bar{\mu}r^{1-n} \ . \tag{3.37}$$

Remarkably, explicit evaluation of the Einstein tensor for this brane metric yields

$$\mathcal{G}^b_a = \mathcal{G}^{(0)}{}^b_a + 8\pi T^b_a \ , \tag{3.38}$$

where

$$8\pi T^b_a = \begin{pmatrix} -\dfrac{Q^2(\Sigma_0 + a^2\sin^2\theta)}{\Sigma^2} & 0 & 0 & -\dfrac{2aQ^2}{\Sigma^3} \\ 0 & -\dfrac{Q^2}{\Sigma^2} & 0 & 0 \\ 0 & 0 & \dfrac{Q^2}{\Sigma^2} & 0 \\ \dfrac{2aQ^2\Sigma_0 a^2\sin^2\theta}{\Sigma^3} & 0 & 0 & \dfrac{Q^2(\Sigma_0 + a^2\sin^2\theta)}{\Sigma^3} \end{pmatrix} \tag{3.39}$$

is the energy momentum tensor for the Maxwell field as computed from the definition

$$T^b_a = \frac{1}{4\pi}\left(A_{ac}A^{bc} - \frac{1}{4}\delta^b_a A_{cd}A^{cd}\right) \ . \tag{3.40}$$

Equation (3.38) shows how the brane metric ansatz we have chosen reproduces exactly the gravitational field generated by the Maxwell field while keeping the extra contribution from the embedding into the bulk untouched. This indicates that we can consistently add the Maxwell field on the brane and correct the brane metric accordingly. Furthermore, we can see that the components of the zeroth order contribution to the Einstein tensor has exactly the form anticipated from the estimate (3.26), so we see explicitly that the correction from the Maxwell field is a perturbation.

Even though the effective metric (3.37) can not be the full solution it can be regarded as a first approximation which is physically consistent (for a rigorous study in the second

[5]This substitution has been noted in a Randall-Sundrum context [60] where Q^2 is interpreted as a tidal charge.

Randall-Sundrum model see [60, 61]). To solve the problem of the backreaction exactly, we would have to construct a bulk energy momentum tensor for the Maxwell field, with some typical thickness, and solve the bulk Einstein equations. This would give the effect of the four dimensional brane Maxwell field on the bulk geometry as well as on the brane. Keeping in mind the ansatz above it is tempting to assume that the physical metric will have a form

$$\Delta \to r^2 + a^2 - \bar{\mu} r^{1-n} + Q^2(\Omega_n) \ . \tag{3.41}$$

where now Q^2 is a function of the transverse bulk coordinates Ω_n such that

$$Q(\Omega_n) = \begin{cases} Q & \text{if } \Omega_n \text{ on the brane} \\ 0 & \text{otherwise} \end{cases} \ .$$

If we imagine a brane with thickness ϵ such that the charge function $Q^2(\Omega_n)$ drops suddenly where the brane ends, then this choice ensures the vacuum Einstein equations are obeyed in the bulk, as well as on the brane (together with the Maxwell field). The only addition is a sharp δ function like energy momentum tensor where the brane ends. This can be checked explicitly in the 5-dimensional case by using a generic function $Q(\chi)$ (χ is the fifth dimensional coordinate) and applying the Gauss-Codazzi equations to obtain brane Einstein equations at each hyperslice parallel to the $\chi = 0$ brane. If the profile chosen is flat inside the brane ($Q(\chi) = Q$) and drops suddenly to zero at some χ_ϵ, then we obtain terms which are proportional to derivatives of $Q(\chi)$ at χ_ϵ. These extra contributions at χ_ϵ spoil the construction but nevertheless we can ignore them or assume they are somehow related to the mechanism that keeps the fields confined to the 4-dimensional brane.

Regardless of these issues, note that the charge introduced in (3.37) consistently reduces the size of the black hole event horizon on the brane as we would expect for a charged black hole. Furthermore the Maxwell field, which is independent of Δ, produces terms in the geodesics which reproduce exactly the usual 4-dimensional electric force. This is certainly a feature we want to keep. Finally, for the TeV gravity scenario of black hole production we are considering we will see that the Q^2 term in the metric is actually a small perturbation. So the charge should not disturb the bulk geometry much and to first order this effective brane metric should be a good approximation.

3.2.3 Systems of units and orders of magnitude

In this section we find the relation between the black hole parameters and the corresponding physical quantities in terms of well known constants, as well as the coupling of charged test particles. In the last section we worked in a natural system of units where all dimensionful quantities are in fact divided by the appropriate Planck unit factor. For example lengths are divided by M_D^{-1} and masses by M_D. Similarly any field comes divided by the appropriate "Planck quantity". Then the charge Q becomes a dimensionless quantity describing the strength of the electric field compared to some reference charge. The precise value of this parameter is found by matching to a known limit. Anticipating the result we write $Q = Z\sqrt{\alpha}$ where $\sqrt{\alpha}$ is the fundamental charge and Z is the charge of the black hole in units of $\sqrt{\alpha}$. For the purpose of matching Q, the rotation parameter can be set to zero.

Let's start by looking at geodesics for charged particles. They are obtained from varying the action

$$S = \int d\lambda \left(\frac{1}{2} \frac{dx^a}{d\lambda} \frac{dx_a}{d\lambda} + q \frac{dx^a}{d\lambda} A_a \right) \tag{3.42}$$

where $q = z\sqrt{\alpha}$ is the charge of the test particle. The coupling $\sqrt{\alpha}$ is found by taking the non-relativistic limit. If we define the generalised momentum

$$P_a = \frac{d\mathcal{L}}{d\dot{x}^a} = \frac{dx_a}{d\lambda} + qA_a \ , \tag{3.43}$$

conservation of the Hamiltonian $\mathcal{H} \equiv \mathcal{L} - P_a \dot{x}^a$ reduces to the 4-momentum constraint $p_a p^a = m^2$ where $p^a = dx^a/d\lambda$. The geodesic equation coupled to electromagnetism is

$$\frac{d^2x^a}{d\lambda^2} + \Gamma^a_{bc} \frac{dx^b}{d\lambda} \frac{dx^c}{d\lambda} + qA^a_b \frac{dx^b}{d\lambda} \ = \ 0 \ . \tag{3.44}$$

We consider radial geodesics $d\theta/d\lambda = d\phi/d\lambda = 0$. In four dimensions, the non-trivial equations are

$$\frac{d^2r}{d\lambda^2} + \frac{1}{2} m^2 U' - \alpha U \frac{zZ}{r^2} E \ = \ 0 \tag{3.45}$$

$$\frac{d^2t}{d\lambda^2} + \left(U'E + \alpha \frac{zZ}{r^2} \right) \frac{1}{U} \frac{dr}{d\lambda} \ = \ 0 \ , \tag{3.46}$$

with $U = \Delta/r^2$. In the non-relativistic limit $dt/d\lambda = E \sim m$, therefore $dt \sim m\, d\lambda$ and

$$m\frac{d^2r}{dt^2} = -\frac{mM}{r^2} + \alpha\frac{zZ}{r^2} + \alpha m\frac{Z^2}{r^3} + O(r^{-4}) \,, \tag{3.47}$$

giving respectively the Newtonian and Coulomb force laws and the first relativistic correction due to the gravitational effect of the Maxwell field. To match α in four dimensions, put back all length scales in terms of Planck units explicitly

$$m\frac{d^2r}{dt^2}\ \frac{1}{M_4^2} = \frac{m}{M_4}\ \left(-\frac{M}{M_4}\frac{L_4^2}{r^2} + \alpha\frac{M_4}{m}zZ\frac{L_4^2}{r^2} + \alpha Z^2\frac{L_4^3}{r^3} + \dots\right) \,, \tag{3.48}$$

where the extra relativistic correction is suppressed by one more power of L_4/r. Rewriting the previous equation and setting the masses to electron masses and charges $z, Z = 1$ (i.e. the unit is the electron charge)

$$m\frac{d^2r}{dt^2}\ \frac{1}{M_4^2} = -\frac{m_e}{M_4}\left(\frac{m_e}{M_4} - \alpha\frac{M_4}{m_e}\right)\frac{L_4^2}{r^2} + \dots \,. \tag{3.49}$$

The ratio of electric to gravitational force between electrons gives

$$\alpha = \frac{F_e}{F_g}\left(\frac{m_e}{M_4}\right)^2 = \frac{\dfrac{e^2}{4\pi\epsilon_0}}{Gm_e^2}\left(\frac{m_e}{M_4}\right)^2 = \frac{e^2}{4\pi\epsilon_0} \simeq \frac{1}{137} \tag{3.50}$$

as expected. Equation (3.50) emphasizes how the electric force $F_e = \alpha F_g(M_4/m_e)^2$ in 4-dimensions is orders of magnitude stronger than the gravitational force. This is simply a statement of the hierarchy problem. However the same cannot apply in TeV gravity scenarios where all forces are controlled by the same scale, so gravity becomes stronger at short distances. Thus it is crucial to determine the relative strength of the $(4+n)$-dimensional gravitational force and the electric force.

Now let us rewrite equation (3.48) using M_D

$$m\frac{d^2r}{dt^2}\frac{1}{M_D^2} = \frac{m}{M_D}\left[-\left(\frac{M_D}{M_4}\right)^2\frac{M}{M_D}\frac{L_D^2}{r^2} + \alpha\frac{M_D}{m}zZ\frac{L_D^2}{r^2} + \left(\frac{M_D}{M_4}\right)^2\alpha Z^2\frac{L_D^3}{r^3} + \dots\right] \tag{3.51}$$

The first and third contributions, which are due to the gravitational fields of the mass

M and the charge Q, are suppressed by the same power of M_D/M_4. However, as we approach short distances, the gravitational coupling must become higher dimensional,[6] gravity becomes strong and the suppression factors must disappear. Note however, that since the Maxwell field is confined to the brane, the r-power in the third term (which is associated with the gravitational effect of the charge) must remain the same. As for the second term, it is associated with the electric force between the test particle and the charged body so it must remain the same, again because the Maxwell field is confined to the brane and the magnitude of the electric force cannot change at shorter distances.

This qualitative discussion agrees with the short distance geodesic equation obtained from the metric (3.37)

$$m\frac{d^2r}{dt^2}\frac{1}{M_D^2} = \frac{m}{M_D}\left[-(n+1)\bar{\mu}M_D^{n+1}\frac{L_D^{n+2}}{r^{n+2}} + \alpha\frac{M_D}{m}zZ\frac{L_D^2}{r^2} + \alpha Z^2\frac{L_D^3}{r^3} + \ldots\right] \quad . \quad (3.52)$$

The first term is correctly modified to a higher dimensional force law, the second term remains the same and the third term is controlled by the same power or r but without the suppression factor $(M_D/M_4)^2$.

It is worth noting that for TeV gravity black holes in proton-proton collisions where the black hole is formed from two partons (so the maximum charge is $|Z| = 4/3$), the fine structure constant factor of $1/137$ makes the Q^2 contribution to the metric very small (unless the black hole happens to charge up to $|Z| \sim 10$ after production).

3.3 Geodesics and the geometrical cross section

In chapter 5, we will study the propagation of quantum perturbations of several fields outside the charged rotating black hole background presented in section 3.2. It is well known that in the high energy limit wave propagation can be treated geometrically. Therefore, in this limit, the study of the classical trajectories of test particles outside the black hole provides useful information on wave propagation. The aim of this section is to obtain the shapes of the absorptive disks as seen by an observer away from the black hole. This also helps to understand how the black hole is perceived at infinity.

A first study in higher dimensions was done for some special cases in [62]. In this section we generalise their arguments to an arbitrary trajectory and include particle charge and mass.

[6] This can be checked explicitly by using the brane metric (3.37).

3.3.1 The critical impact parameter

A classical particle stuck on the brane follows a geodesic curve $X^\mu(\lambda)$ determined by varying the action (3.42). In this formulation, the conserved quantities are identified by looking at the symmetries of the Lagrangian, or equivalently, the Killing vectors of the metric. The brane metric (3.37), has the analytic form of the Kerr-Newman metric. This type of metric produces two obvious conserved quantities associated with its time and azimuthal Killing vectors and a third one related to a Killing tensor. For example in [62] the three conserved quantities were combined with the Hamiltonian (which is also conserved since the Lagrangian (3.42) does not depend on λ) to obtain a radial equation of motion for a particle with mass μ. We can apply the same reasoning to our case and obtain more general equations. For simplicity we switch to horizon radius units where $r_H = 1$ so that $\bar{\mu} \to 1 + a^2 + Q^2$ and we have the following mapping of parameters

$$\begin{aligned} \frac{r}{r_H} &\to r & a_\star = \frac{a}{r_H} &\to a \\ \omega r_H &\to \omega & \mu r_H &\to \mu \\ q r_H &\to q & \frac{Q}{r_H} &\to Q \end{aligned} \quad , \tag{3.53}$$

(where ω will be the energy of the particle) so Δ becomes

$$\Delta = r^2 + a^2 + Q^2 - (1 + a^2 + Q^2) r^{1-n} \ . \tag{3.54}$$

The equations for the geodesics are then

$$\begin{aligned} \Sigma \frac{dt}{d\lambda} &= \frac{r^2 + a^2}{\Delta} \left[(r^2 + a^2)\, \omega - a\ell_z - qQr \right] + a\ell_z - a^2 \omega \sin^2\theta \\ \Sigma \frac{d\phi}{d\lambda} &= \frac{a\omega\,(r^2 + a^2) - a^2 \ell_z - aqQr}{\Delta} - a\omega + \frac{\ell_z}{\sin^2\theta} \\ \left[\Sigma \frac{d\theta}{d\lambda} \right]^2 &= \mathcal{Q} - \cos^2\theta \left[a^2 (\mu^2 - \omega^2) + \frac{\ell_z^2}{\sin^2\theta} \right] \\ \left[\Sigma \frac{dr}{d\lambda} \right]^2 &= \left[\omega(r^2 + a^2) - \ell_z a - qQr \right]^2 - \Delta \left[\mu^2 r^2 + (\ell_z - a\omega)^2 + \mathcal{Q} \right] \end{aligned} \tag{3.55}$$

where $\omega, \ell_z, \mathcal{Q}$ are the constants of motion associated with time translations, azimuthal translations and the Killing tensor respectively. Next we redefine $\lambda \to \lambda\omega$, express the remaining constants of integration in terms of the impact parameter b (in units of r_H), the

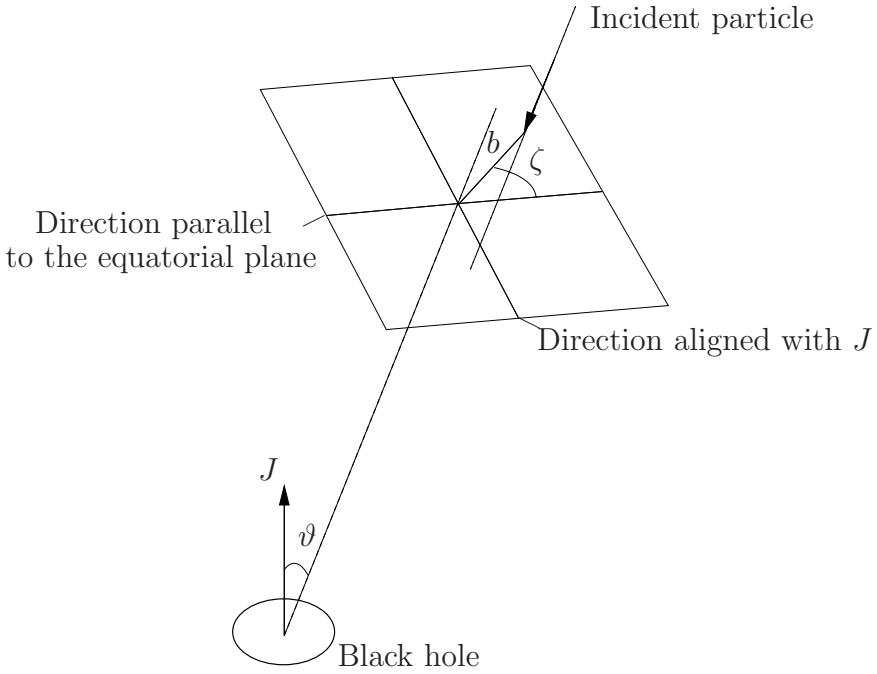

Figure 3.3: Diagram defining the ζ angle and the impact parameter b on the plane transverse to the direction of incidence.

polar angle of incidence ϑ, the angular momentum magnitude ℓ, the angular momentum orientation at infinity ζ, and the reduced mass $\nu = \mu/\omega$ and charge $\epsilon = q/\omega$:

$$\begin{aligned}
\Sigma\frac{dt}{d\lambda} &= \frac{r^2+a^2}{\Delta}\left[r^2+a^2-ab_z-\epsilon Qr\right]+ab_z-a^2\sin^2\theta \\
\Sigma\frac{d\phi}{d\lambda} &= \frac{a\left(r^2+a^2\right)-a^2b_z-a\epsilon Qr}{\Delta}-a+\frac{b_z}{\sin^2\theta} \\
\left[\Sigma\frac{d\theta}{d\lambda}\right]^2 &= \mathcal{P}-\cos^2\theta\left[a^2\left(\nu^2-1\right)+\frac{b_z^2}{\sin^2\theta}\right] \\
\left[\Sigma\frac{dr}{d\lambda}\right]^2 &= \left[r^2+a^2-ab_z-\epsilon Qr\right]^2-\Delta\left[\nu^2r^2+\left(b_z-a\right)^2+\mathcal{P}\right]\equiv\mathcal{R}
\end{aligned} \tag{3.56}$$

where

$$b\equiv\frac{\ell}{\omega},\quad b_z\equiv\frac{\ell_z}{\omega}=b\cos\zeta\sin\vartheta,\quad \mathcal{P}\equiv b^2-b_z^2-a^2\cos^2\vartheta\quad . \tag{3.57}$$

The impact parameter b corresponds to the distance of closest approach to the origin, if the spacetime was flat. ζ is the polar angle of the impact parameter on the plane perpendicular to the direction of incidence (see figure 3.3) or equivalently the angle between the angular momentum of the black hole and the angular momentum of the incident particle.

The most general trajectory is parametrised by the set $\{b, \zeta, \vartheta, a, Q, \nu, \epsilon\}$. Our goal is to determine whether a particle is absorbed or not for a given set. This can be achieved by looking at the radial equation of motion in (3.56), and noting that $\mathcal{R}$ must be non-negative over the trajectory. Let's start by defining the functions A, B, C through

$$\mathcal{R} = \frac{1}{r^n}\left[-Ab^2 + 2Bb + C\right] \ . \tag{3.58}$$

To investigate whether a particle is absorbed or not, we need to know if $\mathcal{R}$ takes negative values at any point of the trajectory. If so, there is a region which is inaccessible. A way to guarantee absorption is to choose the value of b in an interval such that $\mathcal{R}$ is positive over the whole space. This requires determining its zeros with respect to b at all points r and finding the intervals of b such that such zeros do not exist over the whole radial domain. In principle this may produce complicated disks or ring-like regions on the $\{b, \zeta\}$ polar plane at infinity.

$Q = 0$ case

In this case

$$\begin{aligned} A &= r^{n+2} + r^n a^2\left(1 - \cos^2\zeta \sin^2\vartheta\right) - (1+a^2)r \\ B &= -a\cos\zeta\sin\vartheta\left(1+a^2\right)r \\ C &= r^{n+4}(1-\nu^2) + r^{n+2}a^2(1-\nu^2+\cos^2\vartheta) + r^n a^4\cos^2\vartheta + \\ &\quad + r^3\nu^2\left(1+a^2\right) + ra^2(1+a^2)\sin^2\vartheta \end{aligned} \tag{3.59}$$

where $C \geq 0$ since $\nu \leq 1$. For a fixed b, it can be shown that A has exactly one zero in the domain $r > 0$ so it changes sign only once[7]. So A starts from positive values at infinity, decreases, goes through zero and takes negative values inwards. Since the signs of B and C are fixed we only need to analyse two regions.

Let's start with the outermost region. We want to determine the impact parameters for which the particle is not able to penetrate completely through the region of $A \geq 0$, thus being scattered back at some point, or equivalently the range of parameters $b_{min} < b < b_{max}$ for which absorption is guaranteed. Then it is certain that any particle with impact parameters within this range will reach the second innermost region. For any

[7]This is done by looking at the sign of the function at infinitesimal r and at infinity, using continuity and the positivity of $d^2A/dr^2 > 0$ for $r > 0$.

solution of the radial equation we must ensure that $\mathcal{R} \geq 0$ to allow the particle through the region. As a function of b, $\mathcal{R}$ has two zeros

$$b_{\pm} = \frac{B \pm \sqrt{B^2 + AC}}{A} \tag{3.60}$$

Since, AC is positive, there is a negative and a positive root. Thus $\mathcal{R}$ is a parabola with a maximum. $\mathcal{R}$ is positive only for $0 < b < b_+$. If we take $b > b_{max} \equiv \min_r \{b_+\}$, where the minimisation is over the radial region we are considering, there will always be a point where $\mathcal{R}$ goes through zero and changes sign. This means that the particle is scattered back at that point. Similarly, in the complementary case, there will never be such a zero so the particle reaches the second interior radial region. Thus we have obtained the first upper bound.

Regarding the remaining interior radial region the situation is a bit more complicated. In that case, $A < 0$ so the roots are

$$b_{\pm} = \frac{-B \mp \sqrt{B^2 - |A|C}}{|A|} \ . \tag{3.61}$$

For $B > 0$ (or equivalently $b_z < 0$, see (3.57)), the previous equation has no positive real roots, so $\mathcal{R} > 0$ and any particle reaching the region is absorbed. Thus, for this sign of B, the absorptive disk is defined by the interval obtained in the outer region. For $B \leq 0$, we can have two real positive roots. Those are

$$b_{\mp} = \frac{|B| \mp \sqrt{B^2 - |A|C}}{|A|} \tag{3.62}$$

so $\mathcal{R}$ is a parabola with a minimum and two zeros. If b takes any value below $\min_r\{b_-\}$ (again the minimisation is in the radial region we are considering), there is no zero, because any r has associated critical b's which are necessarily larger. The same occurs for b above $\max_r\{b_+\}$, since all the b's that allow a zero are smaller. Conversely, for b between the last two values, there is always a point where $\mathcal{R}$ goes through zero and becomes negative, so the particle is scattered back. Therefore, the impact parameters for absorption must be smaller than $\min_r \{b_-\}$ or larger than $\max_r \{b_+\}$. However, note that at $r = r_A$, (r_A defined such that $A(r_A) = 0$) b_+ diverges, so there is no finite $b > \max_r \{b_+\} \to +\infty$.

The range of impact parameters for absorption can be summarised as

$$0 < b < b_c \equiv \min_{\{r \geq r_{low}\}} \left\{ \frac{C}{\sqrt{B^2 + AC} - B} \right\} \tag{3.63}$$

with

$$r_{low} \equiv \begin{cases} r_A, & b_z \leq 0 \\ 1, & b_z > 0 \end{cases} . \tag{3.64}$$

The expression to be minimised in (3.63) is rearranged to remove the apparent singularity at r_{low} when $B < 0$ and to make it explicit when $B \geq 0$. This form is more suitable for numerical minimisation because the only singularities are at the extreme points of the interval.

$Q \neq 0$ and $\epsilon \neq 0$ cases

More generally when the charges are non-zero, the signs of B and C can also change throughout the radial domain. The expressions for the coefficients are now more complicated

$$\begin{aligned} A &= r^{n+2} + r^n a^2 \left(1 - \cos^2\zeta \sin^2\vartheta + Q^2\right) - (1 + a^2 + Q^2) r \\ B &= a \cos\zeta \sin\vartheta \left[\epsilon Q r^{n+1} + Q^2 r^n - \left(1 + a^2\right) r\right] \\ C &= r^{n+4}(1 - \nu^2) - 2\epsilon Q r^{n+3} + r^{n+2}\left[a^2(1 - \nu^2 + \cos^2\vartheta) + \epsilon^2 Q^2 - \nu^2 Q^2\right] + \\ &\quad + a^2\left(a^2 \cos^2\vartheta - Q^2 \sin^2\vartheta\right) r^{n+1} + r^n a^2 \left(a^2 \cos^2\vartheta - Q^2 \sin^2\vartheta\right) + \\ &\quad + r^3 \nu^2 \left(1 + a^2 + Q^2\right) + r a^2 (1 + a^2 + Q^2) \sin^2\vartheta \, . \end{aligned} \tag{3.65}$$

Nevertheless we can still write a general algorithm which scans the functions A, B, C from infinity, through a finite number of regions where the signs of the various functions remain fixed, and computes bounds on b. Also it is easy to show that inside the black hole horizon $\mathcal{R}$ is positive, so at most we have to scan down to $r = 1$. Furthermore, A still contains only one zero so we have two regions for A. For B and C, in general it is not possible to say how many zeros we have, but since they are polynomials, at most we have $n + 1$ and $n + 4$ zeros respectively. Thus there are at most $2(n + 2)(n + 5)$ qualitatively different regions for a fixed n. If we combine this with the two possible combinations of signs for B at infinity[8] the possible number of cases is doubled to $4(n + 2)(n + 5)$.

[8]Note A and C are always positive at infinity.

We start with the first region where $\{A, B, C\}$ have their signs as at infinity. Then $A > 0$ and $C > 0$ so the roots of $\mathcal{R}$ are

$$b_\pm = \frac{B \pm \sqrt{B^2 + AC}}{A} \,. \tag{3.66}$$

Following arguments similar to those for the first case when $Q = 0$, in this region we need

$$0 < b < b_{max} \equiv \min_{\{r\}} \left\{ \frac{C}{\sqrt{B^2 + AC} - B} \right\} \,. \tag{3.67}$$

Now we have two possibilities as we enter a new region. Either A changes sign and B, C keep their signs or A keeps its sign.

Let us start with the case when B, C change signs before A. We have four possible cases for the signs s_1, s_2 of B, C: $(s_1, s_2) = (+,+), (+,-), (-,+), (-,-)$ so

$$\begin{aligned} b_\pm &= \frac{|B| \pm \sqrt{B^2 + A|C|}}{A} \\ b_\pm &= \frac{|B| \pm \sqrt{B^2 - A|C|}}{A} \\ b_\pm &= \frac{-|B| \pm \sqrt{B^2 + A|C|}}{A} \\ b_\pm &= \frac{-|B| \pm \sqrt{B^2 - A|C|}}{A} \,, \end{aligned} \tag{3.68}$$

respectively. Now $\mathcal{R}$ (as a function of b) is a parabola with a maximum. For the first and third cases we have a positive and a negative zero so the condition is exactly the same as in the previous region. For the second case we have two positive zeros, so

$$\max_{\{r\}} \left\{ \frac{-C}{\sqrt{B^2 + AC} + B} \right\} \equiv b_{min} < b < b_{max} \equiv \min_{\{r\}} \left\{ \frac{C}{\sqrt{B^2 + AC} - B} \right\} \,. \tag{3.69}$$

Finally the fourth case has no positive zeros, so $\mathcal{R} < 0$ and no b is allowed (the procedure stops).

The next cases are inside the region where A changes to negative. The four cases are

$(s_1, s_2) = (+,+), (+,-), (-,+), (-,-)$, with the respective roots

$$\begin{aligned} b_\pm &= \frac{-|B| \pm \sqrt{B^2 - |A||C|}}{|A|} \\ b_\pm &= \frac{-|B| \pm \sqrt{B^2 + |A||C|}}{|A|} \\ b_\pm &= \frac{|B| \pm \sqrt{B^2 - |A||C|}}{|A|} \\ b_\pm &= \frac{|B| \pm \sqrt{B^2 + |A||C|}}{|A|} \,. \end{aligned} \tag{3.70}$$

Since $A < 0$, $\mathcal{R}$ is a parabola with a minimum. For the first case both zeros are negative so $\mathcal{R}$ is always positive for $r > 0$ and no constraint arises. For the second and fourth cases where $C < 0$, we have a positive and a negative zero regardless of the sign of B so we need

$$b > b_{min} \equiv \max_{\{r\}} \left\{ \frac{-C}{\sqrt{B^2 + AC} + B} \right\} \,. \tag{3.71}$$

For the third case, we have two positive roots so

$$b < b_{down} \equiv \min_{\{r\}} \left\{ \frac{C}{\sqrt{B^2 + AC} - B} \right\} \;\vee\; b > b_{up} \equiv \max_{\{r\}} \left\{ \frac{C}{-\sqrt{B^2 + AC} - B} \right\} \,. \tag{3.72}$$

This method can be implemented numerically for the general case where all parameters are nonzero. In particular we can check that it reduces to the procedure described for $Q = 0$. However, note that $\nu = \mu/\omega$ and $\epsilon = q/\omega$, so since the geometrical description is good at high energies, these parameters should be small even when non-zero. Furthermore as pointed out in 3.2.3 the charges in the scenario we are considering are typically small and the same applies to the masses of the particles. Thus in the next sections we present results for the simpler case where the charges and the particle mass are neglected.

3.3.2 Perturbative and numerical minimisation

We want to obtain the absorptive disks as seen from infinity in various directions of observation. The most efficient way is to numerically determine the critical impact parameter for each set of parameters through the minimisation of (3.63).

Another useful approach is to solve the problem analytically in a particular case and expand around it perturbatively. This method is useful as a check of the numerical analysis

and shows most of the features of the result. Equation (3.63) is easy to minimise when $a = 0$ (the Schwarzschild case), leading to

$$r_0 \equiv \left(\frac{n+3}{2}\right)^{\frac{1}{n+1}} \quad b_0 \equiv \left(\frac{n+3}{2}\right)^{\frac{1}{n+1}} \sqrt{\frac{n+3}{n+1}}\,, \tag{3.73}$$

r_0, b_0 are the minimiser and minimum respectively. For small rotation parameters, it should be possible to find a good approximate solution of (3.63), by expanding perturbatively around (3.73), i.e.

$$r_c \equiv \sum_{p=0}^{+\infty} \frac{r_p}{p!} a^p\,. \tag{3.74}$$

Since r_c, b_c are the minimiser and minimum when $a \neq 0$, r_c must obey

$$\left.\frac{\partial b}{\partial r}\right|_{r=r_c} = 0\,, \tag{3.75}$$

so that

$$b_c = b|_{r=r_c}\,. \tag{3.76}$$

Note that from now on, b is given by the expression to be minimised in (3.63) and all other parameters ζ, ϑ, n are omitted. Expanding (3.75) in powers of a and imposing each coefficient to vanish independently, we obtain conditions on the r_p coefficients (see equation (3.74))

$$\frac{d^m}{da^m}\left(\left.\frac{\partial b}{\partial r}\right|_{r=r_c}\right)\Bigg|_{a=0} = 0\,. \tag{3.77}$$

The total derivatives can be expanded in the following manner

$$\begin{aligned}
\frac{d^m}{da^m} &= \frac{d^{m-1}}{da^{m-1}}\left(\frac{\partial}{\partial a} + \frac{dr_c}{da}\frac{\partial}{\partial r_c}\right) \\
&= \frac{d^{m-1}}{da^{m-1}}\frac{\partial}{\partial a} + \frac{dr_c}{da}\frac{d^{m-1}}{da^{m-1}}\frac{\partial}{\partial r_c} + \frac{d^m r_c}{da^m}\frac{\partial}{\partial r_c} \\
&= \sum_{k=0}^{1}\left(\frac{dr_c}{da}\right)^k \frac{d^{m-1}}{da^{m-1}}\frac{\partial}{\partial a^{1-k}\partial r_c^k} + \frac{d^m r_c}{da^m}\frac{\partial}{\partial r_c}\,.
\end{aligned} \tag{3.78}$$

Successive iterations of (3.78), suggest the following identity for any order $p < m$

$$\frac{d^m}{da^m} = \sum_{q=0}^{p} \frac{p!}{(p-q)!q!} \left(\frac{dr_c}{da}\right)^q \frac{d^{m-p}}{da^{m-p}} \frac{\partial^p}{\partial a^{p-q} \partial r_c^q} + \\ + \sum_{q=0}^{p-1} \frac{d^{m-q} r_c}{da^{m-q}} \sum_{k=0}^{q} \frac{q!}{(q-k)!k!} \left(\frac{dr_c}{da}\right)^k \frac{\partial^{q+1}}{\partial a^{q-k} \partial r_c^{k+1}} \,, \quad (3.79)$$

which can be checked by induction on p. Finally, setting $p = m-1$ (valid for any $m > 0$)

$$\frac{d^m}{da^m} = \sum_{q=0}^{m-1} \frac{(m-1)!}{(m-1-q)!q!} \left(\frac{dr_c}{da}\right)^q \frac{\partial^m}{\partial a^{m-q} \partial r_c^q} + \\ + \sum_{q=0}^{m-1} \frac{d^{m-q} r_c}{da^{m-q}} \sum_{k=0}^{q} \frac{q!}{(q-k)!k!} \left(\frac{dr_c}{da}\right)^k \frac{\partial^{q+1}}{\partial a^{q-k} \partial r_c^{k+1}} \,. \quad (3.80)$$

Using (3.80) in (3.77), relabelling $r_c \to r$ in the partial derivatives, and defining

$$\beta_{i,j} \equiv \left. \frac{\partial^{i+j} b}{\partial a^i \partial r^j} \right|_{a=0, r=r_0} \quad (3.81)$$

gives the recursion relations ($m > 1$) for all the corrections

$$\begin{aligned} r_1 \beta_{0,2} &= -\beta_{1,1} \\ r_m \beta_{0,2} &= -\beta_{m,1} - \sum_{q=1}^{m-1} \left[\binom{m-1}{q} r_1^q \beta_{m-q,q+1} + r_{m-q} \sum_{k=0}^{q} r_1^k \binom{q}{k} \beta_{q-k,k+2} \right] . \end{aligned} \quad (3.82)$$

The first correction is

$$r_1 = -\frac{2\cos\zeta \sin\vartheta}{\sqrt{(n+1)(n+3)}} \,. \quad (3.83)$$

Furthermore, a similar expansion for b_c can be found by using (3.80). Define

$$b_c \equiv \sum_{m=0}^{\infty} \frac{b_m}{m!} a^m \quad (3.84)$$

where

$$b_{m+1} \equiv \left. \frac{d^{m+1} b_c}{da^{m+1}} \right|_{a=0} = \left[\frac{d^m}{da^m} \left(\frac{\partial}{\partial a} + \frac{dr_c}{da} \frac{\partial}{\partial r_c} \right) b_c \right]_{a=0} = \left[\frac{d^m}{da^m} \frac{\partial b_c}{\partial a} \right]_{a=0} \,. \quad (3.85)$$

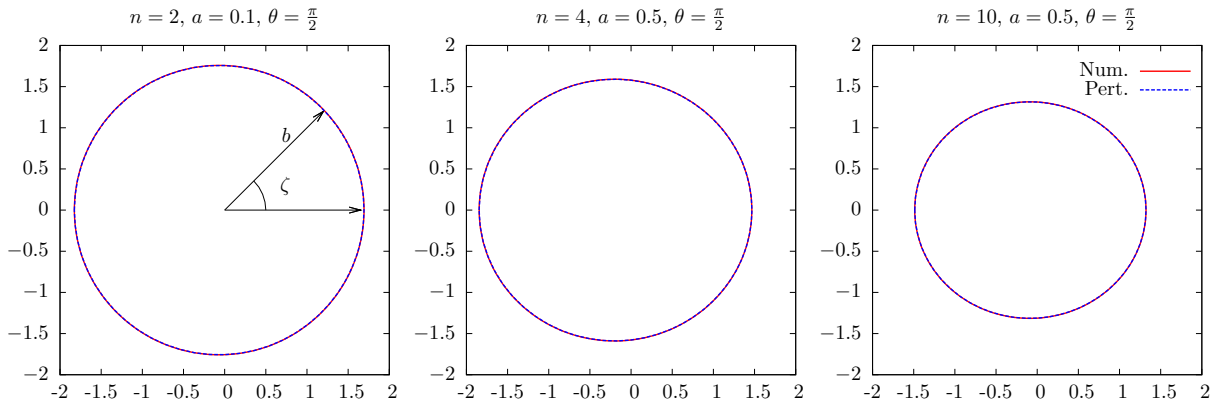

Figure 3.4: The perturbative result (dashed blue) agrees with the numerical minimisation (solid red), for $a \lesssim 1$ (some combinations of (n, a, ϑ) indicated). The polar system (b, ζ) used throughout to draw the absorptive disks (defined on the plane transverse to the radial direction of observation at infinity) is indicated on the left plot.

The last step follows from (3.77). The result is ($m \geq 1$)

$$\begin{aligned} b_1 &= \beta_{1,0} \\ b_{m+1} &= \sum_{q=0}^{m-1} \left[\binom{m-1}{q} r_1^q \beta_{m+1-q,q} + r_{m-q} \sum_{k=0}^{q} r_1^k \binom{q}{k} \beta_{q+1-k,k+1} \right] . \end{aligned} \tag{3.86}$$

The first correction is actually independent of the perturbation in r

$$b_1 = -\frac{2\cos\zeta \sin\vartheta}{n+1} . \tag{3.87}$$

This perturbative method was used to check the exact numerical results obtained from numerical minimisation. Figures 3.4 and 3.5 show a perfect agreement for small a and they are good up to $a \sim 1$. For larger a, the perturbative expansion seems to hold as an asymptotic series. The inclusion of higher order corrections degrades the result and the closest we get from the exact numerical result is by keeping $O(2)$ corrections (see figure 3.5). However, even though the perturbative result fails for large a, it is consistently larger than the numerical one, which is supposed to be the true minimum. The lowest order correction shows that for small a, the distortion is suppressed for large number of extra dimensions. Furthermore, for incidence along the vertical axis, the distortion is independent of ζ (this follows trivially from the azimuthal symmetry). For incidence along the equatorial plane (or intermediate angles), the disk of absorption is distorted into an oval, indicating the orientation of the angular momentum of the black hole. The exact

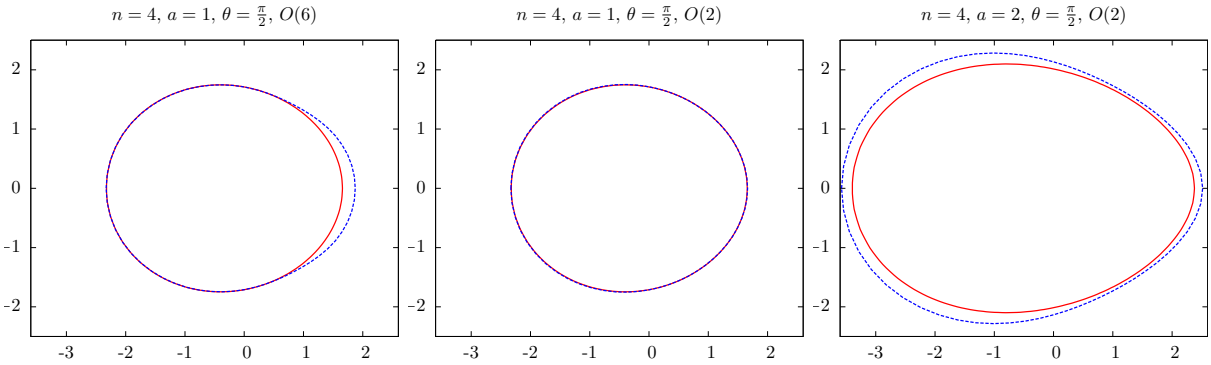

Figure 3.5: The perturbative result starts to fail compared to the numerical minimisation, for $a \gtrsim 1$ (same color scheme as figure 3.4). $n = 4$, $a = 1$ (*left*) starts to disagree if we include $O(6)$ corrections. However, truncating at $O(2)$ (*centre*) the result is still good. Increasing $a = 2$ (*right*) further degrades the perturbative result.

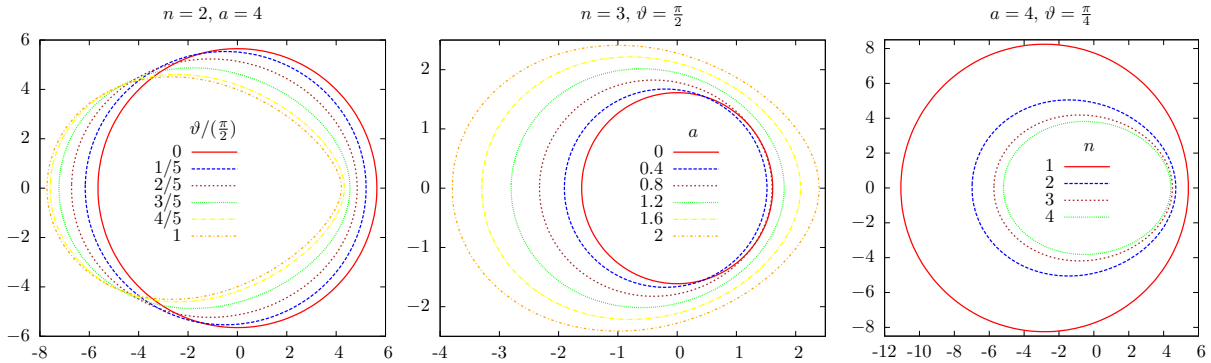

Figure 3.6: The plots shows the variation of the absorptive disk by varying one parameter with all the others fixed.

numerical results[9] in figure 3.6 confirm the non-perturbative validity of these qualitative features. The only exception is the conclusion regarding the suppression with n (actually the opposite occurs for $a_\star \gtrsim 1$, see right plot in figure 3.6 where the distortion is greater for larger n when $a = 4$). This figure also shows that for larger rotation parameter, the distortion becomes much stronger.

The main conclusion of this analysis is that if the black hole is between a distant observer and a source which radiates ultra-relativistic particles, it is possible to infer its angular momentum by looking at the shape of the black disk in different directions. The egg-shape disk is a clear indication of a rotating rather than a spherically symmetric black hole and the details of the shape contains information on n and the angle of observation.

[9]These were obtained by running a code in Maple which was written using the Maple inbuilt minimisation routine.

Besides providing a more intuitive idea of the properties of the black hole as seen by a distant observer, these disks can be used to compute the interaction cross section for a beam of classical particles incident on the black hole along a given direction, which is simply the area of the critical disk. At high energies, wave propagation can be described geometrically, so these results will be useful in chapter 6 to check the absorption cross sections. The latter are closely related to the transmission factors which determine the spectrum of Hawking radiation.

Chapter 4

Strong gravity II: Models for black hole production

In the beginning of chapter 3 we have motivated the study of black hole solutions in higher dimensions from the point of view of strong gravitational interactions in D dimensions which lead to black hole production. In particular we are interested in collisions of two highly relativistic particles at impact parameters of the order of the Schwarzschild radius for the centre of mass energy $\sqrt{s}$. The kinematics of the colliding system in the centre of mass frame for two particles of masses m_1 and m_2 at an impact parameter b is in general

$$p_1^M = \left(\sqrt{m_1^2 - p^2}, 0, 0, p, 0, \ldots, 0\right) \tag{4.1}$$

$$p_2^M = \left(\sqrt{m_2^2 - p^2}, 0, 0, -p, 0, \ldots, 0\right) \tag{4.2}$$

with

$$p \equiv \frac{M}{2}\sqrt{1 - 2\frac{(m_1^2 + m_2^2)}{M^2} + \left(\frac{m_1^2 - m_2^2}{M^2}\right)^2}\,. \tag{4.3}$$

We have defined the invariant mass of the system $M \equiv \sqrt{s}$ and assumed a collision of particles on the brane along the z-axis. For the gravitational interaction to be described classically we need the typical wavelength for each particle to be small compared to the typical gravitational interaction length. The Heisenberg principle for a wave packet with

minimal uncertainty then gives the condition [63]

$$\Delta x \sim \frac{1}{p} \ll r_H \ , \tag{4.4}$$

which for highly-relativistic particles[1] and a large enough invariant mass M is always possible (since r_H grows with M). Furthermore, in the trans-Planckian regime where M is well above M_D, the gravitational interaction is much stronger than all other SM interactions, and at high energies $\sim M$ it occurs at large length scales, whereas high energy SM interactions occur at short distances. Thus the interaction is gravitationally dominated.

From this setup, the first estimates for the production cross section using the hoop conjecture were obtained in [24, 45, 46]

$$\sigma \sim \pi r_H^2 \tag{4.5}$$

where a higher dimensional Schwarzschild black hole[2] with mass M and horizon radius r_H was assumed to be formed. The cross section is simply the area of the black disk with radius r_H, and b is the impact parameter. In this chapter, we review some models which improve this early simplistic picture.

4.1 Setting up the initial state

To model the gravitational interaction between the particles, in addition to the kinematical information of the initial state, we need to provide a spacetime metric which describes their initial gravitational field when they are far apart. For the simplest case of two particles with no spin or charges, this can be achieved in their centre of mass frame by superposing two boosted metrics of the form (3.15) boosted in opposite directions. As long as the initial positions of the particles are well separated, we can sum the two flat parts of each metric with a shock centered at the two initial points (say $x \to x \pm x_0$ respectively and set for one of the shocks a transverse coordinate $x_2 \to x_2 - b$ where b is the impact parameter). This can be used to fix the initial conditions for the collision.

For a more general configuration where the colliding particles may have charges and spin, in principle, the initial state is prepared similarly. As long as a metric is known

[1] And even moderately relativistic particles as long as their masses are not too close to the threshold $\sim M/2$.

[2] Also known as the Schwarzschild-Tangherlini solution.

which describes the gravitational field of the particle in its rest frame, a simple boost and a translation will suffice.

4.2 Gravitational collapse

In the introduction of this chapter, we have argued that the hoop conjecture indicates that a black hole must form as long as the impact parameter b between the colliding particles is small enough. Before presenting the model that we will use for production, it is instructive to discuss what we would expect based on some order of magnitude estimates and some known results in general relativity.

Assuming a black hole does form in the collision, in general it will start by having a complex shape horizon. Furthermore, the production may be accompanied by emission of gravitational and gauge radiation from the gravitational interaction between the energetic particles and the gauge interactions sourced by their SM charges. In four-dimensional general relativity, according to the 'no hair' theorem [64], the solution should quickly relax to one of the axisymmetric stationary black hole solutions of Einstein's equations. We would expect a higher dimensional black hole on the brane to be formed similarly, however other axisymmetric solutions are known in higher dimensions such as the 'black ring'[3]. Furthermore the Myers-Perry black hole is known to be unstable for large angular momentum (see e.g. [67,68]). Nevertheless, at least for not too large angular momentum, we would expect the black hole formed to be of Myers-Perry type.

It has been argued [24] that the typical time scale for loss of asymmetries related to the production shock is of the order of the horizon radius r_H (note we are using natural units – see appendix A.2). This is physically reasonable because the asymmetries are related to a distortion of the geometry (with respect to the stationary solution). Regardless of the details of the interaction responsible for removing them, it will involve a signal propagating over a region of typical size r_H. On the other hand the time scale Δt for evaporation of a trans-Planckian black hole is controlled by the Hawking energy flux. Since we are only interested in the order of magnitude, we can estimate it by using the D-dimensional Schwarzschild case combined with dimensional analysis (see for example section 3 of [24]) to obtain

$$\frac{\Delta t}{r_H} \propto \left(\frac{M}{M_D}\right)^{\frac{D-2}{D-3}} \quad . \tag{4.6}$$

[3]This is known to exist in five dimensions [65], and there is strong evidence for $D \geq 6$ [66].

The prefactor is a constant of order unity containing the dimensionally reduced energy flux and other convention-dependent constants, and M_D is the Planck mass in D dimensions[4]. For $M \gg M_D$ the time for evaporation will be much longer than for the loss of asymmetries (usually called the balding phase).

Another issue is that of quantum gravity corrections to the classical production description. It has been shown, within some quantum gravity approximation schemes, that these are small provided that the parton collision energy is sufficiently far above the Planck scale [69–72]. This agrees with the qualitative considerations we have presented in the introduction of this chapter.

In principle, the problem of evolving the Einstein equations classically to obtain the final black hole solution and the radiation released in the collision, given the initial setup described in section 4.1, can be solved numerically. The two pieces of information which are most relevant to the theoretical modelling of the black hole production phase in parton-parton collisions are: the maximum allowed impact parameter b, and the fractions of the initial centre of mass energy and angular momentum that are trapped within the rotating black hole. This has not yet been fully achieved for higher dimensional black holes (see section 4.4). In the next section we comment on analytic or semi-analytic methods used to study the production and present a model based on trapped surface bounds.

4.3 Trapped surface and other analytic bounds

The trapped surface inspired model presented in this section and in appendix B is due to Jonathan R. Gaunt and was published as part of [4]. It is included here for completeness because it is used in the event generator described in chapter 7.

4.3.1 Theoretical studies of black hole production

The main approach to studying higher dimensional black production has been the trapped surface method [59,73–76]. This method utilises the fact that the black hole horizon begins forming in the spacetime region outside the future lightcone of the collision event, where we can solve for the geometry. By studying apparent horizons in spacetime slices of this region, and in particular looking at certain areas associated with the apparent horizon as b is varied, one can set bounds on the parton-level cross section and the mass M and

[4]See Appendix A.2 for our convention for the definition of M_D.

angular momentum J trapped for a given b.

Few trapped surface calculations conducted thus far have attempted to obtain results for nonzero b. The one offering best bounds is that of Yoshino and Rychkov [76] who considered dimensions $D = 4 \ldots 11$. They produced (M, J) bounds up to the maximum impact parameters which give rise to apparent horizons in their method. The results of this calculation are the primary theoretical input to the model of production we use. A more detailed discussion of the Yoshino-Rychkov method is given in appendix B.1.

The Yoshino-Rychkov calculation models the colliding partons as boosted Schwarzschild black holes (equation (3.21)), and so neglects the effects of the spin, charge, and finite size of the colliding partons. For each effect individually, trapped surface calculations have been carried out [77–79] - but all are for $b = 0$. One important observation from those calculations is that charge effects may be significant.

Alongside the trapped surface method, alternative techniques have been developed which use a perturbative approach and/or other approximations to estimate directly the mass lost in the production phase. In one setup [80], the collision is modelled as an ultra-relativistic particle falling into a Schwarzschild black hole, and the gravitational emission is calculated by assuming that the gravitational effects of the in-falling particle may be treated as a perturbation on top of the Schwarzschild metric. Another calculation [81] also uses a perturbative approach and assumes that the collision is instantaneous. As a final example, D'Eath and Payne [82–84] have estimated the mass loss in the $D = 4$ axisymmetric collision case by finding the first two terms of Bondi's news function, and then extrapolating off axis. Here some assumptions about the angular dependence of the radiation are made.

The results produced so far by these methods have been limited to $b = 0$ and certain values of D. The $b = 0$ results from different techniques are compared with the trapped surface bound in figure 4.1. The general indication from these is that much less mass is lost during the production phase than the Yoshino-Rychkov upper limits indicate.

4.3.2 The model for `CHARYBDIS2`

Cross section

In earlier versions of `CHARYBDIS` [85], parton-level cross sections for different D values were calculated according to the simple formula $\sigma = \pi r_s^2(\sqrt{s})$ which is based on Thorne's hoop conjecture [44]. Here $r_s(\sqrt{s})$ is the radius of the D-dimensional Schwarzschild black

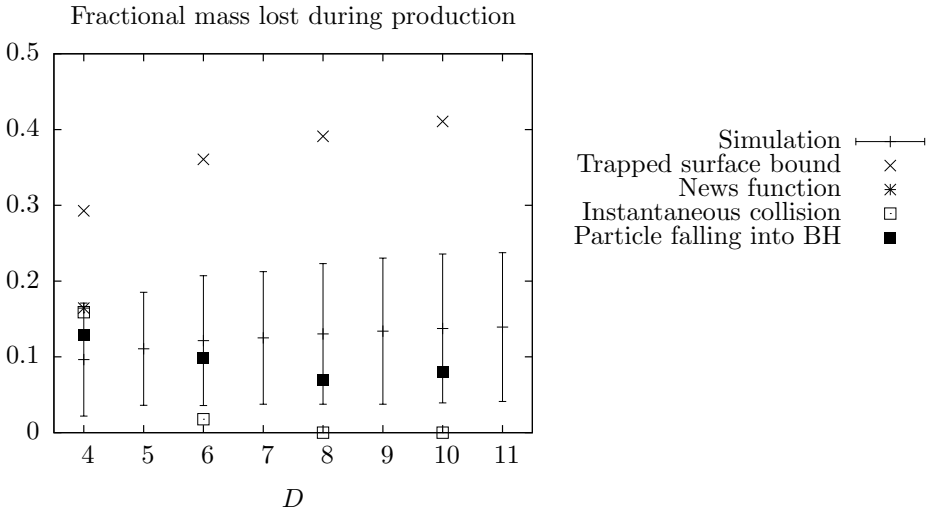

Figure 4.1: A comparison of various theoretical results for the production phase mass loss in the $b = 0$ case, with the average mass loss produced for $b = 0$ by our model for `CHARYBDIS2`. Black squares: 'Particle falling into black hole' results from [80]. Open squares: 'Instantaneous collision' results from [81]. Asterisk: 'Bondi's news function' result from [82–84]. Crosses: 'Trapped surface method' upper bound on mass loss. Points with error bars: average $b = 0$ mass loss from our simulation. The error bars represent the standard deviation in the $b = 0$ output.

hole with mass $\sqrt{s}$. Incorporation of the Yoshino-Rychkov cross section results simply requires multiplying these σ values by the 'formation factors' given in Table II of [76]. The increase in σ ranges from a factor of 1.5 at $D = 5$ to 3.2 at $D = 11$. The maximum impact parameters for black hole production, b_{max}, to be generated in `CHARYBDIS2`, is adjusted accordingly (the two are related through $\sigma = \pi b_{max}^2$).

Mass and angular momentum loss

Following Yoshino and Rychkov, we denote the fractions of the initial state mass and angular momentum, trapped after production, by ξ and ζ respectively. For a given number of dimensions D and impact parameter b, the Yoshino-Rychkov bound on these quantities is a curve in the (ξ, ζ) plane. Examples of such curves for various D and b values are given as the solid lines in figure 4.2. A boundary curve $\xi_b(\zeta)$ always possesses the following two key properties. First, it always passes through $\zeta = 0$ with a ξ value between 0 and 1, where $\xi_b(0) = \xi_{lb}(b, D)$ in the language of [76]. Second, it increases monotonically after this, passing through $\zeta = 1$ with a value satisfying $\xi_{lb} < \xi_b(1) \leq 1$. The allowed region is then delimited by this curve and the lines $\zeta = 0$, $\zeta = 1$, and $\xi = 1$.

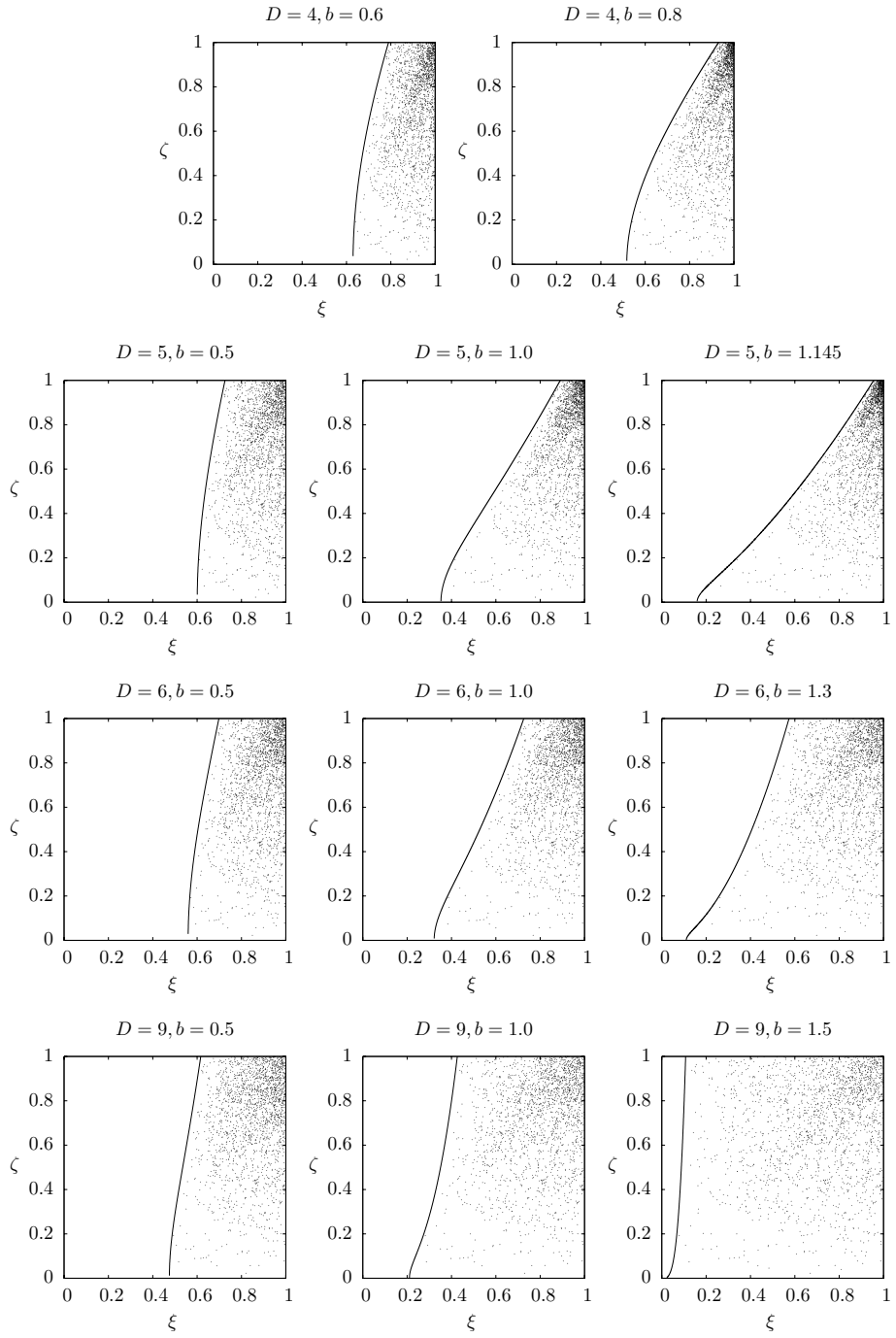

Figure 4.2: Plots displaying the Yoshino-Rychkov bound (solid line) and some output (ξ, ζ) points from our simulation of the production phase (dots), for selected D and b values (these are given above the plots in each case). Each plot contains 2000 sample output points, which have been generated with `CVBIAS` set to `.TRUE.`.

The new simulation of mass and angular momentum loss based on these curves consists of a point being generated at random in the square $0 \leq \xi \leq 1$, $0 \leq \zeta \leq 1$. The probability distribution for generating this point goes to zero along the Yoshino-Rychkov bound corresponding to the D and b values of the event, such that the generated point is always inside the bound. The ξ and ζ coordinates of this point are then taken as the fractional mass and angular momentum trapped during the production phase for that event.

The precise rules for the generation of the (ξ, ζ) point are as follows. First, the ζ value for the point, ζ^*, is generated, according to a linear ramp distribution. This distribution extends between $\zeta = 0$ and $\zeta = 1$, with value 0 at $\zeta = 0$ and value 2 at $\zeta = 1$. The ξ value for the point is then also generated. The distribution in this case is similar, except that now it extends between $\xi = \xi_b(\zeta^*)$ and $\xi = 1$, ensuring that the point ends up inside the Yoshino-Rychkov bound. The details of how the program calculates $\xi_b(\zeta^*)$ for the D and b appropriate to the event are given in Appendix B.1.

The decision to implement a probability distribution favouring smaller mass losses than the Yoshino-Rychkov upper bound was made based on the results from the direct calculations given in figure 4.1. In this figure we have plotted the mean mass lost in an event with $b = 0$ using the above probability distribution. The error bars represent the standard deviation in the $b = 0$ mass loss. We observe a reasonably good agreement between the mean values obtained with our chosen probability distribution and the estimation method results, especially in the important $D = 4$ case where the estimation method results agree closely. Given that we favour smaller mass losses, it then seems sensible to ensure that the probability distribution also favours smaller angular momentum losses – hence the ramp distributions in ξ and ζ.

One possible picture of the production phase is one in which the production phase radiation is 'flung out' radially in a frame co-rotating with the forming event horizon. In this scenario, the angular velocity of the event horizon does not change during the production process (where we have to regard the forming black hole as a pseudo-Myers-Perry solution at all points during the production phase for this statement to have any meaning).

Based on this picture, we consider the option to bias the above probability distribution such that (ξ, ζ) points corresponding to smaller changes in the horizon angular velocity are more likely. An additional condition is added to this bias – for the points to have their chance of being picked enhanced, they must also have an associated value of the oblateness parameter $a_* = a/r_H$, which is sufficiently close to that of the initial state. This is to

remedy the problem that, for $D > 5$, there are two curves with the same angular velocity as the initial state in the square $0 \leq \xi \leq 1$, $0 \leq \zeta \leq 1$, but only one is connected to the initial state. In the `CHARYBDIS2` generator described in chapter 7 the bias may be turned on or off using the user switch `CVBIAS`. The details of its implementation are discussed in appendix B.2.

In each of the plots in figure 4.2, there are 2000 (ξ, ζ) points generated for the appropriate D and b using the model we have described, with the bias applied. One can see in each case that there is an increased density of points around the 'constant horizon angular velocity' curve.

4.4 Latest developments in numerical relativity

The model in the previous section gives a physically reasonable estimate for the maximum impact parameter which allows black hole production, and to the amount of mass and angular momentum lost. However a complete solution within classical general relativity will give a point instead of a distribution on the (ξ, ζ) plane. This is in general a complicated and computationally intensive problem in $D = 4 + n$ dimensional numerical relativity.

The most well studied cases up to the date are in four dimensions. For example some recent results of simulations of ultra-relativistic collisions of black holes [86–88] or solitons [89] in four dimensions indicate that $\sim 25\%$ of mass and $\sim 65\%$ of angular momentum are lost in collisions at the maximum impact parameter for black hole formation. However, note that the value obtained for the maximum impact parameter in this case is $\sim 50\%$ above the Yoshino-Rychkov lower bound, corresponding to an initial-state angular momentum that is more than double the maximum value possible for the black hole that is formed. Therefore an angular momentum loss greater than 50% is inevitable in this case. In $D > 5$ dimensions there is no upper limit on the angular momentum of a black hole and such a large loss is not required.

Results for higher dimensions are not yet known but should be available in the near future [90] to implement in our modelling for production.

Chapter 5

Black hole decay and Hawking radiation

In this chapter we discuss theoretical aspects of the Hawking effect [91] for the various fields propagating in the black hole background constructed in section 3.2. The Hawking effect is part of the more generic problem of instabilities of a black hole background. It arises only at the quantum level, i.e. from the quantum fluctuations of field modes which are classically stable. The reason it is relevant for the scenario we are studying is because we assume that a classically stable black hole solution is formed during the production. Since the black hole is produced in a vacuum, the only way to decay is then through quantum effects.

We start with a general discussion of the SM fields, to assess the order of magnitude of the various interactions in their equations of motion. In section 5.2 we summarize the key results known from the theory of Hawking radiation which are relevant to this study. In section 5.3 we provide the rules to couple various brane fields to the charged background constructed in chapter 3. Separated wave equations are provided for scalars and fermions, and some comments are made for higher spin fields (this study was published as part of [1, 2]). We end the chapter with a discussion of how to decompose the spheroidal wave modes constructed for the fields, in terms of plane wave modes (published in [4]).

5.1 Perturbation theory and approximate decoupling

Before discussing the theory of Hawking fluxes emitted by the black hole, it is important to summarise the various field perturbations which are allowed to propagate in the

background spacetime. Similarly to the construction of the brane charged metric in section 3.2, we adopt a perturbative approach where all fields are expanded linearly around their background value. Typically, in our study, the only fields which have a non-zero background value are the gravitational field and the electromagnetic field, but more general configurations are in principle possible.

First, we consider the bulk higher dimensional background given by the Myers-Perry solution with one angular momentum (3.11). By expanding the bulk metric as in equation (2.12) a generalised version of the Fierz-Pauli Lagrangian (1.21) to a curved background vacuum solution is obtained

$$\mathcal{S}_H = \int d^D x \sqrt{|G^{(0)}|} \left[\frac{1}{8} \left(H^{AB;C} H_{AB;C} - 2H^{AB;C} H_{AC;B} + 2H^{AC}{}_{;A} H_{;C} - H_{;B} H^{;B} \right) + \right. \\ \left. + \frac{1}{2M_D^{\frac{D}{2}-1}} T_{AB} H^{AB} \right] , \quad (5.1)$$

to describe the gravitational perturbations of the background. Note that we have denoted the background covariant derivative ∇_A by $_{;A}$ for notational simplicity. Equation (5.1) can be thought of as a covariantised version of the flat spacetime action for the gravitational perturbations. This is similar to the covariantisation of the action for matter fields by fixing it to its flat spacetime form in the locally inertial frame. T_{AB} is the higher dimensional energy momentum tensor for the matter fields which, for brane confined fields, must contain a delta function like factor.

As discussed in section 3.2, a simple projection of the metric (3.11) gives the brane metric. In that section we have introduced a brane metric correction to approximate the effect of a small black hole charge. On the brane, we use the corrected brane metric (3.37) and the Maxwell field (3.32). The brane coupled SM low energy effective action is

$$\begin{aligned} \mathcal{S}_{s=\{0,1\}} \;=\; & \int d^4 x \sqrt{|g|} \left[\frac{1}{2} \nabla^a h \nabla_a h - \frac{m_h^2}{2} h^2 - \frac{\lambda}{8} h^3 \left(h + 4v \right) - \frac{1}{4} \mathbf{G}_{ab} \cdot \mathbf{G}^{ab} + \right. \\ & - \frac{1}{2} W^\dagger_{ab} W^{ab} + m_W^2 W^\dagger_a W^a - \frac{1}{4} Z_{ab} Z^{ab} + \frac{m_Z^2}{2} Z_a Z^a - \frac{1}{4} A_{ab} A^{ab} + \\ & + \frac{1}{4} h \left(h + 4v \right) \left(\frac{2e^2}{\sin^2(2\theta_W)} Z_a Z^a + \frac{e^2}{\sin^2 \theta_W} W^\dagger_a W^a \right) + \\ & \left. + i W_a W^\dagger_b \left(e A^{ab} + \frac{e}{\tan \theta_W} Z^{ab} \right) + \frac{e^2}{2 \sin^2 \theta_W} \left(|W_a W^a|^2 - \left(W^\dagger_a W^a \right)^2 \right) \right] \end{aligned} \quad (5.2)$$

and

$$\begin{aligned}\mathcal{S}_{s=\frac{1}{2}} &= \int d^4x\sqrt{|g|}\left[\bar{\mathbf{e}}\left(i\not{\nabla}-m_e\right)\mathbf{e}+\bar{\nu}i\not{\nabla}\nu+\bar{\mathbf{u}}\left(i\not{\nabla}-m_u\right)\mathbf{u}+\bar{\mathbf{d}}\left(i\not{\nabla}-m_d\right)\mathbf{d}+\right.\\ &\quad -\frac{h}{v}\left(m_e\bar{\mathbf{e}}\mathbf{e}+m_u\bar{\mathbf{u}}\mathbf{u}+m_d\bar{\mathbf{d}}\mathbf{d}\right)+ \\ &\quad \left.-\frac{e}{2\sqrt{2}\sin\theta_W}\left(J_W^aW_a+c.c.\right)-eJ_A^aA_a-\frac{e}{\sin(2\theta_W)}J_Z^aZ_a-g_1\mathbf{J}_G^a\cdot\mathbf{G}_a\right]\end{aligned} \tag{5.3}$$

where we have suppressed the family indices to avoid confusion with curved spacetime indices, and made the fermion fields bold face. We are using the induced effective brane metric with appropriate curved spacetime covariant derivatives and gamma matrices as described in section 2.1. To leading order in the gravitational field, this introduces a coupling to the background. Note that now the field strengths have the general form

$$\mathbf{F}_{ab}=\nabla_a\mathbf{F}_b-\nabla_b\mathbf{F}_a+g\left[\mathbf{F}_a,\mathbf{F}_b\right]\ , \tag{5.4}$$

and the various currents are

$$J_A^a = -\bar{\mathbf{e}}\gamma^a\mathbf{e}+\frac{2}{3}\bar{\mathbf{u}}\gamma^a\mathbf{u}-\frac{1}{3}\bar{\mathbf{d}}\gamma^a\mathbf{d} \tag{5.5}$$

$$\mathbf{J}_G^a = \sum_i\left(\bar{\mathbf{u}}\gamma^aT_i\mathbf{u}+\bar{\mathbf{d}}\gamma^aT_i\mathbf{d}\right)T_i \tag{5.6}$$

$$J_W^a = \bar{\nu}\gamma^a\left(1-\gamma_5\right)\mathbf{e}+\bar{\mathbf{u}}\gamma^a\left(1-\gamma_5\right)\mathbb{V}\mathbf{d} \tag{5.7}$$

$$\begin{aligned}J_Z^a &= \frac{1}{2}\left[\bar{\nu}\gamma^a\left(1-\gamma_5\right)\nu-\bar{\mathbf{e}}\gamma^a\left(1-\gamma_5-4\sin^2\theta_W\right)\mathbf{e}\right]+\\ &\quad +\frac{1}{2}\left[\bar{\mathbf{u}}\gamma^a\left(1-\gamma_5-\frac{8}{3}\sin^2\theta_W\right)\mathbf{u}-\bar{\mathbf{d}}\gamma^a\left(1-\gamma_5-\frac{4}{3}\sin^2\theta_W\right)\mathbf{d}\right]\ ,\end{aligned} \tag{5.8}$$

where we have denoted the CKM matrix acting on family space by $\mathbb{V}$ to avoid using family indices. Note that in addition we need to expand $A_a=A_a^{(0)}+A_a^{(1)}$ around the background value $A_a^{(0)}$ given in equation (3.32).

Now that we know the action, we want to assess the magnitude of the couplings to the background fields, and among the SM perturbations. This is to justify keeping only the coupling to the background. For example consider the Higgs field. Ignoring the

perturbation of the graviton and the brane displacements, the equation of motion is

$$\begin{aligned}\left(\partial_a\partial^a - m_h^2\right) h + \Gamma^a_{ab}\partial^b h \\ - \frac{\lambda}{2}h^2\left(h+3v\right) + \frac{1}{2}\left(h+2v\right)\left(\frac{2e^2}{\sin^2(2\theta_W)}Z_aZ^a + \frac{e^2}{\sin^2\theta_W}W_a^\dagger W^a\right) \\ - \frac{1}{v}\left(m_e\bar{\mathbf{e}}\mathbf{e} + m_u\bar{\mathbf{u}}\mathbf{u} + m_d\bar{\mathbf{d}}\mathbf{d}\right) = 0\ , \quad (5.9)\end{aligned}$$

where we have singled out the coupling of the scalar field to the gravitational background connection in the first line. If we take the neutral non-rotating limit of the background and look at the term $\partial^r h$ which couples to $\Gamma^a_{ar} = \partial_r \log\sqrt{|g|} \sim 1/r$, then the coupling in front is $\sim p_r/r \sim \omega/r$ (we assume p_r is a typical radial momentum). In our problem the typical length scale is the horizon radius. If we look at processes at $r \sim r_H$ and energies $\omega \sim 1/r_H$, then the coupling to gravity is of order $1/r_H^2$. Table 1.1, shows that all the other dimensionless couplings appearing in (5.9) are typically small. Furthermore, the operators are all quadratic (or higher) in the perturbations, so if we assume that the perturbations have small amplitudes of the form $A \sim \epsilon/r_H$ for bosons or $A \sim \epsilon/r_H^{3/2}$ for fermions ($\epsilon \ll 1$) the higher order interactions are naturally suppressed. Note however that though they are small compared to the gravitational interaction with the background close to the horizon, they become dominant away from the black hole due to the $1/r$ dependence of the gravitational field. In general if we have a SM coupling with a number p of fields and a reduced dimensionless coupling α (close to the horizon), and we use a typical reduced amplitude ϵ for all perturbations, then equating the leading term with the power p term gives

$$\frac{r_H}{r}\epsilon \sim \alpha\epsilon^p \Rightarrow r \sim \frac{r_H}{\alpha\epsilon^{p-1}}\ . \quad (5.10)$$

So in general if the higher order coupling and the amplitude of the perturbation is small, such terms are only relevant far away from the black hole. Similar arguments can be used for all the other perturbations, to motivate neglecting interactions between perturbations of order higher than 2 (at the level of the Lagrangian). This also holds for the n massless scalar fields $\mathcal{Z}^m$ which describe brane fluctuations. Note that though massless, those fields couple to other perturbations through derivative terms which further suppresses their excitation at low energy.

These considerations justify treating each channel of the evaporation at linear order in the equations of motion. In the remainder of this work we consider only the kinetic parts of the Lagrangian covariantised with respect to the background for each type of

perturbation.

Another important question in the semi-classical decay is whether the emitted particles can interact at longer distances (away from the black hole) before they are detected by an observer at infinity. In general this depends on the typical length scale for SM interactions in flat spacetime and on the angular separation between the quanta emitted from the black hole radially. Furthermore, any such interaction is bound to occur before the hadronisation of strongly interacting particles, which occurs at a typical length scale $1/\Lambda_{QCD} \sim (100 \text{ MeV})^{-1}$. This scale is orders of magnitude larger than the typical black hole radii we will consider. Another process occurring before hadronisation at a length scale of $\sim (1 \text{ GeV})^{-1}$ is parton showering (also a large distance process). Similarly, it has been shown [92] that if secondary scattering occurs, it does mostly at the 1 GeV^{-1} scale. The two former effects can be taken into account separately with existing showering and hadronisation programs [93–95], whereas the latter can be safely neglected [92].

5.2 Hawking radiation

Since the pioneering work of Hawking [91] several studies in the literature have examined the quantisation of various fields in black hole backgrounds which are analytically similar to the one we are using [96–100]. In particular the metric (3.37) and the Maxwell field (3.32) are similar in form to Kerr-Newman, so the quantisation procedure is formally the same and we will not repeat the technical details [96–100].

For illustrative purposes consider a massless real scalar field Φ. The basic procedure consists of choosing a vacuum state which corresponds to no incoming particles from past null infinity $\mathcal{J}^-$ (i.e. the collapse occurs in a vacuum with no extra particles other than the collapsing matter). It is well known (see for example the discussion in [48] and Hawking's original paper [91]) that the details of the collapse are not important for the Hawking radiation generated at late times, so alternatively the calculation can be carried out in the eternal version of the black hole, with the Unruh vacuum [48]. The latter needs an extra condition: no up-going particles from the past event horizon H^- (with respect to the Kruskal time). Formally the calculation is done by constructing a complete basis of modes to expand the field operator[1] on $\mathcal{J}^- \cup H^-$ (schematically)

$$\Phi = \sum_\alpha \mathbf{a}_{in}\Phi^{in}_\alpha + \mathbf{a}^\dagger_{in}(\Phi^{in}_\alpha)^\dagger + \sum_\alpha \mathbf{a}_{up}\Phi^{up}_\alpha + \mathbf{a}^\dagger_{up}(\Phi^{up}_\alpha)^\dagger \,, \tag{5.11}$$

[1] α denotes a complete set of quantum numbers.

where Φ^{in}_α and Φ^{up}_α are the modes corresponding to incoming particles on $\mathcal{J}^-$ and up-going particles on H^-. Then the boundary condition is implemented by requiring that the annihilation operators, $\mathbf{a}_{in}$ and $\mathbf{a}_{up}$, associated with modes which are positive frequency with respect to the timelike killing vector $\mathbf{k}_t$ and the Kruskal time respectively, vanish when acting on the vacuum. With these boundary conditions, the field operator can be constructed by scattering the expansion modes through spacetime. At late times (in $\mathcal{J}^+$), the modes decompose into outgoing modes (corresponding to outgoing particles) and down-going modes (corresponding to particles falling into the black hole). The outgoing modes become populated in the chosen vacuum state, because part of the initial negative frequency mode functions $(\Phi^{in})^\dagger_\alpha$ gets absorbed by the black hole and part gets reflected. The reflected part is decomposed (at $\mathcal{J}^+$), as a sum of a wave with negative frequency, and a non-zero wave with positive frequency. This corresponds to part of a negative energy mode being absorbed by the black hole (which reduces its mass) and a positive energy mode escaping to infinity.

Once the field operator is known, the expectation value of any other operators (such as the energy momentum tensor) can be computed. The physically relevant fluxes at $\mathcal{J}^+$ can be obtained from specific components of those expectation values. The main result of Hawking's original paper is then that black holes emit a continuous flux of particles. In horizon radius units, the fluxes of particle number, energy, angular momentum and charge are respectively [91]

$$\frac{d^2N}{dtd\omega} = \frac{1}{2\pi}\sum_{j=|s|}^{\infty}\sum_{m=-j}^{j}\frac{1}{\exp(\tilde{\omega}/T_H)\pm 1}\mathbb{T}^{(4+n)}_k(\omega,\mu,a,q,Q)\ , \tag{5.12}$$

$$\frac{d^2E}{dtd\omega} = \frac{1}{2\pi}\sum_{j=|s|}^{\infty}\sum_{m=-j}^{j}\frac{\omega}{\exp(\tilde{\omega}/T_H)\pm 1}\mathbb{T}^{(4+n)}_k(\omega,\mu,a,q,Q)\ , \tag{5.13}$$

$$\frac{d^2J}{dtd\omega} = \frac{1}{2\pi}\sum_{j=|s|}^{\infty}\sum_{m=-j}^{j}\frac{m}{\exp(\tilde{\omega}/T_H)\pm 1}\mathbb{T}^{(4+n)}_k(\omega,\mu,a,q,Q)\ , \tag{5.14}$$

$$\frac{d^2Q}{dtd\omega} = \frac{1}{2\pi}\sum_{j=|s|}^{\infty}\sum_{m=-j}^{j}\frac{q}{\exp(\tilde{\omega}/T_H)\pm 1}\mathbb{T}^{(4+n)}_k(\omega,\mu,a,q,Q)\ , \tag{5.15}$$

where $\tilde{\omega}=\omega-m\Omega_H-q\Phi_H$, $k=\{j,m\}$ are the angular momentum quantum numbers,

s is the helicity of the particle

$$T_H = \frac{(n+1)+(n-1)(a^2+Q^2)}{4\pi(1+a^2)r_H} \,, \tag{5.16}$$

and the signs $\pm$ are for fermions and bosons respectively. $\Omega_H = a/(1+a^2)$ and $\Phi_H = Q/(1+a^2)$ are the angular velocity and electric potential of the horizon respectively. Φ_H can be defined using the timelike Killing vector close to the horizon. For metric (3.37), we can pick a Killing vector field which is timelike at a given point, using the two Killing vector fields $\mathbf{k}_t = e_t$ and $\mathbf{k}_\phi = e_\phi$. We denote such a vector

$$\mathbf{k}_p = e_t + \Omega_p e_\phi \,, \tag{5.17}$$

where the subscript p labels a space-time point. Then if $\mathbf{k}_p$ is timelike at p, $\Omega_- < \Omega_p < \Omega_+$ where

$$\Omega_\pm = \frac{-g_{t\phi} \pm \sqrt{g_{t\phi}^2 - g_{tt}g_{\phi\phi}}}{g_{\phi\phi}} \,. \tag{5.18}$$

At the horizon $\Omega_+ = \Omega_- = \Omega_H$, so in some sense there is a natural vector field which defines the timelike direction close to the horizon. The electric potential at the horizon Φ_H is defined as the projection of the A_a field along $\mathbf{k}_H$. It can also be shown that Ω_H corresponds to the angular velocity of a physical observer close to the horizon whose frame is dragged by the gravitational field of the rotating black hole [101].

Finally $\mathbb{T}_k^{(4+n)}$ are the so called transmission factors defined as the fraction of an incident wave from infinity which is absorbed by the black hole. The boundary conditions are such that close to the horizon the wave is purely ingoing for the above physical observers [101].

Later on we will be particularly interested in the effect of electric charges. Before going into a detailed calculation of the fluxes, it is instructive to look at an estimate from the Schwinger formula for fermions [102]:

$$\frac{dN}{dVdt} = \frac{q^2E^2}{\pi^2}\sum_{n=1}^{+\infty}\frac{e^{-\frac{n\pi\mu^2}{qE}}}{n^2} \simeq \frac{q^2E^2}{6} \,, \tag{5.19}$$

where we took the small mass limit and E is the electric field. Equation (5.19) is valid in flat space for a uniform electric field, and it gives the rate of production of opposite charge pairs due to the electric field only. For (3.32), we know that the electric field drops like

$1/r^2$ so strictly speaking this formula is not valid. Nevertheless we can still use (5.19) to estimate the contribution of the background electric field to particle production and compare it with the contribution from the gravitational field alone (i.e. the typical Hawking flux for a neutral black hole). A rough estimate is obtained by considering the electric field at the horizon and a volume of order $(2r_H)^3$ around the black hole. Using our system of units and noting that the electric field at the horizon is $E_H \sim Q/r_H^2$ we get

$$\frac{dN}{dt} r_H \sim q^2 Q^2 = z^2 Z^2 \alpha^2 \simeq z^2 Z^2 10^{-5} \ . \tag{5.20}$$

So for order $z, Z \sim 1$ charges we get a very small rate when compared to the typical Hawking fluxes for a neutral black hole (which are of order ~ 1). This indicates that pair production due to the gravitational field is much stronger than pair production due to the electric field. So the common claim that TeV-scale black holes lose their charges earlier in their lifetime, is not necessarily true on the basis of Schwinger discharge alone [24]. We will confirm this result with a more detailed calculation in chapter 6.

5.3 Perturbations of a brane charged black hole

Previous attempts to model the evaporation focused on neutral rotating black holes [103–113]. In this section we use the background constructed in section 3.2 to generalise the treatment to the case when both the background and some fields on the brane are charged. In addition we also introduce particle mass which is necessary for heavy SM particles such as the W, Z bosons and the top quark.

5.3.1 Wave equations I: Coupling the background

In section 5.1 we have argued that the dominant interaction comes from the coupling of the various SM fields to the background. We start by writing the action for a brane charged complex scalar field

$$S_\Phi = \int \mathrm{d}^4x \sqrt{|g|} \left(\frac{1}{2} \left(D_a \Phi \right)^\dagger D^a \Phi - \frac{1}{2} \mu^2 \Phi^\dagger \Phi \right) \ , \tag{5.21}$$

where we have grouped together the covariant derivative with the electromagnetic coupling in the gauge covariant derivative

$$D_a = \nabla_a + iqA_a \ . \tag{5.22}$$

The mass of the particle is μ and we have anticipated the matching of the coupling q to the one introduced in section 3.2.3. Variation of (5.21) gives the wave equation

$$\left(D^a D_a + \mu^2\right) \Phi = 0 \ . \tag{5.23}$$

To check the normalisation of the coupling is correct we take the classical limit in flat space-time. Consider a slowly varying vector potential A_a, set

$$\Phi \sim e^{iS} \ , \tag{5.24}$$

and identify the mechanical 4-momentum of the classical particle with $p_a = -\nabla_a S - qA_a$. Then to leading order, equation (5.23) gives the mass-shell condition

$$p_a p^a = \mu^2 \ .$$

Conversely, $P_a = -\nabla_a S$ is the usual canonical momentum of the classical particle so we match q to $z\sqrt{\alpha}$ as in equation (3.43). This coupling agrees with other well studied cases (see for example [97,114–116]). Note that this differs by a factor of $\sqrt{4\pi}$ ($z\sqrt{\alpha} = ze/\sqrt{4\pi}$) compared to (5.2) and (5.3) which is due to the different normalisation of the background electromagnetic field (3.32). The latter is given by the SM electomagnetic field multiplied by $\sqrt{4\pi}$. In the remainder we use this new normalisation.

For fields with higher spin the procedure is similar. For a Dirac field the action is

$$S_\Psi = \int \mathrm{d}^4x \sqrt{|g|} \bar{\Psi} \left(i\not{D} - \mu\right) \Psi \ , \tag{5.25}$$

with the gauge covariant derivative

$$\not{D} = \not{\nabla} + iq\not{A} \ . \tag{5.26}$$

For a massive complex vector field V^a we have the action

$$S_\Psi = \int \mathrm{d}^4x\sqrt{|g|}\left(-\frac{1}{2}V^\dagger_{ab}V^{ab} + \mu^2 V^\dagger_a V^a + iqV_aV^\dagger_b A^{ab}\right) , \tag{5.27}$$

for the W^a field action ($q = \sqrt{\alpha}$), or $Z^a/\sqrt{2}$ action ($q = 0$), or the electromagnetic field $A^a/\sqrt{2}$ when $q = \mu = 0$.

5.3.2 Wave equations II: Separability

In this section we present the separated wave equations on the background of section (3.2).

5.3.2.1 The scalar field

Using equation (3.37), the separation ansatz $\Phi = e^{-i\omega t+im\phi}R(r)S(\theta)$ and inserting in (5.23) we obtain the radial equation

$$\Delta\frac{d}{dr}\left(\Delta\frac{dR}{dr}\right) + \left(K^2 - \Delta U\right)R = 0 , \tag{5.28}$$

where

$$K = \omega(r^2+a^2) - am - qQr \tag{5.29}$$

$$U = \mu^2 r^2 + \Lambda_{c,j,m} + \omega^2 a^2 - 2a\omega m . \tag{5.30}$$

The boundary condition at the horizon is [101]

$$R = x^{-i\frac{K_\star}{\delta_0}}(1 + \ldots) \tag{5.31}$$

with $x = r - 1$, $K_\star = \omega(1 + a^2) - am - qQ$, and $\delta_0 = n + 1 + (n - 1)(1 + a^2 + Q^2)$ is the leading order coefficient of the expansion of Δ in powers of x. The angular equation has exactly the same form as for the chargeless case studied for example in [105]:

$$\frac{1}{\sin\theta}\frac{d}{d\theta}\left(\sin\theta\frac{dS}{d\theta}\right) + \left(c^2\cos^2\theta - \frac{m^2}{\sin^2\theta} + \Lambda_{c,j,m}\right)S = 0 , \tag{5.32}$$

but now $c^2 = a^2(\omega^2 - \mu^2)$ and $\Lambda_{c,j,m}$ is the corresponding angular eigenvalue obtained by imposing regularity of the solution at $\cos\theta = \pm 1$. For $a = 0$ we have the closed form $\Lambda_{0,j,m} = j(j + 1)$ with j a non-negative integer [117].

Equation (5.28) is similar to the chargeless case with the additional terms:

1. Q^2 in Δ, which changes the location of the horizon and therefore the Hawking temperature of the black hole.

2. qQr in K which is related to the electric potential.

In K, ω is shifted by

$$-\frac{am}{r^2+a^2}-\frac{qQr}{r^2+a^2}\ . \tag{5.33}$$

Evaluated at the horizon, both quantities in (5.33) are associated with the well known phenomenon of superradiance [101, 118–121], i.e. for $\tilde{\omega}<0$ a wave incident from infinity is scattered back with a larger amplitude. This factor is also present in the expressions for the fluxes such as (5.12) where the Planckian suppression factor in the denominator becomes negative for superradiant modes.

5.3.2.2 The Dirac field

For a fermion field the standard procedure to separate the wave equation is to use the Newman-Penrose formalism[2]. The method has been developed for the Kerr metric by Chandrasekhar [123] and applied to the Kerr-Newman background by Page [115]. Page points out how a simple substitution of some of Chandrasekhar's quantities suffices to obtain separated equations for the fermion field with charge. Below we state the final result and refer the technical details to references [115, 122, 123].

The separated wave equation for the massive charged Dirac field relies on the ansatz $\Psi=e^{-i(\omega t-m\phi)}\chi(r,\theta)$ where

$$\chi=\begin{pmatrix}(r-ia\cos\theta)^{-1}P_{-1/2}(r)S_{-1/2}(\theta)\\ \sqrt{2}\Delta^{-1/2}P_{+1/2}(r)S_{+1/2}(\theta)\\ \sqrt{2}\Delta^{-1/2}P_{+1/2}(r)S_{-1/2}(\theta)\\ -(r+ia\cos\theta)^{-1}P_{-1/2}(r)S_{+1/2}(\theta)\end{pmatrix}\ . \tag{5.34}$$

The radial and angular equations are

$$\Delta^{\frac{1}{2}}\left(\frac{d}{dr}-2si\frac{K}{\Delta}\right)P_{-s}=(\lambda+2is\mu r)\,P_s \tag{5.35}$$

[2]Technical details on this formalism can be found in several textbooks – see for example [48, 122].

$$\left[\frac{d}{d\theta}+2s\left(a\omega\sin\theta-\frac{m}{\sin\theta}\right)+\frac{1}{2}\cot\theta\right]S_{-s}=(2s\lambda+a\mu\cos\theta)\,S_s \tag{5.36}$$

where λ is the angular eigenvalue. To make contact with well know limits, it is useful to obtain second order radial and angular equations by elimination (the prime denotes $\frac{d}{dr}$):

$$\frac{d^2P_s}{dr^2}+\left((1-|s|)\frac{\Delta'}{\Delta}+\frac{2is\mu}{\lambda-2is\mu r}\right)\frac{dP_s}{dr}+ \\ +\left[\frac{K^2}{\Delta^2}-is\frac{K}{\Delta}\frac{\Delta'}{\Delta}-\frac{4s^2\mu}{\lambda-2is\mu r}\frac{K}{\Delta}+\frac{2isK'-\lambda^2-\mu^2r^2}{\Delta}\right]P_s=0 \tag{5.37}$$

$$\frac{1}{\sin\theta}\frac{d}{d\theta}\left(\sin\theta\frac{dS_s}{d\theta}\right)+\frac{a\mu\sin\theta}{-2s\lambda+a\mu\cos\theta}\left(\frac{d}{d\theta}-2s\left(a\omega\sin\theta-\frac{m}{\sin\theta}\right)+\frac{\cot\theta}{2}\right)S_s+ \\ +\left[a^2(\omega^2-\mu^2)\cos^2\theta-2sa\omega\cos\theta-\frac{(m+s\cos\theta)^2}{\sin^2\theta}+\lambda^2-a^2\omega^2+2a\omega m-|s|\right]S_s=0\,. \tag{5.38}$$

Here $s=\pm1/2$. In the zero mass limit we recover a radial equation with the same analytic form as in references [111,112] except for the extra term in K'. Similarly, in that limit, the angular equation is exactly the same as for the spin-half spheroidal functions. In general, the eigenvalues are obtained by imposing regularity of the solution at $\cos\theta=\pm1$.

Finally setting the rotation parameter a to zero, note that the angular equation is the same with or without mass and charge. Then the angular eigenvalue takes a closed form [117] ($\lambda=j+1/2$ with j a positive semi-integer) and we do not need to integrate the angular equation to study the effects of both mass and charge. This simplification was explored for example in Page's paper in four dimensions [114].

5.3.3 Higher spins

For higher spins the procedure is similar and it has been studied in the literature for some special cases of the background metric we are using. Most notably the massless vector perturbations [103, 108] and the tensor gravitational perturbations [124, 125] in the zero charge limit with non-zero angular momentum.

When the background charge is present there are several extra complications to consider. Regarding electromagnetic perturbations, it is known in four dimensions that they couple linearly to gravitational perturbations (at the level of the equations of motion) for

the Kerr-Newman black hole (see for example Sect. 111, Chapter 11 of [122] and references therein). Similarly, in the higher dimensional case, we would expect them to couple to gravitational modes on the brane. However, in the limit of small charge, the perturbations should approximately decouple. This is indeed the case and an approximation scheme was developed by Dudley and Finley [126]. It amounts to considering separately one perturbation (either electromagnetic or gravitational) while setting the other to zero on the fixed background. This approximation was used for example in [127] and [128] to compute quasinormal modes. In [128] this was compared to other methods to confirm the validity of the approximation for small Q (the special case $J = 0$ was used). The approximate second order wave equation for a perturbation of spin s is [128]

$$\Delta^{1-s}\frac{d}{dr}\left[\Delta^{1+s}\frac{dR}{dr}\right] + \left[K^2 - is\frac{d\Delta}{dr}K + \Delta\left(2is\frac{dK}{dr} - \lambda^2\right)\right]R = 0\ , \tag{5.39}$$

where K is the same as in (5.29), but does not contain the particle charge q-term. This correctly reduces to the exact result for scalars and fermions when a background charge is present (if K contains the q-term in (5.29)) and it describes the electromagnetic or gravitational perturbations in four dimensions, approximately, for small Q, or exactly for $Q = 0$. Note also that the angular eigenvalue is determined by the angular equation (5.38) which is valid for $s = 0, 1/2, 1$ when $\mu = Q = 0$.

An important feature of electromagnetic and gravitational perturbations, compared to scalars and fermions, is that they are electrically neutral. No electric coupling means that qualitatively not much will change compared to the case of no background charge. Specially for small charges we see from (5.39) that the charge of the background only enters through the Q^2 term in Δ. This affects mostly the Hawking temperature which in the small Q limit will simply rescale the flux curves without much difference in shape. In fact we will see later on in chapter 6 (figure 6.4) that for scalars and fermions, the effect of a small background charge on neutral particles is indeed small on the transmission factors and the flux curves are simply rescaled by the different Hawking temperature in the thermal factor. So qualitatively nothing changes for neutral scalars and fermions which obey (5.39) and we would expect the same for higher spins.

Furthermore, if we assume electroweak symmetry is not restored outside the black hole and that the electrically charged weak vector boson W and the neutral Z provide a good effective description of the weak degrees of freedom, it is tempting to guess that (5.39) holds similarly for those perturbations (with K containing the electric q-coupling). This

is because the black hole background can only be electrically charged (or colour charged) so the background values of the weak field perturbations vanish. Then we would expect (5.39) to be exact since there is no reason for the weak field perturbations to couple to the linearized gravitational perturbations. This is in contrast with the equations for electromagnetic perturbations where terms linear in the gravitational perturbations arise from linearising bilinears in the gravitational/electromagnetic fields around their background values. For weak W and Z field perturbations (as for scalars and fermions) such gravitational terms can not be present because even if they exist before linearisation, when evaluated on the background for the W and Z fields they are identically zero.

Furthermore, because the W and Z fields are massive, they are described by a complex or a real Proca field respectively (see equation (5.27)), which is an extra complication.

Alternatively, if electroweak symmetry is restored in the region outside the black hole[3], then we have to use the fundamental weak gauge fields associated with the $SU(2)_L \times U(1)_Y$ sector of the Standard Model (instead of the electromagnetic, the W and the Z fields).

Due to these extra complications, the detailed study of massive charged vector perturbations will be left to future work and the charge of the background will be neglected for electromagnetic perturbations, since the former are neutral and the effect is negligible.

5.3.4 Decomposition of spheroidal waves into plane waves

For the purpose of developing the event generator in chapter 7 it will be important to know how to express the quantum states associated with the spheroidal waves used to expand the fields, in terms of plane waves. The latter are related to the natural basis of quantum states for an observer in flat spacetime who typically measures a track in a detector with a certain well defined 4-momentum. We work out in detail the result for a spin-1/2 field which is the first relatively non-trivial case (for a scalar field a simplified version of the reasoning is straightforward). Since the effect of particle mass is a small perturbation (which will be implemented in a future release of the generator) we restrict the argument to the massless limit.

It is well known (see for example [6]), that in the massless limit the Dirac field decomposes into two independent fields with helicities $h = \pm 1$. If we denote each of those

[3]This should be the case if the black hole size is smaller than the electroweak breaking scale which is typically $1/m_W$, the inverse mass of the W.

2-component spinors by Ψ_h, then their equations of motion in flat space become

$$(\partial_t + h\sigma \cdot \partial)\, \Psi_h = 0 \ , \tag{5.40}$$

where $\sigma = (\sigma^1, \sigma^2, \sigma^3)$ are the Pauli matrices. Then whichever spatial coordinates $\mathbf{x}$ we decide to use, the field operator will have the expansion (in terms of positive and negative energy solutions)

$$\hat{\Psi}_h = \sum_\lambda \frac{1}{\sqrt{2\omega_\lambda}} \left[\hat{a}_{h,\lambda} \psi_{h,\lambda}(\mathbf{x}) e^{-i\omega_\lambda t} + \hat{b}^\dagger_{h,\lambda} \psi_{-h,\lambda}(\mathbf{x}) e^{i\omega_\lambda t} \right] \ , \tag{5.41}$$

where $\hat{a}_{h,\lambda}, \hat{b}^\dagger_{h,\lambda}$ are respectively, the usual fermionic annihilation and creation operators for particles and anti-particles; λ is an unspecified complete set of quantum numbers; $\psi_{h,\lambda}$ are spinorial normal modes $(\omega + ih\sigma \cdot \partial)\, \psi_{h,\lambda} = 0$, normalised according to

$$\int \mathrm{d}^3\mathbf{x}\, \psi^\dagger_{h,\lambda} \psi_{h',\lambda'} = \delta_{h,h'} \delta(\lambda, \lambda') \ ; \tag{5.42}$$

δ is a Dirac delta function such that

$$\sum_{\lambda'} f(\lambda') \delta(\lambda, \lambda') = f(\lambda) \ ; \tag{5.43}$$

and the sum sign represents integration if the quantum numbers are continuous. Similarly to Klein-Gordon theory, it is possible to define a scalar product between 2-spinors ψ, χ using a bilateral derivative:

$$(\psi, \chi) = i \int d^3x \left(\psi^\dagger \partial_t \chi - \partial_t \psi^\dagger \chi \right) \quad . \tag{5.44}$$

Then we find an expression for the operators

$$\hat{a}_{h,\lambda} = \left(\psi_{h,\lambda} e^{-i\omega_\lambda t}, \hat{\Psi}_h \right) \tag{5.45}$$

$$\hat{b}^\dagger_{h,\lambda} = \left(\psi_{-h,\lambda} e^{i\omega_\lambda t}, \hat{\Psi}_h \right) \ . \tag{5.46}$$

Ψ_h can also be expanded in a basis of spinors with a different set of quantum numbers γ, which may be associated with a different choice of coordinates. The previous expressions

will then give a Bogoliubov transformation between operators in one basis and the other:

$$\hat{a}_{h,\lambda} = \sum_{\gamma} \frac{1}{\sqrt{2\omega_\gamma}} \left[\left(\psi_{h,\lambda} e^{-i\omega_\lambda t}, \psi_{h,\gamma} e^{-i\omega_\gamma t}\right) \hat{a}_{h,\gamma} + \left(\psi_{h,\lambda} e^{-i\omega_\lambda t}, \psi_{-h,\gamma} e^{i\omega_\gamma t}\right) \hat{b}^\dagger_{h,\gamma} \right] \quad (5.47)$$

$$\hat{b}^\dagger_{h,\lambda} = \sum_{\gamma} \frac{1}{\sqrt{2\omega_\gamma}} \left[\left(\psi_{-h,\lambda} e^{i\omega_\lambda t}, \psi_{h,\gamma} e^{-i\omega_\gamma t}\right) \hat{a}_{h,\gamma} + \left(\psi_{-h,\lambda} e^{i\omega_\lambda t}, \psi_{-h,\gamma} e^{i\omega_\gamma t}\right) \hat{b}^\dagger_{h,\gamma} \right] . \quad (5.48)$$

The second term of the first expansion, and the first term in the second one will be zero. This is because they are responsible for particle creation, which does not occur in this change of basis, given that we are in the same Lorentz frame in Minkowski space-time. This can be seen explicitly for our case of a transformation between plane wave states and spheroidal states. First note that in the Kinnersley basis the plane wave spinors take the form [129]

$$\chi^+_{\mathbf{p}} = \begin{pmatrix} e^{i\frac{\tilde{\phi}}{2}} \cos\frac{\theta_{\mathbf{p}}}{2} \cos\frac{\theta}{2} - e^{-i\frac{\tilde{\phi}}{2}} \sin\frac{\theta_{\mathbf{p}}}{2} \sin\frac{\theta}{2} \\ e^{i\frac{\tilde{\phi}}{2}} \cos\frac{\theta_{\mathbf{p}}}{2} \sin\frac{\theta}{2} + e^{-i\frac{\tilde{\phi}}{2}} \sin\frac{\theta_{\mathbf{p}}}{2} \cos\frac{\theta}{2} \end{pmatrix} , \quad (5.49)$$

$$\chi^-_{\mathbf{p}} = \begin{pmatrix} e^{i\frac{\tilde{\phi}}{2}} \cos\frac{\theta_{\mathbf{p}}}{2} \sin\frac{\theta}{2} + e^{-i\frac{\tilde{\phi}}{2}} \sin\frac{\theta_{\mathbf{p}}}{2} \cos\frac{\theta}{2} \\ e^{i\frac{\tilde{\phi}}{2}} \cos\frac{\theta_{\mathbf{p}}}{2} \cos\frac{\theta}{2} - e^{-i\frac{\tilde{\phi}}{2}} \sin\frac{\theta_{\mathbf{p}}}{2} \sin\frac{\theta}{2} \end{pmatrix} , \quad (5.50)$$

where $\Omega_{\mathbf{p}} = (\theta_{\mathbf{p}}, \phi_{\mathbf{p}})$ defines the orientation of the momentum vector $\mathbf{p}$, $\tilde{\phi} = \phi - \phi_{\mathbf{p}}$ and we have omitted the $e^{i\mathbf{p}\cdot\mathbf{x}}$ dependence. As long as we are looking at a fixed plane wave, ϕ can be shifted by choosing a new origin, which amounts to setting $\phi_{\mathbf{p}} = 0$. The upper/lower component of $\chi^\pm_{\mathbf{p}}$ has the interesting property of being invariant under the exchange $\theta_{\mathbf{p}} \leftrightarrow \theta$. Using the asymptotic form (3.7) for the Cartesian coordinates in terms of spheroidal coordinates we obtain

$$\mathbf{p}\cdot\mathbf{x} = \cos\theta_{\mathbf{p}} \cos\theta \sqrt{(ar)^2 + c^2} + ar \sin\theta_{\mathbf{p}} \sin\theta \cos\phi , \quad (5.51)$$

which is again symmetric under the exchange of θ's. On the other hand, the spheroidal spinors in the Kinnersley basis have the form [112]

$$\chi^\pm_\lambda = e^{im\phi} \begin{pmatrix} {}_-R^\pm_{j,m}(r) S_{-\frac{1}{2},j,m}(c, \cos\theta) \\ {}_+R^\pm_{j,m}(r) S_{\frac{1}{2},j,m}(c, \cos\theta) \end{pmatrix} . \quad (5.52)$$

We are seeking for a relation between plane waves and spheroidal waves. This can be

achieved by writing down the general decomposition

$$\chi^{\pm}_{\mathbf{p}} e^{i\mathbf{p}.\mathbf{x}} = \sum_{j,m} c_\lambda(\mathbf{p}) \chi^{\pm}_\lambda(\mathbf{x}) \ , \tag{5.53}$$

where now $\lambda = \{\omega, j, m\}$. But we know that the upper/lower component of the left hand side spinor with helicity $\pm$ is invariant under exchange of θ's, so the c_λ prefactor must be proportional to the upper/lower spheroidal function with argument $\theta_{\mathbf{p}}$. Furthermore we put back the $\phi_{\mathbf{p}}$ dependence by shifting ϕ to obtain

$$\chi^{h}_{\mathbf{p}} e^{i\mathbf{p}.\mathbf{x}} = \sum_{j,m} \tilde{c}_\lambda \cdot S^\star_{-h,j,m}(c, \Omega_{\mathbf{p}}) \chi^{h}_\lambda(\mathbf{x}) \ , \tag{5.54}$$

where the $\phi_{\mathbf{p}}$ dependence in $S^\star_{-h,j,m}(c, \Omega_{\mathbf{p}})$ is implicit. An integral relation is obtained when multiplying by an appropriate spinor, integrating over $\mathbf{x}$ and using the normalisation condition (5.42)

$$\int d^3\mathbf{x} \chi^{h'}_\lambda(\mathbf{x})^\dagger \chi^{h}_{\mathbf{p}} e^{i\mathbf{p}.\mathbf{x}} = \tilde{c}_\lambda \cdot S^\star_{-h,j,m}(c, \Omega_{\mathbf{p}}) \delta_{h,h'} \delta(\omega - \omega_{\mathbf{p}}) \ . \tag{5.55}$$

Finally, we can use this in the Bogoliubov transformations to obtain

$$\hat{a}^\dagger_{h,\lambda} \ \propto \ \int d\Omega_{\mathbf{p}} \cdot S_{-h,j,m}(c, \Omega_{\mathbf{p}}) \hat{a}^\dagger_{h,\mathbf{p}} \tag{5.56}$$

$$\hat{b}^\dagger_{h,\lambda} \ \propto \ \int d\Omega_{\mathbf{p}} \cdot S^\star_{h,j,m}(c, \Omega_{\mathbf{p}}) \hat{b}^\dagger_{h,\mathbf{p}} \ , \tag{5.57}$$

where the prefactor is independent of the angular variables. These expressions show how a state of a particle/anti-particle with helicity h decomposes into plane wave states with the same helicity and momentum orientations $\Omega_{\mathbf{p}}$. The probability of a certain orientation is given by the square modulus of the spheroidal function with spin weight $s = \mp h$.

Since massless scalar, spinor and vector perturbations all follow the same master equations, these conclusions apply similarly to the remaining cases.

Chapter 6

Analytic and numerical study of perturbations

In this chapter we perform a numerical study of the perturbations discussed in the previous chapter. We start by analysing the angular equations using a series expansion method, which was described in [4]. In sections 6.2, 6.3 and 6.4 we discuss in detail the methods used to solve the radial equations for massive charged scalar and fermion fields. We use first an approximate method which is valid for low energies [62, 130–132] and a WKB approximation in the high energy limit (they reduce in some limits to the results in [62,97, 130–132] which can be used as a check). The full numerical result is obtained in section 6.3 and a discussion of the effects of charge and mass is presented in section 6.4. This study was published in [1, 2]. Section 6.4.4 is a review of the known effects of rotation which will be useful to the implementation in the `CHARYBDIS2` event generator. In section 6.5 we make contact between the geometrical cross-sections from the analysis of geodesic motion and the high energy limit of wave propagation. We end the chapter with a summary of the main conclusions of the studies presented.

6.1 The angular equations

Before integrating the radial equations, the angular eigenvalues must be computed because they enter the radial potential. Furthermore to study angular distributions the angular functions are necessary, so we need to find the full solution. In general this must be done numerically.

The most important cases we are studying are massless brane degrees of freedom. For

massless particles up to spin-1 the spheroidal wave functions $S_k(c, x = \cos\theta)$, satisfy the differential equation

$$\left[\frac{d}{dx}\left((1-x^2)\frac{d}{dx}\right) + c^2x^2 - 2hcx - \frac{(m+hx)^2}{1-x^2} + \mathcal{A}_k(c) + h\right] S_k(c,x) = 0 \ , \qquad (6.1)$$

where $c = a\omega$ and $\mathcal{A}_k(c) = \lambda^2 - a^2\omega^2 + 2a\omega m - |h| - h$ is the angular eigenvalue and for notational convenience we have set[1] $s \to h$. Note however that this equation also works for massive scalar fields with $c = a\sqrt{\omega^2 - \mu^2}$. In the event generator presented in chapter 7, we will use the method of Leaver [133], so we present this in detail. In [133] the spheroidal wave functions for arbitrary spin are expanded as a series in $x = \cos\theta$ around $x = -1$. In that paper there is an extra parameter p which can take either sign. Alternatively, we can expand around $x = +1$. So in general, we can construct three more expansions. Even though all four of them converge uniformly in $x \in [-1, 1]$, the numerical errors behave differently if we consider a fixed region. Therefore it is useful to look at all the options and use different expansions for different regions. The only extra complication will be to match them in a common region. The possible expansions are

$$S_k^{s,p}(c,x) = e^{px}\,(1+x)^{\alpha}\,(1-x)^{\beta}\sum_{n=0}^{+\infty} b_n\,(1+sx)^n \qquad (6.2)$$

where α, β are chosen as to reproduce the correct behaviour around the regular singular points $x = \pm 1$,

$$\alpha = \left|\frac{m-h}{2}\right| \ , \quad \beta = \left|\frac{m+h}{2}\right| \ , \qquad (6.3)$$

and $s = \pm 1$ for expansions around $x = -1$ and $x = 1$ respectively. Substituting into (6.1) we obtain the recurrence relation (for $n > 0$),

$$b_n = \left(\frac{1}{2} + \frac{\epsilon_1}{n+\sigma} - \frac{\epsilon_2}{n(n+\sigma)}\right) b_{n-1} + \left(1 + \frac{\gamma}{n}\right)\frac{sp}{n+\sigma} b_{n-2} \qquad (6.4)$$

and the simplifying condition $p^2 = c^2 \Rightarrow p = \pm c$. We can set $b_{-1} = 0$ and choose the

[1] This is just because the s symbol is used in this section for another purpose.

normalisation $b_0 = 1$. The parameters above are given by the following expressions:

$$\begin{aligned}
\sigma &= \alpha(s+1) + \beta(1-s) \\
\epsilon_1 &= \frac{\alpha(1-s) + \beta(1+s) - 1 - 4sp}{2} \\
\epsilon_2 &= \frac{\mathcal{A}_k + h(h+1) + c^2 - (\alpha+\beta)(\alpha+\beta+1)}{2} + \alpha + \beta \\
&\quad + p\left[\alpha(s+1) + \beta(s-1) - s + sh\,\mathrm{sign}(p)\right] \\
\gamma &= \alpha + \beta - 1 + h\,\mathrm{sign}(p)\ .
\end{aligned} \tag{6.5}$$

For almost all values of $\mathcal{A}_k$, the ratio b_{n+1}/b_n in (6.4) goes to $1/2$ as $n \to \infty$. So as the order increases, the remainder will behave as (when $N \to \infty$)

$$\sum_{n=N}^{+\infty} b_n \left(1+sx\right)^n \to b_N \left(1+sx\right)^N \frac{2}{1-sx} \quad , \tag{6.6}$$

which diverges at $x = s$ and goes exponentially faster to zero as we move closer to $x = -s$. So if we do not tune to particular values of $\mathcal{A}_k$ this is how the numerical errors will behave. However, from the analytical point of view we still want to have an expansion which converges uniformly, which is not the case in general as suggested by (6.6). Therefore we need to know how the ratio b_{n+1}/b_n behaves for large n. Following [134] we determine this by assuming that for large n

$$\frac{b_{n+1}}{b_n} \sim \frac{b_n}{b_{n-1}} \sim k(n) + \ldots \tag{6.7}$$

where $\ldots$ denotes sub-leading contributions. Inserting this in (6.4) and solving for k we get two possible behaviours

$$k(n) \sim \begin{cases} \frac{1}{2} + \frac{2sp}{n} \\ -\frac{2sp}{n} \end{cases} \to \begin{cases} \frac{1}{2} \\ 0 \end{cases} \ . \tag{6.8}$$

It is straightforward to check that uniform convergence for $x \in [-1, 1]$ is only achieved in the second case. A solution with these convergence properties is called a minimal sequence solution [133]. Furthermore, there is a theorem (see Theorem 1.1 of [135] and the reasoning in [134]) which ensures that the sequence obtained from the eigenvalue problem in (6.4) with the initial conditions given above is a minimal sequence. Therefore,

after determining the eigenvalue we can compute the solution (up to a normalisation) by fixing $b_0 = 1$.

However, from the numerical point of view, a small error in the eigenvalues implies that b_{n+1}/b_n will fail to go to zero when numerically evaluated through (6.4). So the remainder will actually behave as (6.6) since in practice we are approximating the eigenfunction by a nearby function, for which the sequence of expansion coefficients behaves as a dominant solution of (6.4) when n is large[2]. Thus the numerical radius of convergence will be a bit smaller and the expansion will fail at $x = s$.

We avoid the above convergence problem by using two expansions, one around each singular point $x = \pm 1$, and then matching the normalisation in a region where both converge appropriately. A simple procedure for matching follows from the observation that

$$\begin{aligned} S_+ &= AS_- \\ \Rightarrow \log|A| &= \log|S_+| - \log|S_-| \quad , \end{aligned} \tag{6.9}$$

where A is a constant and $S_\pm$ denotes expansion around $x = \pm 1$ respectively. We can find $|A|$ by averaging the quantity on the right-hand side over an overlap region. Furthermore we can estimate the relative matching error through the quadratic deviation,

$$\begin{aligned} \frac{\Delta|A|}{|A|} &= \Delta \log|A| \\ &\sim \sqrt{\left\langle \log^2|A| \right\rangle - \left\langle \log|A| \right\rangle^2} \end{aligned} \tag{6.10}$$

where $\langle \ldots \rangle$ denotes average over the points used. In practice we use points in the overlap region $x \in [-0.25, 0.25]$.

For the expansions above to be useful we need to estimate an order of truncation, n_{trunc}. A simple condition is that the ratio of consecutive terms b_{n+1}/b_n is approximately constant above the order of truncation. This is equivalent (in the region $sx < 0$ where there is strong convergence) to an exponentially suppressed upper bound on the remainder when n_{trunc} is large (see (6.6)). From this and (6.4)

$$n_{\text{trunc}} \sim \max\{[j + |h| + 4c], [\sqrt{|\mathcal{A}_k| + |h|(|h|+1) + (c + |m| + 2|h| + 3)^2}]\} \; . \tag{6.11}$$

[2]See for example [135] for a discussion of numerical issues when generating minimal sequences which are solutions of three-term recursion relations.

An initial estimate of the truncation error is obtained from (6.6). Another criterion for truncation is that the first neglected higher order term is small compared to the truncated sum.

In practice, after the spheroidal function is calculated with a certain truncation, then ten more terms in the series are included and the two estimates are compared. Simultaneously, the first neglected term is compared with the estimate for the sum. If these errors are still large then ten more terms are calculated. This procedure is repeated until the desired accuracy is obtained.

To compute the eigenvalues $\mathcal{A}_k$ efficiently, the recurrence relation can be put in a symmetric tridiagonal form by performing a change of basis,

$$a_n = x_n b_n \tag{6.12}$$

such that the coefficient of the b_{n-2} term for a certain order n is the same as the coefficient of the b_{n-1} term at order $n-1$. This is possible if

$$x_n = \sqrt{\frac{n(n+\sigma)}{-sp(n+1+\gamma)}}x_{n-1} = \sqrt{\frac{n(n+\sigma)}{c(n+1+\gamma)}}x_{n-1} \quad , \tag{6.13}$$

were we have taken (without loss of generality) $x_0 = 1$ and the convenient choice $p = -sc$. Furthermore we checked that $x_n \neq 0 \ \forall n \geq 1$, so the transformation is well defined. Thus the recurrence relation takes the form

$$\sqrt{cn(n+\sigma)(n+1+\gamma)}a_n - n\left(\frac{n+\sigma}{2}+\epsilon_1\right)a_{n-1} + \sqrt{c(n-1)(n-1+\sigma)(n+\gamma)}a_{n-2} = -\epsilon_2 a_{n-1}. \tag{6.14}$$

This is a tridiagonal symmetric eigenvalue problem which can be solved numerically very efficiently, by starting with a truncation order (as estimated above) and checking for precision by repeating the calculation with some more corrections.

Various other methods exist in the literature to integrate the angular equation (6.1) and obtain the angular eigenvalue. A particularly useful check of the numerical expansions developed above that was used, were the series expansions of the angular eigenvalue provided in [117]. In addition, the spheroidal functions were checked numerically against a publicly available code for scalars [136]. For higher spins, several properties of the spheroidal functions as well as some special cases were checked against the results in [117].

6.2 The radial equations I: Analytic methods

In this section we present analytic approximations to solve the radial equations and compute transmission factors. These solutions are interesting because they provide the main qualitative features in a good part of the interesting range of parameters where they are valid. Furthermore, they can be used as a check of the results obtained numerically and provide simple analytic expressions which can be quickly evaluated. We are going to focus mostly on a low energy approximation, but we also present a high energy approximation. The low energy approximation has been shown, in earlier studies, to give good results even in the intermediate energy regime for spins up to one [130] so it will provide a good overall qualitative picture of how the transmission factors behave in the full range.

We present the main steps of the calculation using the method in [130] adapted to our problem. It consists of writing down approximations for the radial equation in two regions: one near the horizon (Near Horizon solution) and the other one far from it (Far Field solution). This provides two analytic approximations which hold exactly close to the horizon and far from it respectively. The final step is to extrapolate them into a common intermediate region to be matched. Below we summarize the solutions and keep track of the conditions of validity. Since the new cases we are studying are for non-zero electric charge and particle mass for spins $s = 0, 1/2$ we present the details for these fields only (though the procedure is similar for other spins).

6.2.1 Near horizon equation

Equations (5.37) and (5.38) are valid for both spin-zero and spin-half fields. The analytic approximations we use are valid for the massive charged scalar field, but however it turns out they only work for the massless limit of charged fermions. Therefore we work with the radial equation (5.37) but set $\mu = 0$ for fermions. Following [130] close to the horizon

define the quantities

$$\begin{aligned}
f &\equiv \frac{\Delta}{r^2+a^2+Q^2} \\
A &\equiv n+1+(n-1)\frac{a^2+Q^2}{r^2} \simeq A|_{r=1} \equiv A_* \\
B &\equiv 1-|s|+\frac{2|s|+n(r^2+a^2+Q^2)}{r^2 A}-\frac{4(a^2+Q^2)}{r^2A^2} \simeq B|_{r=1} \equiv B_* \\
P &\equiv \frac{K^2}{r^2A^2} \simeq \frac{\omega(1+a^2)-am-qQ}{A_*} \equiv p \\
D &\equiv \frac{r^2+a^2+Q^2}{r^2A^2}\left[\lambda^2+\mu^2r^2\delta_{s,0}+2isqQ-4is\omega r\right] \simeq D|_{r=1} \equiv D_* \,. \qquad (6.15)
\end{aligned}$$

Then equation (5.37) is equivalent to

$$f(1-f)\frac{d^2R}{df^2}+(1-Bf)\frac{dR}{df}+\left[\frac{P^2-isP}{f}+\frac{P^2-isP-D}{1-f}\right]R=0\,, \qquad (6.16)$$

and the approximations on the right hand side of each line of (6.15) can be used. The approximations require the condition $r-1 \ll 1$. Equation (6.16) can be solved in terms of hypergeometric functions. The general solution is a combination of two linearly independent hypergeometric functions. The wave must be purely ingoing at the horizon. This implies $R \sim e^{-ipr_*}$ with r_* the tortoise coordinate defined by $dr_* = dr/f$ (up to a constant). Then, it can be shown that the convergent solution with this boundary condition is [137]

$$R_{NH} = f^\alpha(1-f)^\beta F(a,b,c;f)\,, \qquad (6.17)$$

where

$$\begin{aligned}
\alpha &= \frac{|s|-s}{2}-ip \\
\beta &= 1-\frac{|s|+B_*}{2}-\sqrt{\left(1-\frac{|s|+B_*}{2}\right)^2-p^2+isp+D_*} \\
a &= \alpha+\beta-1+B_* \\
b &= \alpha+\beta \\
c &= 1-|s|+2\alpha\,. \qquad (6.18)
\end{aligned}$$

In the next section an extrapolation of this solution away from the horizon will be needed, i.e. around $f \to 1 \Rightarrow 1-f \simeq (1+a^2+Q^2)/r^{n+1}$. Note that the larger the value of n,

the more consistent this condition is with $r-1 \ll 1$ so the terms neglected in approximations (6.15) become less important[3]. Using some identities that relate hypergeometric functions with argument f to argument $1-f$ and expanding around $f=1$ we obtain [137] (up to an overall normalisation constant)

$$R \to A_1 r^{-(n+1)\beta} + A_2 r^{-(n+1)(2-\beta-B_*)} \,, \tag{6.19}$$

with

$$\begin{aligned} A_1 &= \frac{(1+a^2+Q^2)^{\beta}\Gamma(c-a-b)}{\Gamma(c-a)\Gamma(c-b)} \\ A_2 &= \frac{(1+a^2+Q^2)^{2-|s|-\beta-B_*}\Gamma(a+b-c)}{\Gamma(a)\Gamma(b)} \,. \end{aligned} \tag{6.20}$$

When matching powers of r in the next section we will have to make the approximations $\omega, a, Q, \mu \ll 1$. Then

$$\begin{aligned} -(n+1)\beta &\simeq -\frac{1}{2} + \sqrt{\frac{1}{4}+\lambda^2} \\ -(n+1)(2-\beta-B_*) &\simeq -\frac{1}{2} - \sqrt{\frac{1}{4}+\lambda^2} \,. \end{aligned} \tag{6.21}$$

For $a \ll 1$ the neglected terms are of order ω^2 or μ^2. So taking into account the leading behaviour of λ^2 when $s=|s|$ the approximation is equivalent to

$$\omega, \mu \ll \sqrt{j(j+1)+2|s|} \,. \tag{6.22}$$

So the larger the ℓ and $|s|$ the wider the energy range where the approximations work.

6.2.2 Far field solution and low energy matching

Away from the black hole $r \to +\infty$ we approximate $\Delta \simeq r^2$ and

$$\frac{K}{\Delta} \simeq \omega - \frac{qQ}{r} + \frac{\omega(1+a^2+Q^2)}{r}\delta_{n,0} \,. \tag{6.23}$$

Equation (6.23) contains: the energy; a long range electric potential, and a long range gravitational potential in four dimensions. Keeping terms up to order $1/r^2$ in equa-

[3]This improvement of the approximation for large n has been noted in [130].

tion (5.28)

$$\frac{d^2R}{dy^2} + \frac{2}{y}\frac{dR}{dy} + \left[1 + \frac{\epsilon}{y} - \frac{\gamma}{y^2}\right] R = 0 \tag{6.24}$$

with

$$\begin{aligned} y &= kr \\ k^2 &= \omega^2 - \mu^2\delta_{s,0} \\ \epsilon &= \frac{2is\omega - 2\omega qQ + (2\omega^2 - \mu^2)\,(1 + a^2 + Q^2)\delta_{n,0}}{k} \\ \gamma &= \lambda^2 - q^2Q^2 - \omega(1 + a^2 + Q^2)\left[2qQ - \omega(1 + a^2 + Q^2) + 2is\right]\delta_{n,0}\,. \end{aligned} \tag{6.25}$$

Note again that we are not studying the massive case for fermions. The $\delta_{s,0}$ factor in k is emphasizing this – it does not mean the μ^2 term is absent for $s = 1/2$. The general solution of equation (6.24) is given in terms of Kummer functions [137]

$$R_{FF} = e^{-iy}y^{\sigma}\left[B_1 M(u, v, 2iy) + B_2 U(u, v, 2iy)\right]\,, \tag{6.26}$$

where

$$\begin{aligned} \sigma &= |s| - \frac{1}{2} + \sqrt{\left(|s| - \frac{1}{2}\right)^2 + \gamma} \\ u &= \sigma + 1 - |s| + i\frac{\epsilon}{2} \\ v &= 2(\sigma + 1 - |s|)\,. \end{aligned} \tag{6.27}$$

Equation (6.26) can be matched to the near horizon solution in the limit $y \ll 1$. This conditions implies $r \ll 1/k$, so for consistency with the limit $r \gg 1$ we need k small. Using the asymptotic expansion for the Kummer functions, the stretched solution is [137]

$$R_{FF} \to k^{\sigma}\left(B_1 r^{\sigma} + B_2\frac{\Gamma(v-1)}{\Gamma(u)}(2ik)^{1-v}r^{\sigma+1-v}\right)\,. \tag{6.28}$$

It can be easily shown that within the same approximations as in equation (6.21) the r-powers match with those in equation (6.28). Then, up to an overall common constant

$$\begin{aligned} B_1 &= A_1 \\ B_2 &= A_2\frac{\Gamma(u)(2ik)^{v-1}}{\Gamma(v-1)}\,. \end{aligned} \tag{6.29}$$

Finally we expand in the far field limit $y \to +\infty$ to obtain (up to an overall common constant)

$$R_{FF} \to Y_s^{(in)} \frac{e^{-ikr}}{r^{1-|s|-s-i\varphi}} + Y_s^{(out)} \frac{e^{ikr}}{r^{1-|s|+s+i\varphi}} \ , \tag{6.30}$$

where

$$\varphi = \frac{\omega q Q}{k} - \frac{\left(\omega^2 - \frac{\mu^2}{2}\right)(1+a^2+Q^2)}{k}\delta_{n,0} \ , \tag{6.31}$$

and

$$\begin{aligned} Y_s^{(in)} &= (2ik)^{-u}\left(\frac{B_1\Gamma(v)e^{i\pi u}}{\Gamma(v-u)} + B_2\right) \\ Y_s^{(out)} &= (2ik)^{u-v}\frac{B_1\Gamma(v)}{\Gamma(u)} \ . \end{aligned} \tag{6.32}$$

Equation (6.30) contains a combination of incoming and outgoing waves. However for the spin-half case the incoming/outgoing wave is dominant for $s = \pm 1/2$ respectively. Using the conserved number current it is possible to show [130] that the transmission factor is

$$\mathbb{T}^{(4+n)}_{s,j,m} = 1 - \left|\frac{Y^{(out)}_{-|s|}}{Y^{(in)}_{|s|}}\right|^2 \ . \tag{6.33}$$

For fermions, to find out the relative normalisation between $P_{1/2}$ and $P_{-1/2}$ we insert back the expansion (6.30) in the first order system (5.35), equate order by order and obtain the relation

$$Y^{(out)}_{-1/2} = \frac{2i\omega}{\lambda} Y^{(out)}_{1/2} \ . \tag{6.34}$$

Since the relative normalisation between incoming and outgoing coefficients for the same s is fixed, now we can insert equation (6.34) in (6.33) to obtain the transmission factor. For scalars, equation (6.33) is also valid if we set $|s| = 0$.

6.2.3 High energy approximation based on WKB arguments

To complete the analytic picture, we present some arguments for a useful approximation in the high energy limit for scalars. This will give the leading asymptotic form for the transmission factors.

The matching procedure in the previous section doesn't work in the high energy limit for two reasons. On one hand the powers in (6.19) and (6.28) no longer match at high

energy, rotation, charges and masses. Secondly we are stretching the near horizon solution into $r \gg 1$ and the far field solution into $r \ll 1/k$. If k is large, then these conditions are incompatible and we are effectively stretching the far field solution too close to the horizon.

To understand this problem we look into the WKB approximation for the scalar radial equation[4]. Some earlier works which have used the WKB approximation to compute transmission factors are [138–142]. First note that the radial equation can be written in a Schrödinger-like form through a change of independent variable. Start by choosing

$$dy = \frac{dr}{\Delta} \,, \tag{6.35}$$

to obtain

$$\left(\frac{d^2}{dy^2} - V\right) R = 0 \,, \tag{6.36}$$

where $V \equiv \Delta U - K^2$ contains a leading term $-k^2 r^4$ corresponding to the highest power of r (all the other terms are suppressed). In the high energy limit, this term dominates the solution. In fact, we can formally write an infinite WKB series [143]

$$R \sim A_+ \exp\left(k \sum_{n=0}^{\infty} \frac{S_n^+(y(r))}{k^n}\right) + A_- \exp\left(k \sum_{n=0}^{\infty} \frac{S_n^-(y(r))}{k^n}\right). \tag{6.37}$$

It is easy to check [143] that the leading correction reproduces the asymptotic form at infinity consistent with (6.30). A necessary condition for the approximation to be valid is

$$\left|\frac{dV}{dy}\right| \ll \left|V^{\frac{3}{2}}\right| \Leftrightarrow \left|\frac{dV}{dr}\Delta\right| \ll \left|V^{\frac{3}{2}}\right| \,, \tag{6.38}$$

which (to leading order in r) is just $r \gg 1/k$. This condition indicates that for large k the field will start to take a WKB form not far from the horizon. Such a result is not surprising if we note that these modes have very short wavelength, so the potential is almost constant along many wavelengths (except very close to the horizon). Furthermore,

[4]Here we focus on the scalar case because the potential is real. A similar treatment can be applied to fermions using the method in Chandrasekhar's book [122] to reduce the complex potential to a real one. However note that we would expect the spin of the particle to become irrelevant at high energies as we reach the geometrical optics limit.

the WKB corrections obey

$$S_n^+ = \begin{cases} -S_n^- & , n \text{ even} \\ S_n^- & , n \text{ odd} \end{cases} \tag{6.39}$$

so the odd terms (which are purely real [143]) only contribute with an overall common factor. As for the even terms, they are products of $\sqrt{V}$ times polynomial terms in V. In general there is an imaginary and a real part for each even order correction, but since our potential is real then it will either be real or imaginary. If $\sqrt{V}$ is imaginary, the relative amplitude between incoming and outgoing waves does not depend on r. But in the limit of k large, the dominant term in the potential is $-k^2r^4$ which is negative, so the square root is purely imaginary and the even order corrections only introduce a phase difference between incoming and outgoing waves. This means that in the region where the WKB solution is valid[5], the relative amplitude between incoming and outgoing modes stays fixed. The transmission coefficient can then be calculated at any point in such a region provided we have a suitable analytic expansion in terms of incoming and outgoing waves. Thus, in the high energy limit, the propagation of the field along a thin region outside the horizon determines the behaviour of the transmission factors.

This behaviour can be seen explicitly in (6.19). There the scalar r-powers have a common factor $r^{-(n+1)(1-B_*/2)}$ multiplied by

$$r^{\pm\sqrt{(1-B_*)^2/4-p^2+D_*}} . \tag{6.40}$$

In the high energy limit the argument of the square root in (6.40) becomes negative and we obtain a relative phase between the two modes which are respectively outgoing and incoming. The transmission coefficient follows under the single approximation $k \gg 1$

$$\mathbb{T}^{4+n}_{0,j,m} = 1 - \left|\frac{A_+}{A_-}\right|^2 = 1 - \left|\frac{A_1}{A_2}\right|^2 . \tag{6.41}$$

6.3 The radial equations II: Numerical methods

To obtain the transmission factor in the full range of parameters a numerical approach must be taken. In this section we complete the study of the scalar and fermion fields with mass and charge by developing the numerical method to solve the radial equations.

Starting with scalars, equation (5.28) can be written as a first order system of differen-

[5]This is the region connected to infinity such that $V < 0$.

tial equations. This is useful to perform the numerical integration using a similar method as for fermions. Since there isn't a unique way of reducing the second order equation to a first order system, we take advantage of the extra freedom to construct a spinor-like object with a conserved Wronskian and, simultaneously, an asymptotic behaviour at infinity which gives the transmission factor straightforwardly. It is then possible to show that a convenient choice is

$$P_{\pm 0} = \frac{\Delta^{\frac{1}{2}}}{2}\left(kR \mp i\frac{dR}{dr}\right) \ . \tag{6.42}$$

So the second order equation (5.28) is replaced by the first order coupled system[6]

$$\frac{d\mathbf{P}_s}{dr} = \mathbf{M}_s(r)\mathbf{P}_s \tag{6.43}$$

where

$$\mathbf{M}_0(r) \ = \ \frac{\Delta'}{2\Delta}\hat{\sigma}_1 - \frac{1}{2}\left(\frac{V}{k} - k\right)\hat{\sigma}_2 + \frac{i}{2}\left(\frac{V}{k} + k\right)\hat{\sigma}_3 \ , \tag{6.44}$$

$$V = \frac{K^2}{\Delta^2} - \frac{U}{\Delta} \ , \tag{6.45}$$

and $\hat{\sigma}_i$ are the Pauli matrices. Now, using (6.43), conservation of the Wronskian is easily checked:

$$\frac{d}{dr}\left(\mathbf{P}_s^\dagger \hat{\sigma}_3 \mathbf{P}_s\right) = \frac{d}{dr}\left(|P_{+|s|}|^2 - |P_{-|s|}|^2\right) = 0 \ . \tag{6.46}$$

We have chosen $k = \sqrt{\omega^2 - \mu^2}$ so that $P_{\pm 0}$ picks respectively the outgoing/incoming part of the wave at infinity (see section 6.3.2). For fermions, the radial equation (5.35) is already in the form (6.43) with

$$\mathbf{M}_{\frac{1}{2}}(r) \ = \ \frac{\lambda}{\Delta^{\frac{1}{2}}}\hat{\sigma}_1 - \frac{\mu r}{\Delta^{\frac{1}{2}}}\hat{\sigma}_2 + i\frac{K}{\Delta}\hat{\sigma}_3 \ . \tag{6.47}$$

So $\mathbf{P}_{1/2}$ obeys the same Wronskian relation (6.46) as (6.43). Again, the incoming solution at the horizon takes the form

$$\mathbf{P}_{\frac{1}{2}} \sim x^{-i\frac{K_\star}{\delta_0}}\left(\mathbf{a}_0 + \dots\right) \tag{6.48}$$

with $\mathbf{a}_0$ a constant spinor.

In the next sections we present the methods used to reduce the linear systems of

[6]Here s is the spin which we leave arbitrary since the same type of equation will hold for fermions.

equations at hand to initial value problems which are more convenient for numerical integration.

6.3.1 Near horizon expansions

The boundary condition at the horizon is most easily implemented through a series expansion. This allows for a high precision initialisation of the radial functions slightly away from the horizon to avoid numerical difficulties associated with the coordinate singularity. The expansions we need are

$$\begin{aligned} R &= x^{\alpha}\sum_{m=0}^{+\infty}\alpha_m x^m \\ \mathbf{P}_{\frac{1}{2}} &= x^{\alpha}\sum_{m=0}^{+\infty}\mathbf{a}_m\left(\sqrt{x}\right)^m \ . \end{aligned} \tag{6.49}$$

Note that R can be used to initialise $\mathbf{P}_0$. By inserting into the wave equations (5.28) and (6.43) respectively we obtain the following recurrence relations

$$\left\{\begin{array}{lcl} \alpha &=& -i\dfrac{K_\star}{\delta_0} \\ \alpha_0 &=& 1,\ \ \alpha_m = \dfrac{-1}{m(m+2\alpha)\delta_0^2}\left[(m+\alpha)\delta_0\bar{\gamma}_m + \displaystyle\sum_{k=0}^{m-1}\left(\gamma_k(k+\alpha)\delta_{m-k} + \alpha_k\sigma_{m-k}\right)\right] \\ \mathbf{a}_0 &=& \begin{pmatrix} 0 \\ 1 \end{pmatrix}, \quad \mathbf{a}_m = (\mathbf{N}_0 - \delta_0(m+2\alpha))^{-1}\left[\mathbf{b}_m - \displaystyle\sum_{j=0}^{m-1}\mathbf{N}_{m-j}\mathbf{a}_j\right] \qquad m \geq 1 \ . \end{array}\right. \tag{6.50}$$

where a choice of normalisation was made, when setting α_0 and $\mathbf{a}_0$. The various coefficients are defined in appendices C.1.1 and C.1.2. Using expansions (6.49) we have initialised $\mathbf{P}_s$ at $x = 0.1$ by truncating the series at eighteenth order. A first estimate of the numerical error can be made by modifying this choice (we have used $x = 0.05$ and $x = 0.01$ as a check).

6.3.2 Far field expansions

Once the radial function is initialised, numerical integration routines can be used to propagate the solution away from the horizon according to (6.43). When sufficiently away

from the horizon, the transmission factor can be evaluated by comparing the numerically propagated solution with its asymptotic form at large r. An asymptotic expansion can be found in the form

$$\mathbf{P}_s = e^{qr} r^{-\gamma} \sum_{m=0}^{+\infty} \mathbf{q}_m^s r^{-m} \ , \tag{6.51}$$

if we expand

$$\mathbf{M}_s = \sum_{m=0}^{+\infty} \mathbf{M}_m^s r^{-m} \tag{6.52}$$

and equate (6.43) order by order. The leading behaviour is

$$\mathbf{P}_s = Y_s^{(out)} e^{iy} y^{i\varphi} \mathbf{d}_s^+ + Y_s^{(in)} e^{-iy} y^{-i\varphi} \mathbf{d}_s^- \ , \tag{6.53}$$

where $y = kr$, $Y_s^{(out)}$ and $Y_s^{(in)}$ are arbitrary constants,

$$\varphi = \epsilon \frac{\omega}{k} - \sigma \frac{\mu}{k} \ , \tag{6.54}$$

$$\epsilon = -qQ + \omega(1 + a^2 + Q^2)\delta_{n,0} \qquad \sigma = \frac{\mu}{2}(1 + a^2 + Q^2)\delta_{n,0} \ , \tag{6.55}$$

and

$$\mathbf{d}_0^+ = \begin{pmatrix} 1 \\ 0 \end{pmatrix} \qquad \mathbf{d}_0^- = \begin{pmatrix} 0 \\ 1 \end{pmatrix} \qquad \mathbf{d}_{\frac{1}{2}}^+ = \begin{pmatrix} 1 \\ -\frac{\mu}{\omega+k} \end{pmatrix} \qquad \mathbf{d}_{\frac{1}{2}}^+ = \begin{pmatrix} -\frac{\mu}{\omega+k} \\ 1 \end{pmatrix} \ . \tag{6.56}$$

We can now factor out the dependence at infinity so that the leading asymptotic form for the upper(lower) component of the spinor becomes $Y_s^{(out)}(Y_s^{(in)})$ respectively. This is achieved by performing a rotation on the spinor $\mathbf{P}_s$ such that it eliminates a fixed number of sub-leading terms in the asymptotic expansion (6.52) (in practise we have eliminated the first two sub-leading terms). Then the new spinor $\mathbf{Q}_s$ is related to $\mathbf{P}_s$ through $\mathbf{Q}_s = \mathbf{R}_s \mathbf{P}_s$ and the the system to integrate becomes

$$\frac{d\mathbf{Q}_s}{dy} = \mathbf{A}_s \mathbf{Q}_s \ . \tag{6.57}$$

The explicit forms for $\mathbf{A}_s$ and $\mathbf{R}_s$ are given in appendix C.2.

Finally, the transmission factor is computed from the definition by taking the limit

$$\mathbb{T}_s = \lim_{r\to+\infty}\left(1-\left|\frac{Q_{+s}}{Q_{-s}}\right|^2\right) = 1-\left|\frac{Y_s^{(out)}}{Y_s^{(in)}}\right|^2 \tag{6.58}$$

($\pm s$ for upper/lower component respectively) and an estimate of the error is obtained by varying the large r used in the limit. Furthermore, with the normalisation chosen in (6.50) we can evaluate the Wronskian (6.46) at the horizon and use its conservation to obtain a second expression

$$\mathbb{T}_s = \lim_{r\to+\infty}\frac{kW_s}{|Q_{-s}|^2} = \frac{kW_s}{|Y_s^{(in)}|^2}\,, \tag{6.59}$$

where

$$W_0 = K_\star \qquad W_{\frac{1}{2}} = \frac{\omega+k}{2}\,. \tag{6.60}$$

By comparing the results from (6.58) and (6.59), we obtain another estimate of the numerical errors. Equation (6.59) is particularly useful since it contains explicitly the zeros of the transmission factor in the numerator.

To integrate (6.57), a code was written in C++ using the Gnu Standard Library (GSL) numerical integration routines. This was checked against an independent code in Maple11.

6.4 Numerical results

In this section we plot various quantities, using the approximations developed in section 6.2 and the numerical method of section 6.3. The physically most relevant are those in (5.12), (5.13), (5.14) and (5.15). When integrated over ω and summed over particle type they give the rates of emission of particle number, energy, angular momentum and charge. Nevertheless we still plot the transmission factors to keep track of where the new effects enter. Most of the samples obtained with the numerical method for the study of mass and charge effects in spin $1, 1/2$ fields, were generated up to[7] $\omega = 10$, but some up to $\omega = 5$ to save computing time. We show plots with $\omega < 5$ since the curves are very quickly stabilised for large ω (either to a constant or a suppressed tail). Except for sections 6.4.4 and 6.4.5, we focus on $a = 0$.

[7]Note we are using horizon radius units $r_H = 1$. Sometimes we emphasize the r_H dependence by explicitly re-introducing r_H.

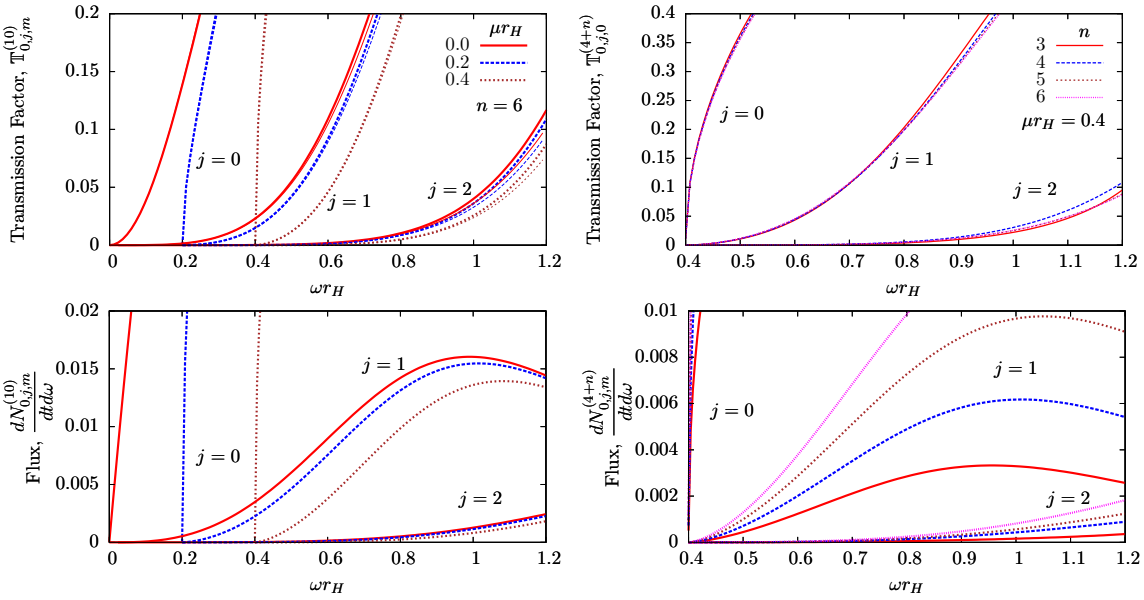

Figure 6.1: *Scalar transmission factors and fluxes for $n = 6$ (left) and variable n (right) using the analytic approximation.* The left plots show variation with particle mass μ in natural units r_H^{-1} for $n = 6$ and the right plots show variation with n for μ fixed. The top plots show the transmission factors $\mathbb{T}^{(4+n)}_k$ and the bottom plots show number fluxes, for a range of j modes. The curves are naturally grouped by j, rotation is off and the line colour/type is the same for top and bottom plots. In the top left plot we have indicated the exact numerical result in thinner lines.

The plots for the review of the effects of rotation (section 6.4.4) were produced using the data files in [144] and spheroidal functions computed with the method in section 6.1.

6.4.1 The effect of particle mass

The effect of particle mass is important if the energy of the particle emitted during the evaporation is comparable to its mass. For Standard Model heavy particles, such as the top quark ($m_t \sim 170$ GeV) the Z ($m_Z \sim 91$ GeV), the W ($m_W \sim 80$ GeV) and the Higgs boson, the effect will not be negligible in TeV gravity scenarios. This is because their masses are of the same order of magnitude as the typical energy scale of a Hawking emission ($\omega \sim 1/r_H$). Typical values of μ for these heavy particles in TeV gravity scenarios (relevant for the LHC), range from 0.1 to 0.5.

In figure 6.1 we present some representative curves for the transmission factor and the number flux in the low energy limit using the analytic approximation. As mentioned before the approximation becomes better with larger n so most of our plots will be for

$n = 6$, except for when we focus on the n dependence where we use $n \geq 3$.

The most prominent property of the left-hand-side plots is a smooth drop close to the mass μ. The higher the partial wave the less steep this is but there is always a horizontal shift (see for example the $j = 1$ mode). This effect is quite important close to the mass threshold where the probability of emission is suppressed. This is in contrast with the simplified approach for the evaporation in current black hole event generators where the spectrum is cut off sharply at $\omega = \mu$. Note that in the top left plot we have included the exact result obtained with the numerical method using thinner lines. At low energies the curves are indistinguishable, and at intermediate energies they are qualitatively concordant. We have checked that this observation holds for the remaining plots presented below, however we will not include further direct comparisons between the analytic approximation and the exact numerical method.

Furthermore, for example the number flux for the $j = 1$ mode shows how increasing the mass of the particle not only suppresses the flux around $\omega \sim \mu$ but also the total area under the curve. Massive particles are therefore less likely to be produced. This effect was previously studied in four dimensions, for example numerically, in Page's paper for leptons [114].

The right hand side plots show how the transmission factor is very mildly dependent on n (at least in the limit of small μ). However the flux plot displays a strong variation with n which is due to the strong dependence of the Hawking temperature appearing in the thermal factor.

In figures 6.2 and 6.3 we confirm the scalar analytic results in the full energy range and extend them to fermions with the exact numerical method. The top plots of figure 6.2 are for $n = 2$ and a range of masses, whereas for the bottom plots we fix μ and vary n. We use a range $\omega \in [0, 2]$ because the transmission factors asymptote to one quickly, so this is the interesting region.

The top plots show the first three partial waves for scalars and fermions, $\mu = 0$, 0.5 and 1. For scalars we confirm the strong suppression at the mass threshold for the $j = 0$ partial waves, and the shift and suppression for higher partial waves. For fermions the behaviour is similar, except that the first partial waves are not so sharply suppressed at threshold.

The bottom plots show the variation with n for fixed $\mu = 0.5$. At higher energies we see a strong n dependence compared to the low energy mild dependence of the scalar transmission factors in the range $n = 3, \ldots, 6$ (figure 6.1). The general tendency is for

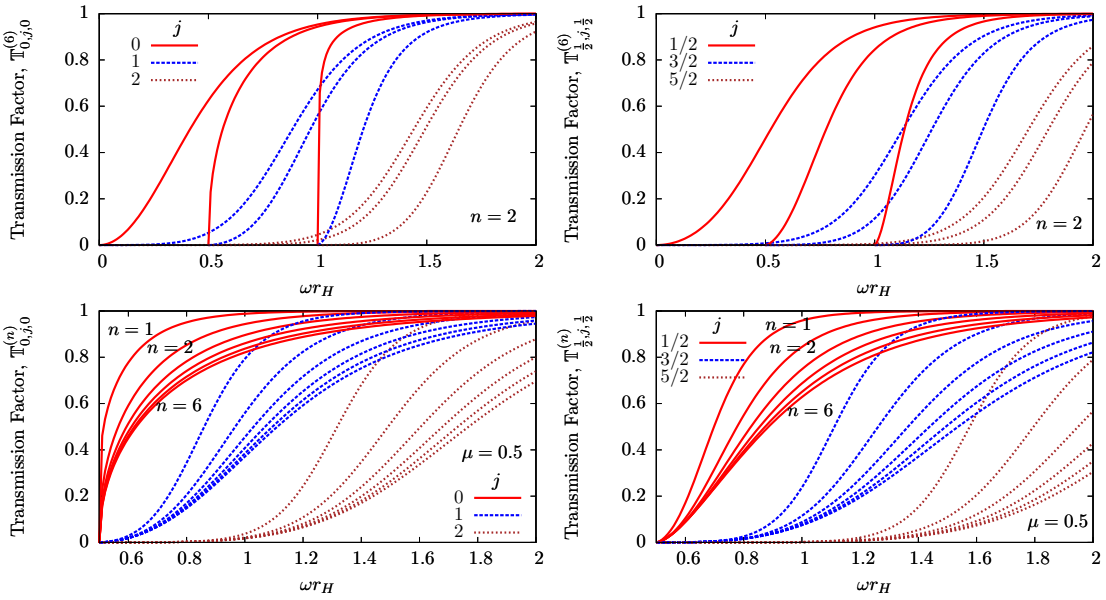

Figure 6.2: *Scalar (left) and fermion (right) transmission factors for $n = 2$ (top) and variable n (bottom) using the numerical method*: The plots show the first three partial waves (note that $a = 0$, so waves with different m for the same j are degenerate). The top plots contain three masses $\mu r_H = 0, 0.5, 1$ corresponding to the points where each curve starts.

the transmission factor to be suppressed at intermediate energies with n, but note that the larger the n the smaller is the separation between curves of different n.

In figure 6.3 we present examples of the number flux for non-zero mass, when the charge and the rotation are set to zero. The top plots show $n = 4$ and $\mu = 0.5$. We also indicate the contributions from the first few j values to the total flux curve. Similarly to the transmission factors, the main feature is a sharp suppression at threshold. The area under the curves is larger for scalars than fermions, which agrees with earlier studies (see for example [107, 112]). The bottom plots show three values of the mass and various n values. The error from using the $\mu = 0$ curve with a sharp cut at the mass is therefore large (most notably for fermions). Regarding variation with n, it is opposite to the tendency for the transmission factors so the n dependence of the Planckian factor $[\exp(\tilde{\omega}/T_H) \pm 1]^{-1}$ dominates the magnitude.

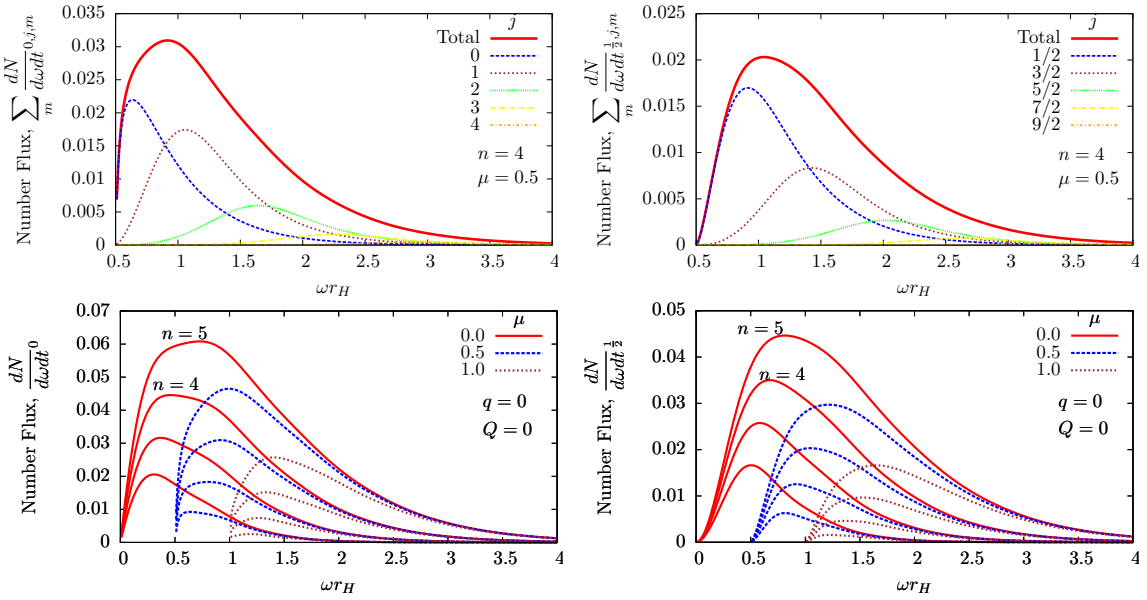

Figure 6.3: *Scalar (left) and fermion (right) number fluxes for $n = 4$ and zero charges*: The top plots show $\mu = 0.5$ and the contributions from each partial wave to the total flux. The bottom plots show variable μ and variable $n = 5, \ldots, 2$. For each μ the curves are naturally order in n from top to bottom, $n = 5$ and $n = 4$ are indicated for $\mu = 0$.

6.4.2 The effect of black hole charge on neutral particles

The next effect we consider is black hole charge. Neutral particles simply feel a different gravitational field around the black hole. So by studying neutral particles we disentangle the gravitational effect from the electromagnetic effect (since $q = 0$).

In figure 6.4 we present plots for transmission factors and fluxes using the low energy analytic approximation. Here we focus on $n = 6$ for scalars and fermions. We should note that some of the plots for fermions will display extrapolated results beyond the small energy limit. This turns out to be quite well behaved, which is due to the better matching of r-powers as pointed out in equation (6.22).

From the gravitational point of view, the main effect of Q is to decrease the horizon radius and consequently increase the Hawking temperature. This is clearly seen in the transmission factors of figure 6.4, where all the curves are pushed up with increasing Q. The same happens with the fluxes where the effect is even larger, due to the strong dependence of the thermal factor on Q through the Hawking temperature – see equation (5.12).

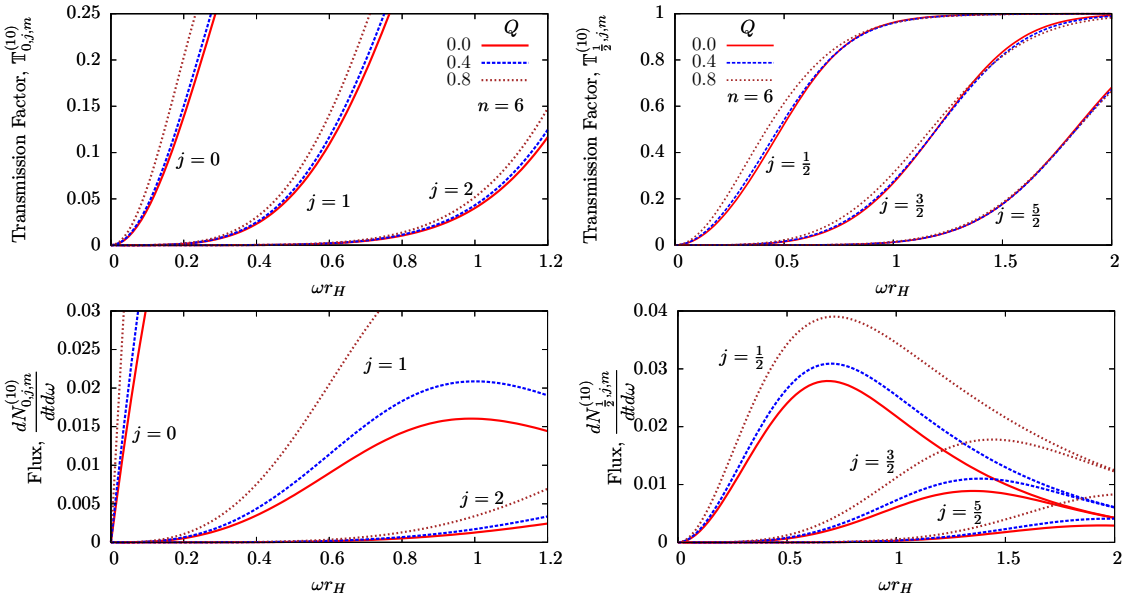

Figure 6.4: *Transmission factors and fluxes for neutral scalars and fermions using the analytic approximation.* The left plots show spin 0 and the right plots show spin 1/2. The top plots show transmission factors $\mathbb{T}_k$ and the bottom plots show number fluxes, for a range of j modes and different black hole charges Q. Rotation is off, $\mu = 0$ and the line colour/type is the same for top and bottom plots.

6.4.3 The effect of particle charge

For particles with non-zero charge, in addition, we have a Coulomb repulsion/attraction according to whether the particle has same/opposite sign charge compared to the black hole. For definiteness we take the black hole charge to be positive.

In figure 6.5 we plot transmission factors and fluxes for scalars and fermions, various charges, $n = 6$ and $Q = 0.6$, using the low energy analytic approximation. It is important to note here that the Coulomb type coupling appearing in the radial equation is

$$qQ = (\sqrt{\alpha}z)(\sqrt{\alpha}Z) \simeq (0.1z)(0.1Z) \tag{6.61}$$

For a TeV gravity black hole produced from proton-proton collisions, $|Z| \leq 4/3$ and $|z| \leq 1$. So the figures we have chosen are above their typical values. However it is easier to see the differences in the curves. Furthermore there may be stages during the evaporation where the black hole charges up so this region of parameters is still important.

The main features of figure 6.5 are as follows. For scalars we can see clearly the phenomenon of superradiance in the top plot, for particles with the same charge as the black

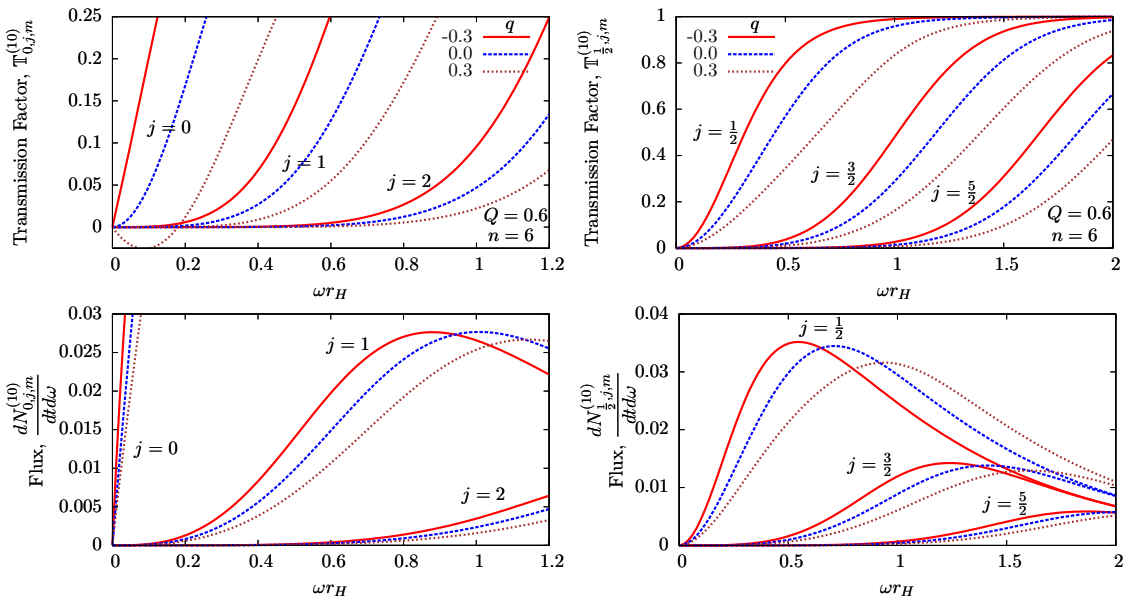

Figure 6.5: *Transmission factors and fluxes for charged scalars and fermions using the low energy analytic approximation.* The left plots show spin 0 and the right plots show spin 1/2. The top plots show transmission factors $\mathbb{T}_k$ and the bottom plots show number fluxes, for a range of j modes and different particle charge q with $Q = 0.6$. Rotation is off, $\mu = 0$ and the line colour/type is the same for top and bottom plots.

hole, where $\mathbb{T}^{(10)}_k < 0$. This means that the associated incident wave gets reflected with a larger amplitude. However, it does not favour the emission of positively charged particles because the negative charge transmission factors are greatly enhanced. This is clear in the flux plot where all the curves at low energies are higher for negative charge. We can understand this physically by recalling that the transmission factor describes the probability of a wave incident from infinity to be transmitted down the black hole. Since negatively charged particles are attracted by the Coulomb potential and positively charged particles are repelled, we would expect negative charges to have higher transmission factors. This is confirmed for fermions in a wider range of energies. The other main feature is that at higher energies, the Planckian factor (which favours discharge) dominates and the tendency is inverted, i.e. positively charged particles are favoured. This is confirmed for the scalar case using the high energy limit approximation shown in figure 6.6, where the transmissions factors are still larger for negatively charged particles, but since they are close to their asymptotic value $\mathbb{T}^{(10)}_k = 1$, the thermal factor dominates.

Figure 6.7 shows the variation with n. Here the transmission factors for scalars are

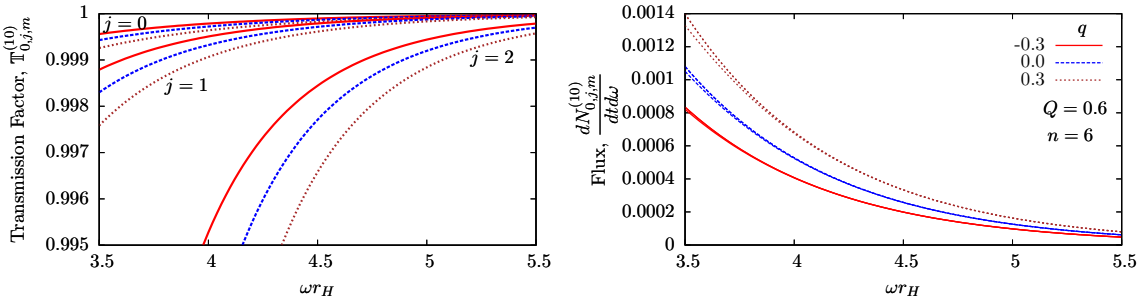

Figure 6.6: *Asymptotic high energy transmission factors and fluxes for charged scalars using the analytic approximation.* The left plot shows transmission factors $\mathbb{T}_k^{(4+n)}$ and the right plot shows fluxes for a range of j modes. Rotation is off, $\mu = 0$ and the line colour/type is the same for both plots.

weakly dependent on n whereas for fermions we have a stronger effect. This is due to extra n dependent factors in the wave equation as for example the term $2|s|/A \sim 1/(n+1)$ in B – equation (6.15). For the fluxes the separation is larger due to their stronger n dependence through the Hawking temperature. In general, similarly to neutral black holes, the effect of n is to increase the total fluxes.

Figures 6.8 and 6.9 show several cases of non-zero charges in the full energy range using the exact numerical method. In figure 6.8 we have kept $Q = 0.4$ and in figure 6.9 we have kept $Q = 0.6$. q ranges between $[-1, 1]$. We use $n = 2$ and $n = 4$ as representative cases.

The plots of figure 6.8 confirm the qualitative features in figures 6.5 and 6.7. They also emphasize the general tendency for the transmission factor to be suppressed with n except for the inverted behaviour for fermions at low energies and a small variation for scalars in the supperradiant region (the latter agrees with figure 6.7). Furthermore, the top plots confirm that the transmission factor favours negative charges at all energies.

The top plots of figure 6.9 show the total flux for the two extreme cases $q = 1$ and $q = -1$ together with the first few partial waves contributing. The first striking observation is the confirmation that for all partial waves there is a first region in energy where charging up is favoured (i.e. the curve corresponding to negative charge is higher) and another (dominant) region where discharge is favoured (the curve with positive charge is higher). It is also clear that if we integrate over the curves discharge is always favoured as expected. The bottom plots show a similar behaviour for a range of intermediate charges. Another interesting point is that the charge splitting is larger for fermions than for scalars.

The inverted splitting at low energies is a direct consequence of the extra dimensions.

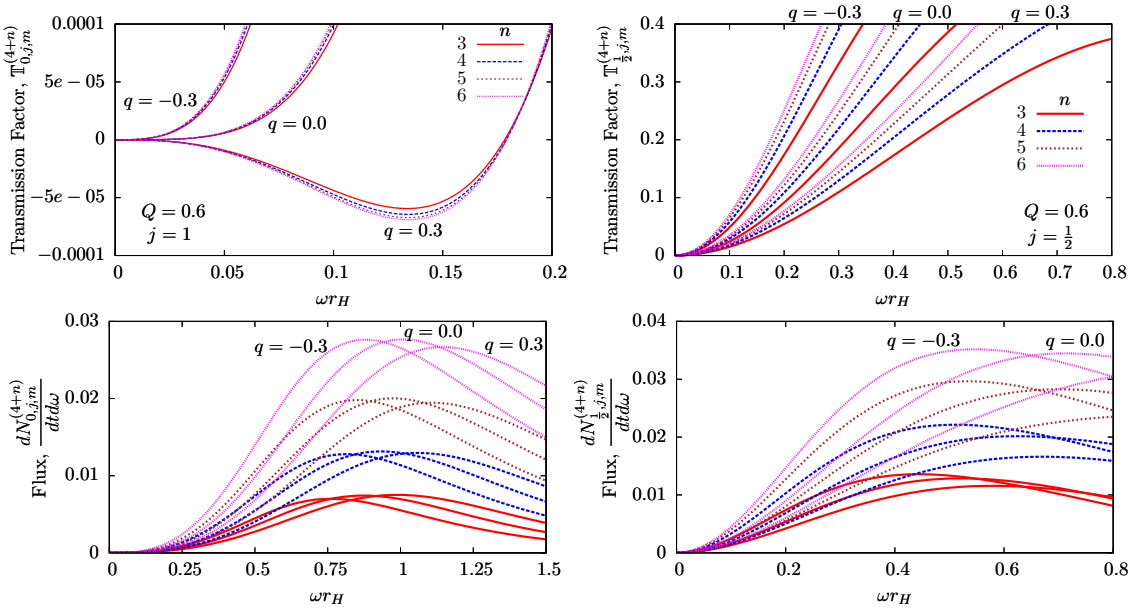

Figure 6.7: *Transmission factors and fluxes for charged scalars and fermions using the analytic approximation.* The left plots show spin 0 and the right plots show spin 1/2. The top plots show transmission factors $\mathbb{T}_k$ and the bottom plots show number fluxes, for a range of charges q and various numbers of extra dimensions n with $Q = 0.6$ and $j = 1$ for scalar and $j = 1/2$ for fermions. Rotation is off, $\mu = 0$ and the line colour/type is the same for top and bottom plots.

In figure 6.10 we show the difference in number flux of positively and negatively charged scalars and fermions when $n = 0, \ldots, 6$. The left plot shows a typical QED coupling of $|q| = Q = 0.1$ and the right plot a QCD like coupling of $|q| = Q = 0.3$. Note however that we are dealing with an abelian theory so the latter is only indicative of the magnitude of the effect for QCD. From this figure it is now clear that the splitting is controlled by an interplay between the magnitude of the transmission factor (which prefers negative charges) and the magnitude of the Planckian factor (which prefers positive charges).

For $n = 0$ and $n = 1$, the splitting is always positive so the Planckian factor dominates. However as n increases, the transmission factor starts dominating at low energies and for all $n \geq 2$ we have the observed inverted region (where the curves are negative). Another interesting feature of figure 6.10 is that the plots on the left have exactly the same shape as the ones on the right. This is not surprising if we note that for qQ small we can expand the fluxes perturbatively around $qQ = 0$ and since $|qQ|$ is 0.01 and 0.09 respectively, we would expect the perturbation to be dominated by the linear term so the difference is proportional to $|qQ|$.

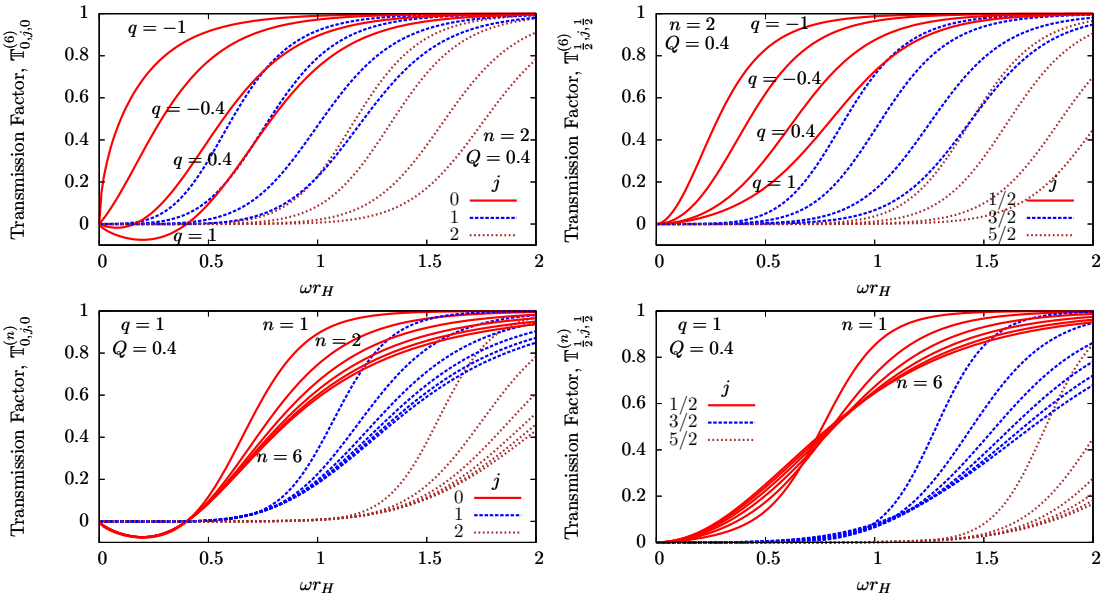

Figure 6.8: *Scalar (left) and fermion (right) transmission factors for variable charge q (top) and variable n (bottom)*: The first three partial waves are presented (note that $a = 0$, so waves with different m for the same j are degenerate).

6.4.4 The effect of black hole rotation

The effect of rotation was studied before in detail for several fields in [103, 105–108, 111–113] with $Q = \mu = 0$ limit. Data files for transmission factors were built by authors in these studies to cover as much as possible the parameter space, for spins $s = 0, 1/2, 1$, and were made publicly available in [144]. In this section we provide a short review of the main results for this special case using the data [144], following [4]. This is important because in chapter 7 we implement black hole rotation in the `CHARYBDIS2` generator, so a good understanding of the features of the various fluxes reveals how the simulation of the physics is affected.

Energy dependence of the fluxes

When rotation is turned on, the partial waves for a given j which contribute to the fluxes (5.12), (5.13) and (5.14) are no longer degenerate. This splitting is such that modes with $m > 0$ (co-rotating) dominate the fluxes. Figures 6.11 and 6.12, illustrate how this arises from the combination of the transmission factor $\mathbb{T}_k$ (TF) and the Planckian factor $[\exp(\tilde{\omega}/T_H) \pm 1]^{-1}$ (PF), for each partial wave contribution. In figure 6.11 we have plotted transmission factors for scalar and vector fields with the corresponding Planckian factors,

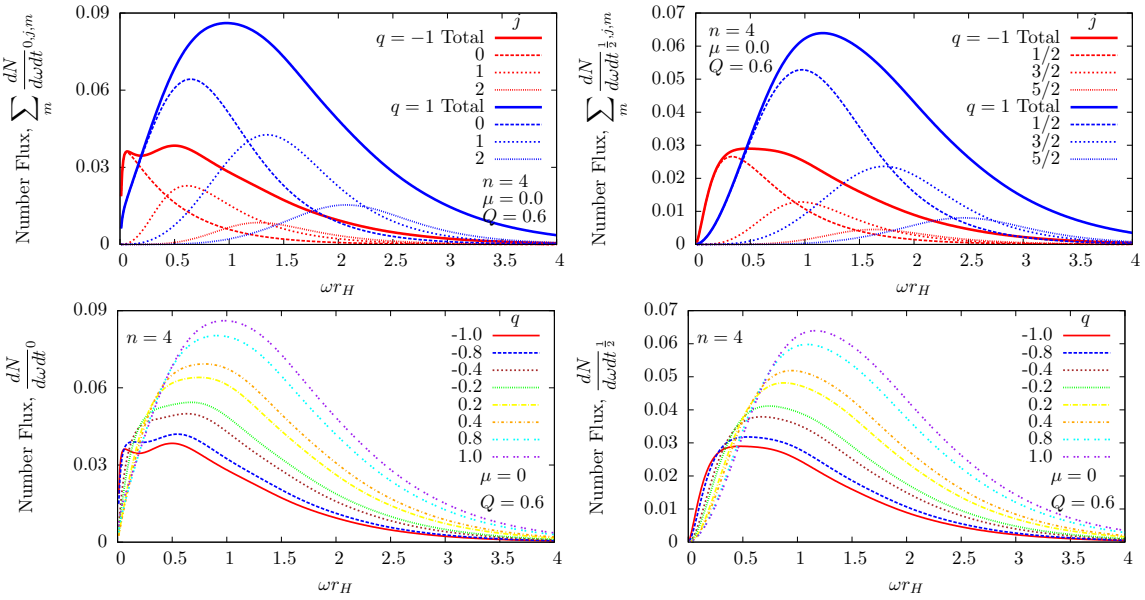

Figure 6.9: *Scalar (left) and fermion (right) number fluxes for $n = 4$, variable q, and $Q = 0.6$*: The top plots show two opposite and large $|q| = 1$ cases to illustrate the charge splitting, together with the first three partial wave contributions. The bottom plots show the variation of the curves between these two large charges.

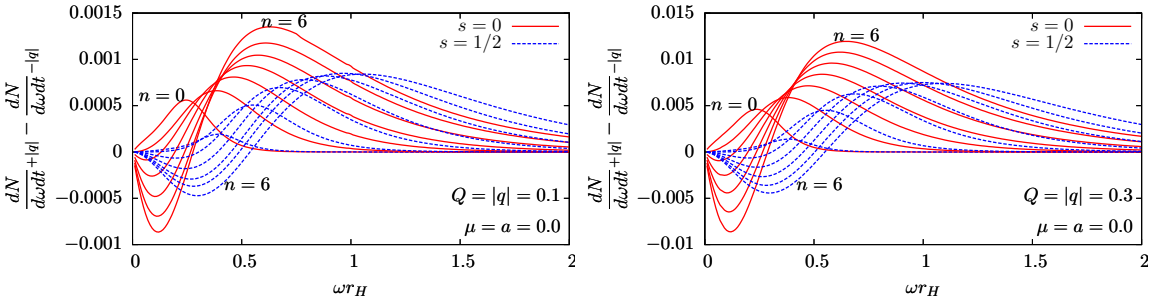

Figure 6.10: *Scalar and fermion number flux asymmetries*: Both plots show curves for the difference in number fluxes between positively charged and negatively charged particles for two values of $|q|Q$. The curves are naturally ordered in n (some cases are labelled) from $n = 0$ (curve with the lowest maximum) to $n = 6$ (highest maximum).

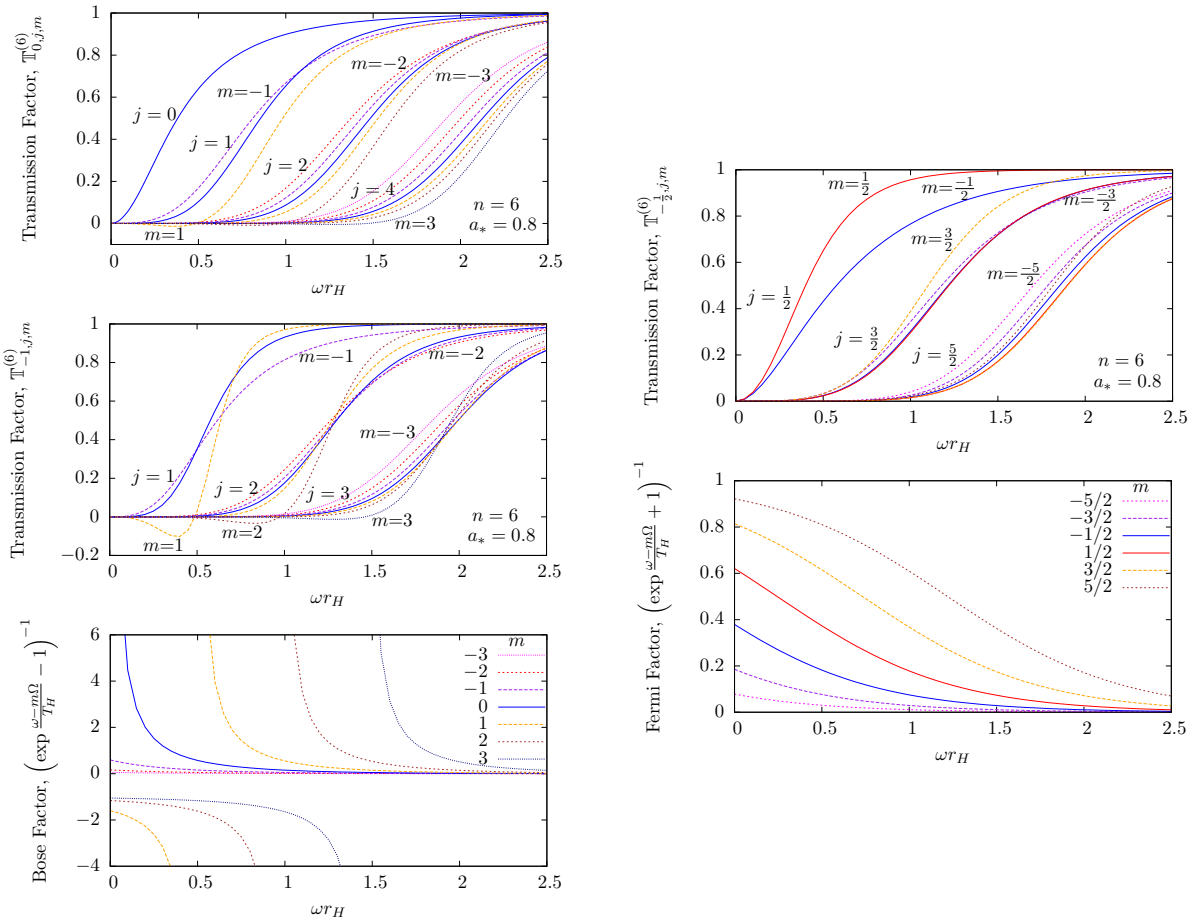

Figure 6.11: *Transmission factors and Planckian factors for* $a_* = 0.8$ *and* $n = 6$. The left plots show spin $0, 1$ and the right plots show spin $1/2$. The top plots show the transmission factors $\mathbb{T}_k$ and the bottom plots show the Planckian factors $[\exp(\tilde{\omega}/T_H) \pm 1]^{-1}$, for a range of j and m modes. Lines with the same m have the same colour and line type.

as well as for fermions[8]. At the level of the transmission factors, the overall tendency is for counter-rotating ($m < 0$) modes to be dominant. Recalling the interpretation of the transmission factor as the fraction of a wave incident from infinity which is absorbed, this means that counter-rotating modes are more easily absorbed by the black hole. It is interesting to note that this agrees with the absorptive disks in figure 3.6, where as we increase a, the left side of the disks (which is associated with geodesics with $\ell_z < 0$ – see central plot of figure 3.6) is larger than the right side. So in some sense, particles with $m < 0$ are more easily absorbed in the geometrical optics approximation as well. For

[8]These are the types of fields implemented in the evaporation phase in `CHARYBDIS2`

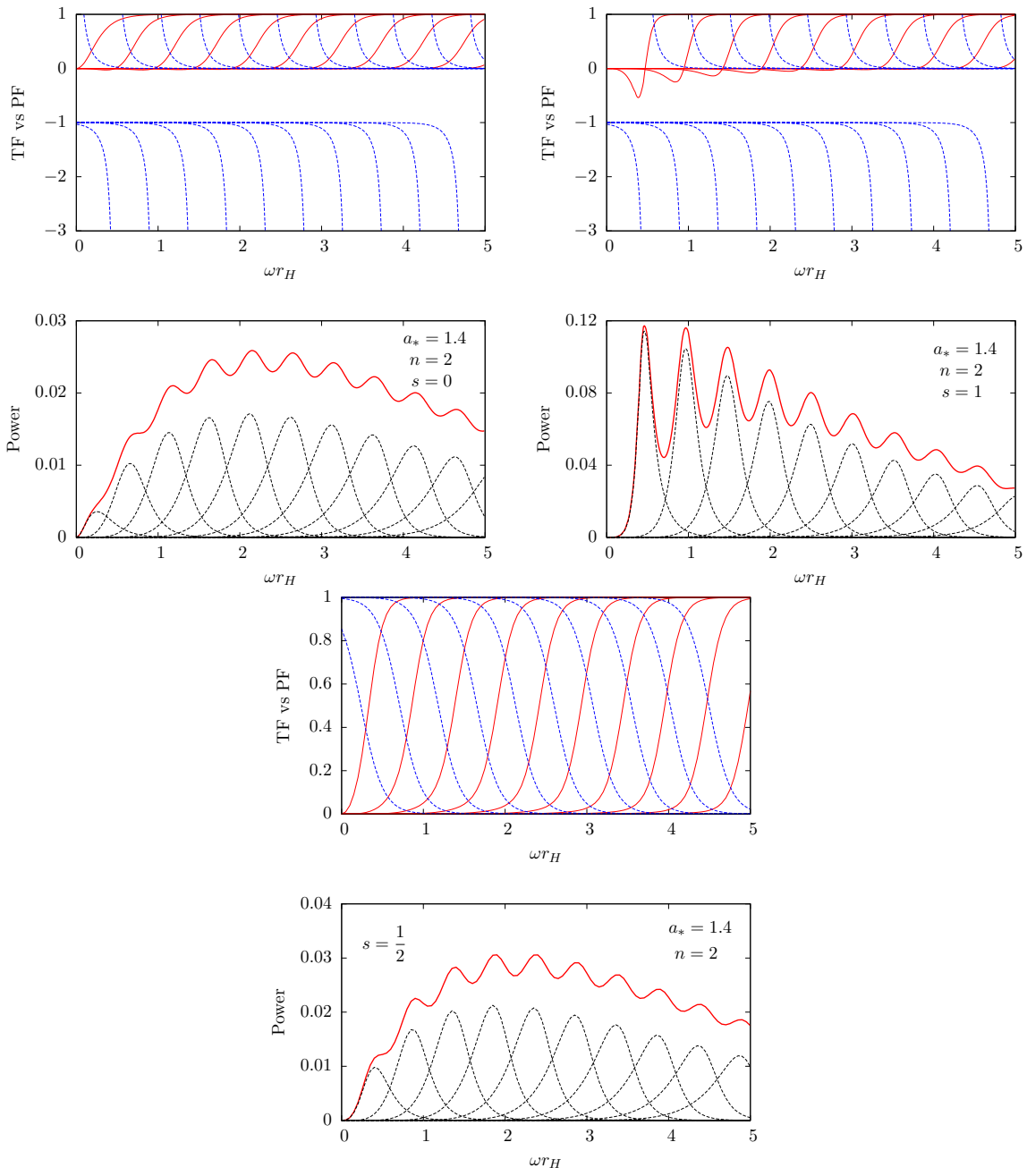

Figure 6.12: *Power spectra for a rotating six-dimensional black hole with* $a_* = 1.4$. For each set of two plots, the top plot shows the transmission coefficients (red, solid) and the Planckian factors (blue, dotted) as a function of ωr_h, for the $m = j$ modes up to $j = 10$ for scalars (top left pair), $j = 10$ for vectors (top right pair) and $j = 19/2$ for fermions (bottom pair). The bottom plots of each pair display the power emission spectrum (thick red curve) containing contributions from all modes, together with the curves for the leading $m = j$ modes. The region of overlap between different modes is small, leading to sharply-peaked oscillations in the power emission spectrum.

the Planckian factors, the tendency is exactly opposite so Hawking radiation is generated preferentially in co-rotating modes. The Planckian factor turns out to dominate so we end up with a spectrum dominated by co-rotating modes. This is particularly striking for lower n. For example in figure 6.12 we show the power spectrum for various spins and the contributions from the $m = j$ partial waves, together with the TFs and PFs for the latter. The oscillations in the spectrum coincide with the $m = j$ peaks showing that they give the largest contribution. The same dominance for co-rotating modes occurs for larger n, however other $m > 0$ modes also contribute which results in a smoother spectrum (see figure 6.13). A preferential emission of co-rotating modes implies an efficient loss of black hole angular momentum through Hawking radiation. Figure 6.13 also shows that in general, rotation increases the area under the curves. This means a larger total emission rate, despite the mild dependence of the Hawking temperature on a_* for a fixed black hole mass. On the other hand, the Hawking temperature grows roughly linearly with n, which increases the flux with n as seen by comparing the vertical axis of the left plots with the right plots.

Another general feature of the spectra is a shift towards emission at higher energies. This is related to the explicit shift $\omega \to \tilde{\omega} = \omega - m\Omega_H$ in the argument of the exponential of the Planckian factor. For the $m = j$ modes, which dominate the spectrum, this produces a positive shift of the exponential suppression towards larger energies. In particular, for bosonic fields (see figure 6.11 and 6.12) it introduces a superradiant region [120, 121, 145] $\tilde{\omega} < 0$ where the Planckian factor becomes negative, together with the transmission factor[9]. It has been shown [106, 108, 146] that this phenomenon increases the emission of bosonic fields on the brane largely, with increasing a_* as well as with n. This feature is particularly striking for spin-1 fields – figure 6.13. It has been suggested [147] that the presence of superradiance might increase dramatically the emission of bulk gravitons in a rotating black hole which would compete with the brane channel, disproving the assumption that brane emission is dominant. However, results for the ratio of bulk to brane emission for the scalar field [113, 148, 149] indicate that bulk emission is typically below 35% for $n = 1, 2, \ldots, 6$ (though a full study of bulk gravitons would be necessary and it is still lacking).

[9]Note that the denominator in equation (5.12) is negative for superradiant modes in the bosonic case, thus cancelling out the negativity of the superradiant transmission factor $\mathbb{T}_k^{(D)}$, and so contributing positively to the fluxes.

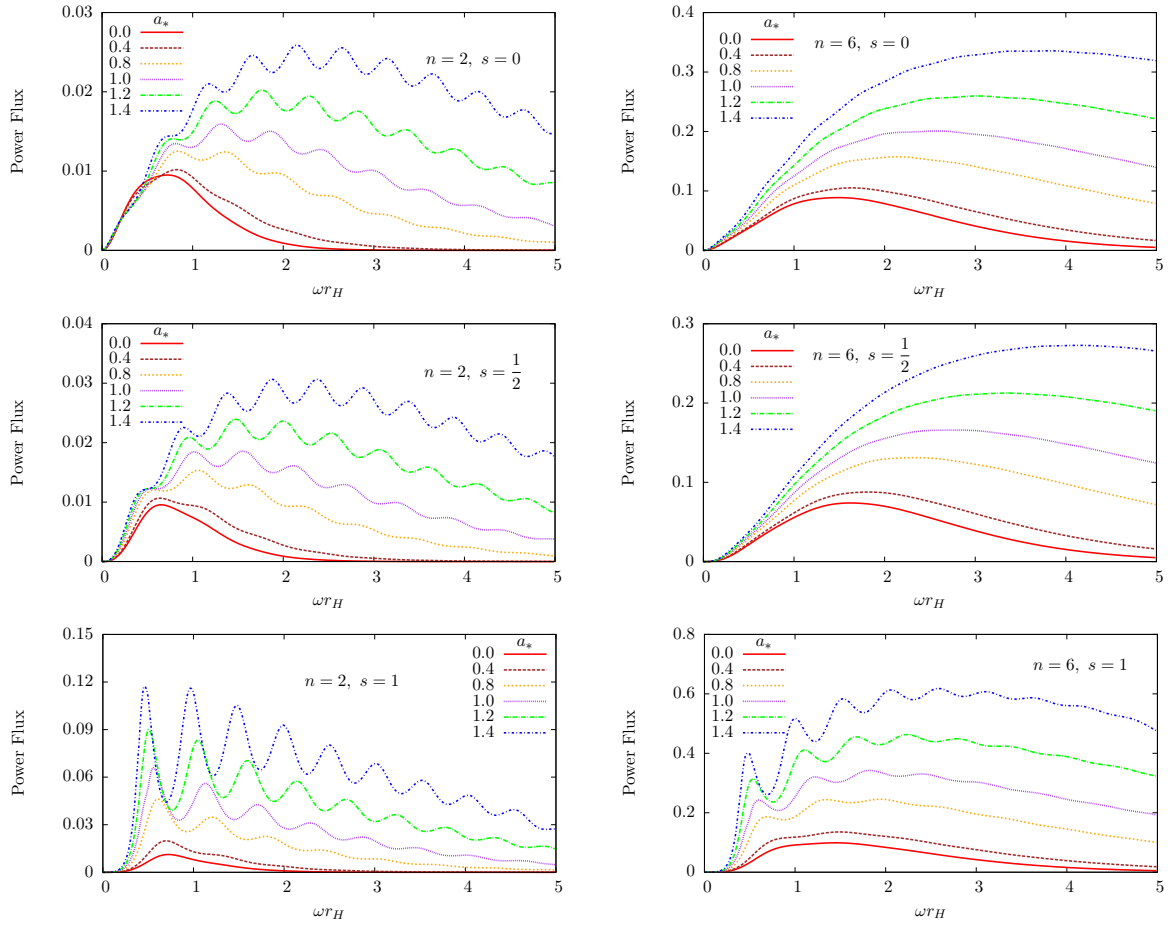

Figure 6.13: *Power Spectrum of spin-zero, spin-half and spin-one fields on the brane.* The plots show the power spectrum for a range of rotations, $a_* = 0, \ldots, 1.4$ for a 6D hole (left) and a 10D hole (right). Note the order-of-magnitude difference in the total power between $n = 2$ and $n = 6$ as well as between $s = 0, 1/2$ and $s = 1$.

Angular fluxes

Some important properties of the angular distributions for our analysis follow from the observation of figures 6.14 and 6.15. We have verified that in general, for any mode, higher rotation tends to make the spheroidal functions more axial (figure 6.15). This means that at low energies (where the modes are departing from being degenerate), the angular distribution of Hawking radiation will tend to become more axial. However, for higher energies, the effect of rotation on the emission spectrum is to favour emission of modes with $m = j$ in order to spin down the black hole. This will produce a more equatorial angular distribution, as we can see from figure 6.15 where the $m = j$ mode is

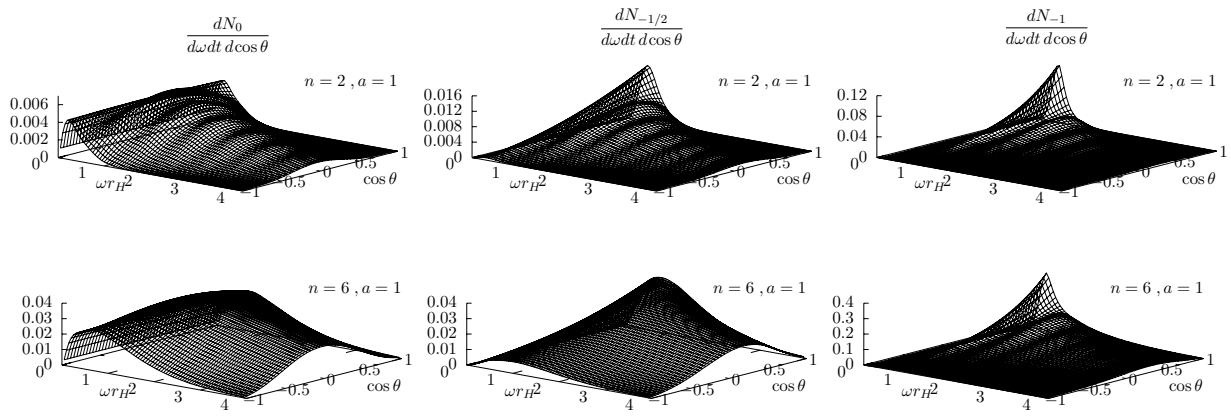

Figure 6.14: Angular dependence of the flux for states of positive helicity $h = -s = 0, 1/2, 1$, non-zero rotation $a = 1$ and two different $n = 2, 6$. The negative helicity plots are obtained by the reflection $\cos\theta \to -\cos\theta$

always more central (in $x = \cos\theta$) than the $m = 0$ mode (for $j \neq 0$). So as we increase the rotation parameter we have a competition between the increase in the angular function's axial character and the increase in probability of emission of more equatorial modes (which are those with larger j). At low (high) energies the former (latter) wins as seen from the energy dependence of the angular profiles shown in figure 6.14

Low-energy vector bosons are more likely to be emitted close to the rotation axis, whereas high energy vector bosons are more likely to be emitted in the equatorial plane. A similar but far less pronounced effect exists for spin-half particles.

In figure 6.14 we see that particles with a single helicity, such as the neutrino, will be emitted asymmetrically by a rotating black hole [150–152]. For example, if the black hole's angular momentum vector is pointing north, then positive(negative) helicity states will be preferentially emitted in the northern (southern) hemisphere. The unstable W and Z vector bosons will be emitted from the black hole in two possible transverse polarisations states, with similar north/south asymmetry. This should lead to asymmetries in their decay products.

6.4.5 Interplay between rotation and charge effects

Though the new results for the charge effects described in previous sections have not yet been implemented in the `CHARYBDIS2` generator, it is interesting to observe how the effect of rotation couples to the effect of charge. Figure 6.16 shows some cases with a rotation parameter $a = 0.9$ (typical order of magnitude for a TeV gravity scenario rotating black

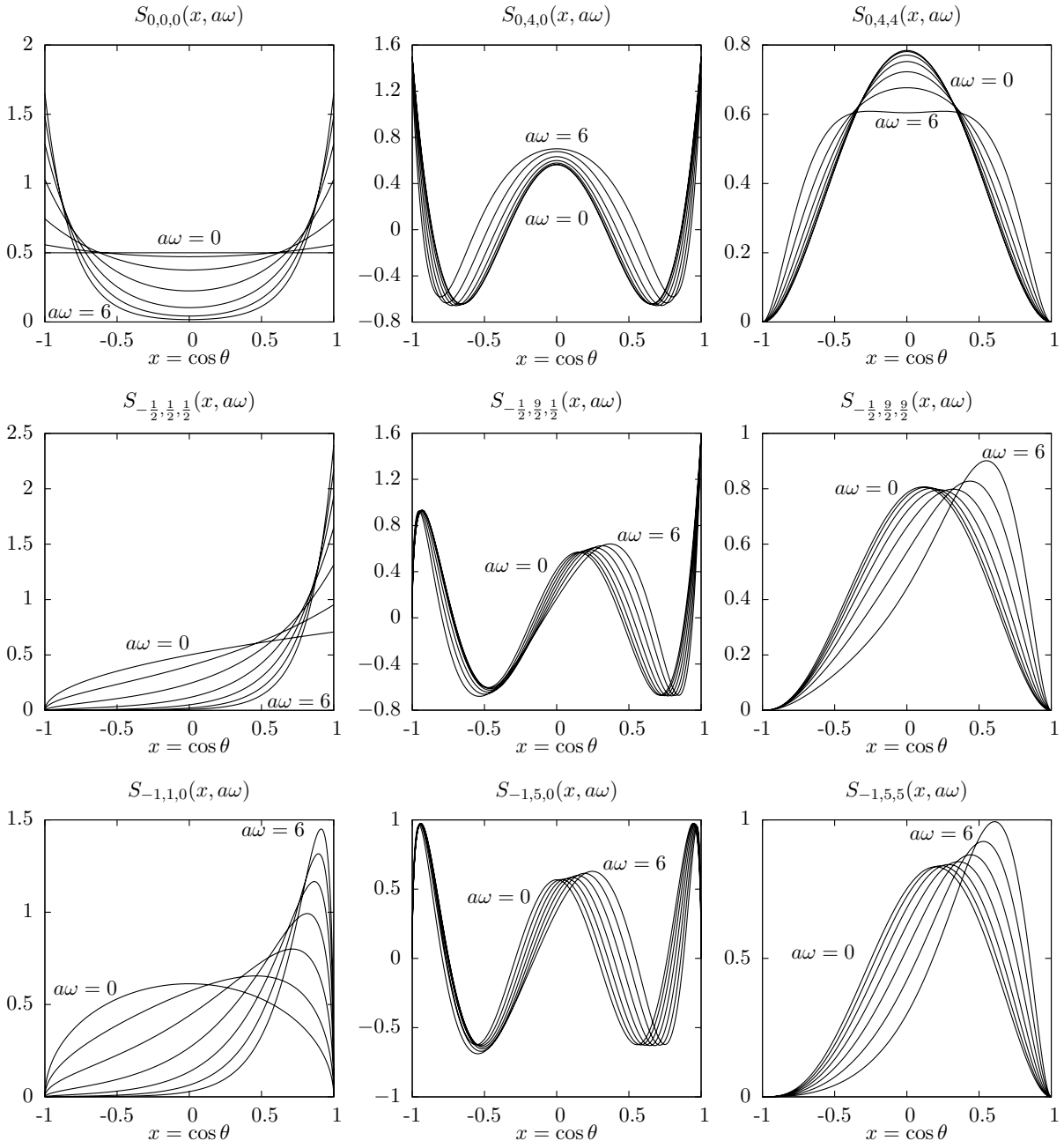

Figure 6.15: The figure shows various spheroidal wave functions $S_{h,j,m}(x, a\omega)$ as a function of $\cos\theta$. Plots for $a\omega = 0, 1, 2, 3, 4, 5, 6$ are shown (only the first and last are indicated, since the curves are regularly ordered). The title of each plot indicates $\{h, j, m\}$.

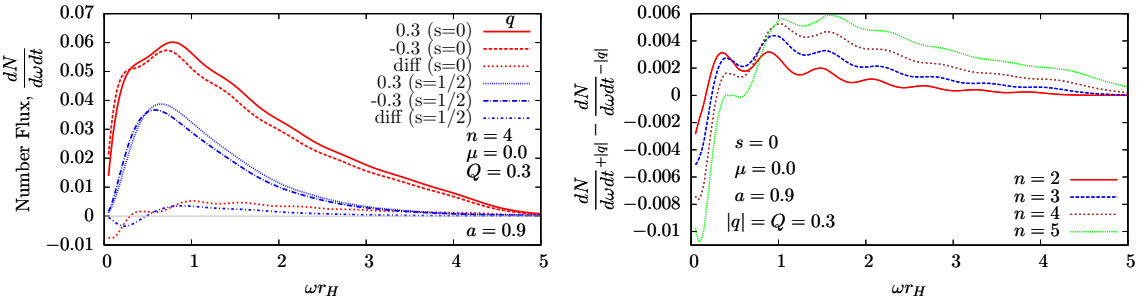

Figure 6.16: *Scalar and fermion asymmetries for* $a = 0.9$: The left plot shows number fluxes for scalars and fermions with positive and negative $|q| = 0.3$ for $n = 4$. The difference between positive and negative $|q|$ curves is also shown in the same plot. The right plot shows the difference for scalars and a range of n's.

hole) and the typical QCD charges $|q| = Q = 0.3$. The left plot shows the split flux curves for the QCD case both for scalars and fermions and the difference between the two. The right plot shows the difference curves for scalars and a range of n's. Qualitatively, the splitting of the curves when $a \neq 0$ follows the same pattern as figure 6.10. The main differences are: the oscillations which are due to the contribution of higher partial waves when $a \neq 0$; and the shift of the spectrum towards higher energies, which is again due to the contribution from the partial waves with larger j which are shifted to higher energies. It is interesting to note that the oscillations persist for large n in the right plot, which is not true for the left flux plots where they tend to be smoother.

6.5 High energy absorption cross sections

To better understand the contributions to the fluxes at high energy, it is instructive to look into an approximation based on the geometrical cross section obtained from the disks computed in section 3.3.

In [153], Unruh proved that the absorption cross section for a plane wave, incident on a Schwarzschild black hole from infinity is[10]

$$\sigma = \sum_{j,m} \frac{\pi}{\omega^2} \mathbb{T}_{j,m} \equiv \sum_{j,m} \sigma_{j,m}. \tag{6.62}$$

This suggests the interpretation of $\sigma_{j,m}$ as the contribution from a partial absorption

[10] We are using horizon radius units.

cross section for a wave with quantum numbers $\{j, m\}$. These cross sections are directly related to the transmission factors so they are usually named greybody factors, because they are responsible for distorting the black body spectrum of Hawking radiation. In this non-rotating limit the flux becomes

$$\frac{dN}{dtd\omega} = \frac{1}{2\pi^2}\frac{\omega^2}{\exp(\omega/T_H) - (-1)^{2s}}\sum_{j,m}\sigma_{j,m}. \tag{6.63}$$

so the Planckian term factors out of the sum. In the limit $\omega \to +\infty$ we would expect an incident plane wave to be well described by a beam of classical particles. Then the absorption cross section is simply the area of the absorptive disk at infinity (which in the non-rotating case is a circular disk). This type of approximation was noted by DeWitt [154], who replaced the transmission coefficient by a theta function cutting the j-sum in (6.63) at the maximum angular momenta allowed by the absorptive disk radius ($j = b_{max}\omega$). The success of his approximation, reinforces the interpretation of σ as the total cross section for a classical beam of particles.

Expression (6.63) is more complicated for a rotating black hole (equation (5.12)) because the Planckian factor depends on m and can not be taken out of the sum. However, it is still possible to prove that for a wave incident at an angle θ, the cross section is [129] (we are using the scalar case)

$$\sigma(\theta) = \frac{4\pi^2}{\omega^2}\sum_{k=\{j,m\}}|S_k(c, \cos\theta)|^2\mathbb{T}_{c,k} \equiv \sum_{k=\{j,m\}}\sigma_{c,j,m}(\theta) \tag{6.64}$$

if we average over the solid angle we get that

$$\sigma \equiv \int\frac{d\Omega}{4\pi}\sigma(\theta) = \sum_{k=\{j,m\}}\frac{\pi}{\omega^2}\mathbb{T}_{c,k} = \sum_{k=\{j,m\}}\sigma_{c,j,m}\ . \tag{6.65}$$

So for the rotating case, the same relation between partial wave cross-sections and transmission factors exists. But in the high energy limit, assuming the geometric description is good, we know how to compute the absorption cross-sections for a given angle of incidence by using the disks obtained in section 3.3. Furthermore, note that at high energies we would expect this result to be independent of the spin of the particle. In figure 6.17 we compare the geometrical result obtained by numerically integrating the absorptive disks, with the asymptotic value of the sum over transmission factors computed for the scalar

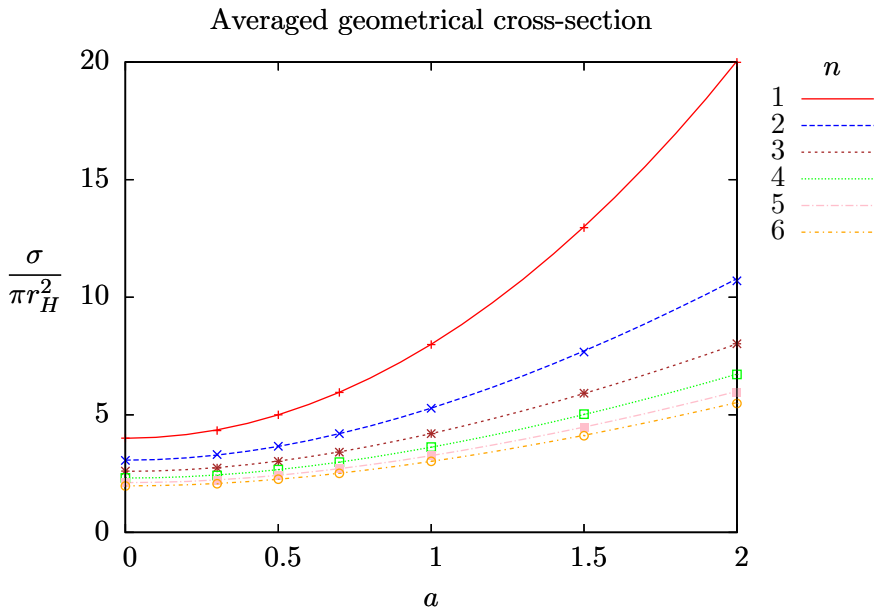

Figure 6.17: The plot shows a perfect agreement between the averaged geometrical cross section (solid lines) and the asymptotic value of the sum of the greybody factors (the points). We show the cases from $n = 1$ (red upper line) to $n = 6$ (bottom line). The curves are organise in order from the top to the bottom.

field. We find an excellent agreement between the points taken from Table I of [62] and our geometrical calculation.

Furthermore, we can extend DeWitt's argument to compute the Hawking flux. If we go back to the scalar angular flux before integration over the solid angle $d\Omega$ we have

$$\begin{aligned}\frac{dN}{dtd\omega d\Omega} &= \frac{1}{4\pi^2}\sum_k \frac{1}{\exp(\tilde{\omega}/T_H)-1}\mathbb{T}_k^{(4+n)}|S_k(c,\cos\theta)|^2 \\ &= \frac{\omega^2}{(2\pi)^4}\sum_k \frac{\sigma_{c,j,m}(\theta)}{\exp(\tilde{\omega}/T_H)-1}\,.\end{aligned} \tag{6.66}$$

Since we know the partial absorption cross sections as a function of the angle by using the geometrical disks, we can find a high energy approximation for the spectrum by cutting off the sums according to the allowed regions on the (b,ζ) plane. A particularly interesting limit is when we approximate the exponential in equation (5.12) as

$$\tilde{\omega} \simeq \omega \tag{6.67}$$

if

$$\omega \gg \left|\frac{am}{1+a^2}\right| \leq \left|\frac{aj}{1+a^2}\right| \leq \left|\frac{aj_{\max}}{1+a^2}\right| = \left|\frac{ab_{\max}\omega}{1+a^2}\right| \tag{6.68}$$

which holds for a small or large or for small enough j. Furthermore $j_{\max}$ is large, when $\omega \to +\infty$, so for most of the modes contributing to the the sum in (5.12) this approximation should work. This implies a similar factorisation in the high energy limit for rotating black holes:

$$\frac{dN}{dtd\omega} \approx \frac{1}{2\pi^2}\frac{\omega^2}{\exp(\omega/T_H)-1}\sigma \ . \tag{6.69}$$

6.6 Conclusions

In this chapter we have presented various interesting effects which are important to the modelling of black hole events in theories with extra dimensions. We have used the approximate charged rotating background geometry studied in chapter 3 and the wave equations separated in chapter 5 to model charged massive scalars and fermions. Transmission factors were obtained using approximate analytic techniques, and numerical methods which give the result in a wider range of energies. The angular functions, which are particularly relevant for non-zero black hole angular momentum, were obtained using series expansions and checked against well known approximations. The transmission factors for vector bosons were included in the discussion of the effect of rotation. Here the data files for $s = 0, 1/2, 1$ available in [144] were used. The most important effects are as follows:

- For massive particles, our analysis shows a damping of the spectrum close to the threshold $\omega \simeq \mu$ as well as an overall reduction of the area under the flux curves. For fermions, the suppression is not so sharp at the threshold energy. The main consequence for LHC phenomenology is that production of massive particles such as the top, $W^{\pm}$, Z and Higgs boson (which have masses of the same order of magnitude as the typical $1/r_H \sim 100$ GeV) is highly suppressed at low energies. The typical mass parameters of these heavy Standard Model particles can go up to ~ 0.5 (in horizon radius units), so this is an important effect.

- Black hole discharge is sub-dominant. This is another important point for LHC phenomenology and the development of event generators which tend to enforce quick discharge. Nevertheless, black hole events at the LHC will have non-zero charge, so statistically we would expect a fraction of them to charge up. For charged black holes our plots show that the flux spectra for positive and negative charges are

split. Thus negatively charged particles are biased towards low energies whereas positively charged particles are biased towards higher energies. So the dynamical model of discharge should still be incorporated since it will produce an asymmetry in the energy spectrum of positive/negative charged particles.

In particular, the inverted charge splitting at low energies is a new effect due to the extra dimensions for $n \geq 2$. So, even though electric discharge may be small in TeV gravity black hole events, this splitting will still be present and it may be possible to reconstruct it if such events occur in future experiments. For QCD charges, it should be even larger but a non-abelian analysis will be necessary to determine which observables will display it.

- Rotation splits the azimuthal symmetry such that the co-rotating modes, which are responsible for spinning down the black hole, are dominant. The energy spectrum receives contributions from partial waves up to a larger j, which results in a shift towards higher energies.

  The non-uniform angular functions correlate with the helicity of the particle. They give low energy axial peaks in the angular spectra both for fermions and vector bosons, but especially for the latter. These peaks are towards the upper/lower hemisphere according to whether the helicity of the particle is positive/negative. At high energies all angular distributions become equatorial.

To summarize, the effects of mass, charge and rotation are important for improving the modelling of black hole events from high energy collisions in large extra dimensions scenarios. They may provide further signatures of black hole events such as charge and angular asymmetries, as well as a shift of the energy spectra towards higher energies. Two points we haven't discussed which deserve further attention are those of QCD charges and the possible restoration of electroweak symmetry close to the black hole. Both may be treated using an improved model based on some of the ideas we have discussed.

In the next chapter, we implement the effect of rotation (which is the dominant one) in the event generator `CHARYBDIS2`.

Chapter 7

CHARYBDIS2

To study the phenomenology of microscopic black hole production and decay in scenarios with extra dimensions, similarly to other electroweak scale processes, it is very convenient to have a Monte Carlo (MC) program. This simulates collision events with frequency and properties as they would occur in a real experiment. Such processes occurring at short distances below the hadronisation scale are usually called hard processes. Several factorisation theorems [155] indicate that we can treat the hard process without worrying about non-perturbative QCD effects. In this chapter we develop a Monte Carlo event generator which simulates black hole events. This can then be interfaced to a general purpose showering and hadronisation program which simulates the physics occurring at larger distances. Figure 7.1 contains a schematic diagram for a proton-proton collision. A parton level event generator simulates the hard process indicated in the centre of the

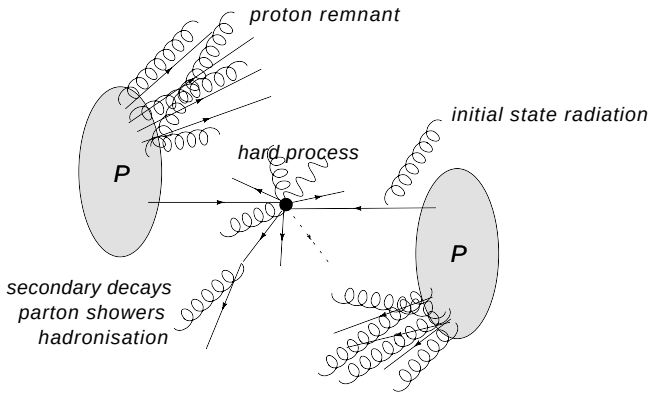

Figure 7.1: A schematic description of a typical proton-proton collision with a hard process occurring at short scales from two colliding partons (centre of the figure). Other processes simulated by a showering and hadronisation program are also indicated. Note that the relative length scales are qualitative, not accurate.

figure, where the black dot represents the interaction and the outgoing lines the various outgoing products. In the MC approach any observable $\mathcal{O}$ can be computed using the approximation [156]

$$\begin{aligned} \mathcal{O}_\Sigma &\equiv \int_\Sigma d\Phi \mathcal{O}(\Phi) \\ &\approx \sum_{i=1}^{N} \frac{V_\Sigma}{N} \mathcal{O}(\Phi_i) \, , \end{aligned} \tag{7.1}$$

where we have defined the observable through an integral over the phase space variables Φ (which denote the set of kinematical quantities labelling the initial state incoming particles), subject to a generic set of constraints (or cuts) Σ on the final state outgoing particles. V_Σ is the volume of the phase space allowed by the cuts and N is the number of events generated uniformly in phase space. The main advantages of the MC method are as follows. First, if we are dealing with a higher dimensional phase space, most of the integration methods based on quadrature by discretisation on a grid and interpolation, converge more slowly than the Monte Carlo method. The errors for the former typically behave like $N^{-q/Dim}$ (where N is the number of times the integrand is evaluated, q is an order 1 integer and Dim is the dimension of the integral), whereas for the latter the errors behave like $N^{-1/2}$. So typically, for high dimensionalities, the MC method will converge faster. On the other hand, a complicated set of cuts is easy to implement in the MC method since they require only a check of whether the proposed phase space point is allowed, whereas methods based on interpolation on a grid would require a complicated parametrisation of the boundaries. Finally, an MC generator typically provides a sample of events with weights which can be used to create samples of events with unit weight (or unweighted), so as to mimic actual collisions at the rates they would occur in an experiment. This is also useful because the final state particles propagating away from the interaction region can be interfaced to experimental software to simulate the interactions with a detector. Then predictions for realistic distributions of any experimental observables can be computed easily.

Earlier black hole event generators [46, 85, 157] used models which are special cases of the theory we have presented in the previous chapters. In particular, their production cross-section was given by hoop conjecture arguments (which are not very rigorous) and the effect of black hole rotation was not taken into account in the evaporation. In this chapter we present an upgraded version of the widely-used `CHARYBDIS` event generator [85,

158, 159], to take into account the recent theoretical work on the production and decay of rotating black holes. This new version is named `CHARYBDIS2`[1] and it is publicly available in [3]. This is used in the next chapter to study the effects of rotation on experimentally observable quantities, assuming that black hole production does indeed take place.

In section 7.1 we start by describing some specifics of the implementation of the model for production which was presented in section 4.3.2. In section 7.2, the implementation of the spin-down Hawking decay of the black hole through the emission of SM particles confined to the physical 3-brane is presented. Here the simulation is refined to take full account of the theoretical results of rotation presented in chapters 5 and 6. Some options are included for the modelling of aspects that are not well understood, such as back-reaction effects. Note however that the new effects of particle mass and charge described in chapter 6 have not yet been incorporated. In section 7.3 we explain the extended range of options we have included for dealing with the final Planck mass remnant. Finally in section 7.4 we present some details of the structure of the program and how to use it, emphasizing the new features compared to the earlier `CHARYBDIS`.

7.1 Production

For the production phase, we use the model described in chapter 4.3.2 which gives the (parton level) hard process cross section. In general, for a hard process occurring at length scales below the hadronisation scale, asymptotic freedom and several factorisation theorems [155] indicate that the differential cross section for a hadron-hadron collision (which describes the rate at which the process occurs) takes the form

$$\frac{d\sigma_{h_i h_j \to X}}{dx_1 dx_2}(s) = f_i(x_1) f_j(x_2) \hat{\sigma}_{ij \to X}(\hat{s}) \ . \tag{7.2}$$

We are working in the hadronic centre of mass frame and the collision is along the z-axis. Here $\{x_1, x_2\}$ are the momentum fractions of the partons $\{i, j\}$ (quarks or gluons) participating in the hard process. The function $f_i(x)$ is the parton density function (PDF) which encodes all the non-perturbative physics of the hadron. It is independent of the hard process and it gives the number density of partons of type i with a momentum fraction x of the original hadron, which can participate in the collision. The partonic

[1] We will refer from now on to the new release as `CHARYBDIS2` and will reserve `CHARYBDIS` for earlier versions. The particular version described here is `CHARYBDIS2.0`.

cross-section $\hat{\sigma}_{ij\to X}$ is the short range cross-section for the two partons to collide with (partonic) centre of mass energy squared $\hat{s} = x_1 x_2 s$. The hadronic centre of mass energy squared is s. Note that we are considering processes where the two hadrons are protons so the two PDFs are of the same type. In this case the particles produced in the hard process are $X = BH +$ radiation, the black hole plus radiation released in the production. The differential cross section provides a distribution function for the process to occur with the given kinematical configuration of the partons $\{i, j\}$. The total cross section $\sigma_{hh\to X}$ is obtained by integrating over the momentum fractions and summing over types of partons

$$\sigma_{hh\to X}(s) = \sum_{ij} \int_{0\leq x_1,x_2\leq 1} dx_1 dx_2 f_i(x_1) f_j(x_2) \hat{\sigma}_{ij\to X}(\hat{s}) \; . \tag{7.3}$$

The total rate of events for the process is

$$\frac{dN(s)}{dt} = L\sigma_{hh\to X}(s) \tag{7.4}$$

where L is the luminosity of the beams. The latter is defined as the number of pairs of particles (one from each beam) crossing the transverse plane of collision per unit area and unit time. The cross-section is a useful quantity which is independent of the experimental details of the beams.

Since the partonic cross-section is the short scale counterpart of the hadronic cross-section it can be similarly defined as

$$\hat{\sigma} = \frac{1}{\hat{L}} \frac{d\hat{N}}{dt} \tag{7.5}$$

where $\hat{L}$ is the partonic luminosity. If $\hat{L}$ is constant it is possible to show (assuming beams with constant density) that

$$\hat{\sigma} = \int dS P(b) \tag{7.6}$$

where $P(b)$ is the probability of interaction with an impact parameter b and dS is the transverse element of area. Thus we can define a differential partonic cross-section

$$\frac{d\hat{\sigma}}{db} = 2\pi b P(b) \tag{7.7}$$

So in general, we can write a more general hadronic differential cross section

$$\frac{d\sigma_{h_i h_j \to X}}{dx_1 dx_2 db}(s) = f_i(x_1) f_j(x_2) \frac{d\hat{\sigma}_{ij\to X}}{db}(\hat{s}) \ . \tag{7.8}$$

In our study of black holes, the b dependence is important because the formation and decay of the black hole depends on b. In particular since the formation is dominated classically $P(b)$ is unity for all allowed impact parameters, i.e. $P(b) = \theta(b_{max} - b)$ so the partonic cross-section is simply the area of the disc with radius b_{max}.

In `CHARYBDIS2`, we have implemented the distribution (7.8) to select: the partons involved in the collision; their momentum fractions, and the impact parameter, given the centre of mass energy $\sqrt{s}$. For the partonic cross-section $\hat{\sigma}(\sqrt{\hat{s}})$ we used the lower bound on the cross-section given by the maximum impact parameter from the model in section 4.3.2. This improved bound can be switched back to the hoop conjecture geometrical estimate by setting the value of the variable `YRCSEC` to `.FALSE.`. Furthermore, for each event, we reduce the mass and angular momentum of the black hole using the model in section 4.3.2 when `MJLOST=.TRUE.`. The mass/energy lost during the production phase is distributed between radiation and the kinetic energy of the formed black hole. The production phase simulation must account for this. On the basis of several calculations [160–162], which indicate that gauge radiation is negligible compared to gravitational radiation in the production phase, we assume that all of the radiation is in the form of gravitons. Given that gravitons are missing energy, it is sufficient for the simulation to represent the entire radiation pattern using a 'net graviton' with a four-momentum equal to the sum of those of the emitted particles.

The net graviton has an invariant mass μ_g, which may potentially lie anywhere between 0 and $1 - \xi$ (in units of the initial state mass), where ξ is the fraction of the partonic system invariant mass that constitutes the black hole. An invariant mass of $1 - \xi$ corresponds to a completely symmetric emission of gravitons, whilst lower values correspond to steadily more antisymmetric emissions (which might result if a small number of gravitons is released, and by chance they are emitted in similar directions). In `CHARYBDIS2`, the invariant mass is randomly generated per event from a power distribution, $P(\mu_g) \propto \mu_g^p$. The mean of this distribution is set equal to `FMLOST`$\times(1 - \xi)$ by the quantity `FMLOST`$= (p + 1)/(p + 2)$ (default value 0.99, corresponding to $p = 98$). The simulation of the production phase emission is then a two body decay from initial state object into formed black hole plus net graviton, which is isotropic in the centre of mass

frame of the initial state object.

7.1.1 Adding the intrinsic spin of the colliding particles

The model for the angular momentum of the black hole after formation used in the previous section is based on using incoming particles with zero spin. Angular momentum conservation requires us to include the intrinsic spin of the incoming particles falling into the black hole. Since the results in the literature taking this effect into account are limited to special cases (see for example [78]) we assume a simple model where first we combine the spin states of the incoming particles into a state

$$|s_1, h_1\rangle_z \otimes |s_2, h_2\rangle_z = |s, s_z\rangle_z \ . \tag{7.9}$$

The collision axis is denoted by z, s_i, h_i are the spin and helicity of the particles[2] and s, s_z are the angular momentum quantum numbers of the combined state in the rest frame. Since we have unpolarised beams we give equal weight to each helicity combination. Then this angular momentum state is combined with the orbital contribution obtained from the model for angular momentum loss. We denote it by

$$|L, L\rangle_{z'} \ , \tag{7.10}$$

where L is the nearest integer to J. Note that z' is an axis in the plane perpendicular to the beam axis (z-axis) chosen with uniform probability. Finally, using a Wigner rotation [163] followed by a tensor product decomposition using Clebsch-Gordan coefficients, we obtain

$$\begin{aligned} |L, L\rangle_{z'} \otimes |s, s_z\rangle_z &= |L, L\rangle_{z'} \otimes \sum_{s'_z=-s}^{s} d^{(s)}_{s'_z,s_z}\left(\cos\frac{\pi}{2}\right)|s, s_{z'}\rangle_{z'} \\ &= \sum_{s'_z=-s}^{s} d^{(s)}_{s'_z,s_z}(0) \sum_{J=|L-s|}^{L+s} C_{J,L,L,s,s_{z'}}\,|J, L+s_{z'}, L, L, s, s_{z'}\rangle_{z'} \ , \end{aligned} \tag{7.11}$$

where $d^{(s)}_{s_{z'},s_z}$ is a Wigner function and $C_{J,L,L,s,s_{s'}}$ is a Clebsch-Gordan coefficient for the tensor product decomposition of $|L, L\rangle_{z'} \otimes |s, s_{z'}\rangle_{z'}$. From (7.11) it is straightforward to determine the probabilities for all possible combinations of helicities and incoming partons.

[2]Note we are assuming the massless limit where $h_i = \pm s_i$

This model introduces a spread in the orientation of the initial black hole angular momentum axis around the plane perpendicular to the z-axis. Note that even though the model for angular momentum loss in the previous sections does not include such an effect, in a realistic situation we would not expect the angular momentum to be exactly perpendicular to the beam axis after the production phase.

7.2 Evaporation

After formation, the black hole is allowed to decay semi-classically by emitting Hawking radiation. We assume that the black hole remains stuck on the brane and that emission occurs mostly in the form of SM fields on the brane [164]. The possibility of ejection would come from graviton emission into the bulk [110, 132]. Since the black hole is formed from SM particles which are themselves confined, we assume that even if gravitons are emitted, the extra-dimensional recoiling momentum is absorbed by the brane, avoiding ejection. One could argue that whichever charges keep the black hole confined to the brane, they are lost at the start of the evaporation through Schwinger emission. We have seen in chapter 6 that discharge is not necessarily large on the basis of the Schwinger effect alone. Furthermore, even if discharge does occur, it will be very unlikely that all the different gauge charges are simultaneously neutralized at any stage during the evaporation, if we assume that the black hole decays by emitting one quantum at a time. Furthermore, there are a lot more SM degrees of freedom than gravitational ones so even if the unlikely event of exact neutralisation occurs, it will still be unlikely that a graviton is emitted during the brief period of neutrality. Thus we would expect the number of events in which the black hole is ejected into the bulk to be at most a small fraction of the total.

In chapter 6 we argued that though electric discharge is indeed favoured, the effect on the flux spectra is not large. In the generator we have kept the early simplified model such that whenever a charged field is selected for emission, the electric charge of the state is selected so as to reduce the total charge of the black hole (unless the BH is neutral, in which case equal probabilities for particles and anti-particles are used). To avoid complications in hadronisation, baryon number conservation is also assumed, and colours are assigned to ensure that colour singlet formation is possible. This model will be improved in future works.

The assumption that brane emission is dominant is supported by early studies of the ratio of brane to bulk emission such as [54,113]. Furthermore we have a very large number

of brane degrees of freedom compared to bulk gravitons. However it is important to note that the fluxes for all the modes for bulk graviton emission in a higher dimensional singly rotating background are not yet known in full (only tensor modes have been considered recently [124, 125]). Nevertheless even if there is an enhancement due to superradiance similar to that for vector fields it is unlikely that it will be enough to overcome the large number of brane degrees of freedom.

In the generator we also assume that the emission of Hawking radiation can be treated semi-classically and that the black hole has time to re-equilibrate between emissions. These assumptions are valid as long as the mass of the black hole is much larger than the (higher-dimensional) Planck mass M_D, in which case the typical time between emissions is large compared to r_H (see for example (4.6)) and as long as the Hawking temperature, which gives the typical energy scale of the emissions, is below M_D.

The numerical methods employed to determine the transmission factors were described in chapter 6. We have used (and checked) the high precision publicly available data [144] for $n = 2, \ldots, 6$ and completed it for $n = 1$ using the methods described in chapter 6. The ranges for the parameters are[3] $n = 1, 2, \ldots 6$, $\omega r_H = 0.05, 0.10, \ldots 5.0$ and $a_* = 0.0, 0.2, \ldots 5.0$ for the angular modes $j = |h|, |h|+1, \ldots |h|+12$ and $m = -j \ldots j$. For each point we have computed the flux spectrum using (5.12). This quantity is used in `CHARYBDIS2` as a probability distribution function for the quantum numbers of a particle with a given spin and to determine the relative probability of different spins (through integration of equation (5.12)). For convenience in the Monte Carlo, we have computed the following cumulative distributions from the transmission factors:

$$C_{h,j,m,a_*,D}(\omega r_H) = \int_0^{\omega r_H} \mathrm{d}x \frac{1}{\exp(\tilde{x}/\tau_H) \pm 1} \mathbb{T}_k^{(D)}(x, a_*) \tag{7.12}$$

$$C_{h,a_*,D}(K) = \sum_{Q=1}^{K} C_{h,jm,a_*,D}(\omega r_H \to \infty), \tag{7.13}$$

where x is energy in units of r_H^{-1}, $\tau_H = T_H r_H$, $\tilde{x} = x - m\Omega/r_H$ and Q is an integer that counts modes. The modes are ordered with increasing j and within equal j modes they are ordered with increasing m.

Cumulative functions are more convenient since they allow for high efficiency when selecting the quantum numbers. This is done by generating a random number in the range $[0, C(\infty)]$, followed by inversion of the corresponding cumulant. In `CHARYBDIS2`,

[3] Note we have restored r_H in these expressions.

when values of a_* between those mentioned above are called, linear interpolation is used. When a_* is larger than 5, we use the cumulative functions for $a_* = 5$. We have checked that for most of the evaporation such large values are very unlikely. The exception is the final stage, when the black hole mass approaches the Planck mass. Here one of the remnant models takes over, as described in section 7.3.1.

7.2.1 Back-reaction and spin-down

The difficult problem of studying the back-reaction is interesting, both from the theoretical and the phenomenological point of view, since it should start to influence the evaporation as the mass of the black hole is lowered.

On the theory side, there is no well established framework to study the evolution of a Hawking-evaporating black hole over the full range of possible initial conditions. The usual approach [91, 114, 165, 166] is to write down mean value differential equations for the variation of the parameters (M and J) such as (5.12) and integrate them with appropriate initial conditions. However, this is only valid for a continuous process of emission where the variation of the parameters is very slow and the symmetry of the background spacetime is kept. Thus, it ignores the momentum recoil of the black hole and the change in orientation of the angular momentum axis between emissions, which are certainly negligible for an ultra-massive black hole, but will start to become important as we approach the Planck mass. Furthermore, since the Hawking spectra at fixed background parameters are used, it also neglects the effect of the backreaction on the metric by the emitted particle. This point has been explored in simplified cases of $j = 0$ waves for fields of several spins using the method in [167] with some results regarding the modification of the thermal factors, but a full treatment is still lacking.

In the program, we have included two possible models for the momentum recoil of the black hole set by the switch `RECOIL`, which takes the values 1 or 2. The orientation of the momentum vector is always computed using the square modulus of the spheroidal function (6.1). This is due to the decomposition of spheroidal one-particle states into plane wave one-particle states,[4] which is analogous to the decomposition of spherical waves into plane waves, for the usual case of scattering off a spherical potential, as presented in section 5.3.4.

`RECOIL` = 1 interprets the selected energy as the energy of the particle in the rest frame of the initial black hole. The momentum orientation is computed in this frame

[4]Note that in the convention of equation (6.1) the physical helicity of the particle is actually $-h$.

with probability distribution given by the square modulus of the spheroidal function (6.1) and the momentum of the final black hole is worked out from conservation. The argument for this model comes from the observation that particles in the decay are highly relativistic. They propagate close to the speed of light, so the background they see is that of the initial black hole, since no signal of the back-reaction on the metric can propagate outwards faster than light. Thus the momentum of the emission is determined by the background metric in this picture.

`RECOIL` = 2 takes the energy of the emission as being the loss in mass of the black hole. This corresponds to the usual prescription for computing the rate of mass loss. The orientation of the momentum in the rest frame of the initial black hole is computed as before with a probability distribution given by the square modulus of the spheroidal function (6.1) and the 4-momentum of the emission as well as that of the black hole are worked out.

Note that for any of the previous options, full polarization information of the emission is kept, as it is generated with the correct angular distribution. This will potentially produce some observable angular asymmetries and correlations, which would not be present if angular distributions averaged over polarizations had been used.

The other quantity we need to evolve is the angular momentum of the black hole. We have two options, controlled by the switch `BHJVAR`. The default `BHJVAR` = `.TRUE.` uses Clebsch-Gordan coefficients to combine the state of angular momentum $M_z = J$ of the initial black hole (i.e. taking as quantisation axis the rotation axis of the black hole), with the emitted j, m state for the particle. The probability of a certain polar angle and magnitude for the angular momentum of the final black hole is given by the square modulus of the corresponding Clebsch-Gordan coefficient, and the azimuthal angle is chosen with uniform probability. If `BHJVAR=.FALSE.`, the orientation of the axis remains fixed even though the magnitude will change by subtraction of the m value of the emission.

From previous versions of `CHARYBDIS`, we have kept the switch `TIMVAR` which allows one to fix the parameters of the black hole used in the spectrum (such as the Hawking temperature) throughout the evaporation. This option corresponds to a model where the evaporation is no longer slow enough for the black hole to re-equilibrate between emission, so in effect it represents a simultaneous emission of all the final state particles from the initial black hole without any intermediate states.

In figure 7.2 we plot the evolution of the physical parameters M and J for BH events with fixed initial M, in the non-rotating case and the highly rotating case, using the

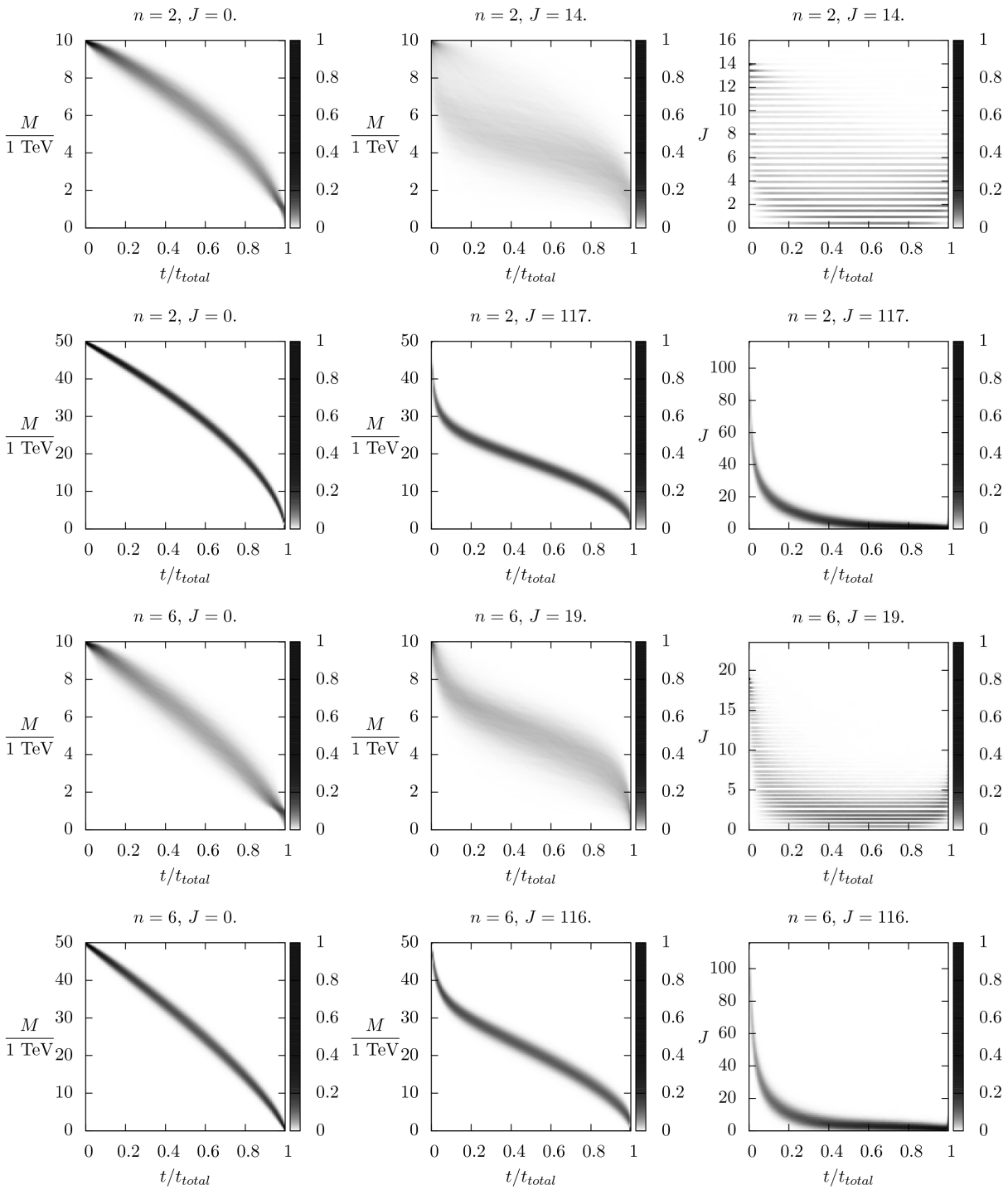

Figure 7.2: Probability maps for physical parameters, constructed from 10^4 trajectories for different BH events with fixed initial conditions M, J (for each horizontal line). Each trajectory contributes with weight 1 to the bins it crosses on the $\{P, t/t_{total}\}$ plane where P is the relevant parameter. Note that the time is normalised to the total time for evaporation t_{total}. The horizontal lines for the plots on the right are due to the discretisation of J in semi-integers.

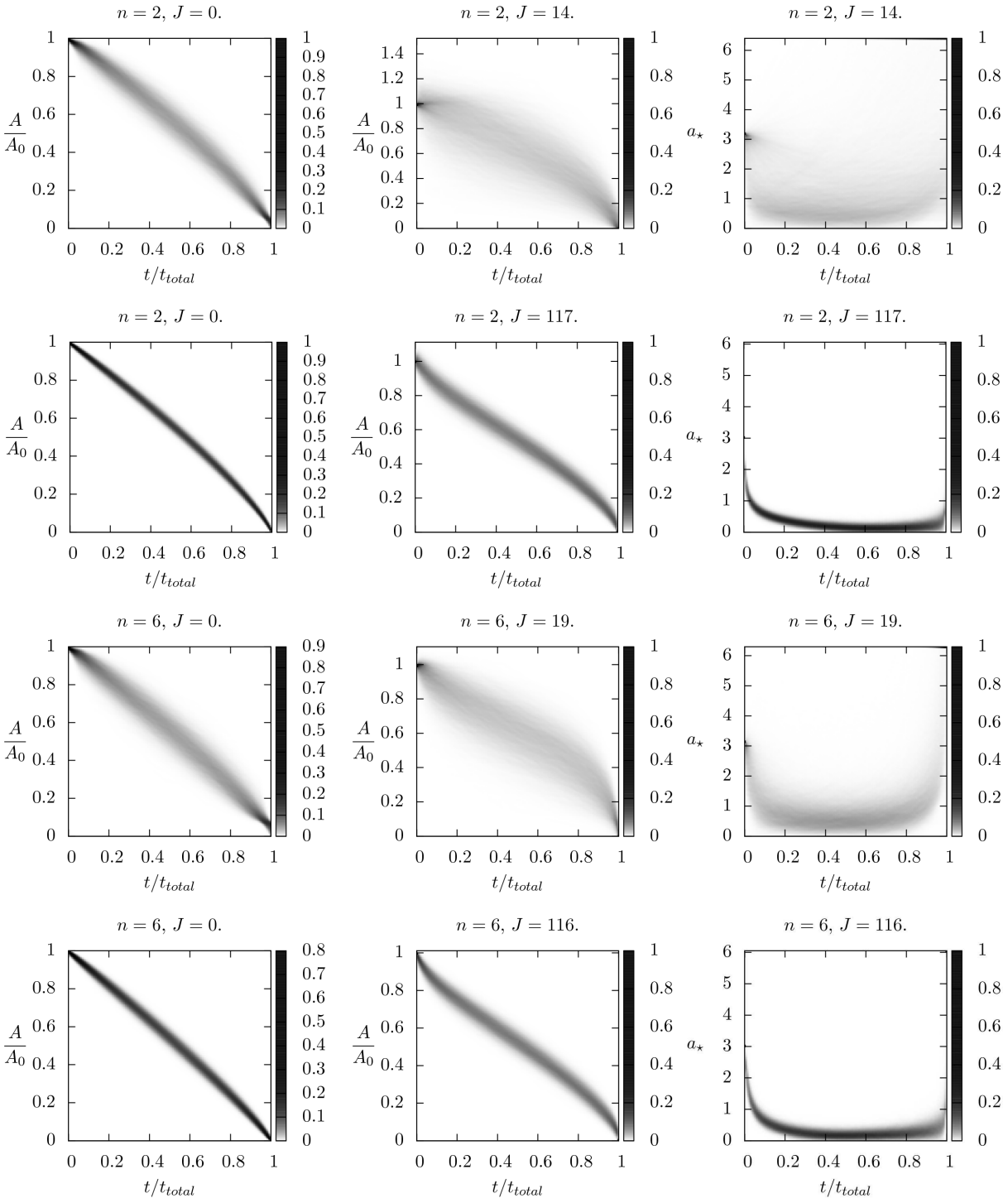

Figure 7.3: Probability maps for the geometrical parameters A and a_* which characterize respectively the size and oblateness of the BH. Note that for the a_* plot in the last $t/t_{total} = 1$ line there is very often a jump to very large a_*. In these plots we have put all such points in the bin on the upper right corner to avoid squashing the interesting region. Each horizontal line has the same initial M, J as the corresponding one in figure 7.2.

default values for the evaporation model (see table 7.1 in section 7.4.2). In figure 7.3 we plot the horizon area and oblateness for the same cases as in figure 7.2.

Events were generated for two possible initial masses, 10 TeV (reachable at the LHC) and 50 TeV. The latter serves as a check of the semi-classical limit. We focus on $n = 2$ and $n = 6$. An important quantity necessary to produce these plots, is the time between emissions. Since our model for the evolution relies on the mean value equation (5.12), before each emission, an average time can be computed (i.e. δt for $\delta N = 1$):

$$\delta N = \frac{dN}{dt}\delta t \quad \Rightarrow \quad \delta t = \left[\frac{dN}{dt}\right]^{-1},$$

where a sum over all species is assumed (see section 7.3.1 for further details).

Each plot contains 10^4 trajectories (one per event generated), each contributing with weight 1 to the density plot. The darker areas correspond to higher probability and in all the plots we can discern a tendency line which is sharper for the 50 TeV case and more diffuse for 10 TeV, reflecting the magnitude of the statistical fluctuations.

The left columns of figures 7.2 and 7.3 show respectively the evolution of the mass parameter and horizon area for non-rotating black holes. The centre and right columns show the evolution of the mass and angular momentum, or the horizon area and oblateness, for the highly rotating case ($a_* \simeq 3$). The main features are as follows:

- *Non-rotating case:* Both M and A decrease approximately linearly with time except for the last $\sim 10 - 20$ % when they drop faster. This is directly related to the behaviour of the temperature which increases slowly (approximately linearly) for most of the evaporation and rises sharply near the end. The rates tend to be faster for higher n which is in agreement with the increase in Hawking temperature with n.

- *Highly-rotating case:* Here the statistical fluctuations tend to smear out the plots for the case of lowest mass. However, the same tendency can be seen as for the $M = 50$ TeV black holes; the latter display better a true semi-classical behaviour. There is in general an initial period of roughly $10 - 15$ % of the total time when M drops faster to about $60 - 70$%. At the same time the angular momentum also drops sharply to 20 %. This corresponds to the usual spin-down phase [166]. Note that the fluctuations are quite large for the low-mass $n = 2$ plots. As for the geometrical parameters, they follow a similar tendency if we make the correspondences $M \leftrightarrow A$ and $J \leftrightarrow a_*$. Again for the low-mass plots the statistical fluctuations smear out

the sharper initial drop in area, in particular for $n = 2$ in which it can occasionally increase substantially. The a_* plots show how the black hole tends to become more spherical in this spin-down phase. The remainder of the evolution resembles the non-rotating case and can be identified with a Schwarzschild phase. Note however that by the end of the evaporation (when M approaches the Planck mass) this description breaks down and a_* rises again, since even only one unit of angular momentum has a very large effect on this quantity at the Planck scale. This means that a_* ceases to have a well defined geometrical meaning, as we reach the Planck phase. Similarly to the non-rotating case, we have checked that the temperature increases slowly and approximately linearly for most of the evaporation except for a sharp rise as the Planck mass is approached.

These observations agree with the usual results in four dimensions[5] and the results of [111] in D dimensions.

7.3 Remnants

Our model for black hole decay relies heavily on the assumptions that we are in the semi-classical regime and the evaporation is slow (i.e. there is enough time for re-equilibration between emissions) [24, 168]. However, as the evaporation evolves, we will reach a point where neither of these assumptions will be true as the mass and/or temperature of the black hole become comparable with the Planck scale, so a complete theory of quantum gravity is required. In the absence of such a theory, various models for the termination of black hole decay have been suggested [169–174]. In the generator we introduce some remnant models based on different physical assumptions. These are discussed in what follows.

7.3.1 Termination of the black hole decay

First of all, we need a criterion to decide whether or not the remnant stage has been reached. The various options in the program are connected to a departure from semi-classicality. This occurs when the expectation value $\langle N \rangle$ for the number of emissions becomes small, which is a sign of the low number of degrees of freedom associated with the black hole. Together with the drop in $\langle N \rangle$, the Hawking temperature will rise sharply.

[5] see for example [166] or chapter 10.5.3 of [48]

This is all related to the approach of the black hole mass to the Planck mass. The options are:

- `NBODYAVERAGE=.TRUE.`: An estimate for the multiplicity of the final state is computed at each step during the evaporation, according to the Hawking spectrum:

$$\langle N\rangle \simeq \frac{dN}{dt}\delta t \simeq \frac{dN}{dt}M\left(\frac{dE}{dt}\right)^{-1} = Mr_H\frac{\sum_i g_i\left(\frac{1}{r_H}\frac{dN}{dt}\right)_i}{\sum_j g_j\left(\frac{dE}{dt}\right)_j}. \tag{7.14}$$

  The sums are over all particle species with appropriate degeneracies g_i. The integrated flux and power are computed using (5.12). A natural criterion for stopping the evaporation is when this estimate drops below some number close to 1. In the generator we use $\langle N\rangle \leq$ `NBODY` $- 1$ where `NBODY` gives the average multiplicity of the remnant decay final state (see section 7.3.3 for further comments). Varying the parameter `NBODY` will give a measure of uncertainties in the remnant model. In addition, if we choose a remnant model that decays, (7.14) gives an estimate of the final state multiplicity for such a decay. When `NBODYAVERAGE` = `.FALSE.`, one of the options below, inherited from earlier versions of `CHARYBDIS`, is used.

- `KINCUT=.TRUE.`: Terminate evaporation if an emission is selected which is not kinematically allowed. This is closely related to the rapid increase in temperature as we approach the Planck mass and consequently the generation of kinematically disallowed energies for the emission. Otherwise if `KINCUT` = `.FALSE.` the kinematically disallowed emissions are rejected and the evaporation terminates when the mass of the black hole drops below the Planck mass[6].

7.3.2 Fixed-multiplicity decay model

The default remnant decay option is a fixed-multiplicity model similar to that in earlier versions of `CHARYBDIS`. At the end of the BH evaporation, the remaining object is decayed isotropically in its rest frame, into a fixed number `NBODY` of primary particles, where the parameter `NBODY` is an integer between 2 and 5. The decay products are chosen with

[6]The Planck mass used in `CHARYBDIS2` to decide on the termination is always the internal one, `INTMPL`, which is obtained by converting the Planck mass input by the user (in a given convention), to the Giddings-Thomas convention – see Appendix A.2.

relative probabilities appropriate to the final characteristics of the black hole (i.e. weighted according to the integrated Hawking fluxes for each spin).

The selection of the outgoing momenta of the decay products may be chosen either using pure phase space (`NBODYPHASE=.TRUE.`) or by using the following probability density function in the rest frame of the black hole (`NBODYPHASE=.FALSE.`):

$$\mathrm{d}P \propto \delta^{(4)} \left(\sum_i p_i - P_{BH} \right) \prod_i \rho_i \left(E_i, \Omega_i \right) \mathrm{d}^3 \mathbf{p}_i \ , \tag{7.15}$$

which amounts to the usual phase space momentum conservation with an extra weight function for each particle

$$\rho_i \left(E_i, \Omega_i \right) = \frac{\mathbb{T}_k^{(D)}(E r_H, a_*)}{\exp(\tilde{E}/T_H) \pm 1} \left| S_k(\cos\theta_i) \right|^2 \ , \tag{7.16}$$

where $k = \{j, m\}$ are chosen according to the cumulants (7.13) combined with angular momentum conservation. Here E_i, Ω_i are the energy and momentum orientation of the emission in the rest frame of the remnant. The method for generating the phase space (7.15) is described in appendix D.2. This choice treats the final state particles on an equal footing, keeping a gravitational character for the decay (since it uses Hawking spectra), as well as some correlations with the the axis of rotation through the spheroidal function factor. Furthermore, at this stage, slow evaporation should no longer be valid, so it makes sense to perform a simultaneous decay at fixed black hole parameters. This remnant option can be used with any of the criteria for termination.

7.3.3 Variable-multiplicity decay model

In addition to a fixed multiplicity final state, an option has been introduced to select the multiplicity of the final state on an event-by-event basis. We follow an idea in [175], which has been used for example in the case of $2 \to 2$ sub-processes in [172]. Here we implement a more general model for arbitrary multiplicity, which is invoked by setting the parameter `NBODYVAR=.TRUE.`.

As argued previously, when the remnant stage is reached, the black hole should no longer have time to re-equilibrate between emissions. Under this assumption, the probability distributions should become time independent. It is relatively straightforward to prove that under these conditions for a time interval δt, the multiplicity follows a Poisson

distribution [175]:

$$P_{\delta t}(n) = e^{-\alpha \delta t} \frac{(\alpha \delta t)^n}{n!} \quad , \tag{7.17}$$

with α some constant. From the Hawking flux, we have computed an estimate for the average number of particles emitted during δt (i.e. the time interval until all mass disappears), so α is determined from this condition. The final result is

$$P_{\delta t}(n) = e^{-\langle N \rangle} \frac{\langle N \rangle^n}{n!} \quad , \tag{7.18}$$

where $\langle N \rangle$ is the estimate in (7.14). This expression gives us an estimate for the probability of emission of n particles from the remnant, so we choose to interpret $n + 1$ as the multiplicity of the final system. In the generator we have removed the $n = 0$ case (i.e. multiplicity 1 final state) since the probability of the remnant to have all the correct quantum numbers and mass of a standard model particle will be vanishingly small.

After the multiplicity is chosen, either the pure phase space decay or the model described in the previous section is used, according to the value of `NBODYPHASE`.

7.3.4 Boiling model

The boiling remnant model, activated by setting `RMBOIL=.TRUE.`, is loosely motivated by the expectation that at the Planck scale the system becomes like a string ball [169, 176], which has a limiting temperature due to the exponential degeneracy of the string spectrum [173]. In this model, evaporation of the BH proceeds until the Hawking temperature for the next emission would exceed a maximum value set by the parameter `THWMAX`. From that point on, the temperature is reset to `THWMAX` and the oblateness is frozen at the current value. The remaining object evaporates like a BH with those characteristics, until its mass falls below a value set by the parameter `RMMINM`. It then decays into a fixed number `NBODY` of primary particles, as in the fixed-multiplicity model, or a variable number if the variable-multiplicity model is on.

7.3.5 Stable remnant model

A number of authors have proposed that the endpoint of black hole evaporation could be a stable remnant [170, 171, 174]. This option is activated by setting `RMSTAB=.TRUE.`. In order for the cluster hadronisation model of `HERWIG` to hadronise the rest of the final state successfully, the stable remnant must be a colourless object essentially equivalent to

a quark-antiquark bound state. Therefore it is required to have baryon number $B_R = 0$ and charge $Q_R = 0$ or ± 1.

The stable remnant appears in the event record as `Remnant0`, `Remnant+` or `Remnant-`, with PDG identity code 50, 51 or –51, respectively, according to its charge. This object will behave as a heavy fundamental particle with conventional interactions in the detector.

If a remnant with $B_R \neq 0$ or $|Q_R| > 1$ is generated, the whole BH evaporation is repeated until $B_R = 0$ and $|Q_R| \leq 1$. This can make the stable remnant option much slower than the other options, depending on the length of the black hole decay chain.

7.3.6 Straight-to-remnant option

Recently, there has been discussion of the possibility that the formation of a semi-classical black hole may lie beyond current experimental reach, with low-multiplicity gravitational scattering more likely at the TeV scale [172]. To simulate this scenario, `CHARYBDIS2` provides the option of bypassing the evaporation phase by setting the switch `SKIP2REMNANT=.TRUE.` and skipping directly to one of the remnant models presented in the previous sections. This permits the study of a wide range of qualitatively different possibilities, from simple $2 \to 2$ isotropic scattering (fixed multiplicity) to more complicated variable-multiplicity $2 \to N$ sub-processes.

The $2 \to N$ model is particularly flexible, allowing either a phase-space distribution or one using the Hawking energy and angular spectra (see section 7.3.3). Apart from this, all particle species are treated on an equal footing consistent with conservation laws. Alternatively the quantum-gravity motivated boiling model can be used. Further work will be presented in future publications exploring the phenomenological consequences of these scenarios.

7.4 Program structure and usage

In this section we describe in detail the structure of the `CHARYBDIS2` program. We will focus on the new features, however a brief description of some features that were kept or derived from `CHARYBDIS` is presented. The code for the original program was developed in fortran 77 so we kept the same programing language.

Section 7.4.1 provides an overall description of the main logical building blocks of the program and how they interact. In the following three sections the main blocks of the run are explained in further detail.

7.4.1 General structure

Figure 7.4 describes the general structure of the code and its interface to a general purpose parton showering and hadronisation generator. This can be split in three types of units of code organised in three horizontal layers in the diagram:

- *The main program:* This is the code which contains the main program and controls the run. It reads the input and initialises all variables which are used in the run; it runs the program by calling the relevant routines of the event generator; it analyses the events, and finally it produces output files. There are three possible main programs available to the user, `maincharybdis.f`, `mainherwig.f` and `mainpythia.f`. The first runs `CHARYBDIS2` standalone without the second layer in the diagram (dashed boxes), so only the hard process in figure 7.1 gets generated. The other two modes interface to `HERWIG` [93, 94] and `PYTHIA` [95] respectively for the parton showering, hadronisation and secondary decays.

- *General purpose event generator:* This is either the `herwig*.f` code or `pythia*.f` code[7] which contains the subroutines responsible for: generating the showering of the initial and final state partons involved in the hard process; performing secondary decays of unstable particles, and hadronising the final state quarks and gluons (see figure 7.1). These routines are called from the main program unit when the respective `HERWIG` or `PYTHIA` interfaces are enabled.

- *Black Hole event generator* (`CHARYBDIS2`): This is the `charybdis2*.F` code which contains the subroutines responsible for generating hard process events with the corresponding weights (according to the differential cross-section (7.8)). In the standalone `CHARYBDIS2` implementation, they are called directly from the main program unit (in `maincharybdis.f`), whereas for the `HERWIG` or `PYTHIA` implementation they are called indirectly by the initialisation and event generation routines of `HERWIG` or `PYTHIA` in the main program unit (`mainherwig.f` or `mainphythia.f`).

On the other hand, the running of the program can be described in three stages (three columns connected by vertical lines in the diagram) which are called in sequence from the main program:

- *Initialisation:* The input conditions for the incoming beams are set, together with the parameters for the model for black hole production and decay. If `HERWIG` or

[7] The asterisk represents the version number.

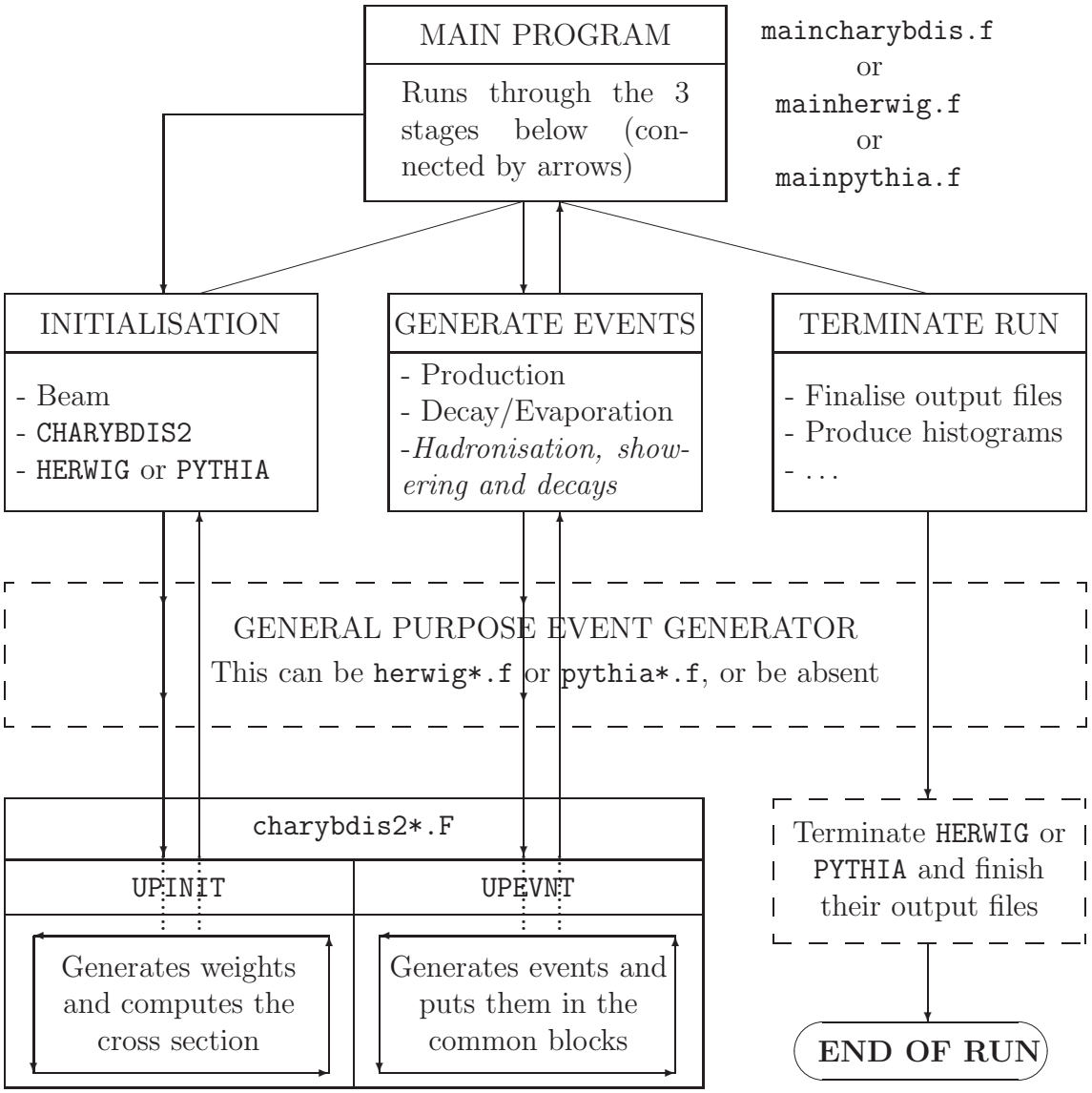

Figure 7.4: Diagram illustrating the general code structure of CHARYBDIS2. The run is controlled by a main program unit which calls in sequence three sets of routines, denoted above by *initialisation*, *generate events* and *terminate run*. Each of these may or may not be interfaced to a general purpose event generator which is represented by the dashed box. The flow of arrows shows the order in which the various blocks of code are executed and returned to.

PYTHIA are used, some initialisation routines are called which perform a weight search and compute the cross-section by calling the CHARYBDIS2 subroutine UPINIT. Otherwise, UPINIT is called directly from the main program. Some routines which perform some user defined initial calculations are called and output files are prepared for the run.

- *Event generation:* The routine UPEVNT which generates the hard process event is called either directly from the main program (standalone mode) or through the event generation routines in HERWIG or PYTHIA. Parton showering, hadronisation and secondary decay routines are also called at this point. The (user-defined) analysis routines are called, and the event is stored in appropriate output files.

- *Termination of the run:* Event generation is stopped, the (user-defined) final calculations are performed and the output files are finalised.

In the next sections we describe in detail each stage. Instructions on how to set up the latest release of the code [3] are provided in appendix D.1.

7.4.2 Initialisation

The diagram in figure 7.5 represents the initialisation routines for the three possible main programs (mainpythia.f, maincharybdis.f and mainherwig.f) divided in three blocks (dashed boxes).

The first block is common to all implementations and consists of two subroutines which set the values of the parameters for the run which control: the characteristics of the beam, the model used for the black hole events, and some conventions. This can be done either by setting the values in the subroutine CHDEFAULTS or by editing the charybdis2.init file provided with the code (this is read by the subroutine CHREADINITFILE). A summary of all the variables that are set in the initialisation is provided in table 7.1.

In the second block the (CHARYBDIS2 defined) UPINIT subroutine which is responsible for searching for the maximum weight of the distribution (7.2) and computing the total cross-section (7.3) is called either directly, in the maincharybdis.f implementation, or through PYINIT or HWIGIN, for the mainpythia.f and mainherwig.f implementations respectively. The UPINIT subroutine is explained in appendix D.3. Note that the mainherwig.f implementation contains other initialisation code, which for example defines the black hole and stable remnant particle codes, and computes other quantities to be used internally by HERWIG.

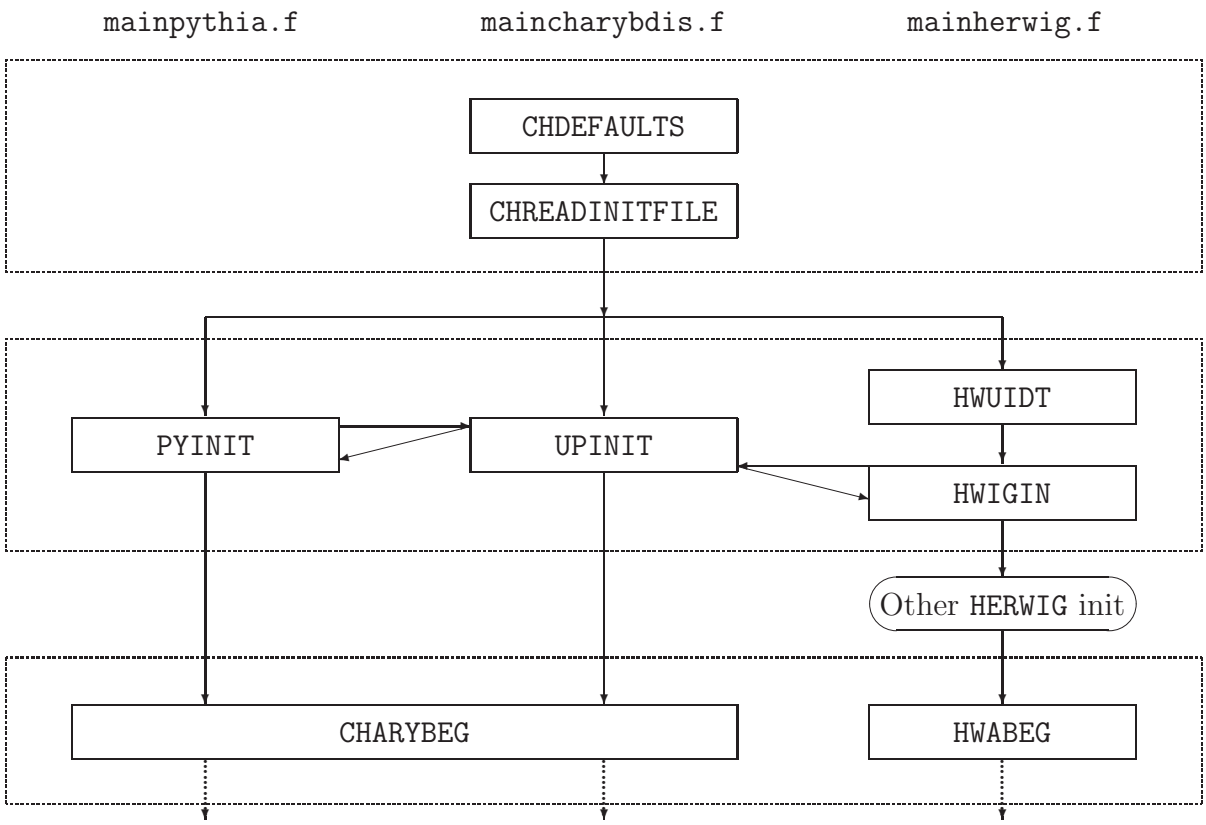

Figure 7.5: Diagram illustrating the run of the initialisation block for the three possible implementations (running vertically, the `PYTHIA`, `CHARYBDIS2` and `HERWIG` implementations respectively). *Top block:* Read input parameters. *Middle block:* Initialise general purpose generator and weight search. *Bottom block:* User-defined Initial calculations routines. The three bottom dotted arrows indicate the event generation block follows (figure 7.6).

Finally, in the last block, user-defined initial calculations and output files are prepared for the run. For example headers are prepared for the Les Houches Event files (LHE) [177] where the events are stored, and the histories file where the black hole histories are stored. The subroutines `CHARYBEG` and `HWABEG` (for `HERWIG`) can be edited according to the needs of the user.

7.4.3 Event generation

The diagram in figure 7.6 is divided in two blocks (dashed boxes) to describe the event generation loop.

In the first block the subroutine `UPEVNT` is called to generate the black hole and its evaporation, either directly (`maincharybdis.f`) or through the `PYEVNT` (`mainpythia.f`)

Variable name	Description	Default
EBMUP(I)	Beam energies (I=1,2)	7 TeV
IDBMUP(I)	Beam identity	2212 (p)
PDFGUP(I)	Codes for PDF group	—
PDFSUP(I)	Codes for PDF set	—
LHAPDFSET	Code for PDF set when using LHAPDF	10000
MINMSS	Minimum partonic centre of mass energy	5 TeV
MAXMSS	Maximum partonic centre of mass energy	14 TeV
NRN(I)	Seeds for the pseudo-random number generator	—
TOTDIM	Total number of dimensions	6
MPLNCK	Higher dimensional Planck mass	1 TeV
MSSDEF	Convention for Planck mass	3
GTSCA	Use Giddings-Thomas scale for PDFs	.FALSE.
YRCSC	Use Yoschino-Rychov cross-section enhancement	.TRUE.
MJLOST	Simulation of M, J lost in production/balding	.TRUE.
CVBIAS	'Constant angular velocity' bias	.FALSE.
FMLOST	Isotropy of gravitational radiation lost	0.99
MSSDEC	Allowed decay products (3=all SM particles)	3
GRYBDY	Include grey-body factors	.TRUE.
TIMVAR	Allow T_H to evolve with BH parameters	.TRUE.
BHSPIN	Simulate rotating black holes	.TRUE.
BHJVAR	Allow black hole spin axis to vary	.TRUE.
BHANIS	Non-uniform angular functions for the evaporation	.TRUE.
RECOIL	Recoil model for evaporation	2
NBODY	Number of particles in the remnant decay	2
KINCUT	Use a kinematic cut-off in the evaporation	.FALSE.
THWMAX	Maximum Hawking temperature	1 TeV
RMSTAB	Stable remnant model	.FALSE.
NBODYAVERAGE	Use flux criterion for remnant – see equation (7.14)	.TRUE.
NBODYVAR	Variable-multiplicity remnant model	.FALSE.
NBODYPHASE	Use uniform phase space for remnants	.FALSE.
SKIP2REMNANT	Bypass evaporation phase	.FALSE.
RMBOIL	Use boiling remnant model	.FALSE.
RMMINM	Minimum mass for boiling model	100 GeV
LHEFILENAME	Name for the les houches *.xml output file	lhouches
HISFILENAME	Name for the black hole histories *.xml output file	histfile

Table 7.1: List of parameters for the run set in the initialisation, and some of their default values. The first group defines the beam, PDFs and the hard process centre of mass energy, the second defines the extra-dimensional model, the third the parameters of the model used for the production phase, the fourth the model for evaporation, the fifth the criterion for terminating the evaporation and performing the remnant model, and the last one defines names for two output files.

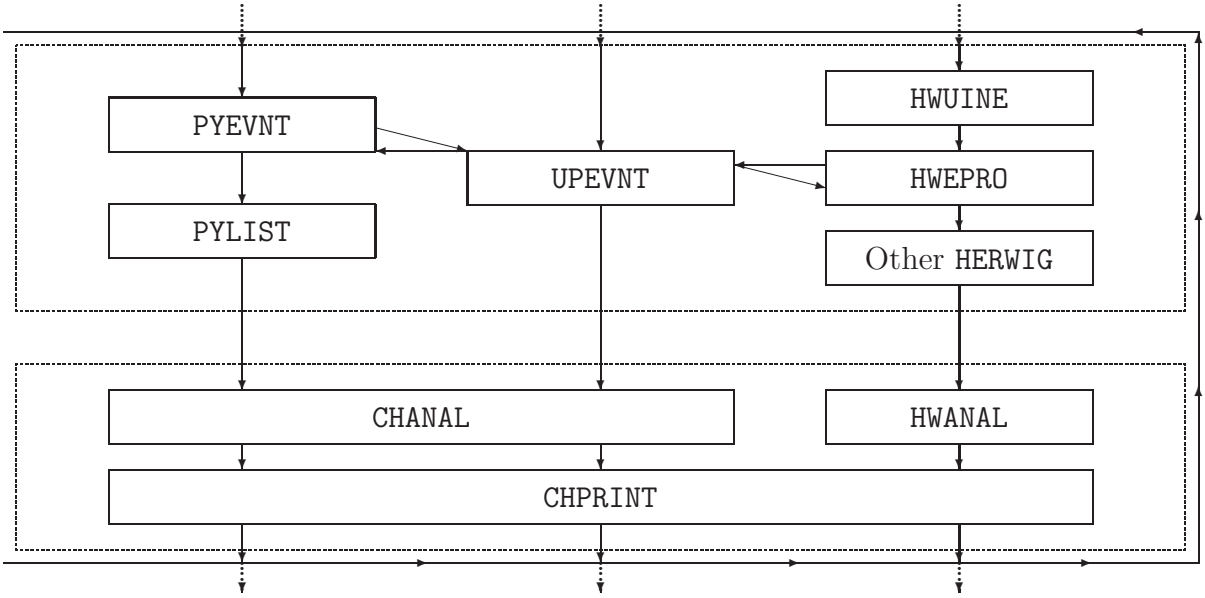

Figure 7.6: Diagram illustrating the event generation loop which follows after initialisation. *Top block:* Generate one hard process event and perform parton showering, secondary decays and hadronisation (for the `PYTHIA` and `HERWIG` implementations). *Bottom block:* Event analysis routines (`CHANAL` and `HWANAL`) and black hole history print-out (`CHPRINT`).

or `HWEPRO` (`mainherwig.f`) subroutines. Note that in the last two implementations other internal subroutines are called which are responsible for the parton showers, secondary decays, hadronisation and printing the event information on screen. A detailed description of the `UPEVNT` and how the model described in the beginning of this chapter is implemented, is provided in appendix D.4. Note that `UPEVNT` generates weighted events. However either in the main program or in the subroutines `PYEVNT` or `HWEPRO` the event is accepted or rejected according to the weight to maximum weight ratio so as to generate unweighted events.

In the second block, the event is analysed by the user-defined subroutines `CHANAL` or `HWANAL`. By default they write the event information in the LHE file `lhouches.xml` and the black hole decay history in the histories file `histfile.xml`. The subroutine `CHPRINT` prints the black hole history on screen.

The arrows around the box in the diagram indicate that the loop is iterated until a maximum number of unweighted events (set by the user) has been generated. The dotted arrows indicate continuation to the termination block when the loop is finished.

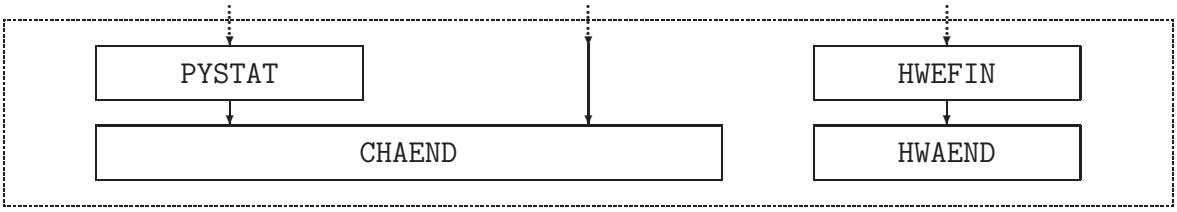

Figure 7.7: Diagram illustrating the termination of the run where the general purpose event generators are terminated and the event analysis is finalised.

7.4.4 Termination

After the maximum number of events for the run (`CHNMAXEV`) is generated, the termination subroutines are called (see figure 7.7). For the `mainpythia.f` and `mainherwig.f` implementations the subroutines `PYSTAT` and `HWEFIN` perform final calculations, obtain the total cross-section and print out some other information for the run. The user-defined subroutines `CHAEND` and `HWAEND` terminate the event analysis and finish the output files.

7.5 CHARYBDIS2 and other generators

In this chapter we have presented an improved black hole event generator to take into account some of the latest theoretical developments, in particular the important effect of rotation in the evaporation phase. The only other current simulation program which models this effect is the `BlackMax` generator [178, 179]. Both programs take black hole angular momentum fully into account, but they have other features and emphases that are complementary. In the formation phase, `BlackMax` uses a geometrical approximation for the cross section and parametrizes the loss of energy and angular momentum as fixed fractions of their initial-state values, whereas `CHARYBDIS2` incorporates a more detailed model based on the Yoshino-Rychkov bounds and comparisons with other approaches. The treatment of the evaporation phase in the two programs appears broadly similar, but `BlackMax` has options for brane tension and split branes, and for extra suppression of emissions that would spin-up the black hole, while `CHARYBDIS2` includes treatment of the polarisation of emitted fermions and vector bosons. The conservation of quantum numbers is also treated somewhat differently. At the Planck scale, `BlackMax` emits a final burst of particles with the minimal multiplicity needed to conserve quantum numbers, whereas `CHARYBDIS2` has a wider range of options.

A deficiency of both programs is the absence of gravitational radiation in the evap-

oration phase. This is because the transmission factors have not yet been computed for this case, due to extra theoretical difficulties in the separation of variables. Unlike Standard-Model particles, gravitons will necessarily be emitted into the bulk, giving rise to a new source of lost energy and the possibility of recoil off the brane. In the non-rotating case, it is known [110, 132] that bulk graviton emission is small for low numbers of extra dimensions, but increases rapidly in higher dimensions due to the growing number of polarisation states. However, the large number of Standard-Model degrees of freedom ensures that brane emission remains dominant. Clearly a full treatment of the rotating case is desirable, but there is hope that the effects will not be too significant, taking into account the uncertainties in energy loss already allowed for in the formation phase.

Chapter 8

Phenomenological study

The work in this chapter was done in collaboration with James A. Frost. The plots labelled with `CHARYBDIS2.0` and the associated discussion are mostly based on his discussion in section 5 of [4]. The complementary discussion in sections 8.2.4 and 8.2.5 was done separately using a different parton level sample.

We present a study of the phenomenological aspects of the black hole events simulated with `CHARYBDIS2` keeping in mind the LHC experiment with proton beam energies of 7 TeV. For the experimental plots in this chapter, a range of `CHARYBDIS2` samples were produced using `HERWIG 6.510` [93, 94] to do the parton showering, hadronisation and Standard Model particle decays. The results of which were then passed through a generic LHC detector simulation, `AcerDET 1.0` [180]. `CHARYBDIS2` parameter defaults are shown in Table 7.1. In all following discussion, the number of extra spatial dimensions is $n =$ `TOTDIM` $- 4$. Samples were generated with a 1 TeV Planck mass (in the PDG convention, i.e. `MSSDEF` $= 3$) so as to investigate the phenomenologically preferred region accessible at the LHC. Black holes events were generated with a lower partonic centre of mass energy of 5 TeV such that the semi-classical approximations for production are valid.

Our settings for `AcerDET 1.0` are as follows: we select electrons and muons with transverse momentum $P_T > 15$ GeV and $|\eta| < 2.5$. The transverse momentum is defined as the projection of the spatial momentum of the particle on the plane perpendicular to the beam direction. The pseudo-rapidity is $\eta = -\log\left(\tan\frac{\theta}{2}\right)$, where θ is the angle of the spatial momentum with the beam axis. The electrons and muons are considered isolated if they lie at a distance $\Delta R = \sqrt{(\Delta\eta)^2 + (\Delta\phi)^2} > 0.4$ from other leptons or jets and if less than 10 GeV of energy was deposited in a cone of $\Delta R = 0.2$ around the central cluster. The same prescription is followed for photons. Jets are reconstructed

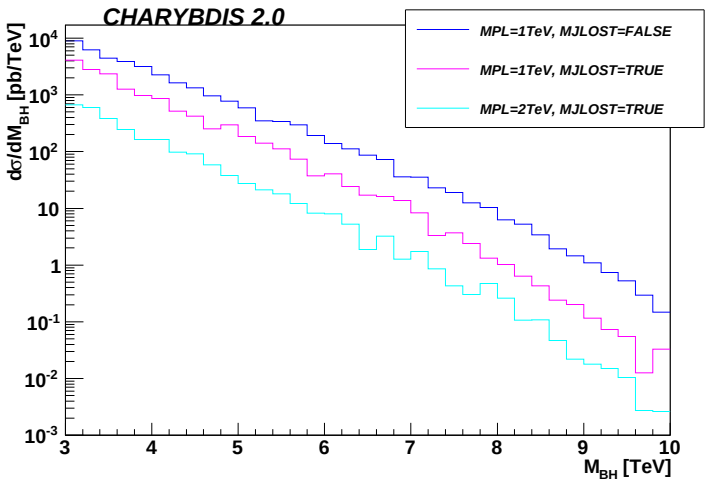

Figure 8.1: *Differential cross-sections for black hole production with* $n = 4$. The differential cross-sections are shown for different Planck masses and `MJLOST` (simulation of mass and angular momentum loss in production/balding).

from clusters using a cone algorithm of $\Delta R = 0.4$, with a lower P_T cut of 20 GeV. Lepton momentum resolutions were parametrised from ATLAS full simulation results published in [181].[1] Where reference is made to reconstructed multiplicities or spectra, the reconstructed objects are either electrons, muons, photons or jets from `AcerDET`.

8.1 Production

The black hole production process we are considering produces typically large hadronic cross-sections for the LHC $\sigma(14\text{ TeV}) \gtrsim 100$ pb. Though not affecting the total black hole cross-section for a certain partonic centre of mass energy range, simulating the mass and angular momentum loss during black hole formation does have a large effect on the cross-section for a particular black hole mass range. The differential cross-section will be reduced, for the same input state will produce a black hole of lesser mass, as is illustrated in figure 8.1. This figure also shows how the total cross-section is a strong function of the Planck mass, since the normalisation of the curve is reduced almost by an order of magnitude from 1 TeV to 2 TeV.

Most collisions with sufficient energy to create a black hole are between two (valence) quarks, however a minority occur in collisions between a quark and a gluon (see top plots

[1] Electrons are smeared according to a pseudo-rapidity dependent parametrisation; for muons, we take the resolutions from $|\eta| < 1.1$.

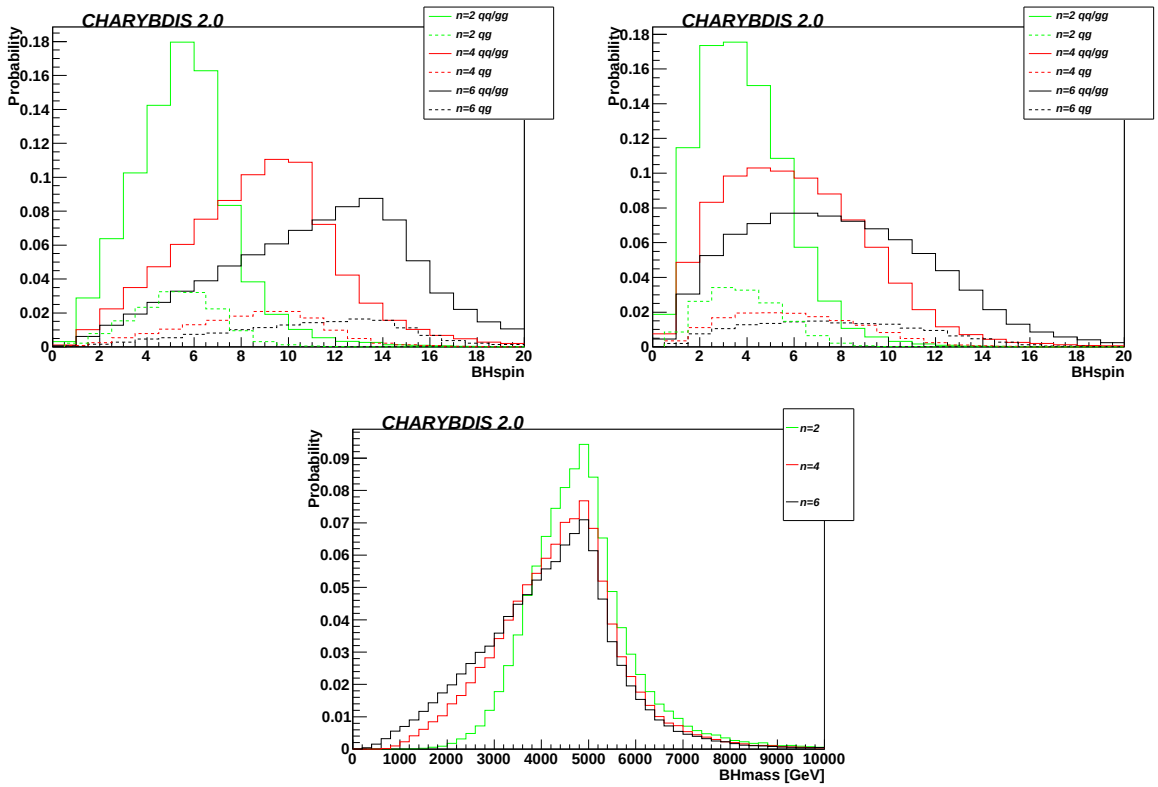

Figure 8.2: *Effects of mass and angular momentum loss in the formation/balding phase:* The left (right) top plot shows the angular momentum distribution before (after) this phase, whilst the bottom plot shows the distribution of black hole masses after the losses. Note how black holes with mass below the partonic centre of mass energy lower cut of 5 TeV are allowed due to the losses.

of figure 8.2). `CHARYBDIS2` adds the spins of the colliding partons when forming a black hole; the initial black hole angular momentum is either integer or half-integer accordingly. An integer loss of orbital angular momentum in the formation process is simulated by the Yoshino-Rychkov model described in section 4.3.2.

At high n the angular momentum of the colliding partonic system tends to be larger, as seen in figure 8.2. The average spin of the produced black hole rises from 5.0 units for $n = 2$, to 8.1 for $n = 4$ and 10.6 for $n = 6$. Setting `MJLOST=.TRUE.` decreases the angular momentum of the produced black hole by an average of 30% for $n = 2$, 4, 6, whilst the mass drops by 18% ($n = 2$) to 30% ($n = 6$). This can be seen qualitatively in figure 8.2 by comparing the top left plot (angular momentum distribution before the loss) and the top right plot (angular momentum distribution after the loss).

8.2 Evaporation

In this section we discuss how the angular momentum affects the phenomenology of the final state particles expected to be observed in the black hole evaporation.

8.2.1 The effect of mass and angular momentum loss

The simulation of loss of mass and angular momentum during the production changes the number and distributions of the final state particles in the decay. For example, the mass of the black hole is the main factor determining the multiplicity of the final state, since it determines the amount of energy available for the evaporation. However, the black hole mass and angular momentum also determine the Hawking temperature and consequently the typical energy of the particles emitted in the decay – a highly rotating, or higher temperature black hole will emit more energetically. These effects result in a decrease of the multiplicity of the final state as seen in the three top plots of figure 8.3. The decrease in the number of Hawking emissions (see the parton level top left plot), follows the drop in mass and is greatest for higher numbers of extra dimensions, with an average of two fewer emissions (or 30%) manifest for $n = 6$.

The reduction in the black hole mass and number of Hawking emissions leads to a decrease in the number of particles observed experimentally and to a reduced differentiation between samples with different numbers of dimensions. The decrease of the initial black hole mass and angular momentum also leads to a softening of the emitted particle spectrum, with the high energy and transverse momentum tail of the distribution being reduced (bottom plots of figure 8.3). This is due to the combined effect of having a smaller amount of energy available, which suppresses Hawking emissions at large energy, and the decrease in angular momentum which shifts the Hawking emission spectrum towards lower energies.

8.2.2 The effect of black hole angular momentum

The inclusion of black hole angular momentum has several large effects upon the spectra of the emitted particles.

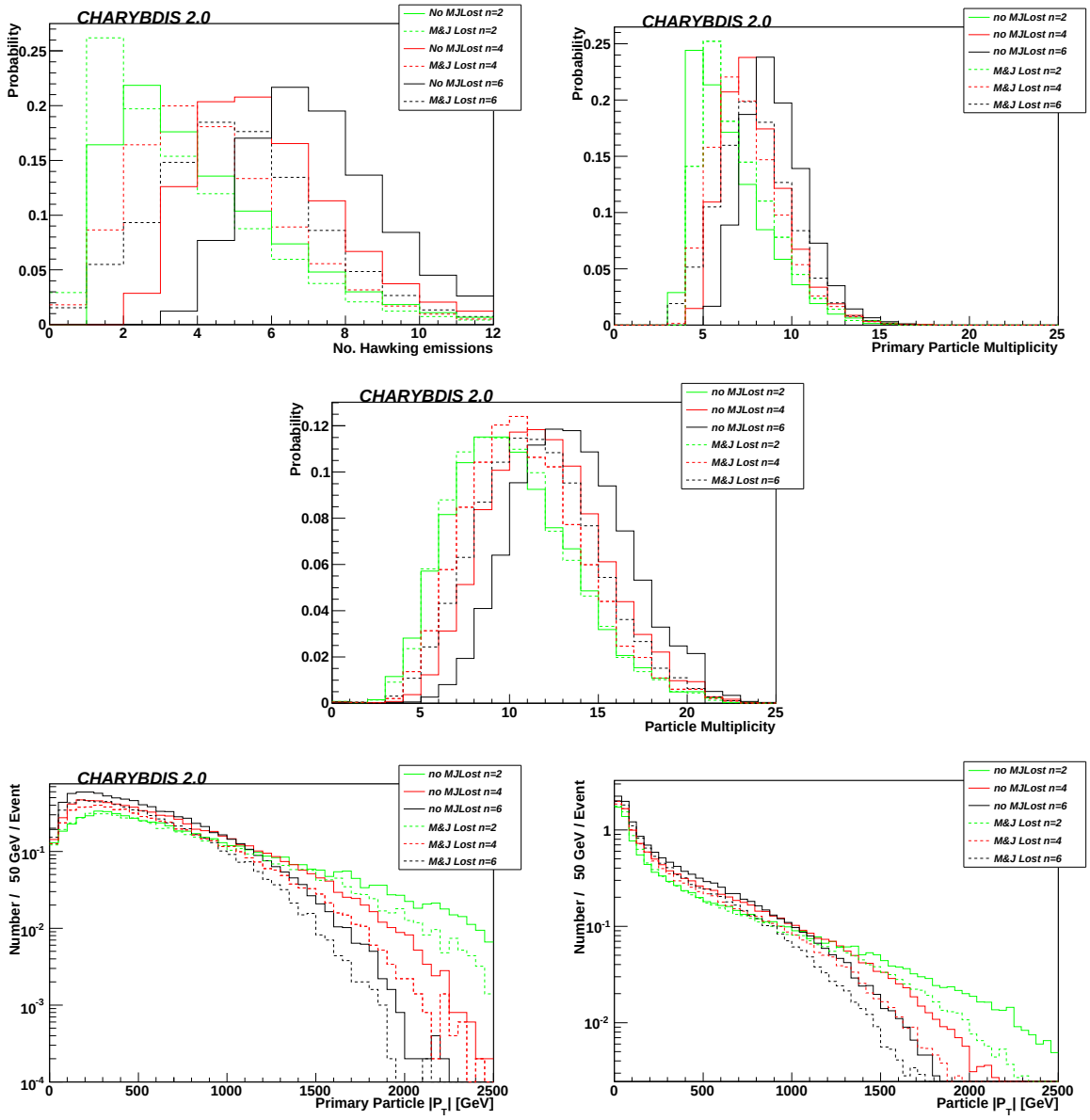

Figure 8.3: *Effect of simulating the mass and angular momentum lost in black hole production:* on particle multiplicity distributions, at parton level (top left), generator level (top right) and after `AcerDET` detector simulation (center); and P_T spectra generator level (bottom left) and after `AcerDET` detector simulation (bottom right). A fixed 2-body remnant decay with the criterion $M <$ `INTMPL` to stop the evaporation was used, with all switches set to their default values.

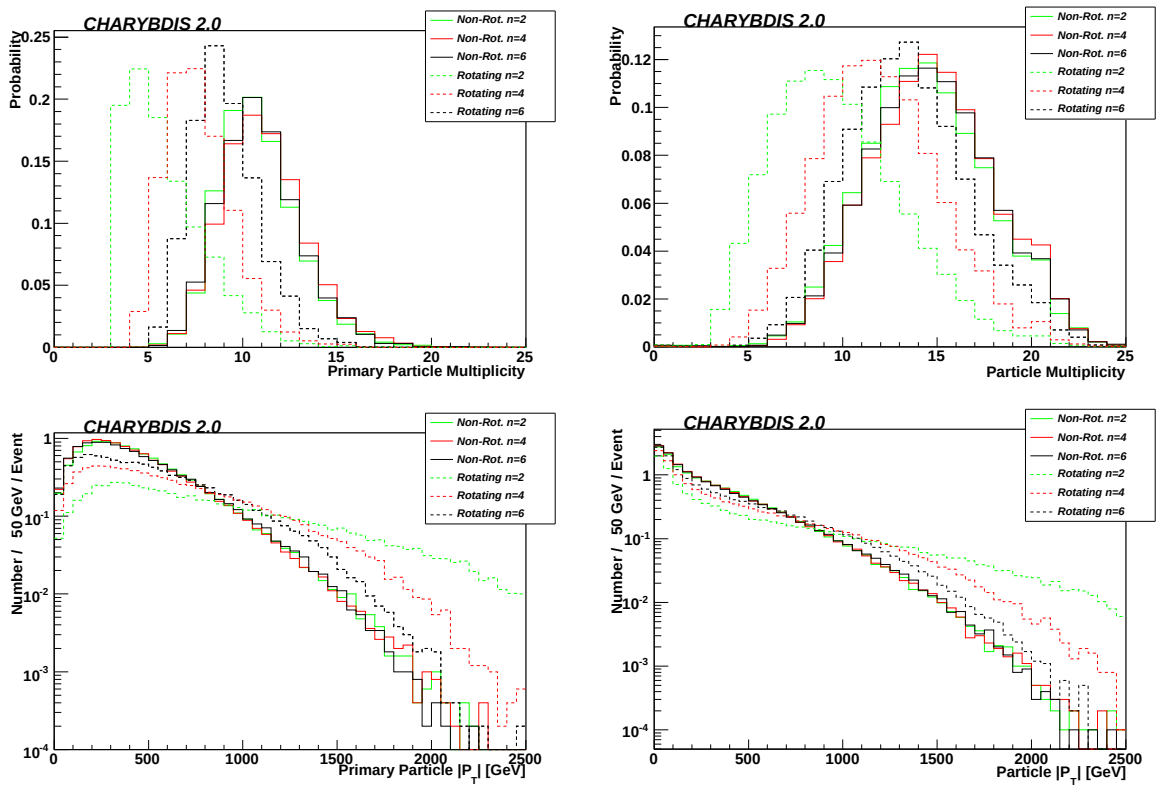

Figure 8.4: Particle multiplicity distributions and P_T spectra at generator level (left) and after `AcerDET` detector simulation (right) for non-rotating and rotating black hole samples, with $n = 2$, 4 and 6 extra dimensions and `MJLOST` = .`FALSE`..

Energy spectra of the final state products

As discussed in section 6.4.4, the Hawking emission spectrum for a rotating black hole is dominated by partial waves with large $m > 0$. The spectrum for these waves is shifted towards higher energies, due to the $-m\Omega_H$ term in the exponential of equation (5.12), which reduces the high energy Planckian suppression. Consequently, the particle energy and transverse momentum (P_T) distributions for emissions from a rotating black hole are harder. The number of primary emissions is correspondingly reduced. Figure 8.4 shows the emitted particle multiplicity and P_T spectra for different numbers of extra dimensions. The effects of black hole rotation are largest for fewest number of extra dimensions, for which the term Ω_H has greater magnitude. This more than compensates for their slightly lower Hawking temperature.

The effect of black hole rotation on the pseudorapidity distribution (figure 8.5) is more subtle. Assuming no strong angular momentum recoil during the balding phase,

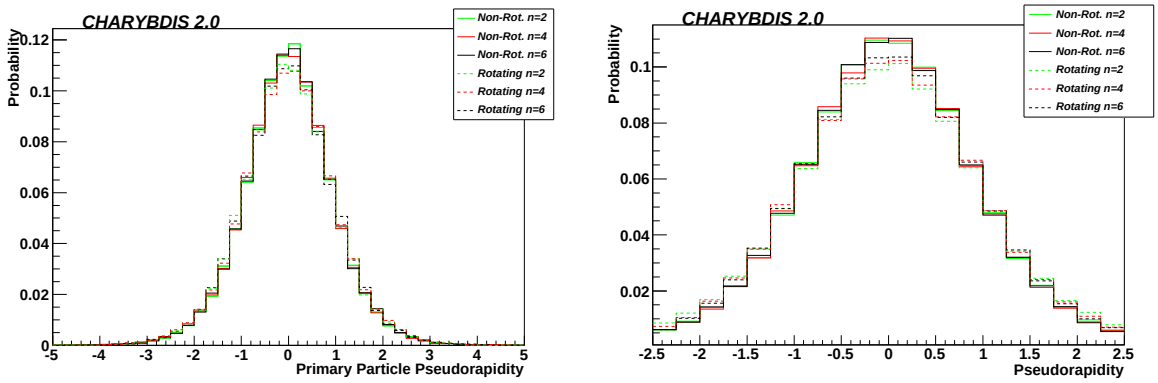

Figure 8.5: Normalised particle η distributions at generator level (left) and after `AcerDET` detector simulation (right) from black hole samples with n extra dimensions and `MJLOST` = `.FALSE.`.

the initial black hole formed will have an angular momentum axis perpendicular to the beam direction. Since emission in the equatorial plane is favoured, particularly for scalars and fermions, one would expect the component along the beam direction, and hence at high η, to be enhanced, at least for initial emissions. This effect is seen experimentally in figure 8.5, but is slight. Another reason why this effect is so washed out is due to the boost between the black hole centre of mass frame and the laboratory frame where the pseudorapidity is defined. In section 8.2.4 we discuss this further at parton level.

Similar trends can be seen in event variables such as missing transverse energy (MET) and $\Sigma|P_T|$ (figure 8.6). The reduced particle multiplicity increases the probability of minimal or no MET, where no neutrinos are present in the event (neither directly emitted by the black hole, nor in weak decays of other primary emissions). The greater energy of the Hawking emissions increases the very high MET tail: a neutrino emitted by a rotating black hole is likely to have higher energy and momentum. The result is a flatter, longer tail for the rotating case, extending further beyond 1 TeV, as shown in figure 8.6. The broadening of the $\Sigma|P_T|$ curves is due to the lower multiplicity which implies bigger fluctuations.

When compared to the number of primary emissions from the evaporation, a greater number of detector objects (leptons, photons, hadronic jets) are observed following fast detector simulation. Neutrinos emitted by the black hole will not be seen experimentally, whereas a single heavy quark or vector boson will result in the detection of multiple particles or jets of hadrons. Equally, the transverse momentum spectrum observed experimentally will be slightly softer in general than that of the primary particles emitted by

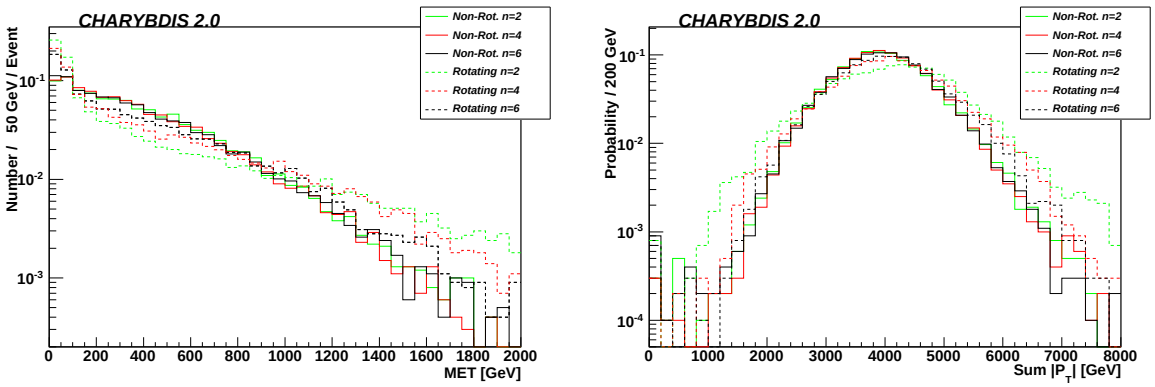

Figure 8.6: Missing transverse energy and scalar P_T sum for rotating and non-rotating black hole samples after `AcerDET` fast detector simulation. Samples used the `NBODYAVERAGE` criterion for the remnant phase and include a simulation of the mass and angular momentum lost during production and balding.

the black hole, due to secondary emissions, decays and radiation.

Particle emission probabilities

Black hole rotation has a large effect on the particle production probabilities (figure 8.7). The most dramatic is the enhanced emission coefficient for vector particles. This is due to the larger fluxes and agrees with the greater differential fluxes per degree of freedom shown for example in figure 6.12 (see vertical axis of the power plots).

The greater proportion of vector emissions would provide strong evidence of rotating, rather than Schwarzschild, black holes. However such measurements are difficult to make in practice – at the LHC it will not be possible to distinguish gluon jets from quark ones. Though highly boosted vector bosons provide experimental challenges, Z bosons can often be studied via their leptonic decay modes. Perhaps the most accessible other means to investigate black hole rotation might be the study of the photon multiplicity or its ratio to other particles, TeV-energy photons being one manifestation of black holes reproduced by neither other new physics scenarios nor SM backgrounds. Another experimental difficulty for the detection and the isolation of the black-hole signal is that rotation decreases the probability of producing a lepton – often useful in reducing jet-like SM backgrounds to black hole events [182].

The emission probabilities for each particle species are largely independent of the number of extra dimensions, which primarily affects the emission energy and multiplicity, so that a reproduction of the distribution of particle species would be powerful evidence

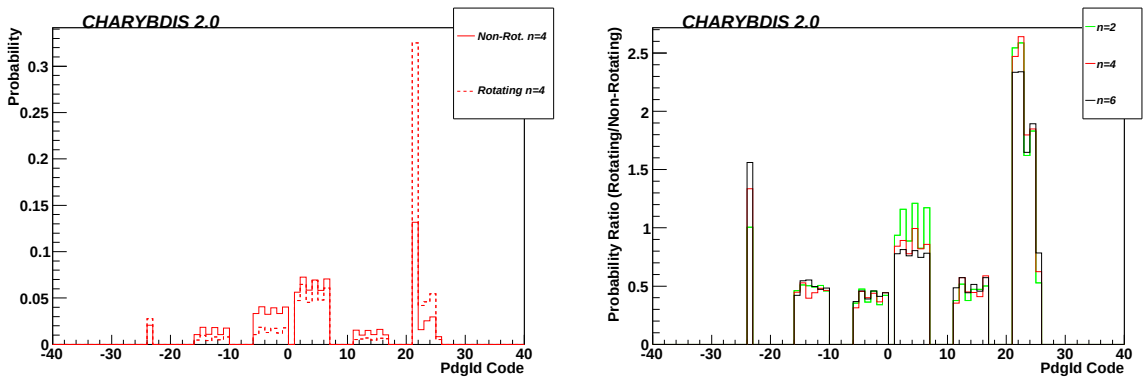

Figure 8.7: Particle emission probabilities for rotating and non-rotating black holes with $n = 4$ (left) and the enhancement factor for each species and different n (right). The horizontal axis shows the PDG code number for the SM particles, as defined in [5]. Quarks codes are 1-6 (down, up, strange, charm, bottom and top), leptons are 11-16 (electron and its neutrino; muon and its neutrino; tau and its neutrino), gauge bosons 21-24 (gluon, photon, Z and W^+) and the Higgs boson 25 (with the `HERWIG` default mass of 115 GeV). Anti-particle states have a negative code.

of black holes. The particle-antiparticle imbalance in figure 8.7 is chiefly caused by the (usually positively charged) input state. According to the model described in section 7.2, up-type quarks and down-type antiquarks are favoured, so as to meet the constraints of charge balance. Similarly, the net positive baryon number of the input state and the need to conserve baryon number for hadronisation leads to a preference for quarks over antiquarks. The apparent increase in this with rotation is a reflection of the reduced particle multiplicity: with fewer particles amongst which to share the charge imbalance, the effect is magnified. This is potentially a source of uncertainty since, unlike charge, black holes do not have to conserve baryon or lepton quantum numbers. At present we are constrained to conserve baryon number by the needs of hadronisation generators. Note that baryon number is in any case not directly observable in experiment (though it may have some subtle effects on the decay), whereas lepton number is. Large lepton number violation could be another signature of a TeV gravity interaction.

Black hole evolution

As the Hawking emission proceeds, the black hole evolves, becoming lighter, hotter and losing angular momentum as detailed in figure 8.8. The higher Ω_H term in the Planckian factor causes there to be fewer, more energetic emissions for few extra dimensions. Half the mass is lost in the first 3 emissions for $n = 2$, compared with 4 ($n = 4$) and 5 for

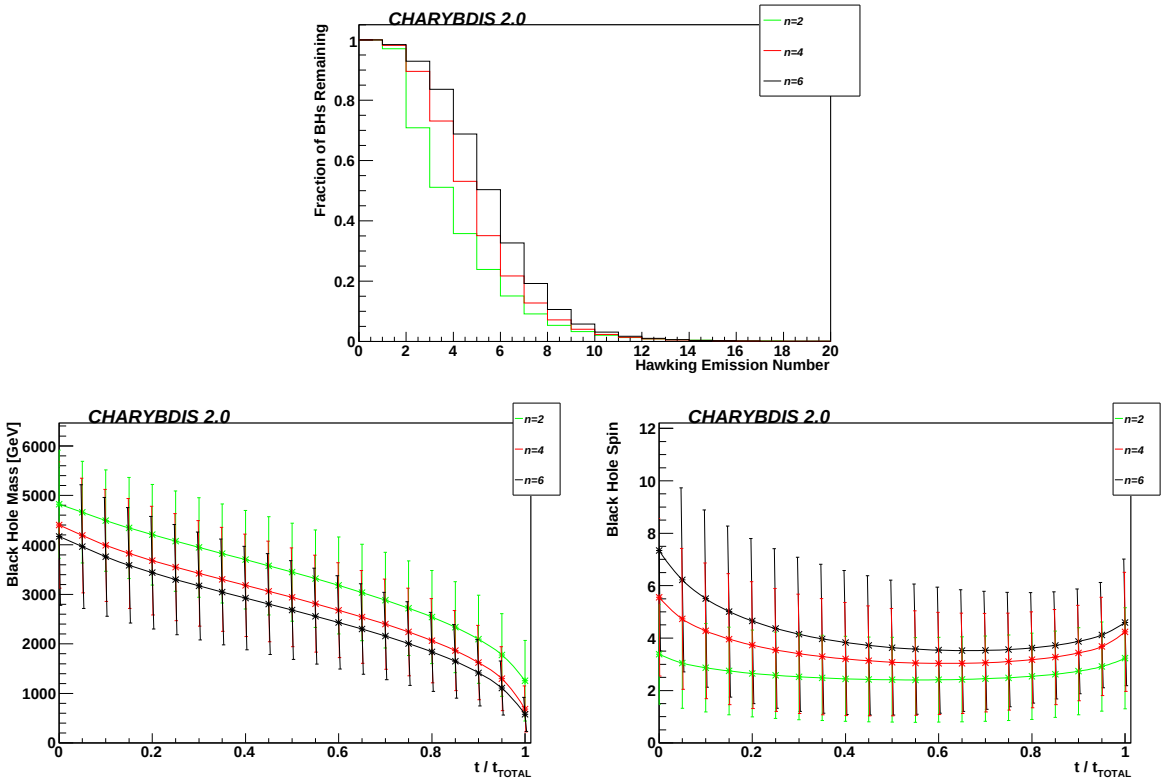

Figure 8.8: *The evolution of black hole parameters during the Hawking evaporation phase* The top plot shows the fraction of black holes which are still evaporating at the Nth emission. The lower two rows show the mean value tendency curves of the black hole mass and angular momentum as a function of fractional time t/t_{Total} through the evaporation. The bars indicate the standard deviation of the distribution.

$n = 6$. The distribution does have a substantial tail however, with 1% of black hole events producing more than 11 primary emissions (top plot of figure 8.8).

Without the simulation of losses in production/balding (`MJLOST`), the black hole spins down more quickly than it loses mass because its initial angular momentum is larger (emissions at high $m \sim j$ are highly favoured). Turning on `MJLOST` suppresses initial states with high black hole angular momentum. Consequently this effect is reduced in magnitude, though the black hole angular momentum still tends to be reduced in the beginnig of the evaporation (see bottom right plot of figure 8.8). Black holes with high initial angular momentum tend to lose much of it during their first few emissions, whereafter further emissions decrease the black hole mass more smoothly, whilst its angular momentum stays relatively low, but non-zero. Thus rotation persists throughout the black hole decay – only a small proportion of black holes settling into a Schwarzschild, non-rotating

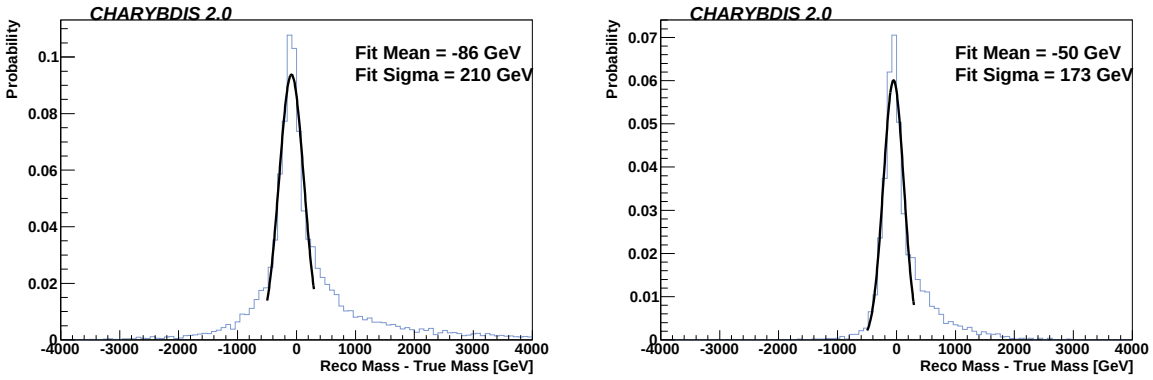

Figure 8.9: Sample black hole mass resolutions after `AcerDET` detector simulation with $n = 2$ and no balding simulation for all events (left) and after a cut of MET$<$ 100 GeV (right). The fits are indicative of the resolution in the peak and do not model the non-Gaussian tails which remain.

state. This is in direct agreement with the theoretical plots in figure 7.2 and 7.3, where a small non-zero angular momentum persists after the majority of the angular momentum has been lost.

As the black hole becomes lighter, its temperature rises, as does its oblateness (a_*) and the typical time interval between emissions drops. These effects are gradual except when the black hole mass becomes very low, at the end of the Hawking radiation phase. At this point we have reached the remnant phase.

8.2.3 Mass reconstruction

In principle, it is possible to reconstruct the black hole mass by combining the 4-momenta of all particles observed in the event and missing transverse energy (MET). Mass resolutions of 200-300 GeV can be achieved for some samples as shown in figure 8.9, but there is significant variation with different samples and black hole parameters. Events with large amounts of MET (particularly from multiple sources) tend to be more poorly reconstructed. Invoking a 100 GeV cut on MET results in better reconstruction at the cost of some signal efficiency. Such a cut may not be entirely conservative however, for there may be additional sources of MET neglected in our simulation, such as that from Hawking emission of gravitons.

8.2.4 Angular momentum reconstruction

The problem of determining the angular momentum axis and/or magnitude is much more difficult than reconstructing the mass. This is because the angular momentum axis, which controls the angular distributions, evolves during the evaporation, changing direction and magnitude. Furthermore, all the decay products in the laboratory frame are in general boosted with respect to the black hole centre of mass frame, and the black hole recoils between each emission. Nevertheless, we may hope to see some of the effects by boosting each event back to the partonic centre of mass frame. In principle we can determine the latter reliably if there is little missing energy emitted in the evaporation. The only missing energy in the SM comes from neutrinos and they represent a small part of the total number of degrees of freedom. However missing energy from neutrinos can arise from the secondary decay of SM heavy particles. Nevertheless the fraction of missing energy from the evaporation should not be so large (for most of the events) as to degrade the results much more compared to other factors such as the recoil. Note however that including gravitons in the evaporation may degrade the reconstruction further. Alternatively to reduce this effect we may cut on events with a small amount of missing energy as we did for the mass reconstruction.

We start our study by considering some distributions which are not observables but help to understand the angular correlations involved. The aim is to understand how the momenta of the particles emitted correlate with the true angular momentum axis by using knowledge of the black hole history.

The first distribution we study is the angle of a particle of a given spin with the true initial angular momentum in the centre of mass frame of the initial black hole

$$\cos\theta_{J_0} \equiv \frac{\mathbf{p}_s \cdot \mathbf{J}_0}{|\mathbf{p}_s||\mathbf{J}_0|} \,. \tag{8.1}$$

The first plot in figure 8.10 shows a spin dependent behaviour as expected. The sample used to produced the plots used all the defaults values except for `MJLOST=.FALSE.`. This produces black hole events with larger angular momentum and mass. This is not essential since we could use a cut on the visible invariant mass for the event to select heavier black holes if `MJLOST=.TRUE.`. We know from the theoretical plots in figure 6.14 that scalars and fermions tend to be more equatorial (though fermions at low energies also have a small axial peak) and vector bosons are very axial at low energies. This is consistent with the larger probability for vector bosons at larger $|\cos\theta|$ in the top left plot (though the effect

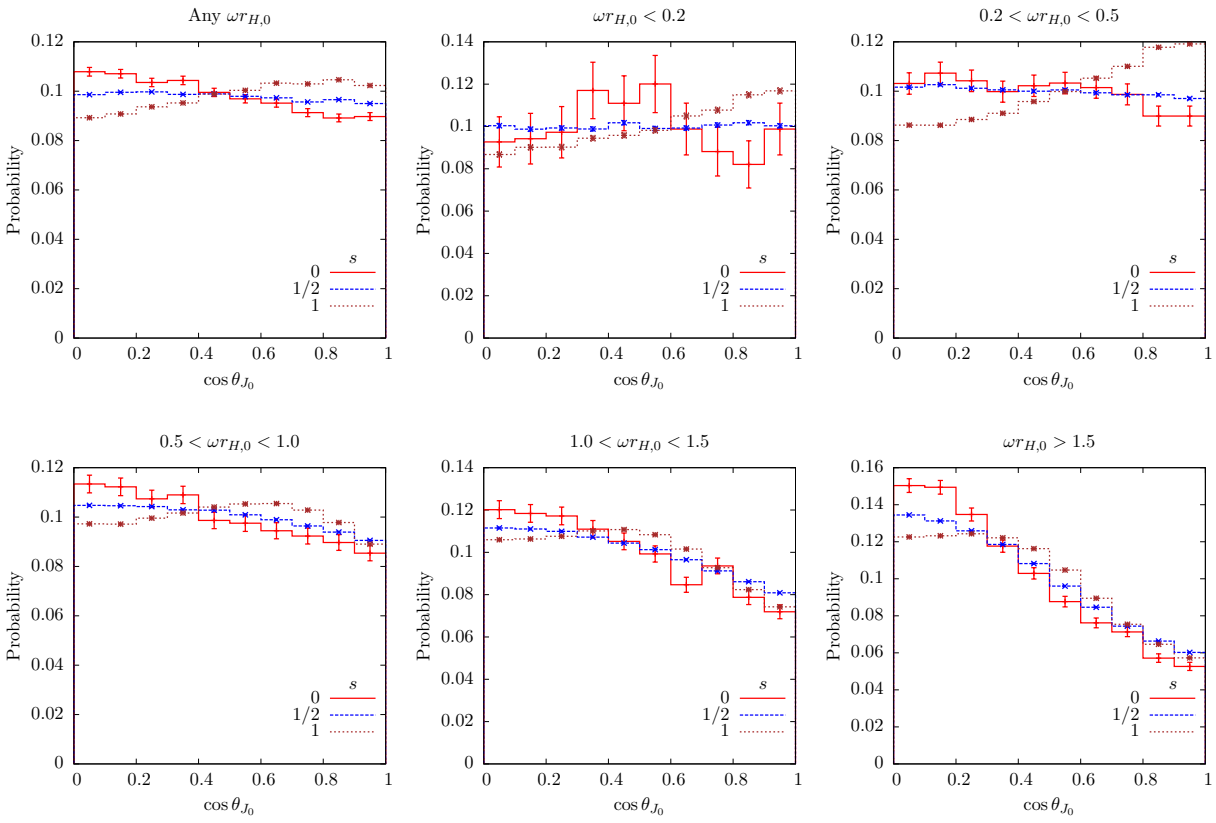

Figure 8.10: *Distribution of angles of particles with various spins with the angular momentum axis.* The top left plot shows the distributions for $\cos\theta$ for various spins for an $n = 3$ sample with black hole masses above 5 TeV. The other plots show the distribution for various ranges of energies as indicated in the title of each plot. Note that the error bars for $s = 0$ are due to the small number of pure scalar degrees of freedom in the SM (only the Higgs particle).

is not very large). We can improve this correlation by selecting particles in particular ranges of energy for each initial black hole. For example if our cut requires high energy particles for all spins we would expect an equatorial correlation, whereas at low energies we expect a flatter distribution for scalars and fermions and an axial distribution for vector particles. This is confirmed in the two top right plots and the bottom plots of figure 8.10 where we have chosen ranges of energy in units of the horizon radius of the initial black hole. This result suggests using soft vector particles as a guess for the axis, to plot angular distributions. This will fail a considerable part of the time and smear out the true correlation.

High energy particles tend to be emitted perpendicularly to the initial black hole angular momentum. This is seen in the bottom right plot of figure 8.10 where the correlation

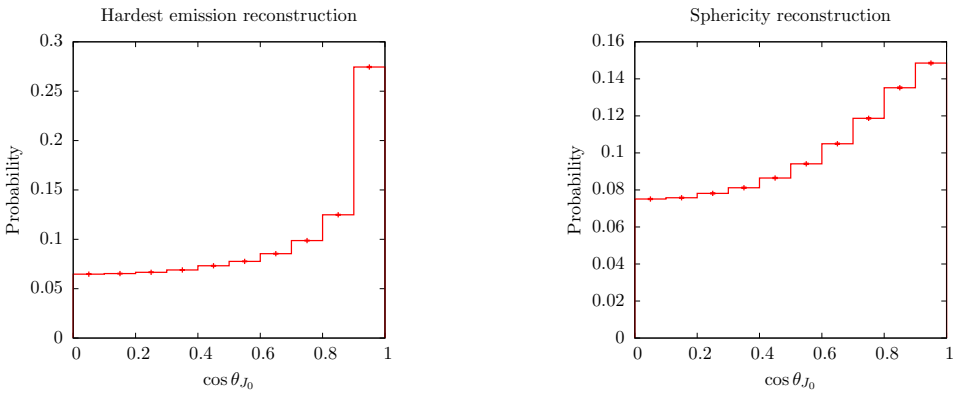

Figure 8.11: *Axis reconstruction:* Using the hardest emission (left) and the eigenvector of the smallest eigenvalue of the sphericity tensor (right).

is stronger. If in addition we assume that the direction of the angular momentum vector is perpendicular to the direction of the black hole momentum (which is true in the limit where the angular momentum does not recoil during the production) we obtain another guess for the axis. The left plot in figure 8.11 shows that this method works better. However it relies on the assumption that the initial angular momentum is perpendicular to the black hole momentum.

A third method to estimate the angular momentum axis is to consider the shape of the event, i.e. to use all the momenta in the decay. For a rotating black hole we expect most of the particles to be emitted equatorially (since only low energy vector bosons are axial). Thus the event should have a disc like distribution of momenta indicating the orientation of the axis. This axis should minimise the amount of momentum projected along its direction. Another advantage of this reasoning is that it gives lower weight to low energy particles which we want to eliminate since low energy vector bosons are more axial, and low energy scalars and fermions are more uniform. If we denote the direction of the angular momentum by $\mathbf{n}$, and use projections of momenta squared, then we want to minimise

$$\begin{aligned}
\frac{\min_{\mathbf{n}} \sum_i (\mathbf{p}_i \cdot \mathbf{n})^2}{\sum_i |\mathbf{p}_i|^2} &= \frac{\min_{\mathbf{n}} \sum_i \sum_{\alpha\beta} \mathbf{n}^\alpha \mathbf{p}_i^\alpha \mathbf{p}_i^\beta \mathbf{n}^\beta}{\sum_i |\mathbf{p}_i|^2} \\
&= \min_{\mathbf{n}} \sum_{\alpha\beta} \mathbf{n}^\alpha \left(\frac{\sum_i \mathbf{p}_i^\alpha \mathbf{p}_i^\beta}{\sum_i |\mathbf{p}_i|^2} \right) \mathbf{n}^\beta \\
&= \min_{\mathbf{n}} \sum_{\alpha\beta} \mathbf{n}^\alpha S^{\alpha\beta} \mathbf{n}^\beta
\end{aligned} \tag{8.2}$$

where we are use Greek letters for spatial indices and the index i runs over all particles in the event. We have defined the sphericity tensor $S^{\alpha\beta}$ as usual [183]. The sphericity tensor has the properties that all eigenvalues are non-negative and their sum is one. In the eigenbasis it is clear that the direction which minimises the quantity in (8.2) is the eigenvector associated with the smallest eigenvalue. In the right plot of figure 8.11 the distribution for the angle between the guessed axis (the eigenvector associated with the smallest eigenvalue) and the angular momentum axis is shown. This method is not as good as the the left plot but it has the advantage of not relying on the assumption that the angular momentum is on the plane transverse to the collision axis.

8.2.5 Parton level angular correlators

An alternative to reconstructing the black hole angular momentum to study angular distributions, is to explore the property that polarised angular distributions are strongly dependent on the helicity of the particle. For example from figure 6.14 we know that there is a strong preference for vector bosons to be emitted in different hemispheres. This motivates defining angular correlators of the form (in the frame of the initial black hole)

$$x_{i,j} = \frac{\mathbf{p}_i \cdot \mathbf{p}_j}{|\mathbf{p}_i||\mathbf{p}_j|} \tag{8.3}$$

which are cosines of angles between particles i and j. So for the case of particles with the same helicity, we would expect the distribution to be higher at $x_{i,j} \sim 1$ and reduced at $x_{i,j} \sim -1$, and the opposite to happen for particles with opposite helicities. Figure 8.12 shows the expected behaviour for pairs of emissions in a fixed black hole background (no recoil). The probability density function used to determine the distribution of (8.3) is derived in appendix D.5. The effect at fixed black hole parameters grows quickly with a_*, especially for particles of helicity $h = \pm 1$. The bottom right plot shows that there is some variation with n though not very strong (the curves are qualitatively similar).

For an evolving black hole, we expect these effects to get smeared, due to the momentum and angular momentum recoil. Again the best we can do is to compute similar quantities in the rest frame of the initial black hole assuming a small amount of the missing energy during the evaporation.

Figure 8.13 shows the correlators defined in (8.3) for various helicity combinations. The top left plot shows the distribution for same helicity (red) and opposite helicity (blue) fermions (solid lines) and vector particles (dashed lines) and the non-rotating case

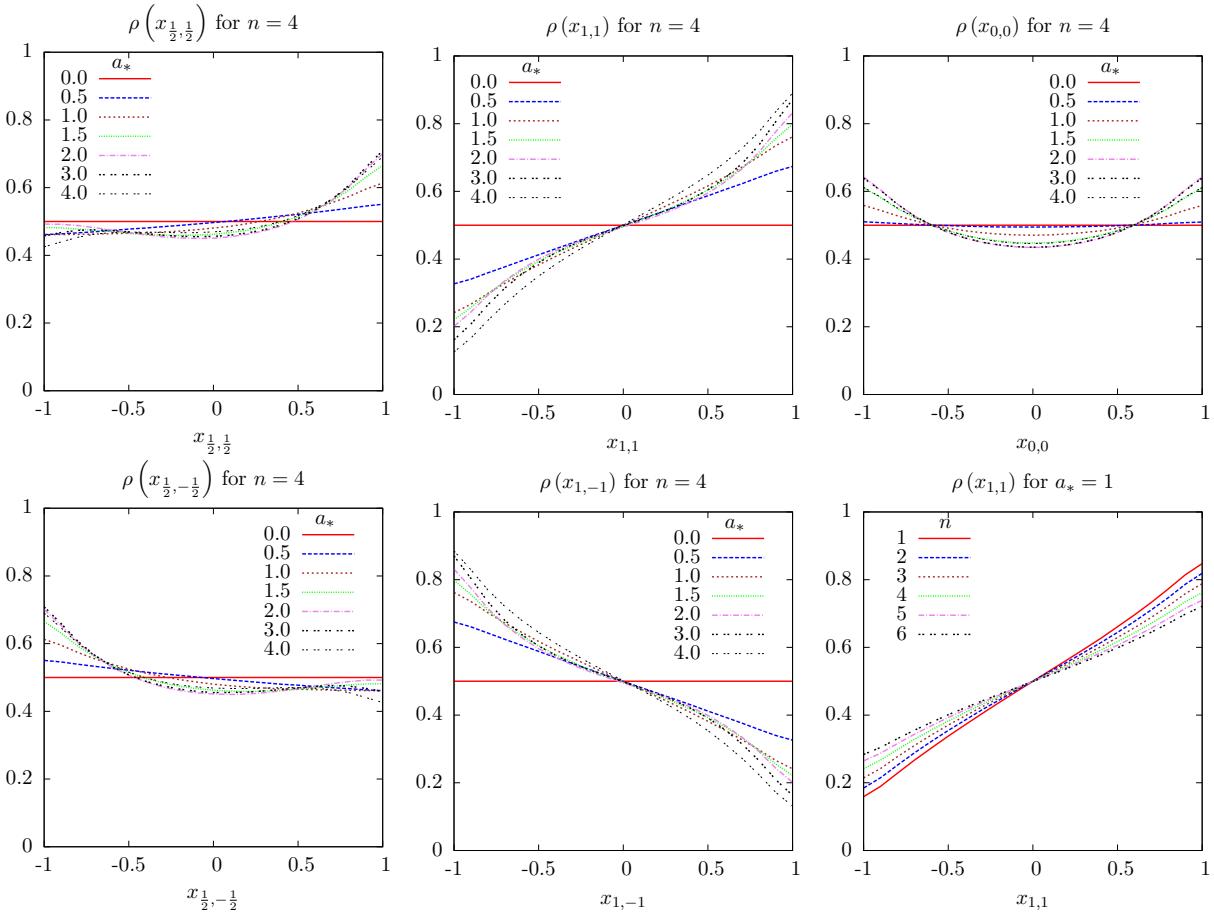

Figure 8.12: *Angular correlators for an eternal black hole.* The top plots show the probability density functions for the angular correlator between particles of same helicity for fermions, vector bosons and scalars (left to right), for a range of a_* values. The two left bottom plots are similar but between particles with opposite helicities. The bottom right plot shows the dependence with n for $a_* = 1$ and two vector bosons with the same helicity.

(black) for comparison. The black curve is not constant due to the recoil of the black hole between emissions. The recoil tends to make different pairs of emissions more back to back (especially subsequent emissions) which causes the rise at $x_{i,j} \sim -1$ and the fall off at $x_{i,j} \sim 1$.

We can see (particularly for vector particles) that the asymmetry predicted in figure 8.12 persists, with an enhancement at $x_{i,j} = -1$ for opposite helicity correlators, compared to the same helicity correlators. It is also clear that the effect of the recoil between emissions is larger in the rotating case. This is because the spectrum is harder, hence the relative boost when the black hole recoils is also larger. Additionally, in the

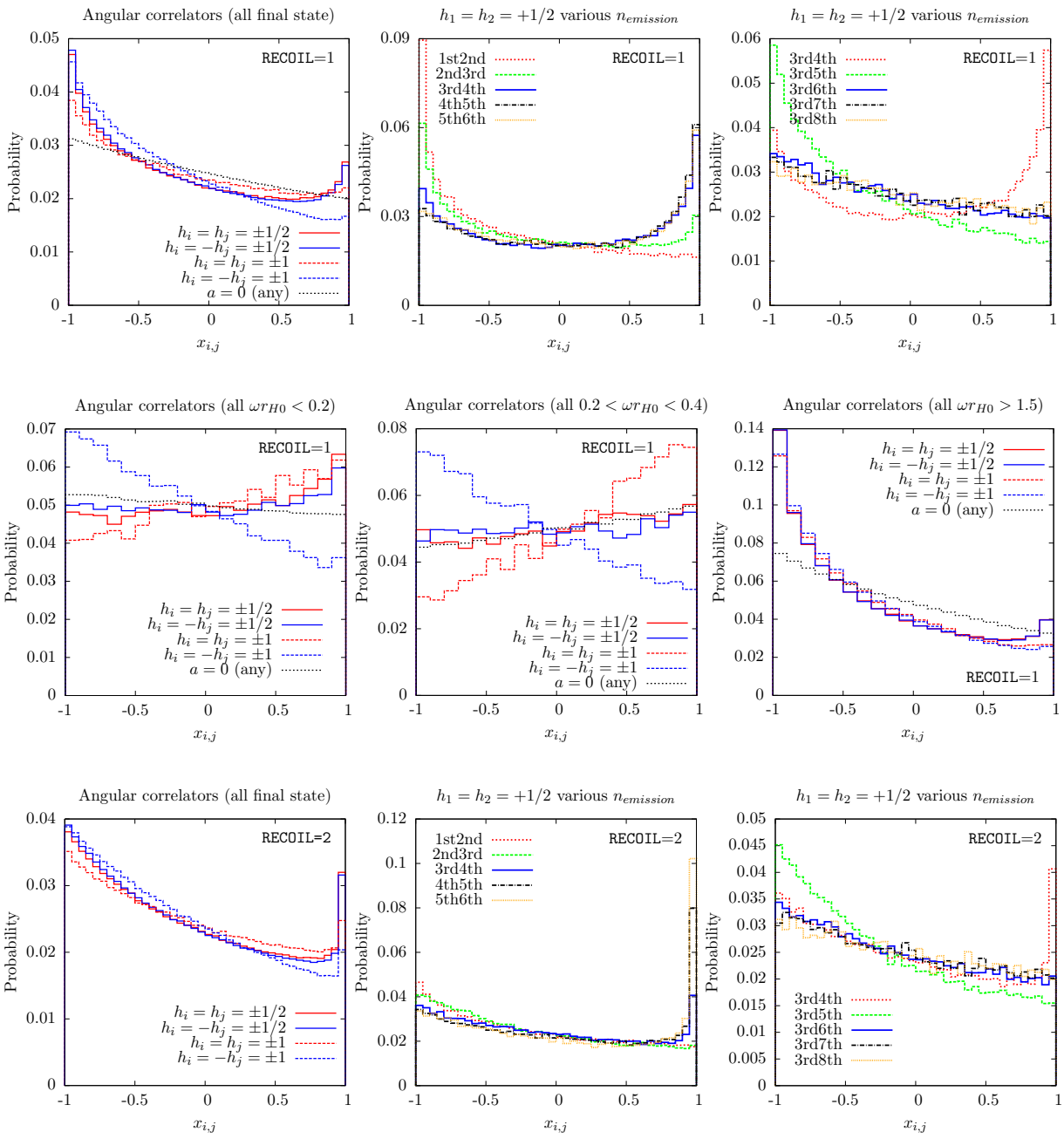

Figure 8.13: *Parton level angular correlators evaluated in the frame of the initial black hole.* The sample used was the same as in figure 8.10. The top left plot shows correlators between any two final state fermions or any two final state vector bosons for some helicity combinations. The correlator for any two particles when rotation is off is shown for comparison. The top centre and top right plots show the same distributions using various pairs of particles according to their ordering during the evaporation. The central row of plots shows the same distributions using specific intervals of energy (compared to the horizon radius for the initial black hole – r_{H0}). Twice the bin size was used to compensate for the lower statistics. The bottom row of plots contains the same plots as the top row, but with a different recoil model `RECOIL=2`.

rotating case, we have a forward peak at $x_{i,j} = 1$. This is due to the possibility of having an accumulated boost in a certain direction for the particles emitted later in the decay, so pairs of those particles will tend to be more collinear. Since in the rotating case the multiplicity of the event is reduced and the spectrum is harder, this effect tends to be important (practically all events end up with a large accumulated boost). This is verified in the top centre and top right plots where for the first pair in the beginning of the evaporation (top centre plot) no forward peak is observed, whereas for later consecutive pairs, the forward peak tends to increase rapidly. For pairs which are increasingly separated in the order of emission, the forward peak also disappears (top right plot). The reason why no forward peak appears in the non-rotating case can be justified as follows. For events with multiplicity N, the number of consecutive pairs which can contribute to a forward peak is $N-2$, whereas the total number of pairs is $N(N-1)/2$. So the fraction of pairs contributing to a forward peak is at most $2(N-2)/(N(N-1))$. Typically, when rotation is turned off, the multiplicity increases from $5 \sim 8$ to $10 \sim 15$ so the fraction of pairs contributing to the peak is reduced roughly by a factor of ~ 2. Furthermore, a larger multiplicity means a smaller magnitude for the boost in the recoil by another factor of ~ 3 (since the same energy is distributed among more particles which are softer). So overall, we have a suppression factor of at least ~ 6. This explains the absence of the forward peak for the non-rotating sample.

The central row of plots shows that by selecting particular ranges of energy we recover the strong asymmetry for low energy vector bosons (left and centre plots). For high energy particles (right), all helicities are equivalent. This is because at high energies all the angular spectra become equatorial regardless of the spin.

The bottom row plots are the same as in the first row, except that `RECOIL`=2 was used (see section 7.2.1). Similar conclusions are obtained with this option (particularly for the ranges of energy selected in the middle row of plots). The only difference is that the forward peak due to the recoil is somewhat sharper and the backward effect is smaller. It can be shown that the mass reduction for a particle with a small energy $E \ll M$ (i.e. in the beginning of the evaporation) in the frame of the initial black hole is

$$M_{final} = \begin{cases} M - E\left(1 + \dfrac{E}{2M}\right) + \ldots & , \texttt{RECOIL} = 1 \\ M - E & , \texttt{RECOIL} = 2 \end{cases} . \tag{8.4}$$

This explains the larger backward effect (at $x = -1$) in the top plots when `RECOIL`=1,

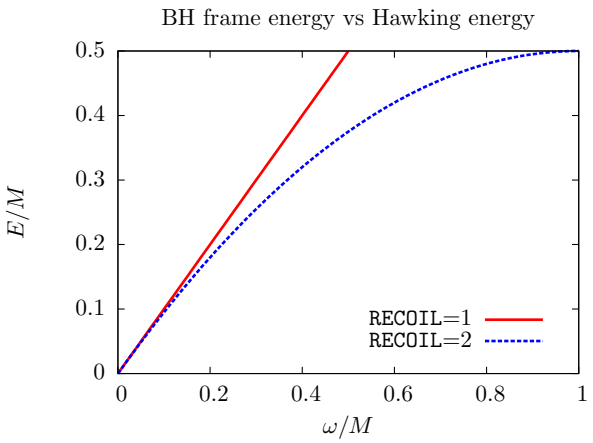

Figure 8.14: *Energy of the particle emitted:* The energy of the particle (E/M) in the frame of the black hole is shown as a function of the energy selected from the Hawking spectrum (ω/M).

since in that case the black hole mass reduction is a bit larger in the beginning of the evaporation, enhancing the effect of the back to back recoil. The sharper forward peak when `RECOIL=2` can be explained by expressing E in terms of the selected Hawking energy ω (neglecting particle mass)

$$\frac{E}{M} = \begin{cases} \frac{\omega}{M} & , \frac{\omega}{M} \in [0, \frac{1}{2}] \quad , \texttt{RECOIL} = 1 \\ \frac{\omega}{M}\left(1 - \frac{1}{2}\frac{\omega}{M}\right) & , \frac{\omega}{M} \in [0, 1] \quad , \texttt{RECOIL} = 2 \end{cases} . \tag{8.5}$$

It is easy to see (figure 8.14) that at high energies E close to the kinematic limit (which are more important in the last part of the evaporation), the range of energies ω contributing to a range of energies E is always much wider for `RECOIL=2`. So there will be more hard particles selected at the end of the evaporation for the latter, contributing to the accumulated boost and hence the forward peak.

Note that the plots in figure 8.13 were produced assuming knowledge of the helicities of the outgoing particles. This is usually not an observable at hadron colliders. However, as mentioned at the end of section 6.4.4, for example the decay modes of the the W and Z bosons are dependent on the helicity of the intermediate states. For example in the decay $W^- \to \ell^- \bar{\nu}_\ell$ the charged lepton tends to be collinear with the W^- for negative helicity, and anti-collinear for positive helicity. For Z decays a similar argument holds, although the correlation should be weaker. The only disadvantage of W decays is the neutrino which makes re-construction difficult, whereas for Z decays the disadvantage is the mixture of

Table 8.1: Parameters used for remnant comparison. All samples have $n = 2$ and `MJLOST=.FALSE.`

Legend	Remnant Criterion	Fixed/Variable	Remnant No./Mean
Kincut on	$M <$ `INTMPL` (`KINCUT=.TRUE.`)	Fixed	2
Kincut off	$M <$ `INTMPL` (`KINCUT=.FALSE.`)	Fixed	2
Nbody2	Flux (`NBODYAVERAGE=.TRUE.`)	Fixed	2
Nbody3	Flux (`NBODYAVERAGE=.TRUE.`)	Fixed	3
Nbody4	Flux (`NBODYAVERAGE=.TRUE.`)	Fixed	4
Nvar2	Flux (`NBODYAVERAGE=.TRUE.`)	Variable	2
Nvar3	Flux (`NBODYAVERAGE=.TRUE.`)	Variable	3
Nvar4	Flux (`NBODYAVERAGE=.TRUE.`)	Variable	4
Boiling	`RMMINM` $< M <$ `INTMPL`	Variable	2

left-handed and right-handed couplings. Nevertheless with a more sophisticated set of cuts it may be possible to keep some of the asymmetry at the experimental level. This study will be completed in a future work.

8.3 Remnants

`CHARYBDIS2` includes several models for the remnant phase. Both fixed multiplicity and variable multiplicity decays have parameter switches to enable the systematics to be studied, as detailed in section 7.3.1.

The fixed multiplicity model, present in `CHARYBDIS` and optional in `CHARYBDIS2`, is linked to the choice of the variable `KINCUT`. If `KINCUT=.FALSE.`, proposed decays that are kinematically disallowed are ignored; if `KINCUT=.TRUE.`, their proposal terminates the evaporation phase. The former choice will give a greater number of less energetic particles, as evidenced by figure 8.15 which contrasts a range of remnant models defined in Table 8.1.

`CHARYBDIS2` uses the `NBODYAVERAGE` remnant criterion as a default, where the fluxes are used to calculate the expected number of further emissions. This provides a physically motivated model. Using this criterion with either a fixed 2-body ("Nbody2") or a variable multiplicity remnant model ("Nvar2") gives a distribution lying between the upper and lower values obtained using the older model switches (upper plots of figure 8.15), indicating good control over the uncertainties mentioned in section 7.3.1. The string-motivated boiling model gives a slightly higher multiplicity, since successive emissions are produced until the remnant mass drops below the remnant minimum mass, resulting in a greater

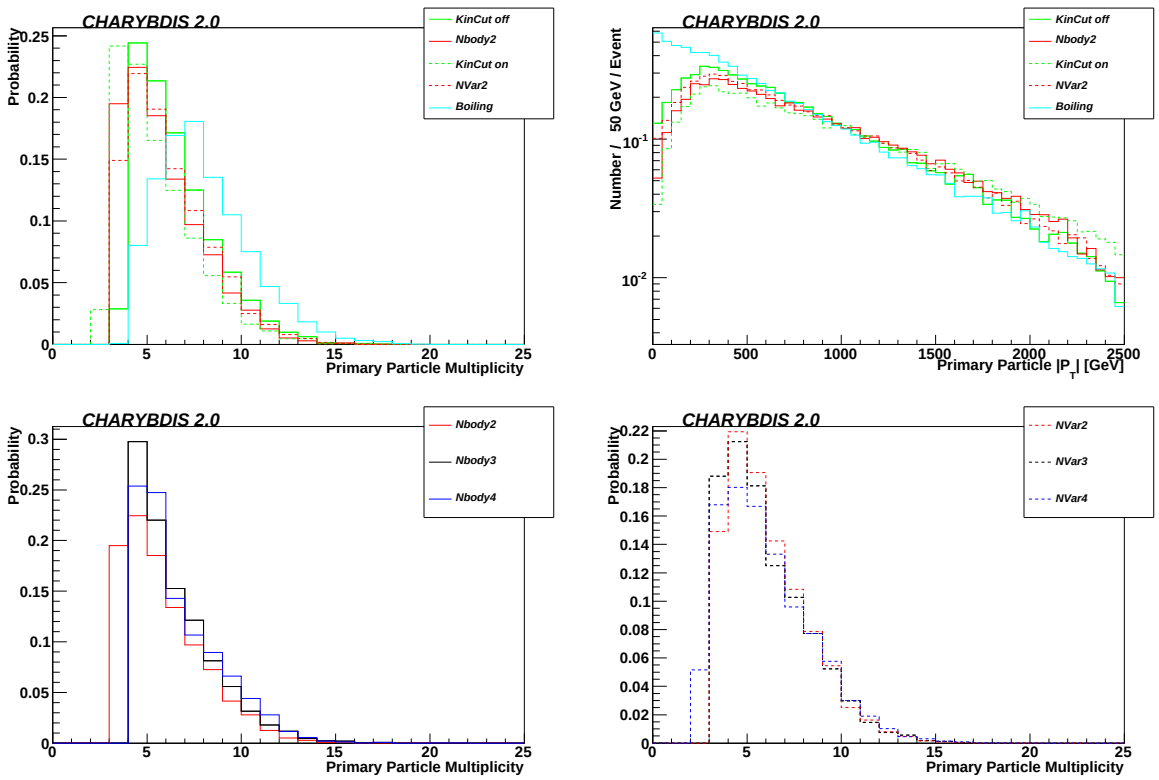

Figure 8.15: Primary particle multiplicity and $|P_T|$ distributions for black hole samples with $n = 2$, using a wide range of remnant options, as defined in Table 8.1.

number of softer particles produced in the remnant phase.

The new `NBODYAVERAGE` model is also more robust with respect to changes in the number of particles produced in the remnant phase. This is because the flux calculation allows the spin-down phase to be terminated whenever the expected number of further emissions is fewer than that selected for the remnant phase. This is illustrated in the lower plots of figure 8.15, where changing the number of particles produced in the remnant phase results in similar multiplicities and spectra; events with 4-body remnant decays do not always have two more particles than their 2-body analogues.

Another advantage of the `NBODYAVERAGE` method is that by using the integrated power and flux, the spin-down phase is terminated at a point that allows a smoother transition to the remnant phase, as shown by their spectra in figure 8.16, where the `NBODYAVERAGE` (lower) method gives a more concordant distribution of particle transverse momenta. Performing a remnant decay only when the mass drops below the Planck mass gives a much softer momentum spectrum, in contrast to the high energies favoured by light rotating black holes. The option to start the remnant decay based on the drop of $\langle N \rangle$

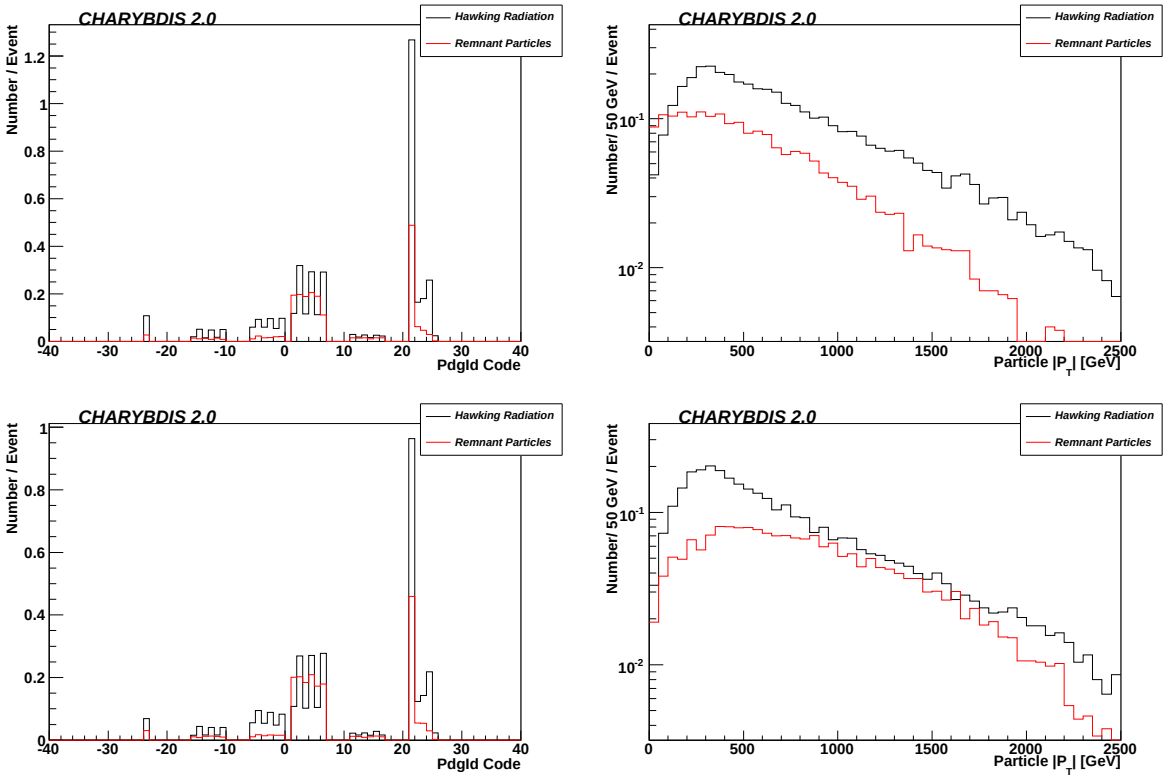

Figure 8.16: Particle type and P_T plots for 2-body remnant decays using the old model "Kin-cut off" (top) and the new model "Nbody2" (bottom) as defined in Table 8.1. Distributions are normalised per event.

provides a smoother transition, since the final decay particles will have a harder spectrum, more similar to the Hawking phase. Emissions in the remnant phase are predominantly coloured, with positive baryon number favoured, so as to meet the constraints of baryon number conservation.

8.4 Conclusions

In this and the previous chapter, we have presented in detail the physics content of the new black hole event generator `CHARYBDIS2`, together with some results illustrating important features of the simulation of the different phases of black hole production and decay. The main new features compared to most earlier generators, including `CHARYBDIS`, are: detailed modelling of the cross section and the loss of energy and angular momentum during formation of the black hole (the so-called balding phase), based on the best available theoretical information; full treatment of angular momentum during the evaporation

phase, including spin of the incoming partons, rotation of the black hole, and anisotropy and polarisation of all Standard Model fields emitted on the brane; and finally a variety of options for the Planck-scale termination phase, ranging from a stable remnant to a variable-multiplicity model connecting smoothly with the evaporation phase.

Our main finding is that angular momentum has strong effects on the properties of the final state particles in black hole events. Even after allowing for a substantial loss of angular momentum in the balding phase, the isotropic evaporation of a spinless Schwarzschild-Tangherlini black hole is not a good approximation, nor is the notion of a rapid spin-down phase followed by mainly isotropic evaporation at foreseeable energies. Although the Hawking temperature does not depend strongly on the angular momentum of a spinning black hole of a given mass, there is a strong bias in the emission spectra towards higher-energy emissions into higher partial waves, which help the black hole to shed its angular momentum. The resultant spectra are flatter, with substantial tails beyond 1 TeV. As a consequence of these more energetic emissions, rotating black holes emit with reduced multiplicity relative to their non-rotating counterparts. However the absolute multiplicity can still be large.

The preferential equatorial emission of scalar, fermionic and high energy vector particles leads to slightly less central distributions at detector level. This effect is reduced by the evolution of the spin axis during evaporation (away from the initial orientation perpendicular to the beam direction). We have seen that this can be improved by working in the frame of the reconstructed black hole. The reconstruction of the black hole angular momentum is in general difficult due to its recoil. However we have shown that angular asymmetries survive if, instead of plotting angular distributions with respect to the reconstructed axis of rotation, we consider angular correlators between pairs of particles. This seems particularly promising for low energy vector particles.

The emission of polarised higher-spin fields is favoured, compared to the spinless case, leading to increased vector emission and marking a further departure from a purely democratic distribution of particle species. This shows little dependence upon the number of dimensions.

These findings will complicate the interpretation of black-hole events, should they occur at the LHC or future colliders. While the basic signature of energetic, democratic emission of all Standard Model species and large missing energy remains valid, the deduction of the fundamental Planck scale and the number of extra dimensions will be more difficult than was anticipated in earlier studies [158]. On the other hand, many interesting

new and potentially observable features emerge, such as the different angular distributions and polarisation of particles of different spins. Further analysis strategies will be investigated in future work.

Chapter 9

Conclusions and Outlook

In this thesis we have studied the theoretical modelling of black hole production and evaporation in extra-dimensional theories with TeV gravity, and some phenomenological consequences for near future collider experiments.

After motivating extra dimensions as a solution to the hierarchy problem and the possibility of black hole production in particle collisions in those scenarios, and after reviewing the formalism of extra-dimensional effective theory, we started by investigating some of the properties of the extra-dimensional black holes (chapter 3). Using the Myers-Perry metric for a singly rotating black hole, we found that it is possible to construct a more general effective background, so as to include (approximately) the effect of the black hole electric charge on the brane, in a consistent way. The result was an effective brane metric which is a modified version of the Kerr-Newman metric. An important observation, which was relevant in later chapters to study black hole discharge and to justify the perturbative treatment, was that the electric force at distances below the extra-dimensional radius, becomes weaker as the gravitational force becomes dominant. To help in characterising the black hole geometrically, we described the method to compute classical absorption cross-sections for an arbitrary direction of incidence, and presented some examples of the shapes of the absorptive disks seen by an observer at infinity (in the rotating case). As expected we found a strong correlation with the angular momentum axis and magnitude as we varied the direction of incidence and number of extra dimensions.

In chapter 4, we considered the problem of modelling the production. This was largely a review of the best known arguments and bounds, on the amount of energy and angular momentum trapped in the black hole, and a description of a model to include those bounds in the `CHARYBDIS2` generator.

A theoretical study of the Hawking evaporation (which is central to modelling the decay of the black holes which may be produced at colliders) was detailed in chapters 5 and 6. After justifying a perturbative approach and summarising the basic theory of Hawking radiation, we used the brane charged effective metric to study the new cases of massive and charged fermionic and scalar perturbations in detail. We then found and separated the wave equations to obtain the general radial and angular equations for those perturbations. In chapter 6 we developed analytic and numerical methods which allowed us to solve the radial equations to obtain transmission factors, the angular functions, and hence the Hawking spectra. A detailed numerical evaluation showed several interesting new features, most notably: i) the large suppression of the spectrum for massive particles at threshold, ii) the sub-dominance of discharge in the evaporation (unlike common claims regarding Schwinger discharge) and iii) the inverted low energy charge splitting of the spectrum for more than one extra dimension. We also performed a comparison with known results concerning the effect of rotation, emphasizing the importance of including the non-trivial spheroidal functions. The latter are helicity dependent and introduce axial peaks in the angular spectrum. Finally we showed that the charge splitting effect survives when considered simultaneously with rotation.

The theoretical study in the first part of the thesis showed that there are still several interesting and relevant effects to consider in the modelling of the evaporation of brane black holes. A very interesting problem to pursue in the future is the construction of an effective background for a black hole spacetime with non-abelian charges, and the study of various non-singlet Standard Model perturbations.

In the second part of the thesis we have implemented several theoretical results into the new event generator `CHARYBDIS2`, and analysed the phenomenological consequences. Concerning the model for mass and angular momentum loss at production, the main conclusion was that there is a considerable reduction of the differential cross-section for a given black hole mass range. We have also implemented a more complete model for the evaporation including the effect of rotation for all Standard Model fields with polarisation information. This has several important effects, namely: the shift of the energy spectra of the final state particles towards higher energies and consequently a reduction of the average multiplicity; non-uniform angular distributions, which may be observable by plotting observables with respect to the reconstructed rotation axis or by analysing angular correlators in the reconstructed black hole frame; and finally a large enhancement of vector emission. We found that all these effects do not change dramatically the classi-

cal signatures of black hole events such as high multiplicity events with many QCD jets and leptons (the average multiplicity is reduced but it is still large), relatively democratic emission of all Standard Model degrees of freedom, and large amounts of transverse momentum. Instead the new effects add new signatures to the scenario. In the future, it would be interesting to include the charge and mass effects we have discussed in the first part of the thesis, which are likely to add up new signatures relatively smoothly on top of the signatures of rotation. Another important open question to address is the effect of the gravitons on a rotating background.

Extra-dimensional black holes are definitely very interesting and theoretically rich objects. They involve a combination of general relativity, quantum mechanics and particle physics, so their modelling is complicated and there are still many open problems and interesting avenues to pursue. With the recent start of the LHC experiment it is particularly timely to provide an increasingly better modelling to either exclude or observe them. The study in this thesis will hopefully help with performing this task and motivate further work in this unusual field.

Appendix A

Conventions and mathematical tools

Throughout this thesis, unless stated otherwise, all theoretical expressions are in natural units where the Planck constant and speed of light are respectively $\hbar = c = 1$.

A.1 Differential geometry

We use the mostly minus convention for the signature of the metric in D dimensions $(+, -, \ldots, -)$.

For the components of the (torsion free) metric connection components in a coordinate basis we use (G_{MN} is the metric)

$$\Gamma^M_{NP} = \frac{1}{2} G^{MQ} \left(\partial_N G_{PQ} + \partial_P G_{NQ} - \partial_Q G_{NP} \right) \ . \tag{A.1}$$

To avoid confusion with the higher-dimensional metric tensor or other quantities, we express geometric objects such as the Riemann tensor, Ricci tensor and scalar, and Einstein tensor by calligraphic letters $\mathcal{R}^M_{NPQ}$, $\mathcal{R}_{MN}$, $\mathcal{R}$ and $\mathcal{G}_{MN}$ respectively. The sign convention for the Riemann tensor is

$$\mathcal{R}^M_{NPQ} = \partial_Q \Gamma^M_{NP} - \partial_P \Gamma^M_{NQ} + \Gamma^M_{RQ} \Gamma^R_{NP} - \Gamma^M_{RP} \Gamma^R_{NQ} \tag{A.2}$$

and the Einstein tensor is defined

$$\mathcal{G}_{MN} = \mathcal{R}_{MN} - \frac{1}{2} G_{MN} \mathcal{R} \ . \tag{A.3}$$

A.2 Planck mass convention

We keep the dependence on the $(4+n)$-dimensional Planck mass explicit in all expressions and adopt as reference convention, the PDG definition[1] which uses the Einstein-Hilbert action

$$S_{EH} = \frac{1}{2}\hat{M}_D^{2+n}\int d^D x\sqrt{|G|}\mathcal{R}_D = \frac{1}{16\pi G_D}\int d^{(4+n)}x\sqrt{|G|}\mathcal{R}_D \ , \tag{A.4}$$

to set the reduced Planck mass $\hat{M}_D$. The Planck mass M_D is then defined as

$$M_D^{2+n} = (2\pi)^n \hat{M}_D^{2+n} \ . \tag{A.5}$$

An alternative convention is obtained by defining

$$M_{4+n}^{2+n} = 2M_D^{2+n} \ . \tag{A.6}$$

This is the Giddings-Thomas convention [24] used internally in the `CHARYBDIS2` generator described in chapter 7.

A.3 The induced vierbein

Following the appendix of [29], we can generalise the arguments for a curved background as follows. The matrix $R(Y)$ is defined as

$$R = \exp\left(i\theta_{\alpha\mu}J^{(\alpha\mu)}\right) \tag{A.7}$$

with $\theta_{\alpha\mu}$ a function of Y and $J^{(\alpha\mu)}$ are part of the generators of the D-dimensional Lorentz group in the vector representation

$$J^{(AB)}{}_D^C = i\eta^{CE}\left(\delta_E^A\delta_D^B - \delta_D^A\delta_E^B\right) \ . \tag{A.8}$$

The particular components involved in (A.7) are

$$\begin{aligned} J^{(\alpha\mu)}{}_\beta^\nu &= -i\eta^{\mu\nu}\delta_\beta^\alpha \\ J^{(\alpha\mu)}{}_\nu^\beta &= i\eta^{\alpha\beta}\delta_\nu^\mu \\ J^{(\alpha\mu)}{}_\sigma^\nu &= J^{(\alpha\mu)}{}_\delta^\gamma = 0 \ . \end{aligned} \tag{A.9}$$

[1] See for example the extra dimensions section of the PDG review [5].

To solve (2.7) expand

$$E_M^B(Y)\partial_a Y^M = E^{(0)}{}_a^B(Y_{(0)}) - \epsilon_a^B(Y) \tag{A.10}$$

where ϵ_a^B is a perturbative parameter which is zero on the background and we choose $Y_{(0)}^M = \delta_a^M x^a$. We expand at order $O(\epsilon^i)$

$$\begin{aligned} \theta_{\alpha\mu} &= \sum_{i=0} \theta_{\alpha\mu}^{(i)} \\ R &= \sum_{i=0} R^{(i)} \quad . \end{aligned} \tag{A.11}$$

The zeroth order solution must obey

$$R^{(0)}{}_B^\mu E^{(0)}{}_a^B(x) = 0 \, . \tag{A.12}$$

For the particular case where $E^{(0)}{}_a^\nu(Y_0) = 0$ the solution is the identity $R^{(0)} = \mathbb{I}$ and the induced vierbein is simply $e^{(0)}{}_a^\alpha = E^{(0)}{}_a^\alpha(x)$. The perturbative corrections can be constructed iteratively using the same arguments as in [29]. Using (A.9) in the $(i+1)$th order expansion of (A.7), we can solve for

$$\theta_{\alpha\mu}^{(i+1)} = \eta_{\mu\nu} e^{(0)}{}_\alpha^a \left[R^{(i)}{}_B^\nu \epsilon_a^B - e^{(0)}{}_a^\beta \, R^{(i+1)}{}_\beta^\nu \Big|_{\theta^{(i+1)}=0} \right] \, , \tag{A.13}$$

where we have defined the inverse of the zeroth order induced vierbein

$$e^{(0)}{}_\alpha^a e^{(0)}{}_b^\alpha = \delta_b^a \tag{A.14}$$

$$e^{(0)}{}_b^\alpha e^{(0)}{}_\beta^b = \delta_\beta^\alpha \tag{A.15}$$

and the second term in $R^{(i+1)}$ is evaluated with the $\theta^{(i+1)}$ term deleted.

Appendix B

The production model

B.1 The Yoshino-Rychkov mass/angular momentum bounds

This appendix is divided into two sections. The first is a brief review of the method in the Yoshino-Rychkov paper [76], focusing on the key equations we used to implement the Yoshino-Rychkov boundary curves in `CHARYBDIS2`. The second section explains how `CHARYBDIS2` calculates the boundary curve $\xi_b(\zeta)$ for a given D and b.

Summary of the Yoshino-Rychkov method

In the spacetime outside the future lightcone of the collision event (i.e. regions I, II and III of figure B.1), the metric for the complete system is obtained by combining two higher dimensional Aichelburg-Sexl metrics (equation (3.21)) corresponding to partons travelling in opposite directions (in the centre of mass frame). This gives the correct spacetime outside region IV of figure B.1, because the colliding partons are taken as travelling at the speed of light, so there can be no interaction between their gravity waves before the collision.

The next stage in the calculation is the selection of a spacetime slice somewhere in the union of regions I, II and III, and the determination of an apparent horizon (AH). An AH is a surface whose outgoing null geodesic congruence has zero expansion. Assuming the cosmic censorship hypothesis [184], an event horizon (EH) must be present outside any AH; thus finding an AH is sufficient to show that a black hole forms. Furthermore, using the fact that the EH must lie outside the AH, combined with the area theorem [185]

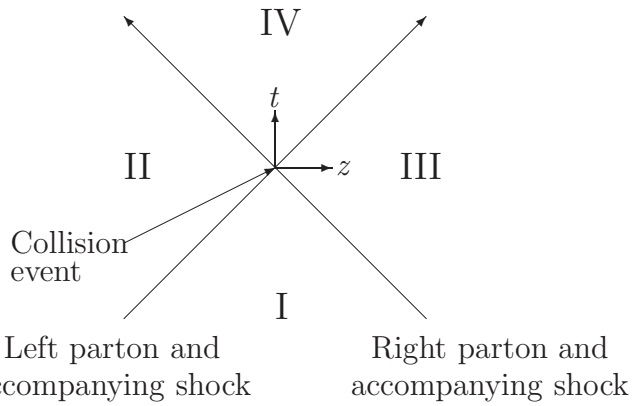

Figure B.1: Spacetime regions in a parton-parton collision. In this diagram, the z axis is defined to lie along the direction of motion of the left parton, and $D-2$ spacelike dimensions are suppressed.

(which states that the EH area never decreases) is used to set bounds on the mass and angular momentum of the formed black hole.

The slice used by Yoshino and Rychkov is the future-most slice outside region IV - i.e. its boundary. This slice gives the most restrictive, and therefore best, bounds on the maximum impact parameter for black hole formation b_{max}. It also gives the best bounds on the mass and angular momentum trapped in the black hole following production.

To obtain the maximum impact parameter for black hole formation, b_{YRmax}, for a given D, the impact parameter b is increased at the given D until it is no longer possible to find an AH. Note that this method gives a lower bound, since there may be impact parameters greater than b_{YRmax} for which an AH forms to the future of the slice considered.

Next we discuss the calculation of the mass and angular momentum bounds for a fixed b and D. In a trapped surface method, this is achieved by calculating the $D-2$ dimensional area corresponding to the AH, A_{AH}. Since the true black hole EH is outside the AH, and the black hole EH area can never decrease according to the area theorem, it is usually the case that the $D-2$ dimensional area of the final produced black hole EH, A_{EH}, is greater than A_{AH}:

$$A_{AH} \leq A_{EH} \ . \tag{B.1}$$

Now, we expect the horizon area of a black hole to be linked to its mass, so we can express the above formula in terms of the mass. The AH mass is defined as the mass of

a Schwarzschild black hole with area A_{AH}:

$$M_{AH} = \frac{(D-2)\Omega_{D-2}}{16\pi G_D}\left(\frac{A_{AH}}{\Omega_{D-2}}\right)^{(D-3)/(D-2)} \quad . \tag{B.2}$$

where the $(D-2)$-area of a unit sphere is

$$\Omega_p = \frac{2\pi^{\frac{p+1}{2}}}{\Gamma\left[(p+1)/2\right]} \, . \tag{B.3}$$

Then (B.1) implies

$$M_{AH} \leq M_{irr} \quad , \tag{B.4}$$

where M_{irr} is the irreducible mass of the produced Myers-Perry black hole – this is the mass of a Schwarzschild black hole having the same horizon area as the Myers-Perry black hole. Since it is defined in terms of the area of the Myers-Perry black hole it is a function of both M and J. Equation (B.4) then represents the trapped surface bound on the mass and angular momentum trapped in the black hole during production, with the equation of the boundary being characterised by

$$M_{AH} = M_{irr} \, . \tag{B.5}$$

To convert (B.5) into a boundary line in the (M, J) plane (which can be scaled to a boundary line in the (ξ, ζ) plane, using notation from section 4.3.2) we first need an equation for the irreducible mass of a Myers-Perry black hole with mass M and angular momentum J. This may be extracted from the definition of M_{irr}:

$$A_{Myers-Perry}(M, J) = A_{Schwarzschild}(M_{irr}) = \Omega_{D-2} r_S^{D-2}(M_{irr}) \, . \tag{B.6}$$

Computing the left hand side of (B.6) using the Myers-Perry metric [50], we find the link between M, J and M_{irr} of a Myers-Perry black hole:

$$r_S^{D-2}(M_{irr}) = r_S^{D-3}(M) r_H(M, J) \, , \tag{B.7}$$

where $r_H(M, J)$ is the Myers-Perry horizon radius, given by

$$r_H^2(M, J) + \left[\frac{(D-2)J}{2M}\right]^2 = r_S^{D-3}(M) r_H^{5-D}(M, J) \, , \tag{B.8}$$

whilst $r_S(M)$ is the horizon radius of a Schwarzschild black hole of mass M, given by

$$r_S(M) = \left[\frac{16\pi G_D M}{(D-2)\Omega_{D-2}}\right]^{1/(D-3)} . \tag{B.9}$$

We now combine equations (B.5) and (B.7) to show that a point on the bound with mass M has horizon radius $r_{Hb}(M)$ given by

$$r_{Hb}(M) = \frac{r_S^{D-2}(M_{AH})}{r_S^{D-3}(M)} . \tag{B.10}$$

Using this and (B.9) in (B.8), we obtain that a point on the bound with mass M has angular momentum J_b where

$$J_b(M) = \frac{2M_{AH}}{(D-2)}\left[\frac{16\pi G_D M_{AH}}{(D-2)\Omega_{D-2}}\right]^{1/(D-3)}\sqrt{(M/M_{AH})^{D-2}-1} , \tag{B.11}$$

which gives an explicit equation for the trapped surface boundary line in the (M, J) plane. Solving for M, the boundary line becomes

$$M_b(J) = M_{AH}\left\{1+\left[\frac{(D-2)J}{2M_{AH}}\right]^2\left[\frac{(D-2)\Omega_{D-2}}{16\pi G_D M_{AH}}\right]^{2/(D-3)}\right\}^{1/(D-2)} . \tag{B.12}$$

To produce valid bounds using (B.1) it is necessary that an arbitrary surface outside the AH has a larger area. Unfortunately, for the Yoshino-Rychkov slice, this does not hold. However, Yoshino and Rychkov found a different area, A_{lb}, which they demonstrated is a true lower bound on A_{EH}. A_{lb} is equal to twice the area of the intersection of the AH with the transverse collision plane using a flat metric. The calculation of the (M, J) bounds then proceeds as described above, with M_{lb} and A_{lb} replacing M_{AH} and A_{AH} in equations (B.1) - (B.12).

Calculation of the mass/angular momentum boundary

After replacing all M_{AH} symbols in the equation by M_{lb} we rewrite equation (B.12) in terms of the fractions of initial state mass and angular momentum ξ and ζ

$$\xi_b(\zeta) = \xi_{lb}\left\{1+\left[\frac{(D-2)b\zeta}{4\xi_{lb}}\right]^2\left[\frac{(D-2)\Omega_{D-2}}{32\pi G_D \mu \xi_{lb}}\right]^{2/(D-3)}\right\}^{1/(D-2)} , \tag{B.13}$$

where $\mu = \sqrt{s}/2$ is the energy of each colliding parton in the centre of mass frame. This equation can be used to calculate the Yoshino-Rychkov bound $\xi_b(\zeta)$ for a given b and D, provided one is able to obtain ξ_{lb} for the b and D values used.

The problem of implementing the Yoshino-Rychkov bound in `CHARYBDIS2` is then one of ensuring that the program has a means of obtaining ξ_{lb} for all values of D and b ($5 \leq D \leq 11$, $0 \leq b \leq b_{YRmax}(D)$). In the program, we use the data files ξ_{lb} vs. b for $D = 5$ to $D = 11$ that were generated by Yoshino and Rychkov (which they used to produce the $D = 5$ to $D = 11$ plots in figure 10 of [76]). The value of ξ_{lb} for a fixed b and D is obtained by linear interpolation between points in these data files, which provides sufficient accuracy due to the close spacing in b.

B.2 Details of the 'constant angular velocity' bias

This section describes the implementation of the constant angular velocity bias in the simulation of the black hole production phase. With the bias off (`CVBIAS=.FALSE.`), the values of (ξ,ζ)[1] are simply those generated from the linear ramp distributions described in section 4.3.2. When the bias is turned on, the (ξ, ζ) point to be passed to the Yoshino-Rychkov boundary routine is obtained in a more complex fashion, which is outlined below.

First, a point is generated using the linear ramp distributions as before. The horizon angular velocity Ω_H and the $a_* = a/r_H$ value corresponding to the point, $\Omega_H(\xi, \zeta)$ and $a_*(\xi, \zeta)$, are calculated using the standard equations (5.18) and (3.13), and compared to those of the initial state, $\Omega_H(1, 1)$ and $a_*(1, 1)$. In particular, the quantities $|\Omega_H(\xi, \zeta) - \Omega_H(1, 1)|/\Omega_H(1, 1)$ and $|\log[a_*(\xi, \zeta)/a_*(1, 1)]|$ are calculated, and compared to the values of some constants Δ and Λ respectively (whose values will be discussed shortly). Note that $|\Omega_H(\xi, \zeta) - \Omega_H(1, 1)|/\Omega_H(1, 1)$ and $|\log[a_*(\xi, \zeta)/a_*(1, 1)]|$ are essentially both measures of the differences between the values at the point and the initial state values.

The point is then assigned a number $\alpha(\xi, \zeta)$ between 0 and 1, whose value largely depends on whether both $|\Omega_H(\xi, \zeta) - \Omega_H(1, 1)|/\Omega_H(1, 1) \leq \Delta$ *and* $|\log[a_*(\xi, \zeta)/a_*(1, 1)]| \leq \Lambda$ or not (i.e. whether $\Omega_H(\xi, \zeta)$ and $a(\xi, \zeta)$ are sufficiently close to $\Omega(1, 1)$ and $a(1, 1)$ or not). If one or both of the conditions are not satisfied, then the point is assigned a constant $k < 1$ (as defined below). If both conditions are satisfied, the point is assigned the value of a function $\chi(\xi, \zeta)$. The function $\chi(\xi, \zeta)$ has the key properties $k < \chi(\xi, \zeta) \leq 1$, and

[1] ξ, ζ are the trapped mass and angular momentum fractions passed to the routine which imposes the Yoshino-Rychkov boundary condition.

approaches 1 as $\Omega_H(\xi,\zeta)$ gets closer to $\Omega_H(1,1)$. The details of our choices for k and $\chi(\xi,\zeta)$ will be discussed shortly.

A random number β is generated according to a uniform distribution between 0 and 1. If $\alpha(\xi,\zeta) > \beta$ then the point is accepted, otherwise it is rejected. If the point is rejected, further (ξ,ζ) points have to be generated by the ramp distributions, and put through the above procedure, until a point is accepted. The final point is passed to the Yoshino-Rychkov boundary routine.

It is reasonably clear that this procedure for generating a (ξ,ζ) point (to be passed to the Yoshino-Rychkov boundary routine) is equivalent to a procedure which generates a point from a biased probability distribution of the form asserted in section 4.3.2. To be specific, the biased probability distribution resembles the basic ramp probability distribution, but all points whose Ω_H and a_* values are sufficiently close to those of the initial state have had their probabilities enhanced. The enhancement is greater the closer $\Omega_H(\xi,\zeta)$ is to $\Omega_H(1,1)$.

We now discuss our choices for the function and the parameters used in the above procedure. A suitable choice for the function $\chi(\xi,\zeta)$, which has the properties stated, is based on the Breit-Wigner form (note that we introduce a further 'width' parameter Γ):

$$\chi(\xi,\zeta) = \frac{\Gamma^2/4}{([\Omega_H(\xi,\zeta) - \Omega_H(1,1)]/\Omega_H(1,1))^2 + \Gamma^2/4} \; . \tag{B.14}$$

The constant k may then be fixed by imposing continuity on $\alpha(\xi,\zeta)$, such that the biased probability distribution represented by the above procedure does not possess any sudden jumps. Note that we hope the dividing curves between the enhanced region and the unenhanced regions to be $|\Omega_H(\xi,\zeta) - \Omega_H(1,1)|/\Omega_H(1,1) = \Delta$ on either side of the 'connected' curve $\Omega_H(\xi,\zeta) = \Omega_H(1,1)$ (which is connected to the point $\xi = 1, \zeta = 1$). As explained in the main text, the a_* condition is only present to remove probability enhancement around the other 'disconnected' $\Omega_H(\xi,\zeta) = \Omega_H(1,1)$ curve, and should not interfere with the angular velocity based enhancement around the right curve.

On the basis of these assumptions, continuity of $\alpha(\xi,\zeta)$ is assured by taking

$$k = \chi(\xi,\zeta)|_{|\Omega_H(\xi,\zeta)-\Omega_H(1,1)|/\Omega_H(1,1)=\Delta} = \frac{\Gamma^2/4}{\Delta^2 + \Gamma^2/4} \; . \tag{B.15}$$

Note that with this choice of $\chi(\xi,\zeta)$ and k, Γ is a constant which sets the 'width' of the probability peak around the connected $\Omega_H(\xi,\zeta) = \Omega_H(1,1)$ curve, and the 'height' of this peak. The smaller Γ is, the sharper and stronger the probability enhancement around the

appropriate curve. The default value of Γ is 0.4 for a probability enhancement which is not too strong - however, the value of this variable could potentially be changed.

The values of Δ and Λ were chosen by looking at a large number of individual (b, D) cases used by `CHARYBDIS2`, and trying to find a suitable combination of values that gave enhancement of a suitable region only around the connected curve. This procedure resulted in the choice $\Delta = 0.2$ and $\Lambda = 0.4$ (these values should not be changed, as small changes can cause drastic changes in the regions where the probability is enhanced).

A final comment is appropriate explaining the slightly peculiar form of the a_* condition for probability enhancement – $|\log[a_*(\xi, \zeta)/a_*(1, 1)]| \leq \Lambda$. The reason for this form is because, when trying to find a condition that discriminated points around the connected curve from those around the disconnected curve, we noticed that those around the disconnected curve, had a_* values that were one order of magnitude (or more) away from the a_* values of the points around the connected curve. To remove the enhancement around the disconnected curve, a condition based on the logarithm of the ratio $a_*(\xi, \zeta)/a_*(1, 1)$ is then more appropriate.

Appendix C

Expansion coefficients and matrices for radial equations

C.1 Expansion coefficients

C.1.1 Scalars

The expansion coefficients we need are defined by

$$\begin{aligned} \Delta &= x\sum_{m=0}^{+\infty}\delta_m x^m \\ K^2-\Delta U &= \sum_{m=0}^{+\infty}\sigma_m x^m \\ \bar{\gamma}_m &= \sum_{k=0}^{m-1}(k+\alpha)\alpha_k\delta_{m-k} \\ \gamma_m &= (m+\alpha)\alpha_m\delta_0+\bar{\gamma}_m \ . \end{aligned} \tag{C.1}$$

It can be shown then that

$$\delta_0 = n+1+(n-1)\left(a^2+Q^2\right) \tag{C.2}$$

$$\delta_1 = 1-\frac{n(n-1)\left(1+a^2+Q^2\right)}{2} \tag{C.3}$$

$$\delta_2 = \frac{n(n^2-1)\left(1+a^2+Q^2\right)}{6} \tag{C.4}$$

$$\delta_{m+1} = -(1+\rho_{m+1})\delta_m \qquad , m\geq 3 \tag{C.5}$$

where

$$\rho_2 = \frac{n-2}{3} \tag{C.6}$$

$$\rho_{m+1} = \left(1 - \frac{1}{m+2}\right)\rho_m \tag{C.7}$$

and

$$\sigma_0 = K_\star^2 \tag{C.8}$$

$$\sigma_1 = 2K_\star(2\omega - qQ) - U_0\delta_0 \tag{C.9}$$

$$\sigma_2 = 2K_\star\omega + (2\omega - qQ)^2 - U_0\delta_1 - U_1\delta_0 \tag{C.10}$$

$$\sigma_3 = 2\omega(2\omega - qQ) - U_0\delta_2 - U_1\delta_1 - U_2\delta_0 \tag{C.11}$$

$$\sigma_4 = \omega^2 - U_0\delta_3 - U_1\delta_2 - U_2\delta_1 \tag{C.12}$$

$$\sigma_m = -U_0\delta_{m-1} - U_1\delta_{m-2} - U_2\delta_{m-3} \qquad , m \geq 5 \tag{C.13}$$

where

$$U_0 = \Lambda + \omega^2 a^2 - 2a\omega m + \mu^2 \tag{C.14}$$

$$U_1 = 2\mu^2 \tag{C.15}$$

$$U_2 = \mu^2 \tag{C.16}$$

C.1.2 Fermions

Similarly to the scalar case define

$$\begin{aligned} 2\Delta\mathbf{M}_{\frac{1}{2}}(r) &= \sum_{m=0}^{+\infty} \mathbf{N}_m \left(\sqrt{x}\right)^m \\ \Delta^{\frac{1}{2}} &= \sqrt{x}\sum_{m=0}^{+\infty} \bar{\delta}_m x^m \\ \mathbf{b}_{2m} &= \sum_{j=0}^{m-1} 2\delta_{m-j}(j+\alpha)\mathbf{a}_{2j} \\ \mathbf{b}_{2m+1} &= \sum_{j=0}^{m-1} \delta_{m-j}(2j+2\alpha+1)\mathbf{a}_{2j+1} \ , \end{aligned} \tag{C.17}$$

The matrices we need are

$$\mathbf{N}_0 = 2iK_\star\hat{\sigma}_3 \tag{C.18}$$

$$\mathbf{N}_1 = 2\lambda\bar{\delta}_0\hat{\sigma}_1 - 2\mu\bar{\delta}_0\hat{\sigma}_2 \tag{C.19}$$

$$\mathbf{N}_2 = 2i(2\omega - qQ)\hat{\sigma}_3 \tag{C.20}$$

$$\mathbf{N}_3 = 2\lambda\bar{\delta}_1\hat{\sigma}_1 - 2\mu\left(\bar{\delta}_1 + \bar{\delta}_0\right)\hat{\sigma}_2 \tag{C.21}$$

$$\mathbf{N}_4 = 2i\omega\hat{\sigma}_3 \tag{C.22}$$

$$\mathbf{N}_{2m} = 0 \ \ , m > 2 \tag{C.23}$$

$$\mathbf{N}_{2m+1} = 2\lambda\bar{\delta}_m\hat{\sigma}_1 - 2\mu(\bar{\delta}_m + \bar{\delta}_{m-1})\hat{\sigma}_2 \ \ , m \geq 1 \tag{C.24}$$

where $\bar{\delta}_i$ are obtained from the following expansion

$$\Delta^{\frac{1}{2}} \ = \ = \sqrt{x}\delta_0^{\frac{1}{2}}\left(1 + \sum_{m=1}^{+\infty}\frac{\delta_m}{\delta_0}x^m\right)^{\frac{1}{2}} \tag{C.25}$$

by fixing a certain order of truncation and expanding the square root in powers of x up to the given order.

C.2 Matrices

In the main text we have used the following matrices:

$$\mathbf{R}_0 = \begin{pmatrix} e^{iy}y^{i\varphi} & 0 \\ 0 & e^{-iy}y^{-i\varphi} \end{pmatrix} \tag{C.26}$$

$$\mathbf{R}_{\frac{1}{2}} = \begin{pmatrix} e^{iy}y^{i\varphi} & 0 \\ 0 & e^{-iy}y^{-i\varphi} \end{pmatrix} \frac{1}{k(\omega+k)} \begin{pmatrix} \omega+k & -\mu \\ -\mu & \omega+k \end{pmatrix} \tag{C.27}$$

$$\mathbf{A}_s = \begin{pmatrix} iB_s & (X_s + iY_s)\,e^{-i\Phi} \\ (X_s - iY_s)\,e^{i\Phi} & -iB_s \end{pmatrix} \tag{C.28}$$

with

$$\Phi = 2\left(y + \varphi \log y - \sum_{m=1}^{j} \frac{c_m}{m y^m}\right) \tag{C.29}$$

$$B_s = \begin{cases} \dfrac{V}{2k^2} - \dfrac{1}{2} - \dfrac{\varphi}{y} - \displaystyle\sum_{m=2}^{j} \frac{c_m}{y^m} & , s = 0 \\ \\ \dfrac{\omega}{k^2}\dfrac{K}{\Delta} - \dfrac{\mu}{k^2}\dfrac{\mu r}{\Delta^{\frac{1}{2}}} - 1 - \dfrac{\varphi}{y} - \displaystyle\sum_{m=2}^{j} \frac{c_m}{y^m} & , s = 1/2 \end{cases} . \tag{C.30}$$

c_m are coefficients such that the corresponding powers in the asymptotic expansion of (C.30) are cancelled;

$$X_s = \begin{cases} \dfrac{1}{\Delta}\left(y + \dfrac{(n-1)\left(1 + a^2 + Q^2\right) k^{n+1}}{2y^n}\right) & , s = 0 \\ \\ \dfrac{\lambda}{\Delta^{\frac{1}{2}}} & , s = 1/2 \end{cases} \tag{C.31}$$

$$Y_s = \begin{cases} \dfrac{V}{2k^2} - \dfrac{1}{2} & , s = 0 \\ \\ \dfrac{1}{\Delta}\left(\dfrac{\mu\omega y}{k^2}\left(y - \Delta^{\frac{1}{2}}\right) + \omega\mu a^2 - a\mu m - \dfrac{qQy}{k}\right) & , s = 1/2 \end{cases} \tag{C.32}$$

and now

$$\Delta = y^2 + k^2\left(a^2 + Q^2\right) - \frac{\left(1 + a^2 + Q^2\right) k^{n+1}}{y^{n-1}} . \tag{C.33}$$

Appendix D

Details of the CHARYBDIS2 implementation

D.1 How to set up CHARYBDIS2

The current release of CHARYBDIS2 [3] contains the following code files (the symbol * denotes the version number):

- `maincharybdis.f`, `mainherwig.f` and `mainpythia.f` – These are the three possible main programs for stand-alone parton level CHARYBDIS2, interface with HERWIG and interface with PYTHIA respectively as described in section 7.4.
- `charybdis2*.F` – Contains the main event generation code.
- `charybdis2*.inc` – Contains the declaration of global common blocks.
- `charybdis2.init` – List of all input variables which can be changed by the user according to the format specified in the header instructions.
- `Makefile` – This contains different flags to select different main program options (CHARYBDIS2, HERWIG or PYTHIA) and libraries, and the compilation instructions to build the executable file.

In addition, the data files with the cumulative functions constructed from the Hawking fluxes and the model for mass and angular momentum loss have to be placed in a sub-directory called `data_files`. Further instruction can be found in the Makefile, the main programs, the `charybdis2.init` file, the `README` file and the project webpage [3].

D.2 Remnant decay generation

D.2.1 Momenta selection

Equation (7.15) assumes that we have a massive object (in this case a black hole), which decays into N objects at once and where the phase space distribution for each of the emissions is independent of the others. To generate the phase space, we will use a decay chain structure as in figure D.1

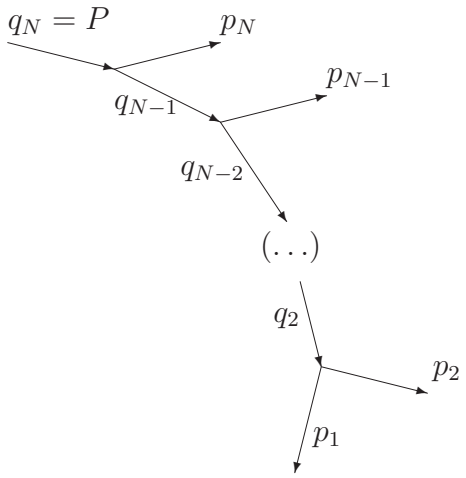

Figure D.1: N-body decay as a chain

The 2-body case

For the special case of a 2-body decay, the phase space is

$$dP\left(\{E_1,\Omega_1\},\{E_2,\Omega_2\}\right) \propto \rho\left(E_1,\Omega_1\right)\rho\left(E_2,\Omega_2\right)\delta^{(4)}\left(P-p_1-p_2\right)dE_1 d\Omega_1 dE_2 d\Omega_2 \quad \text{(D.1)}$$

the delta function produces the following constraints

$$\begin{cases} E_{\{1,2\}} = \dfrac{M}{2}\left[1+\left(\dfrac{m_{\{1,2\}}}{M}\right)^2-\left(\dfrac{m_{\{2,1\}}}{M}\right)^2\right] \\ \Omega_2 = -\Omega_1 \end{cases} \quad \text{(D.2)}$$

so we can eliminate 4 parameters by integrating $dE_1 dE_2 d\Omega_2$. The integration over E_1 is straightforward and we eliminate the $\delta(M-E_1-E_2)$ factor. The remaining integration is done by changing from variables $dE_2 d\Omega_2$ to d^3p_2. After calculating the appropriate

Jacobian factor we get

$$dP\left(\Omega_1\right) \propto \frac{\rho_1\left(E_1,\Omega_1\right)\rho_2\left(E_2,\Omega_2\right)}{E_2\left|p_2\right|}d\Omega_1 \propto \rho_1\left(E_1,\Omega_1\right)\rho_2\left(E_2,\Omega_2\right)d\Omega_1 \tag{D.3}$$

where E_1, E_2, Ω_2 are determined by the expressions above.

Therefore, to generate a 2-body decay we only need to generate the orientation of the momentum vector in the rest frame of the initial object. The energies and momentum magnitudes are fixed by the kinematically allowed values (D.2). Since the weight is independent of ϕ_1 it is generated uniformly and accepted with probability 1. To generate $\cos\theta_1$ we note that for all ρ_i

$$\rho(E,\Omega) = n(E)A(E,\cos\theta)\ . \tag{D.4}$$

where

$$n(E) = \frac{\mathbb{T}_k^{(D)}(Er_H, a_*)}{\exp(\tilde{E}/T_H) \pm 1} \tag{D.5}$$

is just a constant and

$$A = \left|S_k(\cos\theta)\right|^2 \tag{D.6}$$

is the angular probability function. Thus we can construct the following cumulative function

$$c(\cos\theta_1) = \int_{-1}^{\cos\theta_1} A_1(E_1,y)A_2(E_2,y)dy\ . \tag{D.7}$$

Then the phase space probability density function becomes (up to a constant prefactor)

$$dP\left(\Omega_1\right) \propto dc\, d\phi_1\ . \tag{D.8}$$

So to generate $\cos\theta_1$ we generate c uniformly, and obtain $\cos\theta_1$ by inverting the function $c(\cos\theta_1)$. For this special case the procedure has efficiency 1.

The N-body case

When we have more particles, the same initial manipulations apply in the rest frame of

$$q_2 \equiv P - \sum_{i=3}^{N} p_i\ . \tag{D.9}$$

The only change is that the initial probability distribution was written in the rest frame of P, so we need to perform an initial boost. The Lorentz transformation gives

$$E_i = \frac{E_{q_2} E_i^{q_2} - \vec{q_2}.\vec{p_i}^{q_2}}{M_{q_2}} \tag{D.10}$$

where M_{q_2} is the invariant mass of the 4-momentum q_2. The phase space factors become

$$dE_i d\Omega_i = \frac{|\vec{p}^{q_2}|}{|\vec{p}|} dE_i^{q_2} d\Omega_i^{q_2} \ . \tag{D.11}$$

Thus the integration of $dE_1 dE_2 d\Omega_2$ is exactly as before. Furthermore it is useful to perform Lorentz transformations of the remaining phase space variables to the rest frames of the following momentum transfers

$$q_j \equiv P - \sum_{i=j+1}^{N} p_j \ . \tag{D.12}$$

It is useful to define in addition

$$\mu_j \equiv \sum_{i=1}^{j} m_i \ . \tag{D.13}$$

The phase space manipulations are the following

$$\begin{aligned}
dP &\propto \rho_1(E_1,\Omega_1)\,\rho_2(E_2,\Omega_2)\ldots\delta^{(4)}(q_2-p_1-p_2)\,dE_1 d\Omega_1 dE_2 d\Omega_2\ldots dE_N d\Omega_N \\
\Leftrightarrow dP &\propto \rho_1\rho_2\ldots\delta^{(4)}(q_2-p_1-p_2)\,\frac{|\vec{p_1}^{q_2}|}{|\vec{p_1}|}\frac{|\vec{p_2}^{q_2}|}{|\vec{p_2}|} dE_1^{q_2} d\Omega_1^{q_2} dE_2^{q_2}\ldots\frac{|\vec{p_N}^{q_N}|}{|\vec{p_N}|} dE_N^{q_N} d\Omega_N^{q_N} \\
\Leftrightarrow \int dP &\propto \rho_1\rho_2\ldots\rho_N \frac{|\vec{p_1}^{q_2}|}{|\vec{p_1}||\vec{p_2}|E_2^{q_2}} d\Omega_1^{q_2} \frac{|\vec{p_3}^{q_3}|}{|\vec{p_3}|} dE_3^{q_3} d\Omega_3^{q_3}\ldots 1.dE_N^{q_N} d\Omega_N^{q_N}
\end{aligned} \tag{D.14}$$

where in the second line we boost each momentum p_i to the frame of q_i and in the third line we integrate over $dE_1 dE_2 d\Omega_2$ and use the fact that $q_N = P$. Note again that

$$\begin{cases} E_{\{1,2\}}^{q_2} = \dfrac{M_{q_2}}{2}\left[1 + \left(\dfrac{m_{\{1,2\}}}{M_{q_2}}\right)^2 - \left(\dfrac{m_{\{2,1\}}}{M_{q_2}}\right)^2\right] \\ \Omega_2^{q_2} = -\Omega_1^{q_2} \end{cases} \ . \tag{D.15}$$

Following [186], we can perform a change of variable and an ordering of the M_j's to generate them uniformly in the allowed region

$$M_i \equiv \mu_i + r^i(M - \mu_N) \tag{D.16}$$

with

$$0 \leq r_2 \leq r_3 \ldots r_{N-1} \leq 1 \; . \tag{D.17}$$

Then it is possible to show (neglecting the masses of the outgoing particles p_i and overall constant factors) that the probability distribution becomes

$$\int dP \propto \rho_1 \rho_2 \ldots \rho_N \frac{|\vec{p_1}^{\,q_2}|}{|\vec{p_1}||\vec{p_2}|E_2^{q_2}} d\Omega_1^{q_2} \frac{|\vec{p_3}^{\,q_3}|}{|\vec{p_3}|} dr_2 d\Omega_3^{q_3} \ldots \frac{|\vec{p_i}^{\,q_i}|}{|\vec{p_i}|} dr_{i-1} d\Omega_i^{q_i} \ldots 1.dr_{N-1} d\Omega_N^{q_N} \; . \tag{D.18}$$

Note that now we have a set of weights for each phase space point, so the efficiency is reduced since we have to perform an acception/rejection procedure according to the weight.

D.2.2 Angular momenta selection

Selecting the angular momentum quantum numbers with the choice of phase space (7.15) would require an integration over the momenta, to obtain a probability distribution for the $\{j_i, m_i\}$. This is in general complicated. Furthermore, for consistency, we would have to impose angular momentum conservation in a way that the partial waves add up to the angular momentum of the remnant before decaying. Since the model for the remnant is only supposed to be a rough description of the decay (possibly constrained by some physically reasonable assumptions) we adopt a method where we simply impose angular momentum conservation combined with a product of independent probabilities for each partial wave

$$P\left(\{j_1, m_1\}, \ldots, \{j_N, m_N\}\right) \sim \prod_{i=1}^{N} P_i\left(j_i, m_i\right) \delta_{J_{rem}, \sum_j m_j} \; , \tag{D.19}$$

where we took the axis of the angular momentum of the remnant as quantisation axis, i.e. $M_{rem} = J_{rem}$. To simplify the method we do not generate exactly this distribution, but apply the following algorithm: First we select the partial wave numbers for the first $N-1$ waves sequentially by using, for each wave, the cumulative functions (7.13). In the process we start by combining the angular momentum of the remnant with the negative of the first wave selected (according to the usual rules). Then the resulting angular momentum is combined with the next partial wave selected, similarly. This is repeated until the $N-1$th partial wave. In this sequence, the range of allowed values for the next j_i is kept. For the last Nth partial wave, m_N is chosen so as to add up the total $M = M_{rem} - \sum_i m_i = 0$.

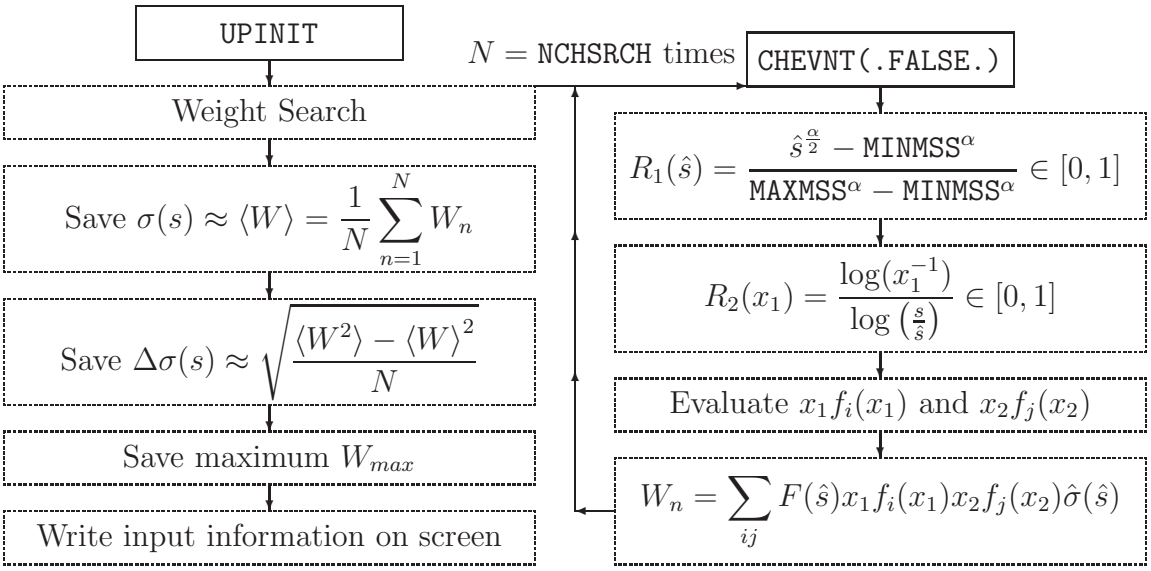

Figure D.2: Diagram illustrating the implementation of the UPINIT subroutine.

Finally, the last j_N is selected among the allowed values using the relative probabilities for waves with $m = m_N$ (this is obtained from (7.13)).

D.3 The UPINIT subroutine

Figure D.2 contains a diagrammatic representation of the UPINIT subroutine in CHARYBDIS2. This is largely the same as the implementation in CHARYBDIS, with the only difference being the Yoschino-Rychkov factors which enhances the cross-section. This subroutine consists of a weight search which calls the CHEVNT subroutine with the option not to generate events (i.e. .FALSE.). The scan of weights is done NCHSRCH times (the default value is 10^5). The aim is to compute the total cross section (7.3). To make the integrand flatter, in the early version of CHARYBDIS the change to the variables $\{R_1, R_2\}$ (as defined in the figure) was performed. The Jacobian times the phase space volume factor that arises by applying the transformation to (7.3) and applying the MC approximation (7.1) is

$$F(\hat{s}) = \frac{2(\mathtt{MAXMSS}^{\alpha} - \mathtt{MINMSS}^{\alpha})}{\alpha \hat{s}^{\frac{\alpha}{2}}} \log\left(\frac{s}{\hat{s}}\right) \tag{D.20}$$

where

$$\alpha = \frac{2}{D-3} - 7\,. \tag{D.21}$$

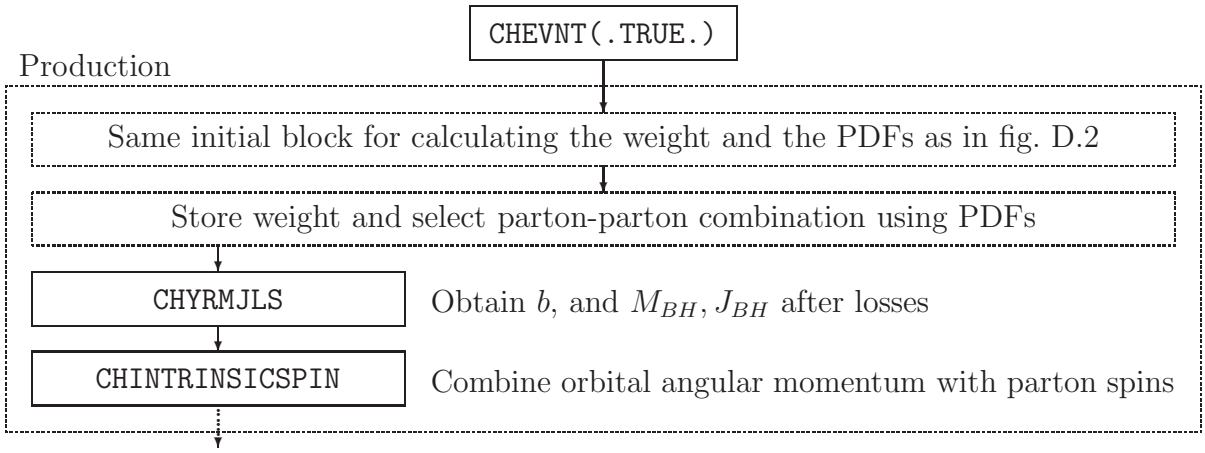

Figure D.3: Diagram illustrating the production in CHEVNT.

Then in each call of CHEVNT(.FALSE.), R_1 and R_2 are randomly generated uniformly in their allowed ranges, the PDFs are evaluated, and finally the weight is computed by multiplying the partonic cross section by the PDF factors and the F factor for the kinematic variables corresponding to $\{R_1, R_2\}$. In this loop the maximum weight W_{max} is determined.

Finally, the sum of the weights and the sum of the squares of the weights is used to compute the total cross section and its error $\Delta\sigma$. The full set of input parameters for the run (table 7.1) are also printed on screen.

D.4 The UPEVNT subroutine

The UPEVNT subroutine simply calls the CHEVNT with argument .TRUE. to generate weighted events. The CHEVNT subroutine can be split into three stages which are responsible for black hole production, evaporation and remnant final decay, respectively.

Figure D.3 shows the production schematically. The first part consists of one step in the weight search of figure D.2. This provides the weight for the event selected. The exact combination of incoming partons is then chosen by generating the following cumulant uniformly

$$C(i,j) = \frac{\sum_{i'=1}^{i}\sum_{j'=1}^{j} f_{i'}(x_1) f_{j'}(x_2)}{\sum_{i'=1}^{13}\sum_{j'=1}^{13} f_{i'}(x_1) f_{j'}(x_2)} \in [0,1]\,, \tag{D.22}$$

where $i = 1, \ldots, 13$ runs over all quarks anti-quarks and the gluon. The weight for the event is then given by the sum over possible parton-parton combinations. The incoming

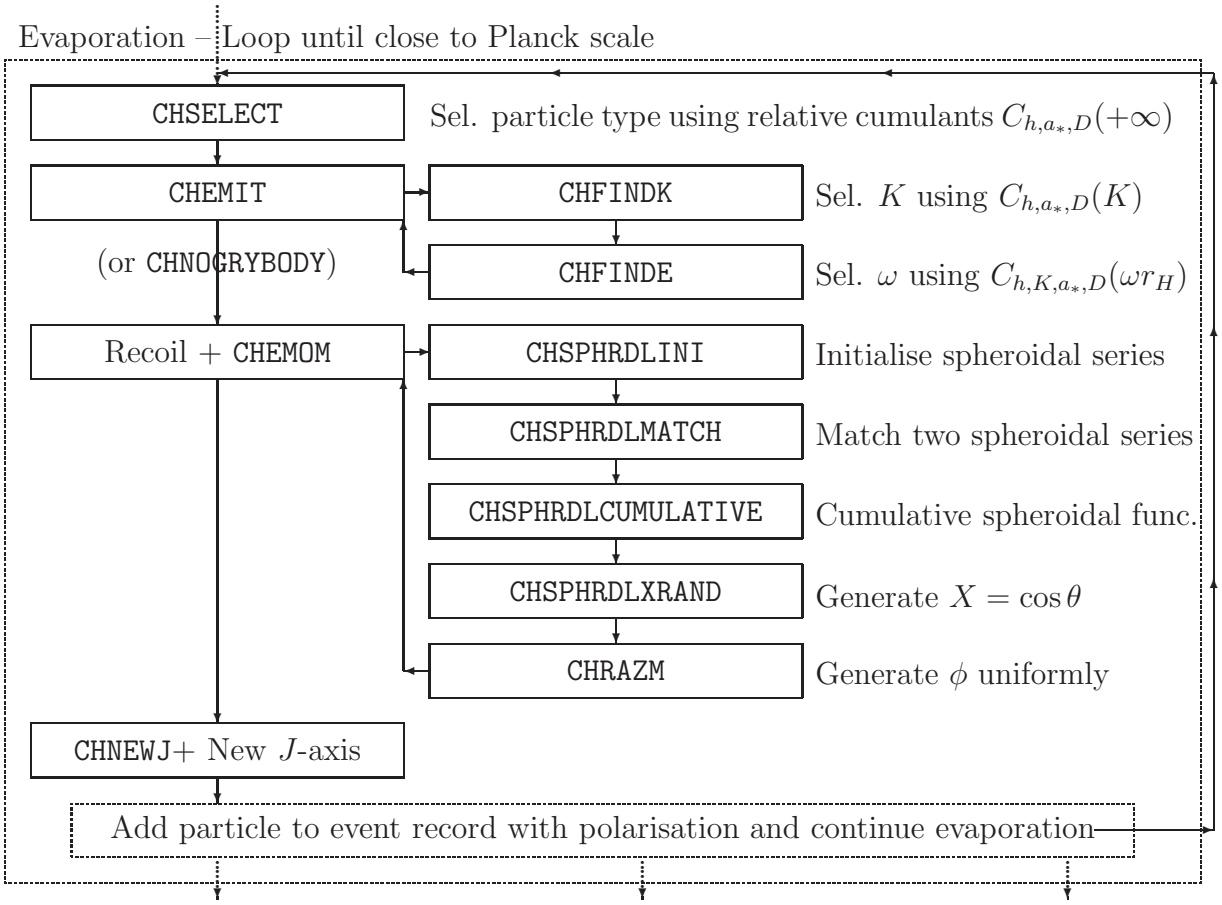

Figure D.4: Diagram illustrating the evaporation in CHEVNT

parton information is stored in the Les Houches common block event record.

Next, the subroutine CHYRMJLS is called to select the impact parameter for the collision and obtain the mass and angular momentum of the black hole produced. Then the orbital angular momentum is combined with the intrinsic spin of the colliding partons by calling CHINTRINSICSPIN. The missing energy associated with gravitational radiation is placed in a collective graviton in the event record.

In figure D.4 the evaporation is described as a loop over the main routines and pieces of code in CHEVNT. For each call of the loop, a Hawking emission is produced.

The first subroutine CHSELECT selects the particle type by generating the following cumulant uniformly

$$C(i) = \frac{\sum_{j=1}^{i} g_j C_{h,a_*,D}(+\infty)}{\sum_{j=1}^{7} g_j C_{h,a_*,D}(+\infty)} \in [0,1] \tag{D.23}$$

where j runs over the following collective sets of particles (organised by spins): leptons,

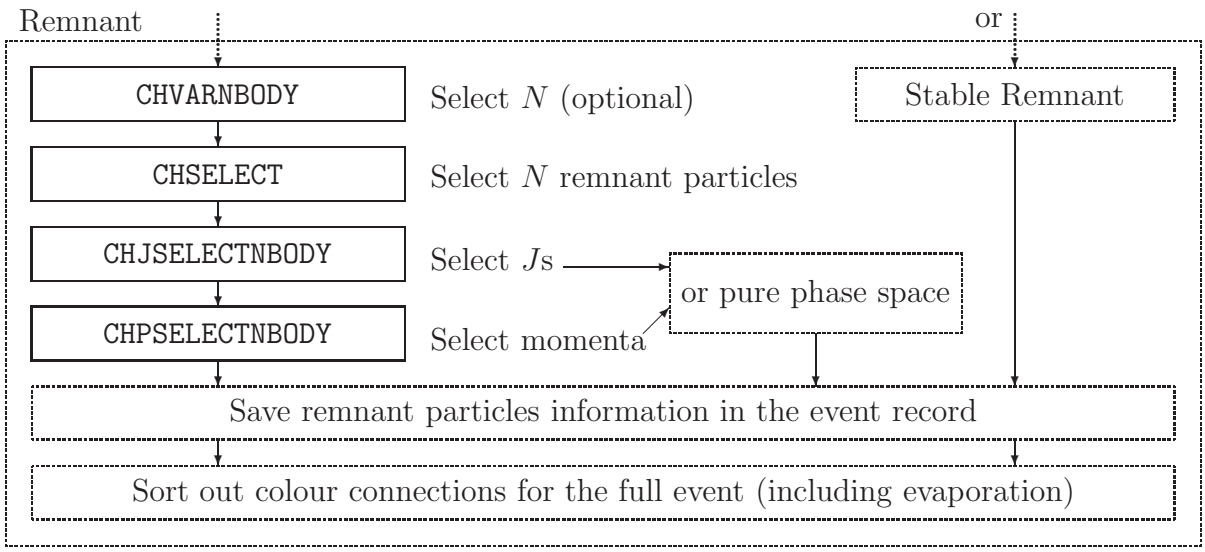

Figure D.5: Diagram illustrating the remnant models in CHEVNT.

neutrinos, quarks, gluon, photon, W, Z and Higgs (note that $C_{h,a_*,D}(+\infty)$ is proportional to the amount of particles of spin h that can be emitted – see equation (7.13)). The longitudinal modes of the W and Z are actually treated as scalars. The g_j count the number of degrees of freedom for each particle from the possible helicities and gauge charges (the latter are generated with uniform probability).

After the particle type has been selected we need to find its momentum vector. The energy is obtained with the subroutine CHEMIT. This starts with the selection of a partial wave number K by calling CHFINDK, which uses the cumulant in equation (7.13). The energy is obtained similarly (after K is fixed) by calling CHFINDE. Next a recoil model according to section 7.2.1 is chosen and the subroutine CHEMOM is called which generates the orientation of the momentum vector. The latter consists of a call of CHSPHRDLINI and CHSPHRDLMATCH to initialise the series for the spheroidal wave functions and match the two expansions (see section 6.1). CHSPHRDLCUMULATIVE generates the cumulant

$$c(\cos\theta) = \int_{-1}^{\cos\theta} |S_k(x)|^2 \, dx \in [0,1] \tag{D.24}$$

uniformly, and $\cos\theta$ is obtained by inverting $c(\cos\theta)$. The azimuthal angle is generated uniformly by calling CHRAZM. The final step checks if the emission is kinematically allowed, stores the emission in the event record and the black hole history, and checks if the evaporation loop should continue.

Figure D.5 shows the final step of the event. The remnant models are those in sec-

tion 7.3 so there is either a decay to SM particles, or the final black hole remnant is made stable. The N-body decay starts with `CHVARNBODY` (if a variable multiplicity model is used), which selects the multiplicity of the decay according to equation (7.18) and the text below it. Then the N particle types are chosen using the subroutine `CHSELECT` at fixed black hole parameters. The momenta of the particles can be chosen using the phase space described in section D.2 by calling `CHJSELECTNBODY` and `CHPSELECTNBODY`, or a pure phase space which was kept from `CHARYBDIS`. Finally, the remnant decay information is stored in the event record and the colour connections for the full event are determined.

D.5 Eternal black hole angular correlators

We define the probability density function for the correlator $x_{i,j}$ (up to a normalisation constant)

$$\rho(x_{i,j}) \propto \int dx_i dx_j d\phi_i d\phi_j \rho_i(x_i)\rho_i(x_j)\delta\left(x_{i,j} - \sqrt{1-x_i^2}\sqrt{1-x_j^2}\cos(\phi_i-\phi_j) - x_i x_j\right) \tag{D.25}$$

where we have defined the spatial momenta of particle i (or j)

$$\mathbf{p}_i = \left(\sqrt{1-x_i^2}\cos\phi_i, \sqrt{1-x_i^2}\sin\phi_i, x_i\right)|\mathbf{p}| \tag{D.26}$$

and

$$\rho_i(x_i) = \sum_{K=0}^{+\infty}\int_0^{+\infty} d\omega \frac{\mathbb{T}_k^{(D)}(x,a_*)}{\exp(\tilde{\omega}r_H/\tau_H)\pm 1}|S_k(a\omega,x_i)|^2 \tag{D.27}$$

is the probability density of having a particle of type i (with any energy) emitted with direction x_i with respect to the angular momentum axis. Due to the azimuthal symmetry, the distribution is uniform in the ϕ_i direction. This can be written in a more convenient form by using the definitions in equations (7.13)

$$\rho_i(x_i) = \sum_{K=0}^{+\infty}\int_0^{+\infty} d\omega \frac{dC_{h,K,a_*,D}(\omega r_H)}{d\omega}|S_k(a\omega,x_i)|^2\,. \tag{D.28}$$

Then making the change of variable $y = f_K(\omega) \equiv C_{h,K,a_*,D}(\omega r_H)/C_{h,K,a_*,D}(+\infty)$

$$\begin{aligned}\rho_i(x_i) &= \sum_{K=0}^{+\infty} \int_0^1 dy\, C_{h,K,a_*,D}(+\infty)|S_k(af_K^{(-1)}(y), x_i)|^2 \\ &= \int_0^1 dy \sum_{K=0}^{+\infty} C_{h,K,a_*,D}(+\infty)|S_k(af_K^{(-1)}(y), x_i)|^2 \end{aligned} \tag{D.29}$$

where $f^{(-1)}$ is the inverse function (not $1/f$). Now if we define

$$\begin{aligned} C_i(x_i) &\equiv \int_{-1}^{x_i} dx\, \rho_i(x) \\ &= \int_0^1 dy \sum_{K=0}^{+\infty} C_{h,K,a_*,D}(+\infty) \int_{-1}^{x_i} dx |S_k(af_K^{(-1)}(y), x)|^2 \end{aligned} \tag{D.30}$$

$$\Rightarrow \rho_i(x_i) = \frac{dC_i(x_i)}{dx_i}\,. \tag{D.31}$$

Going back to equation (D.25) we perform the changes of variables

$$\Phi = \phi_i + \phi_j \tag{D.32}$$

$$\phi = \phi_i - \phi_j \tag{D.33}$$

$$w_i = g_i(x_i) = C_i(x_i)/C_i(1) \tag{D.34}$$

to obtain

$$\begin{aligned}\rho(x_{i,j}) &\propto \int_0^1 \int_0^1 \int_0^{4\pi} \int_{-2\pi}^{2\pi} dw_i\, dw_j\, d\Phi\, d\phi\, \delta\left(x_{i,j} - \sqrt{1-x_i^2}\sqrt{1-x_j^2}\cos\phi - x_i x_j\right) \\ \Rightarrow \rho(x_{i,j}) &= \frac{1}{2\pi}\int_0^1 \int_0^1 \int_0^{2\pi} dw_i\, dw_j\, d\phi\, \delta\left(x_{i,j} - \sqrt{1-x_i^2}\sqrt{1-x_j^2}\cos\phi - x_i x_j\right) \end{aligned} \tag{D.35}$$

where $x_i = g^{(-1)}(w_i)$ and we have normalised the distribution. The histogram for $\rho(x_{i,j})$ is obtained by generating the phase space w_i, w_j, ϕ uniformly and adding a unit weight to the bin for the corresponding

$$x_{i,j} = \sqrt{1-x_i^2}\sqrt{1-x_j^2}\cos\phi + x_i x_j\,. \tag{D.36}$$

Bibliography

[1] M. O. P. Sampaio, *Charge and mass effects on the evaporation of higher-dimensional rotating black holes*, *JHEP* **10** (2009) 008, [arXiv:0907.5107].

[2] M. O. P. Sampaio, *Distributions of charged massive scalars and fermions from evaporating higher-dimensional black holes*, *JHEP* **02** (2010) 042, [arXiv:0911.0688].

[3] J. A. Frost, J. R. Gaunt, M. O. P. Sampaio, and B. R. Webber, *CHARYBDIS2 project*, April, 2009. http://projects.hepforge.org/charybdis2/.

[4] J. A. Frost, J. R. Gaunt, M. O. P. Sampaio, M. Casals, S. R. Dolan, M. A. Parker, and B. R. Webber, *Phenomenology of production and decay of spinning extra-dimensional black holes at hadron colliders*, *JHEP* **10** (2009) 014, [arXiv:0904.0979].

[5] **Particle Data Group** Collaboration, C. Amsler *et al.*, *Review of particle physics*, *Phys. Lett.* **B667** (2008) 1.

[6] M. E. Peskin and D. V. Schroeder, *An introduction to quantum field theory*. Reading, USA: Addison-Wesley, 1995. 842 p.

[7] C. M. Will, *The confrontation between general relativity and experiment*, *Living Reviews in Relativity* **9** (2006), no. 3.

[8] D. J. Kapner, T. S. Cook, E. G. Adelberger, J. H. Gundlach, B. R. Heckel, C. D. Hoyle, and H. E. Swanson, *Tests of the gravitational inverse-square law below the dark-energy length scale*, *Physical Review Letters* **98** (2007), no. 2 021101, [hep-ph/0611184].

[9] L.-C. Tu, S.-G. Guan, J. Luo, C.-G. Shao, and L.-X. Liu, *Null test of Newtonian inverse-square law at submillimeter range with a dual-modulation torsion pendulum*, *Physical Review Letters* **98** (2007), no. 20 201101.

[10] M. B. Green, J. H. Schwarz, and E. Witten, *Superstring theory. Vol. 1: Introduction*. Cambridge, UK: Cambridge University Press, 1987. 469 pages (Cambridge monographs on mathematical physics).

[11] C. Kiefer, *Quantum gravity*, *Int. Ser. Monogr. Phys.* **124** (2004) 1–308.

[12] C. Rovelli, *Loop quantum gravity*, *Living Rev. Rel.* **11** (2008) 5.

[13] J. F. Donoghue, *Introduction to the effective field theory description of gravity*, `gr-qc/9512024`.

[14] L. Susskind, *Dynamics of spontaneous symmetry breaking in the Weinberg-Salam theory*, *Phys. Rev.* **D20** (1979) 2619–2625.

[15] A. Djouadi, *The anatomy of electro-weak symmetry breaking. I: The Higgs boson in the standard model*, *Phys. Rept.* **457** (2008) 1–216, [`hep-ph/0503172`].

[16] S. P. Martin, *A Supersymmetry primer*, `hep-ph/9709356`.

[17] N. Arkani-Hamed, A. G. Cohen, and H. Georgi, *Electroweak symmetry breaking from dimensional deconstruction*, *Phys. Lett.* **B513** (2001) 232–240, [`hep-ph/0105239`].

[18] I. Antoniadis, *A possible new dimension at a few TeV*, *Phys. Lett.* **B246** (1990) 377–384.

[19] N. Arkani-Hamed, S. Dimopoulos, and G. R. Dvali, *The hierarchy problem and new dimensions at a millimeter*, *Phys. Lett.* **B429** (1998) 263–272, [`hep-ph/9803315`].

[20] I. Antoniadis, N. Arkani-Hamed, S. Dimopoulos, and G. R. Dvali, *New dimensions at a millimeter to a Fermi and superstrings at a TeV*, *Phys. Lett.* **B436** (1998) 257–263, [`hep-ph/9804398`].

[21] N. Arkani-Hamed, S. Dimopoulos, and G. R. Dvali, *Phenomenology, astrophysics and cosmology of theories with sub-millimeter dimensions and TeV scale quantum gravity*, *Phys. Rev.* **D59** (1999) 086004, [`hep-ph/9807344`].

[22] L. Randall and R. Sundrum, *A large mass hierarchy from a small extra dimension*, *Phys. Rev. Lett.* **83** (1999) 3370–3373, [hep-ph/9905221].

[23] L. Randall and R. Sundrum, *An alternative to compactification*, *Phys. Rev. Lett.* **83** (1999) 4690–4693, [hep-th/9906064].

[24] S. B. Giddings and S. D. Thomas, *High energy colliders as black hole factories: The end of short distance physics*, *Phys. Rev.* **D65** (2002) 056010, [hep-ph/0106219].

[25] G. F. Giudice, R. Rattazzi, and J. D. Wells, *Transplanckian collisions at the LHC and beyond*, *Nucl. Phys.* **B630** (2002) 293–325, [hep-ph/0112161].

[26] G. F. Giudice, R. Rattazzi, and J. D. Wells, *Quantum gravity and extra dimensions at high-energy colliders*, *Nucl. Phys.* **B544** (1999) 3–38, [hep-ph/9811291].

[27] E. A. Mirabelli, M. Perelstein, and M. E. Peskin, *Collider signatures of new large space dimensions*, *Phys. Rev. Lett.* **82** (1999) 2236–2239, [hep-ph/9811337].

[28] T. Appelquist, A. Chodos, and P. G. O. Freund, *Introduction to 'Modern Kaluza-Klein theories.'*. Redwood City, Calif ; Wokingham : Addison-Wesley Pub. Co, 1987.

[29] R. Sundrum, *Effective field theory for a three-brane universe*, *Phys. Rev.* **D59** (1999) 085009, [hep-ph/9805471].

[30] T. Appelquist, H.-C. Cheng, and B. A. Dobrescu, *Bounds on universal extra dimensions*, *Phys. Rev.* **D64** (2001) 035002, [hep-ph/0012100].

[31] T. Flacke, D. Hooper, and J. March-Russell, *Improved bounds on universal extra dimensions and consequences for LKP dark matter*, *Phys. Rev.* **D73** (2006) 095002, [hep-ph/0509352].

[32] U. Haisch and A. Weiler, *Bound on minimal universal extra dimensions from* $\bar{B} \to X_s\gamma$, *Phys. Rev.* **D76** (2007) 034014, [hep-ph/0703064].

[33] N. Arkani-Hamed and M. Schmaltz, *Hierarchies without symmetries from extra dimensions*, *Phys. Rev.* **D61** (2000) 033005, [hep-ph/9903417].

[34] N. Arkani-Hamed, Y. Grossman, and M. Schmaltz, *Split fermions in extra dimensions and exponentially small cross-sections at future colliders*, *Phys. Rev.* **D61** (2000) 115004, [hep-ph/9909411].

[35] P. Callin and F. Ravndal, *Higher order corrections to the Newtonian potential in the Randall-Sundrum model*, *Phys. Rev.* **D70** (2004) 104009, [hep-ph/0403302].

[36] T. Han, J. D. Lykken, and R.-J. Zhang, *On Kaluza-Klein states from large extra dimensions*, *Phys. Rev.* **D59** (1999) 105006, [hep-ph/9811350].

[37] **CDF** Collaboration, T. Aaltonen *et al.*, *Search for large extra dimensions in final states containing one photon or jet and large missing transverse energy produced in $p\bar{p}$ collisions at $\sqrt{s}$ = 1.96-TeV*, *Phys. Rev. Lett.* **101** (2008) 181602, [arXiv:0807.3132].

[38] **LEP Exotica Working Group** Collaboration, W. Adam *et al.*, *Combination of LEP results on direct searches for large extra dimensions*, . http://lepexotica.web.cern.ch/LEPEXOTICA/notes/2004-03/ed_note_final.ps.gz.

[39] **D0** Collaboration, V. M. Abazov *et al.*, *Search for large extra spatial dimensions in dimuon production at D0*, *Phys. Rev. Lett.* **95** (2005) 161602, [hep-ex/0506063].

[40] **D0** Collaboration, V. M. Abazov *et al.*, *Search for large extra spatial dimensions in the dielectron and diphoton channels in $p\bar{p}$ collisions at $\sqrt{s}$ = 1.96-TeV*, *Phys. Rev. Lett.* **102** (2009) 051601, [arXiv:0809.2813].

[41] **D0** Collaboration, V. M. Abazov *et al.*, *Search for Randall-Sundrum gravitons in dilepton and diphoton final states*, *Phys. Rev. Lett.* **95** (2005) 091801, [hep-ex/0505018].

[42] S. Hannestad and G. G. Raffelt, *Supernova and neutron-star limits on large extra dimensions reexamined*, *Phys. Rev.* **D67** (2003) 125008, [hep-ph/0304029].

[43] S. Hannestad, *Strong constraint on large extra dimensions from cosmology*, *Phys. Rev.* **D64** (2001) 023515, [hep-ph/0102290].

[44] K. S. Thorne, *Magic without magic: John Archibald Wheeler*. San Francisco, USA: Freeman, 1972. edited by J. Klauder.

[45] P. C. Argyres, S. Dimopoulos, and J. March-Russell, *Black holes and sub-millimeter dimensions*, *Phys. Lett.* **B441** (1998) 96–104, [hep-th/9808138].

[46] S. Dimopoulos and G. L. Landsberg, *Black holes at the LHC*, *Phys. Rev. Lett.* **87** (2001) 161602, [hep-ph/0106295].

[47] S. W. Hawking and G. F. R. Ellis, *The large scale structure of space-time.* Cambridge, UK: Cambridge University Press, 1973.

[48] V. P. Frolov and I. D. Novikov, *Black hole physics: Basic concepts and new developments*, . Dordrecht, Netherlands: Kluwer Academic (1998) 770 p.

[49] S. W. Hawking and W. Israel, *General relativity. An Einstein century survey.* Cambridge, UK: Cambridge University Press, 1979. 919 p.

[50] R. C. Myers and M. J. Perry, *Black holes in higher dimensional space-times*, *Ann. Phys.* **172** (1986) 304.

[51] N. Kaloper and D. Kiley, *Exact black holes and gravitational shockwaves on codimension-2 branes*, *JHEP* **03** (2006) 077, [hep-th/0601110].

[52] D. Kiley, *Rotating black holes on codimension-2 branes*, *Phys. Rev.* **D76** (2007) 126002, [arXiv:0708.1016].

[53] D.-C. Dai, N. Kaloper, G. D. Starkman, and D. Stojkovic, *Evaporation of a black hole off of a tense brane*, *Phys. Rev.* **D75** (2007) 024043, [hep-th/0611184].

[54] T. Kobayashi, M. Nozawa, and Y.-i. Takamizu, *Bulk scalar emission from a rotating black hole pierced by a tense brane*, *Phys. Rev.* **D77** (2008) 044022, [arXiv:0711.1395].

[55] S. Chen, B. Wang, R.-K. Su, and W. Y. P. Hwang, *Greybody factors for rotating black holes on codimension-2 branes*, *JHEP* **03** (2008) 019, [arXiv:0711.3599].

[56] S. Hannestad and G. G. Raffelt, *Stringent neutron-star limits on large extra dimensions*, *Phys. Rev. Lett.* **88** (2002) 071301, [hep-ph/0110067].

[57] V. H. Satheeshkumar and P. K. Suresh, *Bounds on large extra dimensions from photon fusion process in SN1987A*, *JCAP* **0806** (2008) 011, [arXiv:0805.3429].

[58] P. C. Aichelburg and R. U. Sexl, *On the gravitational field of a massless particle*, *Gen. Rel. Grav.* **2** (1971) 303–312.

[59] D. M. Eardley and S. B. Giddings, *Classical black hole production in high-energy collisions*, *Phys. Rev.* **D66** (2002) 044011, [gr-qc/0201034].

[60] A. N. Aliev and A. E. Gumrukcuoglu, *Charged rotating black holes on a 3-brane*, *Phys. Rev.* **D71** (2005) 104027, [hep-th/0502223].

[61] A. Chamblin, H. S. Reall, H.-a. Shinkai, and T. Shiromizu, *Charged brane-world black holes*, *Phys. Rev.* **D63** (2001) 064015, [hep-th/0008177].

[62] S. Creek, O. Efthimiou, P. Kanti, and K. Tamvakis, *Greybody factors for brane scalar fields in a rotating black-hole background*, *Phys. Rev.* **D75** (2007) 084043, [hep-th/0701288].

[63] S. B. Giddings and V. S. Rychkov, *Black holes from colliding wavepackets*, *Phys. Rev.* **D70** (2004) 104026, [hep-th/0409131].

[64] S. W. Hawking, *Information loss in black holes*, *Phys. Rev.* **D72** (2005) 084013, [hep-th/0507171].

[65] R. Emparan and H. S. Reall, *A rotating black ring in five dimensions*, *Phys. Rev. Lett.* **88** (2002) 101101, [hep-th/0110260].

[66] D. Ida and K.-i. Nakao, *Isoperimetric inequality for higher-dimensional black holes*, *Phys. Rev.* **D66** (2002) 064026, [gr-qc/0204082].

[67] M. Shibata and H. Yoshino, *Nonaxisymmetric instability of rapidly rotating black hole in five dimensions*, *Phys. Rev.* **D81** (2010) 021501, [arXiv:0912.3606].

[68] O. J. C. Dias, P. Figueras, R. Monteiro, H. S. Reall, and J. E. Santos, *An instability of higher-dimensional rotating black holes*, arXiv:1001.4527.

[69] T. Banks and W. Fischler, *A model for high energy scattering in quantum gravity*, hep-th/9906038.

[70] S. N. Solodukhin, *Classical and quantum cross-section for black hole production in particle collisions*, *Phys. Lett.* **B533** (2002) 153–161, [hep-ph/0201248].

[71] S. D. H. Hsu, *Quantum production of black holes*, *Phys. Lett.* **B555** (2003) 92–98, [hep-ph/0203154].

[72] A. Jevicki and J. Thaler, *Dynamics of black hole formation in an exactly solvable model*, *Phys. Rev.* **D66** (2002) 024041, [hep-th/0203172].

[73] E. Kohlprath and G. Veneziano, *Black holes from high-energy beam-beam collisions*, *JHEP* **06** (2002) 057, [gr-qc/0203093].

[74] H. Yoshino and Y. Nambu, *High-energy head-on collisions of particles and hoop conjecture*, *Phys. Rev.* **D66** (2002) 065004, [gr-qc/0204060].

[75] H. Yoshino and Y. Nambu, *Black hole formation in the grazing collision of high-energy particles*, *Phys. Rev.* **D67** (2003) 024009, [gr-qc/0209003].

[76] H. Yoshino and V. S. Rychkov, *Improved analysis of black hole formation in high-energy particle collisions*, *Phys. Rev.* **D71** (2005) 104028, [hep-th/0503171].

[77] D. M. Gingrich, *Effect of charged partons on black hole production at the large hadron collider*, *JHEP* **02** (2007) 098, [hep-ph/0612105].

[78] H. Yoshino, A. Zelnikov, and V. P. Frolov, *Apparent horizon formation in the head-on collision of gyratons*, *Phys. Rev.* **D75** (2007) 124005, [gr-qc/0703127].

[79] H. Yoshino and T. Shiromizu, *Collision of high-energy closed strings: Formation of a ring-like apparent horizon*, *Phys. Rev.* **D76** (2007) 084021, [arXiv:0707.0076].

[80] E. Berti, M. Cavaglia, and L. Gualtieri, *Gravitational energy loss in high energy particle collisions: Ultrarelativistic plunge into a multidimensional black hole*, *Phys. Rev.* **D69** (2004) 124011, [hep-th/0309203].

[81] V. Cardoso, E. Berti, and M. Cavaglia, *What we (don't) know about black hole formation in high-energy collisions*, *Class. Quant. Grav.* **22** (2005) L61–R84, [hep-ph/0505125].

[82] P. D. D'Eath and P. N. Payne, *Gravitational radiation in high speed black hole collisions. 1. Perturbation treatment of the axisymmetric speed of light collision*, *Phys. Rev.* **D46** (1992) 658–674.

[83] P. D. D'Eath and P. N. Payne, *Gravitational radiation in high speed black hole collisions. 2. Reduction to two independent variables and calculation of the second order news function*, *Phys. Rev.* **D46** (1992) 675–693.

[84] P. D. D'Eath and P. N. Payne, *Gravitational radiation in high speed black hole collisions. 3. Results and conclusions*, *Phys. Rev.* **D46** (1992) 694–701.

[85] C. M. Harris, P. Richardson, and B. R. Webber, *CHARYBDIS: A black hole event generator*, *JHEP* **08** (2003) 033, [hep-ph/0307305].

[86] U. Sperhake, V. Cardoso, F. Pretorius, E. Berti, and J. A. Gonzalez, *The high-energy collision of two black holes*, *Phys. Rev. Lett.* **101** (2008) 161101, [arXiv:0806.1738].

[87] M. Shibata, H. Okawa, and T. Yamamoto, *High-velocity collision of two black holes*, *Phys. Rev.* **D78** (2008) 101501, [arXiv:0810.4735].

[88] U. Sperhake *et al.*, *Cross section, final spin and zoom-whirl behavior in high-energy black hole collisions*, *Phys. Rev. Lett.* **103** (2009) 131102, [arXiv:0907.1252].

[89] M. W. Choptuik and F. Pretorius, *Ultra relativistic particle collisions*, arXiv:0908.1780.

[90] M. Zilhao *et al.*, *Numerical relativity for D dimensional axially symmetric space-times: formalism and code tests*, arXiv:1001.2302.

[91] S. W. Hawking, *Particle creation by black holes*, *Commun. Math. Phys.* **43** (1975) 199–220.

[92] C. Alig, M. Drees, and K.-y. Oda, *QCD effects in the decays of TeV black holes*, *JHEP* **12** (2006) 049, [hep-ph/0610269].

[93] G. Corcella *et al.*, *HERWIG 6.5: an event generator for hadron emission reactions with interfering gluons (including supersymmetric processes)*, *JHEP* **01** (2001) 010, [hep-ph/0011363].

[94] G. Corcella *et al.*, *HERWIG 6.5 release note*, hep-ph/0210213.

[95] T. Sjostrand, S. Mrenna, and P. Z. Skands, *PYTHIA 6.4 Physics and manual*, *JHEP* **05** (2006) 026, [hep-ph/0603175].

[96] W. G. Unruh, *Second quantization in the Kerr metric*, *Phys. Rev.* **D10** (1974) 3194–3205.

[97] G. W. Gibbons, *Vacuum polarization and the spontaneous loss of charge by black holes*, *Commun. Math. Phys.* **44** (1975) 245–264.

[98] P. Candelas, P. Chrzanowski, and K. W. Howard, *Quantization of electromagnetic and gravitational perturbations of a Kerr black hole*, *Phys. Rev.* **D24** (1981) 297–304.

[99] A. C. Ottewill and E. Winstanley, *The renormalized stress tensor in Kerr space-time: General results*, *Phys. Rev.* **D62** (2000) 084018, [gr-qc/0004022].

[100] M. Casals and A. C. Ottewill, *Canonical quantization of the electromagnetic field on the Kerr background*, *Phys. Rev.* **D71** (2005) 124016, [gr-qc/0501005].

[101] J. M. Bardeen, W. H. Press, and S. A. Teukolsky, *Rotating black holes: Locally nonrotating frames, energy extraction, and scalar synchrotron radiation*, *Astrophys. J.* **178** (1972) 347.

[102] J. S. Schwinger, *On gauge invariance and vacuum polarization*, *Phys. Rev.* **82** (1951) 664–679.

[103] D. Ida, K.-y. Oda, and S. C. Park, *Rotating black holes at future colliders: Greybody factors for brane fields*, *Phys. Rev.* **D67** (2003) 064025, [hep-th/0212108].

[104] C. M. Harris and P. Kanti, *Hawking radiation from a (4+n)-dimensional black hole: Exact results for the Schwarzschild phase*, *JHEP* **10** (2003) 014, [hep-ph/0309054].

[105] C. M. Harris and P. Kanti, *Hawking radiation from a (4+n)-dimensional rotating black hole*, *Phys. Lett.* **B633** (2006) 106–110, [hep-th/0503010].

[106] D. Ida, K.-y. Oda, and S. C. Park, *Rotating black holes at future colliders. II: Anisotropic scalar field emission*, *Phys. Rev.* **D71** (2005) 124039, [hep-th/0503052].

[107] G. Duffy, C. Harris, P. Kanti, and E. Winstanley, *Brane decay of a (4+n)-dimensional rotating black hole: Spin-0 particles*, *JHEP* **09** (2005) 049, [hep-th/0507274].

[108] M. Casals, P. Kanti, and E. Winstanley, *Brane decay of a (4+n)-dimensional rotating black hole. II: Spin-1 particles*, *JHEP* **02** (2006) 051, [hep-th/0511163].

[109] V. Cardoso, M. Cavaglia, and L. Gualtieri, *Black hole particle emission in higher-dimensional spacetimes*, *Phys. Rev. Lett.* **96** (2006) 071301, [hep-th/0512002].

[110] V. Cardoso, M. Cavaglia, and L. Gualtieri, *Hawking emission of gravitons in higher dimensions: Non-rotating black holes*, *JHEP* **02** (2006) 021, [hep-th/0512116].

[111] D. Ida, K.-y. Oda, and S. C. Park, *Rotating black holes at future colliders. III: Determination of black hole evolution*, *Phys. Rev.* **D73** (2006) 124022, [hep-th/0602188].

[112] M. Casals, S. R. Dolan, P. Kanti, and E. Winstanley, *Brane decay of a (4+n)-dimensional rotating black hole. III: Spin-1/2 particles*, *JHEP* **03** (2007) 019, [hep-th/0608193].

[113] M. Casals, S. R. Dolan, P. Kanti, and E. Winstanley, *Bulk emission of scalars by a rotating black hole*, *JHEP* **06** (2008) 071, [arXiv:0801.4910].

[114] D. N. Page, *Particle emission rates from a black hole. 3. charged leptons from a nonrotating hole*, *Phys. Rev.* **D16** (1977) 2402–2411.

[115] D. N. Page, *Dirac equation around a charged, rotating black hole*, *Phys. Rev.* **D14** (1976) 1509–1510.

[116] T. Nakamura and H. Sato, *Absorption of massive scalar field by a charged black hole*, *Phys. Lett.* **B61** (1976) 371–374.

[117] E. Berti, V. Cardoso, and M. Casals, *Eigenvalues and eigenfunctions of spin-weighted spheroidal harmonics in four and higher dimensions*, *Phys. Rev.* **D73** (2006) 024013, [gr-qc/0511111].

[118] S. A. Teukolsky, *Perturbations of a rotating black hole. 1. Fundamental equations for gravitational electromagnetic and neutrino field perturbations*, *Astrophys. J.* **185** (1973) 635–647.

[119] W. H. Press and S. A. Teukolsky, *Perturbations of a rotating black hole. II. Dynamical stability of the Kerr metric*, *Astrophys. J.* **185** (1973) 649–674.

[120] A. A. Starobinskii, *Amplification of waves during reflection from a rotating black hole*, *Zh. Eksp. Theor. Fiz.* **64** (1973) 48.

[121] A. A. Starobinskii and S. M. Churilov, *Amplification of electromagnetic and gravitational waves scattered by a rotating black hole*, *Zh. Eksp. Theor. Fiz.* **65** (1973) 3.

[122] S. Chandrasekhar, *The mathematical theory of black holes*. Oxford, UK: Clarendon, 1992. 646 p.

[123] S. Chandrasekhar, *The solution of Dirac's equation in Kerr geometry*, *Proc. Roy. Soc. Lond.* **A349** (1976) 571–575.

[124] J. Doukas, H. T. Cho, A. S. Cornell, and W. Naylor, *Graviton emission from simply rotating Kerr-de Sitter black holes: Transverse traceless tensor graviton modes*, *Phys. Rev.* **D80** (2009) 045021, [arXiv:0906.1515].

[125] P. Kanti, H. Kodama, R. A. Konoplya, N. Pappas, and A. Zhidenko, *Graviton emission in the bulk by a simply rotating black hole*, *Phys. Rev.* **D80** (2009) 084016, [arXiv:0906.3845].

[126] A. L. Dudley and J. D. Finley, *Separation of wave equations for perturbations of general type-D space-times*, *Phys. Rev. Lett.* **38** (1977) 1505–1508.

[127] K. D. Kokkotas, *Quasinormal modes of the Kerr-Newman black hole*, *Nuovo Cim.* **B108** (1993) 991–998.

[128] E. Berti and K. D. Kokkotas, *Quasinormal modes of Kerr-Newman black holes: Coupling of electromagnetic and gravitational perturbations*, *Phys. Rev.* **D71** (2005) 124008, [gr-qc/0502065].

[129] S. R. Dolan, *Scattering, absorption and emission by black holes*. Cambridge Ph.D. thesis., 2006.

[130] S. Creek, O. Efthimiou, P. Kanti, and K. Tamvakis, *Greybody factors in a rotating black-hole background-ii : fermions and gauge bosons*, *Phys. Rev.* **D76** (2007) 104013, [arXiv:0707.1768].

[131] S. Creek, O. Efthimiou, P. Kanti, and K. Tamvakis, *Scalar emission in the bulk in a rotating black hole background*, *Phys. Lett.* **B656** (2007) 102–111, [arXiv:0709.0241].

[132] S. Creek, O. Efthimiou, P. Kanti, and K. Tamvakis, *Graviton emission in the bulk from a higher-dimensional Schwarzschild black hole*, *Phys. Lett.* **B635** (2006) 39–49, [hep-th/0601126].

[133] E. W. Leaver, *An analytic representation for the quasi normal modes of Kerr black holes*, *Proc. Roy. Soc. Lond.* **A402** (1985) 285–298.

[134] W. G. Baber and H. R. Hassé, *The two centre problem in wave mechanics*, *Proc. Camb. Phil. Soc.* **25** (1935) 564.

[135] W. Gautschi, *Computational aspects of three-term recurrence relations*, *SIAM Review* **9** (1967) 24.

[136] S. Zhang and J. Jin, *Computation of special functions*, . John Wiley & sons, see http://jin.ece.uiuc.edu/routines/routines.html.

[137] M. Abramowitz and I. A. Stegun, *Handbook of mathematical functions*. Dover Publications, Inc., 1965.

[138] S. Iyer and C. M. Will, *Black hole normal modes: A WKB approach. 1. Foundations and application of a higher order WKB analysis of potential barrier scattering*, *Phys. Rev.* **D35** (1987) 3621.

[139] H. T. Cho and Y. C. Lin, *WKB analysis of the scattering of massive Dirac fields in Schwarzschild black hole spacetimes*, *Class. Quant. Grav.* **22** (2005) 775–790, [gr-qc/0411090].

[140] A. S. Cornell, W. Naylor, and M. Sasaki, *Graviton emission from a higher-dimensional black hole*, *JHEP* **02** (2006) 012, [hep-th/0510009].

[141] J. Grain and A. Barrau, *A WKB approach to scalar fields dynamics in curved space- time*, *Nucl. Phys.* **B742** (2006) 253–274, [hep-th/0603042].

[142] H. T. Cho, A. S. Cornell, J. Doukas, and W. Naylor, *Bulk dominated fermion emission on a Schwarzschild background*, *Phys. Rev.* **D77** (2008) 016004, [arXiv:0709.1661].

[143] C. M. Bender and S. A. Orszag, *Advanced mathematical methods for scientists and engineers*. McGraw-Hill, Inc., 1978. page 487.

[144] S. R. Dolan, M. Casals, P. Kanti, and E. Winstanley, *Greybody factors for higher-dimensional black holes*, . http://mathsci.ucd.ie/∼sdolan/greybody/.

[145] Y. B. Zel'dovich, *The generation of waves by a rotating body*, *ZhETF Pis. Red.* **14** (1971) 270.

[146] D. Ida, K.-y. Oda, and S. C. Park, *Anisotropic scalar field emission from TeV scale black hole*, hep-ph/0501210.

[147] V. P. Frolov and D. Stojkovic, *Quantum radiation from a 5-dimensional rotating black hole*, *Phys. Rev.* **D67** (2003) 084004, [gr-qc/0211055].

[148] H. Nomura, S. Yoshida, M. Tanabe, and K.-i. Maeda, *The fate of a five-dimensional rotating black hole via Hawking radiation*, *Prog. Theor. Phys.* **114** (2005) 707–712, [hep-th/0502179].

[149] E. Jung and D. K. Park, *Bulk versus brane in the absorption and emission: 5D rotating black hole case*, *Nucl. Phys.* **B731** (2005) 171–187, [hep-th/0506204].

[150] D. A. Leahy and W. G. Unruh, *Angular dependence of neutrino emission from rotating black holes*, *Phys. Rev.* **D19** (1979) 3509–3515.

[151] M. Casals, S. R. Dolan, P. Kanti, and E. Winstanley, *Angular profile of emission of non-zero spin fields from a higher-dimensional black hole*, *Phys. Lett.* **B680** (2009) 365–370, [arXiv:0907.1511].

[152] A. Flachi, M. Sasaki, and T. Tanaka, *Spin polarization effects in micro black hole evaporation*, *JHEP* **05** (2009) 031.

[153] W. G. Unruh, *Absorption cross-section of small black holes*, *Phys. Rev.* **D14** (1976) 3251–3259.

[154] B. S. DeWitt, *Quantum field theory in curved space-time*, *Phys. Rept.* **19** (1975) 295–357.

[155] J. C. Collins and D. E. Soper, *The theorems of perturbative QCD*, *Ann. Rev. Nucl. Part. Sci.* **37** (1987) 383–409.

[156] W. Press, B. Flannery, S. Teukolsky, and W. Vetterling, *Numerical recipes in C: The art of scientific computing*. Cambridge University Press, 1992.

[157] M. Cavaglia, R. Godang, L. Cremaldi, and D. Summers, *Catfish: A Monte Carlo simulator for black holes at the LHC*, *Comput. Phys. Commun.* **177** (2007) 506–517, [hep-ph/0609001].

[158] C. M. Harris *et al.*, *Exploring higher dimensional black holes at the large hadron collider*, *JHEP* **05** (2005) 053, [hep-ph/0411022].

[159] C. M. Harris, *Physics beyond the standard model: Exotic leptons and black holes at future colliders*, hep-ph/0502005.

[160] V. Cardoso, J. P. S. Lemos, and S. Yoshida, *Electromagnetic radiation from collisions at almost the speed of light: an extremely relativistic charged particle falling into a Schwarzschild black hole*, *Phys. Rev.* **D68** (2003) 084011, [gr-qc/0307104].

[161] R. Casadio, B. Harms, and O. Micu, *Microscopic black holes as a source of ultrahigh energy gamma-rays*, astro-ph/0202513.

[162] R. Casadio, S. Fabi, and B. Harms, *Electromagnetic waves around dilatonic stars and naked singularities*, *Phys. Rev.* **D70** (2004) 044026, [gr-qc/0307022].

[163] M. Chaichian and R. Hagedorn, *Symmetries in quantum mechanics: From angular momentum to supersymmetry*. Bristol, UK: IOP, 1998. 304 p.

[164] R. Emparan, G. T. Horowitz, and R. C. Myers, *Black holes radiate mainly on the brane*, *Phys. Rev. Lett.* **85** (2000) 499–502, [hep-th/0003118].

[165] D. N. Page, *Particle emission rates from a black hole: Massless particles from an uncharged, nonrotating hole*, *Phys. Rev.* **D13** (1976) 198–206.

[166] D. N. Page, *Particle emission rates from a black hole. 2. massless particles from a rotating hole*, *Phys. Rev.* **D14** (1976) 3260–3273.

[167] M. K. Parikh and F. Wilczek, *Hawking radiation as tunneling*, *Phys. Rev. Lett.* **85** (2000) 5042–5045, [hep-th/9907001].

[168] J. Preskill, P. Schwarz, A. D. Shapere, S. Trivedi, and F. Wilczek, *Limitations on the statistical description of black holes*, *Mod. Phys. Lett.* **A6** (1991) 2353–2362.

[169] S. Dimopoulos and R. Emparan, *String balls at the LHC and beyond*, *Phys. Lett.* **B526** (2002) 393–398, [hep-ph/0108060].

[170] B. Koch, M. Bleicher, and S. Hossenfelder, *Black hole remnants at the LHC*, *JHEP* **10** (2005) 053, [hep-ph/0507138].

[171] H. Stoecker, *Stable TeV - black hole remnants at the LHC: Discovery through di-jet suppression, mono-jet emission and a supersonic boom in the quark-gluon plasma*, *Int. J. Mod. Phys.* **D16** (2007) 185–205, [hep-ph/0605062].

[172] P. Meade and L. Randall, *Black holes and quantum gravity at the LHC*, *JHEP* **05** (2008) 003, [arXiv:0708.3017].

[173] O. Lorente-Espin and P. Talavera, *A silence black hole: Hawking radiation at the Hagedorn temperature*, *JHEP* **04** (2008) 080, [arXiv:0710.3833].

[174] F. Scardigli, *Glimpses on the micro black hole Planck phase*, arXiv:0809.1832.

[175] J. D. Bekenstein and V. F. Mukhanov, *Spectroscopy of the quantum black hole*, *Phys. Lett.* **B360** (1995) 7–12, [gr-qc/9505012].

[176] D. M. Gingrich and K. Martell, *Study of highly-excited string states at the large hadron collider*, *Phys. Rev.* **D78** (2008) 115009, [arXiv:0808.2512].

[177] J. Alwall *et al.*, *A standard format for Les Houches event files*, *Comput. Phys. Commun.* **176** (2007) 300–304, [hep-ph/0609017].

[178] D.-C. Dai *et al.*, *BlackMax: A black-hole event generator with rotation, recoil, split branes and brane tension*, *Phys. Rev.* **D77** (2008) 076007, [arXiv:0711.3012].

[179] D.-C. Dai *et al.*, *Manual of BlackMax, a black-hole event generator with rotation, recoil, split branes, and brane tension*, arXiv:0902.3577.

[180] E. Richter-Was, *AcerDET: A particle level fast simulation and reconstruction package for phenomenological studies on high p(T) physics at LHC*, `hep-ph/0207355`.

[181] **ATLAS** Collaboration, G. Aad *et al.*, *The ATLAS experiment at the CERN large hadron collider*, *JINST* **3** (2008) S08003.

[182] **The ATLAS** Collaboration, G. Aad *et al.*, *Expected performance of the ATLAS experiment - Detector, trigger and physics*, `arXiv:0901.0512`.

[183] J. D. Bjorken and S. J. Brodsky, *Statistical model for electron-positron annihilation into hadrons*, *Phys. Rev.* **D1** (1970) 1416–1420.

[184] R. Penrose, *Gravitational collapse: The role of general relativity*, *Riv. Nuovo Cim.* **1** (1969) 252–276.

[185] S. W. Hawking, *Gravitational radiation from colliding black holes*, *Phys. Rev. Lett.* **26** (1971) 1344–1346.

[186] E. Byckling and K. Kajantie, *Particle kinematics*. John Wiley & sons, 1973. page 162.